Anodic Treatment of Strengthening Coatings in Electrolytes for Electrochemical Machining: II. Micromachining of Steel Surfaces Nitrated by Electrochemical Thermal Treatment: Chloride Solutions

S. A. Silkin[a], E. A. Pasinkovskii[b], V. I. Petrenko[b], and A. I. Dikusar[a, b]

[a]Shevchenko Pridnestrov'e State University, ul. 25 Oktyabrya 128, Tiraspol, Republic of Moldova

[b]Institute of Applied Physics, Academy of Sciences of Moldova, ul. Academiei 5, Chisinau, MD-2028 Republic of Moldova

e-mail: dikusar@phys.asm.md

Received Jule 4, 2011

Abstract—The anodic dissolution of the nitrated layer of steel 45 specimens at small depths after the chemical thermal treatment is studied. Investigations of the anode dissolution in 2 M NaCl were carried out using a rotating disk electrode with a partially isolated surface. The correlation between the macrokinetics of the anode processes and the technological parameters such as the roughness and microhardness of the nitrided steel surface is registered. The values of the minimal surface roughness and the maximal microhardness are shown to be almost equal to those of the initial surface prior to the treatment and be reached under high current densities ($\sim$50 A/cm^2) and intense hydrodynamic modes of treatment, i.e., in a state of thermokinetic instability (upon the constant formation and destruction of surface layers induced by the critical temperature drop and a "thermal explosion"), which arises upon an excess of the anodic limiting current.

DOI: 10.3103/S1068375512010140

This work is a continuation of [1, 2], which are devoted to the anodic treatment of the strengthening surfaces and to the solution of the problems of electrochemical micromachining (ECMM) [3]. One ECMM peculiarity is the possibility to use generally applied for electrochemical machining (ECM) ecologically relatively pure electrolytes, namely, concentrated solutions of salts (chlorides, nitrates, or their blends), which reduce the environmental load [3]. The technologies whose characteristic linear sizes of the treated surfaces are in the micrometer range can be related to the ECMM category. The treatment of strengthening electrochemical coatings is referred by definition to the ECMM category, since the thickness of such coatings remains usually in the range of a few tens of micrometers.

The development of technologies based on the anodic etching (anodic treatment) of these coatings raised a number of principal questions that have yet to be answered [2].

(1) The degree to which the currently known electrolytes and modes of machining (that were meant for bulk materials) can be used for the treatment of films with sizes reaching several tens of micrometers, which actually are strengthening coatings.

(2) Whether the functional (e.g., mechanical) properties of these coatings are conserved after the anodic modification of the surface, and what the methods to control them are in the process of the anodic etching.

(3) Whether certain dimensional effects exist in the modification of properties, i.e., whether the properties may change depending on the depth of the treated surface (the amounts of the removed material).

(4) Whether there are certain commonly used patterns to control the surface roughness, since, owing to the small thickness of the coatings and the absence of an allowance for fine machining (if needed), the roughness seems crucial for the machining of this kind of surfaces.

This work is aimed at the study of the anode dissolution of nitrided steels in chloride electrolytes. The nitriding was carried out by electrochemical thermal treatment (ECTT) in an electrolyte that contained ammonium chloride and ammonia [4]. The problem of the anodic dissolution of such coatings in chlorides is described in [5].

To establish the correlation between the fundamental characteristics of the electrochemical process of the anodic dissolution of these coatings (which are determined by the kinetics of their anodic dissolution) and the technological indices of their ECMM is the aim of this work. Here, the answers to questions 2 and 4 of the above list of problems are mainly considered, since the process was studied only in one electrolyte, namely, in a concentrated 2M NaCl solution, and the

anodic treatment was performed at a fixed depth (~25 μm).

It is noteworthy that the results of this study can be used not only for the treatment of ECTT nitrated surfaces but also for surfaces that were obtained by the classical methods of steel nitriding.

EXPERIMENTAL

Electrochemical Thermal Treatment

The frontal surfaces of the cylindrical steel 45 specimens with a 10-mm diameter and a 6-mm height were subjected to anodic ECTT. The treatment was performed using a ITEC-1 facility at a pilot-production plant of the Institute of Applied Physics of the Moldova Academy of Sciences in the nitriding mode using the following aqueous solution (wt %): 10% NH_4Cl + 5% NH_4OH. The specimen under treatment was fed the voltage (170 V), and it was then submerged into the electrolyte to be treated for 10 min. During this process, a vapor–gas shell was found to be formed on the specimen under treatment and the temperature increased to 750°C. After the treatment, the voltage was switched off, the shell collapsed, and there was a 10-sec cooling. The average value of the microhardness of the manufactured surfaces (PMT-3, Vickers indenter) was 760–650 kG/mm^2, while that of the nontreated specimens was ~230–250 kG/mm^2. The microhardness values were also measured at certain distances from the nitrated surface (using polished sections). It was shown that the maximum value of the microhardness is reached at a depth of ~20 μm, and, at a distance up to 100 μm from the surface, the average measured values at the depth under study changed by up to ±10% from the average across the entire depth. The values measured at various indenter loads (50, 100, and 200 g) were found to be approximately within the above limits.

Prior to the nitriding, the specimens were mechanically polished. The roughness of the nitrated surface according to parameter R_a (Surtonic-25 profilometer, Taylor Hobson, GB) was in the range of ~0.2–0.3 μm.

The anodic microtreatment of the manufactured surfaces was performed using a rotating disk electrode (RDE) in the form of a recessed rotating disk electrode (RRDE) [6]. The specimens were inserted flush into the fluoroplastic cartridge and were fixed at the RDE shaft. ORACAL polymer pressure-sensitive 30-μm-thick films were used for the purpose of having both treated and nontreated surfaces on a specimen (at different areas of its surface) and for performing measurements at these surfaces. The masks were made by cutting plots from the film, which were attached onto the nitrated surface of a specimen. The mask was a ring with a 20-mm external and a 3-mm internal diameter. A 3-mm diameter circle on the coating was thus avail-

able for the anodic treatment. Since the mask's thickness was comparable to the thickness of the soluble layer, this RDE version can be considered as the RRDE [6, 7]. The speed of the RDE rotation was varied from 250 to 2000 rot/min.

The nitrated surface was examined by measuring the galvanodynamic polarization curves (the current varied at a rate of 20 mA/s) in 2M NaCl at different speeds of the RDE rotation and the bulk temperature of the solution of 25°C using a PI-50-1 potentiostat (the maximum current of the polarization was 1.1 A). The surface potential was measured with respect to a saturated Ag/AgCl electrode using a Luggin capillary with a 0.3–0.9 mm external diameter, which was brought to the dissolution surface at a distance that approximately equaled the capillary's diameter.

The anodic treatment itself was carried out in the above solution under conditions that corresponded to different regions of the polarization curve (upon varying the current densities and different speeds of rotation) under the galvanostatic condition. Moreover, the time of the treatment at different current densities was selected so that the depth of the etching equaled ~25 μm.

After the anodic dissolution, the microhardness, roughness (R_a), and profile of the treated surface were studied. The roughness was measured in the center of the cavity of the etching at ~1.25 mm. Five measurements were made. Below, the average R_a values and the standard deviations are given.

The microhardness was measured as described above. Below, both the absolute and relative measured values will be presented in the form of a ratio (HV^x–HV^h/HV^h), where HV^x and HV^h are the average values of the microhardness that were measured after and prior to the anodic etching, correspondingly, at the uninsulated and insulated surfaces.

A number of measurements were made under pulse conditions of the etching. The specific parameters of the applied pulse current will be given in the proper chapter of this work. In other respects, the methods of the study were not different whatsoever from those of [2].

RESULTS AND DISCUSSION

The Macrokinetics of the Anodic Dissolution of Nitrated Steel

The efficiency of the anodic treatment of electrochemically strengthened surfaces using high current densities for the microtreatment (so-called over-limit currents or specific conditions for transpassive dissolution) [8–11] was reported in [2]. The results of [5] and the galvanodynamic polarization curves (Fig. 1) make it possible to estimate the major peculiarities of the kinetics of the high-speed anodic dissolution of
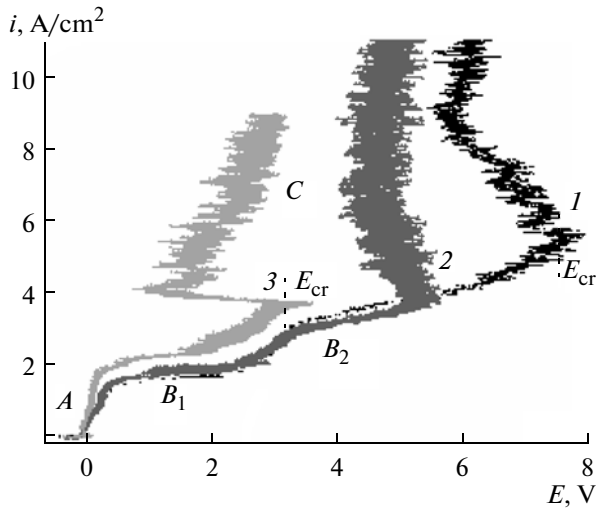
Fig. 1. Galvanodynamic polarization curves of the anodic dissolution of nitrided steel in 2M NaCl at the following RDE rotation speeds, rot/min: *1*—285.2, *2*—575.3, and *3*—1600.

Fig. 2. Dependence of the anode limiting current density in the region B_1 on the square root from the rotation frequency (*1*). See the text for the rest of the explanation.

such materials and the conditions of the transition to the necessary modes of treatment.

The following characteristic regions can be distinguished in the above curves. The *A* region of the active dissolution (activated by chloride anions) is restricted by the anode limiting currents of B_1 and B_2. Anode limiting currents were often shown earlier [9–12] to occur during the dissolution of iron and steel in chlorides owing to reaching the saturation concentration in the ternary system of iron chloride—sodium chloride—water.

Under certain critical values of the potential (E_{cr}), activation (the partial disturbance of the passivity) and transition to transpassive dissolution (the region of over-limit currents *C*) take place.

Figure 2 shows that values of the anode current density in B_1 at sufficiently high speeds of the RDE rotation for the nitrated surfaces are substantially lower than those for the nonnitrided steel (compare straight lines *1* and *3*; *3* is the straight line of the dependence of the anode current density on the RDE rotation frequency for Fe and steel in a chloride solution with the same concentration (see [5] and [12]).

The peculiarities of the diffusion kinetics of the anodic dissolution of the nitrided layer will be easy-to-understand if dependence *1* in Fig. 2 is accepted to result from the mixed kinetics of the anodic dissolution.

Dividing the measured anodic limiting current density into the diffusional and kinetic components (see also Fig. 3), we can write that
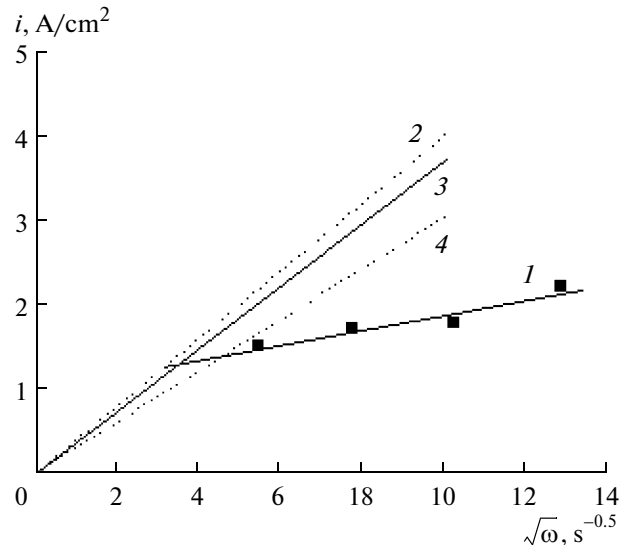
$$1/i = 1/i_k + 1/i_d, \qquad (1)$$

where i_k and i_d are the kinetic and diffusional current densities, correspondingly. Taking into account that, for the RDE $i_d = K\sqrt{\omega}$ [13], we obtain from (1)

$$i_d/i_{mx} = 1 + K\sqrt{\omega/i_k}, \qquad (2)$$

where i_{mx} is the current density under the mixed kinetics, i.e., within the framework of the accepted model $i = i_{mx}$.
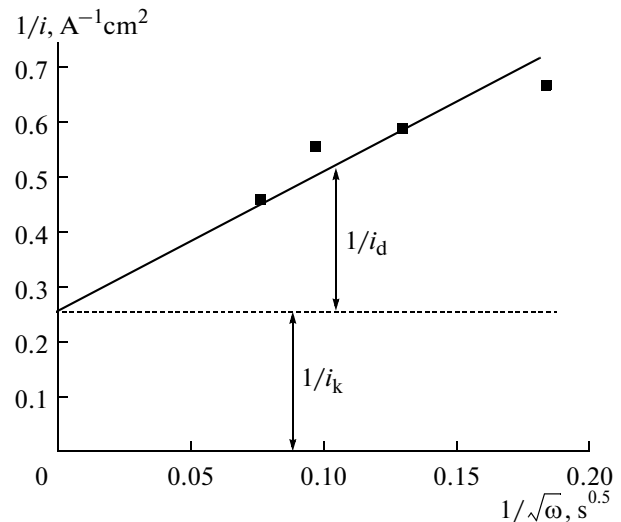

Fig. 3. Differentiation of the diffusion currents measured in region B_1 (Fig. 1) into the diffusion and kinetic constituents. The dependence of i_d on $\sqrt{\omega}$ obtained on this basis is presented by straight lines *2* and *4* in Fig. 2.

From (2), it follows that (1) the excess of the diffusion current of the dissolution of the steel versus the current of the dissolution of the nitrided surface will grow with an increase in the stirring rate (ω) and, (2) at sufficiently small ω, the second term in (2) can be close to 0, and the dissolution rate of the nitrided steel will be purely diffusional ($i_d \approx i_{mx}$).

These peculiarities of the anodic dissolution in region B_1 follow from Fig. 2. Moreover, as is shown in [5], during the dissolution of the nitrided steel in the region of low rates of stirring, the salt film that has formed in this process covers the entire surface under the treatment, and the dissolution occurs through this film, i.e., in a purely diffusional mode. Similar peculiarities of the macrokinetics of the anodic dissolution with the formation of salt films are reported more thoroughly in [14] using the example of the anodic dissolution of iron in nitrate solutions.

The results of the analysis that are based on the determination of i_d from the results shown in Fig. 3 justify the correctness of the proposed model. Straight line 2 (Fig. 2) is the dependence of i_d on $\sqrt{\omega}$ that was obtained on the basis of the data in Fig. 3. That is, the diffusional constituent of the current density almost coincides with the relationship for the dissolution of iron and steel that was obtained earlier [5, 12]. Since the data presented in Fig. 3 (as well as in Fig. 2) are the results of the dissolution of one particular nitrided surface, the determination of i_d and i_k (the way it is done in Fig. 3) for the other nitrided specimens yields the spread of dependences of i_d on $\sqrt{\omega}$ that correspond to curves 2 and 4 in Fig. 2.

Taking into account that the nitrogen concentration and the qualitative characteristics of the concentrations of the phases that compose the nitrided surface can differ on different surfaces, the agreement of the diffusion current values obtained in [5, 12] and calculated under the condition that the dissolution of the nitrided steel follows the laws of mixed kinetics can be considered satisfactory.

There is a question that remains unanswered, namely, what kind of a chemical or electrochemical reaction that occurs in the kinetic mode is responsible for the obtained i_k value. One possible answer is the chemical dissolution of iron nitride as was described in [5].

Due to the acidation of the near-electrode layer that results from the hydrolysis of the dissolution products, the following chemical reaction possibly occurs at a rate comparable with that of the convective diffusion of the dissolution products of the steel:

$$\text{FeN} + 4\text{H}^+ \rightarrow \text{NH}_4^+ + \text{Fe}^{+3}. \tag{a}$$
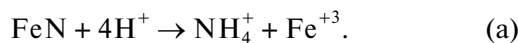
As is shown in [5], the specific dissolution rate (mg/C) in region A can exceed the rate according

Faraday law with the formation of Fe(II) being considered, and it depends on the nitriding temperature, which indirectly attests to the contribution of reaction (a).

However, the stoichiometry of the reaction in region B_1 can vary. Thus, at a potential of +1.4 V, the dissolution current output under the condition that the salt film covers the entire surface of the specimen (at low rates of stirring) is only 85–90% with the formation of Fe(II) being considered [5]. It is clear that, with an increase in the potential, the acidation of the surface occurs, and, at a sufficiently high anode potential Fe(III), it will completely transfer into the solution rather than Fe(II). The saturation concentration in the system iron (III) chloride–sodium chloride–water is found to be substantially higher than that in a similar system for Fe(II) [15]. This leads to the arising of the limiting current B_2, which is higher than B_1, which is caused by an increase of the dissolution of the salt film upon the formation of Fe(III) as the dissolution product (Fig. 1).

The above analysis shows that the dissolution kinetics may be different in the regions of low and high rates of stirring. It can be either diffusional (at low rates of the RDE rotation, when the salt film covers the entire treated surface) or mixed (at high rates of the RDE rotation, when the salt film just partially covers the surface). Moreover, it is clear (see, e.g., (1')) that the higher the rate of the RDE rotation, the more the kinetic control will determine the total rate of the process. Such changes may vary the activation energies of the overall process.

One way of the transition to the C region (over limiting currents of transpassive dissolution region) is reaching the conditions for the existence of the phenomenon of thermokinetic instability (TKI) [9, 10].

Based on the measured values of E_{cr} (Fig. 1), the critical temperature drops of the transition to the TKI (table) were calculated. Here, the measured values of E_{cr}^{msd} were corrected for the ohmic potential drop between the end of the Luggin capillary and the surface [16]:

$$\Delta E_{ohm} = i(l - 0.3d)/\chi, \tag{3}$$

where d is the Luggin capillary's diameter, l is the distance of it from the electrode's surface, and χ is the electroconductivity of the solution. In the calculations, the results of which are listed in the table, it is taken into account that, in the described experiments (Fig. 1), $d = l = 0.9$ mm.

The value of the critical temperature drop ΔT_s^{cr} was calculated by (4) on the assumption that the Peltier

heat can be neglected owing to the very high values of the dissolution potentials:

$$\Delta T_s^{cr} = i_{cr} E_{cr}/\alpha, \qquad (4)$$

where α is the coefficient of heat transfer from the RDE surface to the solution (see [10]).

The value of the critical surface temperature of the transition to the TKI can be calculated using (5) [10, 16]:

$$T_s^{cr} = E_a/2R[1 - (\sqrt{1 - 4RT_0})/E_a], \qquad (5)$$

in which E_a is the energy of activation of the process and T_0 is the bulk temperature of the solution. The results of the calculations are listed in the table. As is seen, the obtained values of the activation energy at low speeds of rotation are very close to those when the speed is determined by the diffusion stage with the salt film being formed [10], while, at higher speeds, the calculated values of E_a correspond to the conditions under which the dissolution occurs in the mode of mixed kinetics. In this situation, the share of the diffusion constituent, which determines the overall rate of the electrode process, decreases with an increase in the rotation speed.

The obtained data is a valid argument in favor of the fact that the transition to region C (Fig. 1) is caused by the KTI of the electrochemical process.

It is noteworthy that the differences in the dissolution kinetics lead to the essentially different critical temperature drops and, hence, to different current densities and potentials in the transition to the TKI.

The Correlation between the Macrokinetics of the Electrode Process and the Surface Roughness after the Treatment

Figures 4–7 show the measurement results, which confirm the presence of a correlation between the peculiarities of the macrokinetics of the anode process and the surface roughness.
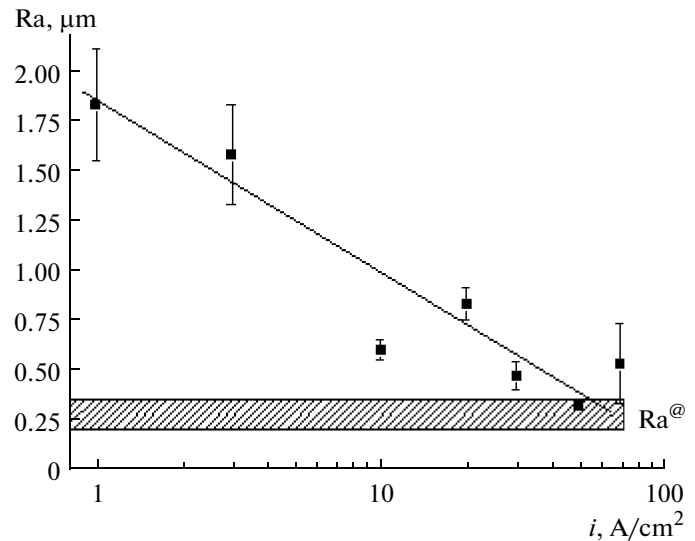

Fig. 4. Effect of the current density of the treatment on the roughness of the obtained surface. The RDE rotation rate is 2000 rot/min.

Figure 1 shows the curves of the limiting current densities during the TKI transition, which are in the range of 4–5 A/cm². They insignificantly vary with the change of the stirring rate. In order to obtain the dependence on the current density in the wide range of the current densities of the treatment, the latter was performed at the RDE speed of 2000 rot/min (Fig. 4). As is seen, an abrupt decrease in roughness is reached at the current densities of the treatment that exceed the critical values of the TKI transition, and the minimum values of R_a are attained at the current density of ~50 A/cm². An increase in the dissolution current density is known (see, e.g., [17, 18]) to cause a decrease in the surface roughness provided no other factors affect it. This is what occurs in the treatment under study at the current densities that exceed those of the TKI transition. Reaching low R_a values is confirmed by the results of scanning electron microscopy

Critical parameters and activation energy of the electrochemical process depending on the hydrodynamic conditions

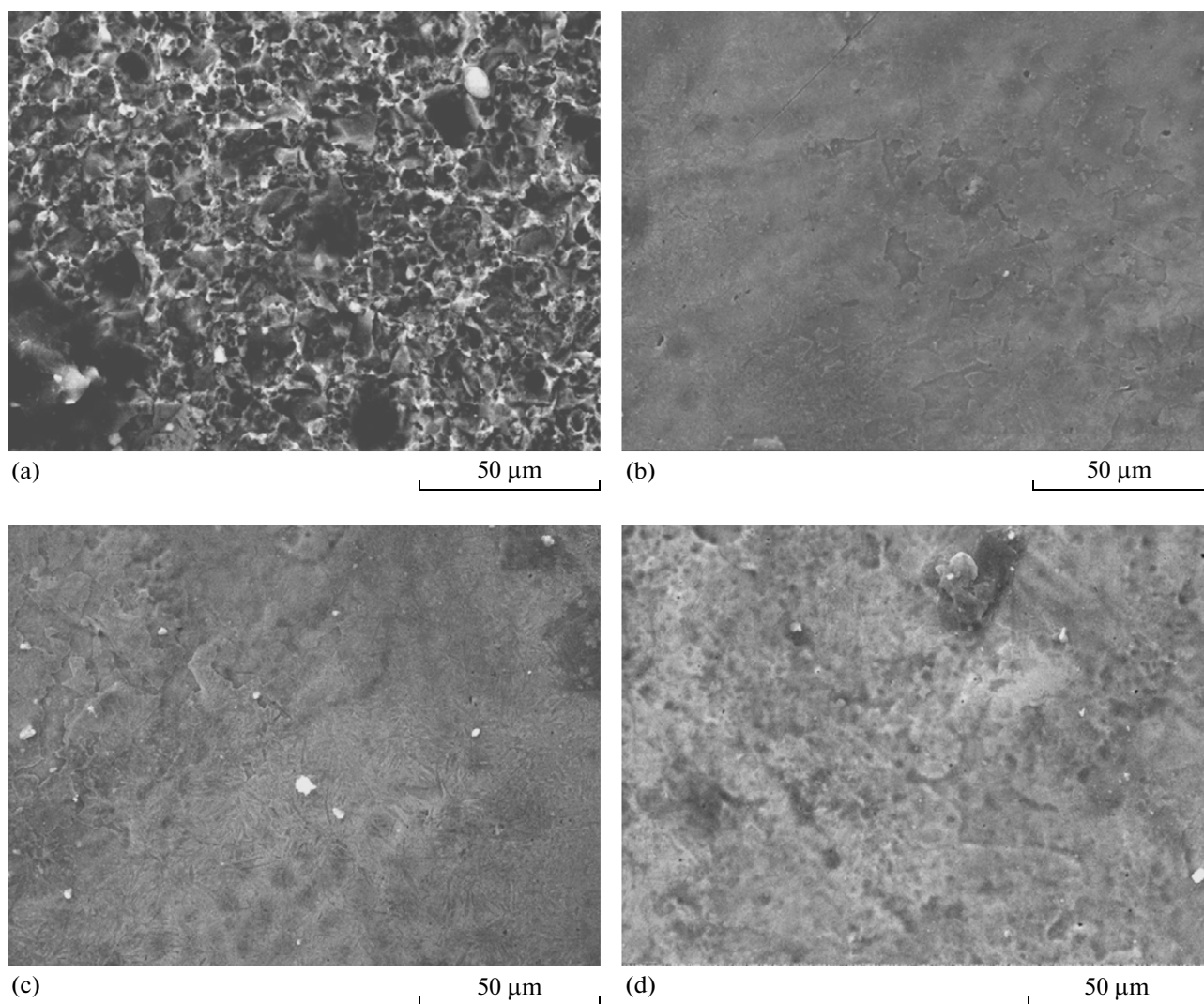| Number	Rotation frequency n, rot/min	Potential (measured), E_{cr}^{msd}, V	Allowance, ΔE_{ohm}, V	Critical potential E_{cr}, V	i_{cr}, A/cm²	α, W/(cm² deg)	ΔT_{cr}^s, °C	E_a, kJ/mol
1	285	7.5	2.3	5.2	5.3	0.37	75	~15
2	575	5.2	1.6	3.6	3.7	0.47	28	~40
3	1600	3.2	1.6	1.6	3.8	0.82	8	~110

Fig. 5. The surfaces after the treatment at the current densities (A/cm^2): 1 (a), 10 (b), 20 (c), and 50 (d). The RDE rotation rate is 2000 rot/min.

of the surface after low treatment (Fig. 5) and by the profiles of the treated surface (Fig. 6).

The results of the study of the effect of the rate of stirring at various current densities of the treatment also confirm the presence of a correlation between the peculiarities of the macrokinetics and the roughness of the surface (Fig. 7). It is seen that, at low current densities of the treatment, the increase in the stirring rate leads to the roughness growth, since here the treatment occurs in region A, and the higher the RDE rotation speed, the less the working current density with respect to the limiting anodic current density. At a current density of the treatment that exceeds the density of the TKI transition (10 A/cm^2), the inverse picture is observed, since the increase in the stirring rate decreases the current density of the TKI transition (table); hence, the ratio i_w/i_{lim} (i_w and i_{lim} are the work-

ing and limiting current densities, correspondingly) increases. At very high current densities (20 A/cm^2), i.e., at a significant excess of the working current density compared to the current density of the TKI transition, the hydrodynamic conditions almost do not affect the surface roughness reached (Fig. 7).

It is thus clear that, during the treatment of the nitrided surfaces in chloride solutions, the highest densities of the current (and, hence, the intense hydrodynamic modes of treatment) must be used in order to reach the minimum surface roughness.

Microhardness Variation after the Treatment

Not only a decrease in the roughness but also the reaching of fairly high values of the surface microhardness can be ensured by the treatment under high cur-
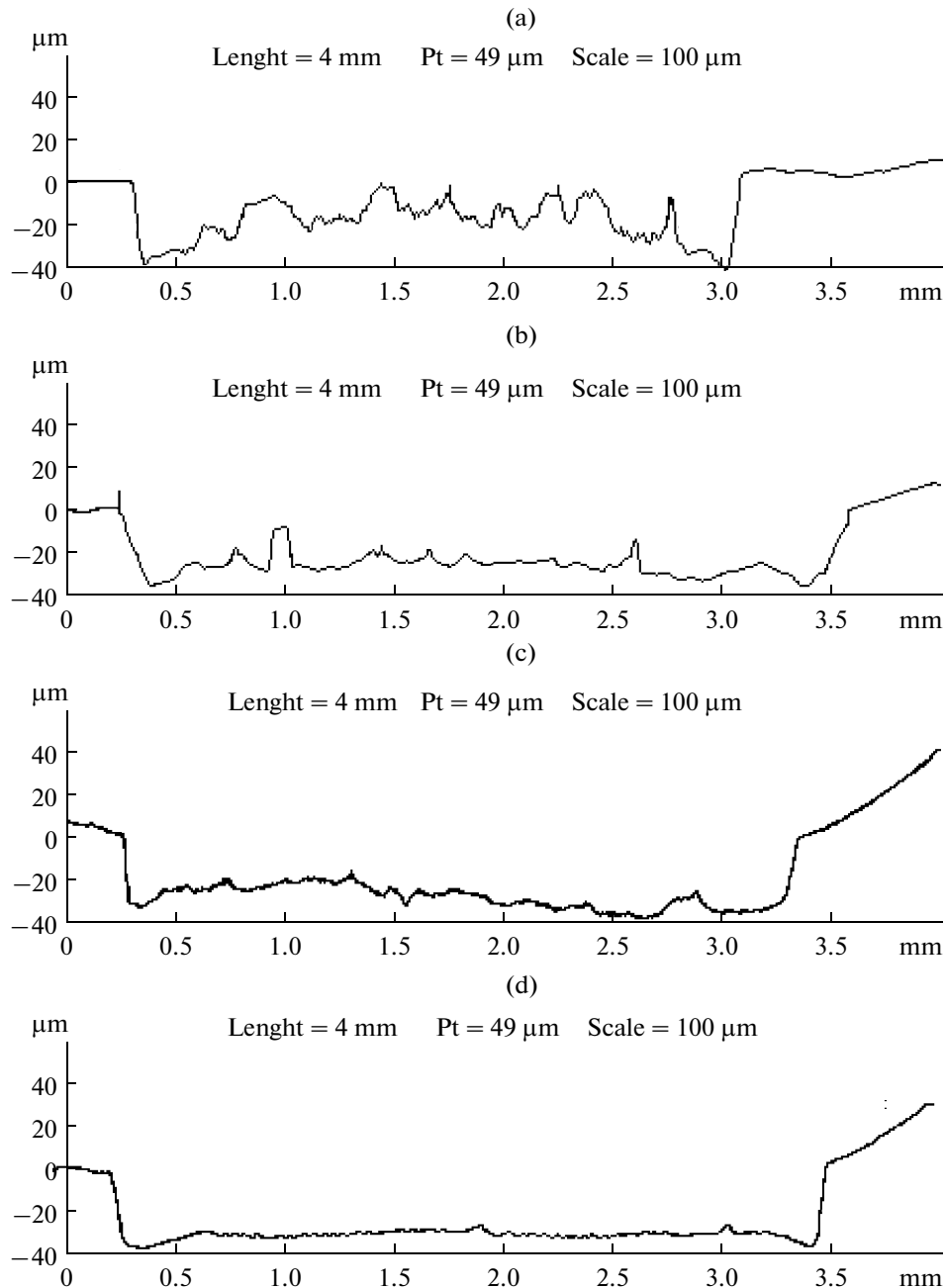
(a)

Lenght = 4 mm   Pt = 49 μm   Scale = 100 μm

(b)

Lenght = 4 mm   Pt = 49 μm   Scale = 100 μm

(c)

Lenght = 4 mm   Pt = 49 μm   Scale = 100 μm

(d)

Lenght = 4 mm   Pt = 49 μm   Scale = 100 μm

Fig. 6. Profiles of the treated surfaces of nitrided steel in 2M NaCl at the current densities (A/cm^2): 1 (a), 10 (b), 20 (c), and 50 (d). The RDE rotation rate is 2000 rot/min.

rent densities. The average value of the microhardness after the anodic treatment in the range of current densities of 20–70 A/cm^2 (650 kG/cm^2) is reduced by less than 10% versus the average value of the microhardness of the initial nitrided surface (~700 kG/cm^2, Fig. 8).

In the region of lower current densities, the degree of softening after the treatment is more vivid (Figs. 8, 9).

At the same time, the softening might not occur provided that the current density and hydrodynamic conditions are selectively adjusted (Fig. 10).

The Anodic Treatment under Pulse Conditions

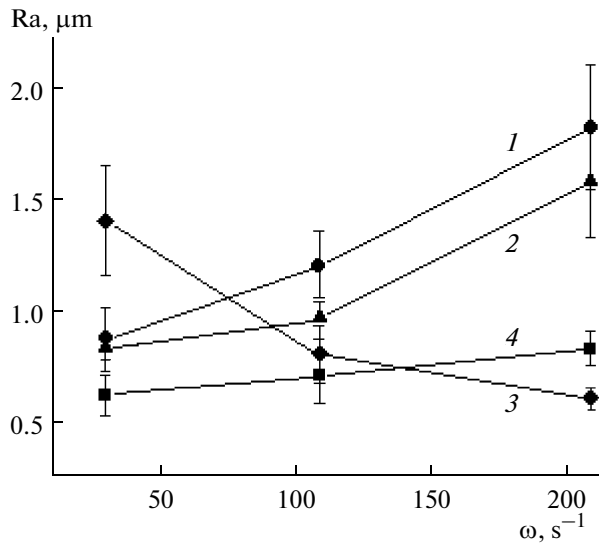Possibilities for the active control over the surface microhardness by the pulse modes of treatment were

Ra, µm

Fig. 7. The effect of the stirring rate on the surface roughness of the nitrided steel treated at the current densities, A/cm^2: *1*—1, *2*—3, *3*—10, and *4*—20.
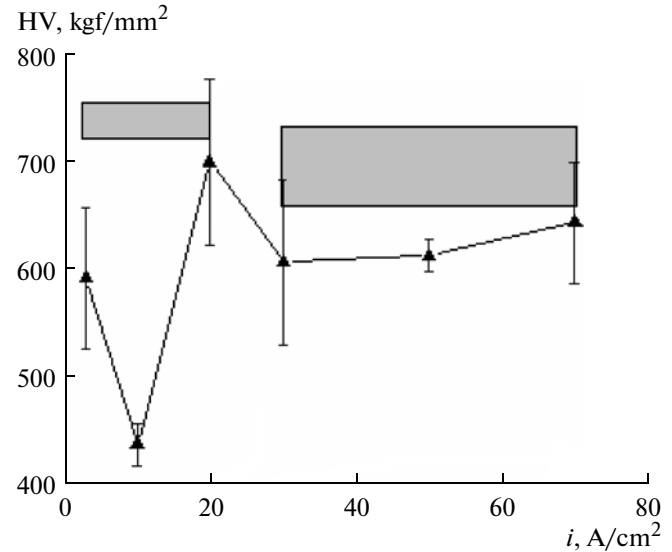
HV, kgf/mm^2

Fig. 8. Effect of the current dencities on the surface microhardness after the treatment at 2000 rot/min. The hatched areas correspond to the values of the microhardness prior to the anodic treatment.
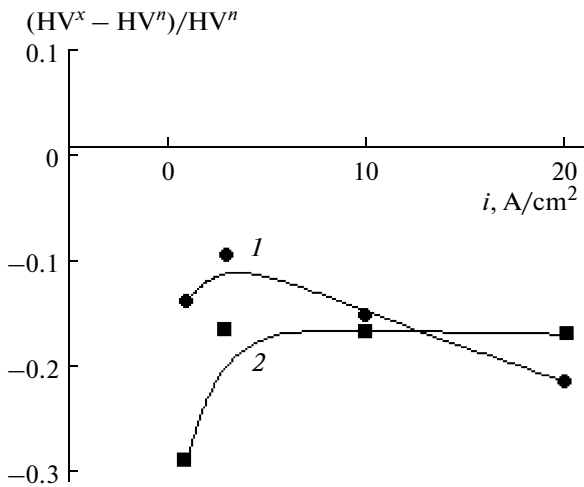
$(HV^x - HV^n)/HV^n$

Fig. 9. Effect of the current density on the relative softening of the surface at the RDE rotation speeds (rot/min): 290 (*1*) and 2000 (*2*).
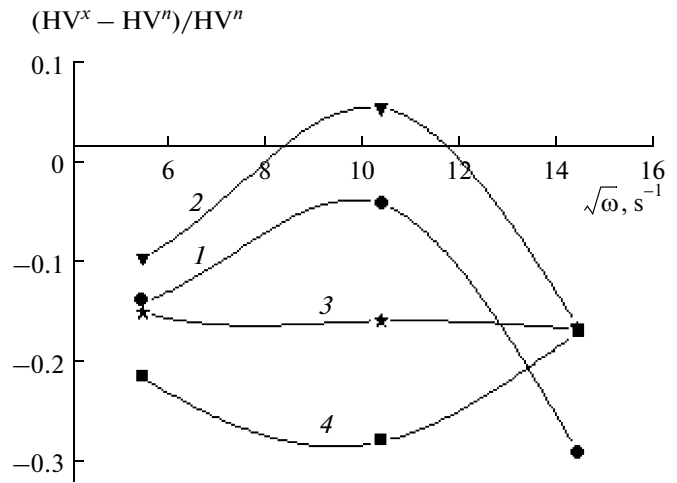
$(HV^x - HV^n)/HV^n$

Fig. 10. Effect of the RDE rotation speed on the relative change of the microhardness after the treatment of the nitrided surfaces at the current densities, A/cm^2: *1*—1, *2*—3, *3*—10, and *4*—20.

reported in [2] using the example of the anodic etching of Co−W coatings. An attempt to study the effect of the pulse conditions of etching on the surface roughness and microhardness was also made in this work (Figs. 11, 12). The treatment was carried out at a pulse current density of 10 A/cm^2 and a pulse time of 0.5 s, and the pause time ranged from 0.1−3 s. In all of the cases, the roughness values were found to be higher

than those obtained under a constant current with the same density, and the degree of softening was higher as well. A possible reason for the observed phenomena is a decrease in the average surface temperature. This certainly does not mean that the pulse conditions are ineffective for the treatment of nitrided surfaces. A search for more efficient pulse conditions of the treatment must be the subject for further investigations.
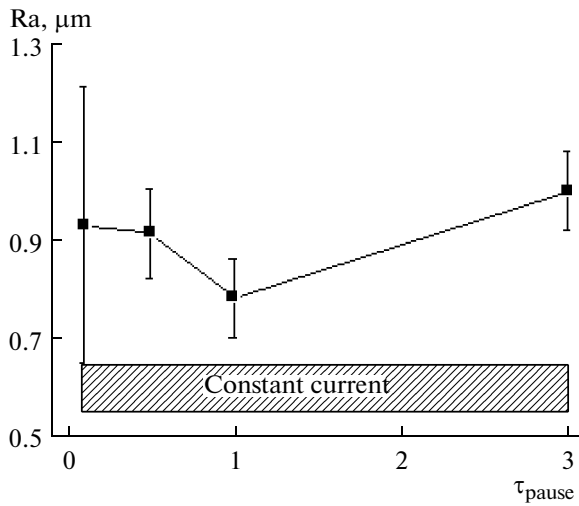
Fig. 11. Effect of the pause time during the pulse anodic dissolution of the nitrided steel (the pulse current density is 10 A/cm^2, and the pulse duration is 0.5 s) on the surface roughness after the treatment.
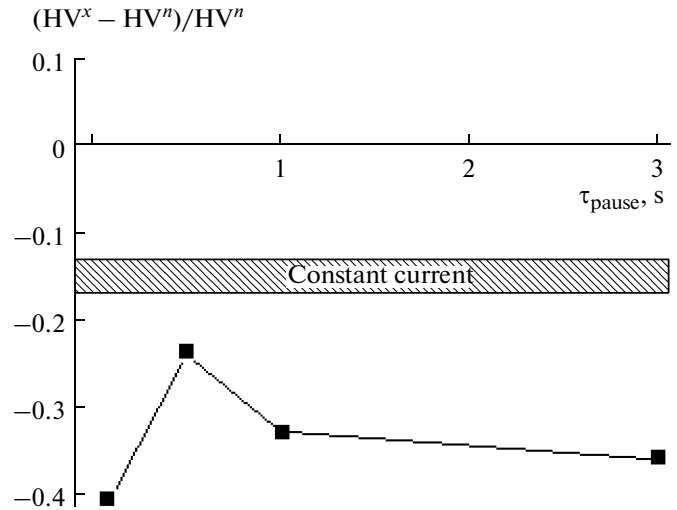

Fig. 12. Effect of the pause time during the pulse anodic dissolution of the nitrided steel (the pulse current density is 10 A/cm^2, and the pulse duration is 0.5 s) on the surface softening after the treatment.

CONCLUSIONS

The results of this study show that the macrokinetics of the anode processes under the conditions of electrochemical dissolution of nitrided steel surfaces in a chloride electrolyte are correlated with the technological indices such as the surface roughness and microhardness. The minimum roughness and maximum microhardness of the surface (which almost conserve the values of the initial surface prior to the treatment) are shown to be reached at high current densities (~50 A/cm^2) and intense hydrodynamic modes of treatment, which can ensure the treatment at these high rates. From the viewpoint of the macrokinetics of the dissolution, this implies that the treatment must be performed in the mode of thermokinetic instability (i.e., constant formation and destruction of surface layers upon reaching the critical drop in temperature and a thermal explosion [10, 19]). It is shown that the condition for the transition to this treatment mode is found to be an excess of the anode over-limit current, which is lower for the dissolution of nitrided (than nonnitrided) steel surfaces (with the treatment occurring in chloride with the same concentration) and is determined by the mixed kinetics. The activation energy in this process (which determines the value of the critical temperature drop) substantially depends on the hydrodynamic conditions of the treatment.

ACKNOWLEDGMENTS

REFERENCES

1. Silkin, S.A., Petrenko, V.I., and Dikusar, A.I., Anodic Dissolution of Electrochemical Chromium Coatings in Electrolytes for Electrochemical Machining. The Dissolution Rate and Surface Roughness, *Surf. Eng. Appl. Electrochem.*, 2010, vol. 46, no. 1, pp. 1–8.

2. Silkin, S.A., Petrenko, V.I., and Dikusar, A.I., Anodic Treatment of Strengthening the Electrochemical Coatings in Electrolytes for Electrochemical Machining: 1. Micromachining of CoW Coatings in Nitrate and Nitrate-Alkaline Solutions. *Surf. Eng. Appl. Electrochem.*, 2011, vol. 47, no. 4, pp. 295–307.

3. Datta, M. and Romankiw, L.T., Application of Chemical and Electrochemical Micromachining in Electronic Industry, *J. Electrochem. Soc.,* 1989, vol. 136, no. 6, pp. 285C–293C.

4. Belkin, P.N., *Elektrokhimiko-termicheskaya obrabotka metallov i splavov* (Electro-Chemical Thermal Treatment of Metals and Alloys), Moscow: Mir, 2005.

5. Silkin, S.A., Pasinkovskii, E.A., Petrenko, V.I., and Dikusar, A.I., High Rate Anodic Dissolution in Chloride Solutions of Steel after Electrothermochemical Treatment, *Surf. Eng. Appl. Electrochem.*, 2008, vol. 44, no. 5, pp. 343–352.

6. Dinan, T.E., Matlosz, M., and Landolt, D., Experimental Investigation of the Current Distribution on Recessed Rotating Disk Electrodes, *J. Electrochem. Soc.*, 1991, vol. 138, no. 10, pp. 2947–2951.

7. Dikusar, A.I., Redkozubova, O.O., Yushchenko, S.P., Kriksunov, L.V., and Harris, D., Role of Hydrodynamic

Conditions in the Distribution of Anodic Dissolution Rates in Cavity Etching Regions During Electrochemical Micromachining of Partially Insulated Surfaces, *Russ. J. Electrochem,*, 2003, vol. 39, no. 10, pp. 1073–1077.

8. Landolt, D., Muller, R.H., and Tobias, C.W., *Transport Processes in ECM. Fundamentals of Electrochemical Machining*, Prinston: 1971.

9. Dikusar, A.I., *Engel'gardt, G.R., Petrenko, V.I., and Petrov, Yu.N., Elektrodnye protsessy i protsessy perenosa pri elektrokhimicheskoi razmernoi obrabotke metallov* (Electrode Processes and Processes during Electrochemical Machining of Metals), Chisinau: Shtiintsa, 1983.

10. Dikusar, A.I., Engel'gardt, G.R., and Molin, A.N., *Termokineticheskie yavleniya pri vysokoskorostnykh elektrodnykh protsessakh* (Thermokinetic Phenomena during High Rate Electrode Processes), Chisinau: Shtiintsa, 1989.

11. Davydov, A.D. and Kozak, E., *Vysokoskorostnoe elektrokhimicheskoe formoobrazovanie* (High Rate Electrochemical Shaping), Moscow: Nauka, 1990.

12. Kuo, H.C. and Landolt, D., On the Role Mass of Transport in High Rate Dissolution of Iron in Concentrated Chloride Media, *Electrochim. Acta*, 1975, vol. 20, no. 5, p. 393.

13. Pleskov, Yu.V. and Filinovskii, V.Yu., *Vrashchayushchiisya diskovyi elektrod* (Rotating Disk Electrode), Moscow: Nauka, 1972.

14. Dikusar, A.I., Redkozubova, O.O., Yushchenko, S.P., and Yahova, E.A., Anodic Dissolution of Armco Iron in a Mixed Kinetics Mode: Effect of Macroscopic Heterogeneity, *Russ. J. Electrochem.*, 2002, vol. 38, no. 6, pp. 632–637.

15. Kirgintsev, A.I., Trushnikova, L.N., and Lavrent'eva, V.G., *Spravochnik po rastvorimosti neorganicheskikh veshchestv v vode* (Handbook on Dissolution of Inorganic Substances in Water), Leningrad: Khimiya, 1972.

16. Piontelli, R., Biandi, G., Bertocci, U., Guersi, C., and Bivolta, B., Metmethoden der Polarisationsspannungen II, *Z. Electrochem.*, 1954, vol. 58, no. 1, pp. 54–64.

17. McGeogh, J.A., *Principles of Electrochemical Machining*, 1974.

18. Gamburg, Yu.D., Davydov, A.D., and Kharkats, Yu.I., Modification of Roughness during Anodic Dissolution and Cathode Release of Metals (review), *Elektrokhimiya*, 1994, vol. 30, no. 4, pp. 422–443.

19. Engelgardt, G.R. and Dikusar, A.I., Thermokinetic Instability of Electrode Processes. Part I. Theoretical Analysis, *J. Electroanal. Chem.*, 1986, vol. 207, no.1, pp. 1–11.

Detailed Elaboration and General Model of the Electron Treatment of Surfaces of Charged Plasmoids (from Atomic Nuclei to White Dwarves, Neutron Stars, and Galactic Cores): Self-Condensation (Self-Constriction) and Classification of Charged Plasma Structures—Plasmoids
Part 1. General Analysis of the Convective Cumulative–Dissipative Processes Caused by the Violation of Neutrality: Metastable Charged Plasmoids and Plasma Lenses

Ph. I. Vysikaylo

Technological Institute of Superhard and Novel Carbon Materials, ul. Tsentral'naya 7a, Troitsk, 142190 Moscow oblast, Russia
e-mail: filvys@rambler.ru
Received June 6, 2011

Abstract—The processes of the accumulation and dissipation of electron flows in polarizable plasma structures with spatially distributed electric charges are investigated. It is proved that a slight violation of neutrality (about 10^{-18}) because of forcing the electrons out of the structures leads to sputtering (bouncing) of neutral structures that were gravitating before. As the de Broglie wavelength of an electron is many times greater than that of a nucleon or atomic nucleus at equal temperatures, in the case of condensation of matter into quantum structures (in which there occurs degeneration of the sharing electron gas), there should happen the violation of neutrality and the generation of giant peripheral electric fields that self-focus the plasmoid thus being a dynamic surface tension. Electric fields are effective catalysts of thermonuclear reactions leading to neutronization of the substance compressed by gravitation. Einstein's idea concerning mass–energy equivalence is confirmed in a new form. The equivalence manifests itself in a similar functionality in the process of the pulsation (focusing and rebounding) of "excessive" energy in the generalized Kepler 2D-problem (for the gravitational and the electric potential) and the "excessive" mass in the Vysikaylo–Chandrasekhar 3D problem concerning the accumulation and dissipation of the de Broglie waves in quantum stars (pulsating accretion of quantum stars) with a mass greater than that of Chandrasekhar (~1.46 masses of the sun). A new mechanism (type) of a thermonuclear reactor at the surface of charged quantum stars and dense cores of ordinary stars and planets is proposed by the author. The acceleration of electrons to MeV energies in the synergistic electric fields of uncompensated for charged particles in the nuclei of giant plasmoids—quantum stars—and their transmutation into the neutrons on the surface layer in the reactions with the protons is the basis for such a mechanism. In the presence of dynamic surface tension caused by the Coulomb forces the cumulation of plasma and energy takes place during the compressing electric field jumps.

INTRODUCTION

It is well known that the Coulomb law (and, correspondingly, the Poisson equation for an electric field in the region of charged structures with a space charge distributed in 4D space–time) operates within a great range of characteristic dimensions from $R \sim 10^{-15}$ m (the atomic nucleus dimensions) to 10^{26} m (the visible universe dimensions). These dimensions correspond to the typical frequencies of convective processes that take place at the velocity of light within the range from 10^{24} s^{-1} to 10^{-18} s^{-1}. The last frequency corresponds to the time of light's passage through the visible universe.

The violation of neutrality of nucleons in atomic nuclei is significant. The number of neutrons and protons in atomic nuclei is almost equal, and the uncompensation charge parameter is $\alpha_i = n_i/n \approx 1/2$. Here, n_i is the density of the particles with an uncompensated positive charge, and n is the density of all the nucleons (protons and neutrons).

The violation of neutrality in the structures in gas-discharge plasma is not large, and α_i in the structures presented in Figs. 1–4 is not more than 10^{-6}. However, a number of the main properties of the metastable structures charged or polarized in the 3D space (plasmoids) self-condensing in the coulomb potential wells
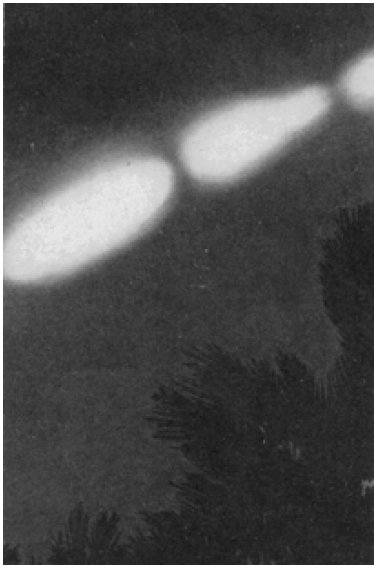
Fig. 1. Beaded lighting. Palm leaves with a diameter ≈0.5 m are seen at the bottom of the photograph.
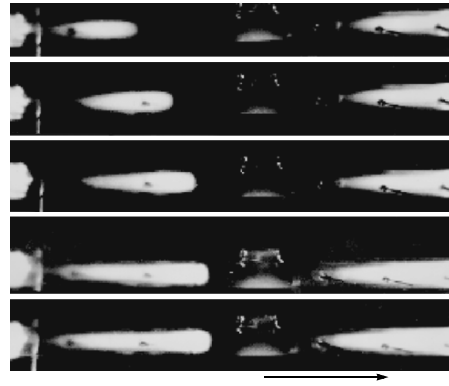

Fig. 2. A discharge in a tube in nitrogen versus the discharge current at $P = 15$ Torr [1, 2]. The cathode is on the left, while the anode is on the right. The discharge is disturbed by a bunch of fast electrons with energy of ~100 keV introduced through a window in the center of the tube. There is observed the classic Faraday dark space in the cathode spot (a bean on the cathode). Under the conditions of a low-current discharge (photos 1 and 2), behind the window there are seen small glowing regions; the following analogs of the Faraday dark space; and, along the arrow, the conic glowing regions indicating the defocusing of the electrons behind the dark area.
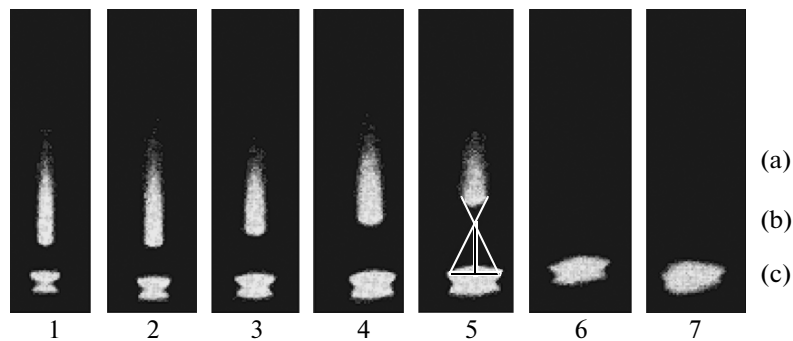

Fig. 3. The width of the cylindrical self-focusing discharge in ultraclean nitrogen versus the current [3]: $I = 0.6$ (1); 0.8 (2); 1.1 (3); 1.65 (4); 2.2 (5); determination of the libration point, 2.9 (6); and 3.25 (7) mA; $P = 5$ Torr. (a)—the positive column (with the blue glow extending to the anode and not recorded by the photo); (b)—the Faraday dark space; (c)—the negative glow or the cathode spot (the lower spot is a flare on the mirror-finished electrode).

are common. Thus, there should be generalized (at least in outline) the data accumulated in the course of the investigation of the charged structures with electric field jumps (shock waves) (Fig. 5) or potential wells for electrons (Fig. 5c—d) with dimensions from 10^{-15} m to quantum stars (10^{10} m). This generalization seems to be rather useful from the point of view of the system of fractionating specific "mysterious" 3-dimensional dynamic phenomena of generation, pulsation, and the lasting existence of various plasma structures (plasmoids), particularly in gas-discharge plasma (Figs. 1—4) and semiconductors. The author proves that it is necessary to apply, study, continuously verify, and develop the general idea presented as a diagram in Fig. 5 in dif-

ferent natural sciences (atomic physics, nanotechnology, astrophysics, gas-discharge plasma, etc.).

SHOCK WAVES OF THE ELECTRIC FIELD OR JUMPS FORMING THE CHARGED METASTABLE COULOMB RESERVOIRS (PLASMOIDS) FOR THE KINETIC ENERGY OF ELECTRONS

Early in the 20th century, Rutherford established through his experiments that the atomic nuclei are very small ($R \sim 10^{-15}$ m) and are charged by a positive charge; hence, they are surrounded by stationary jumps of the electric field with strength up to 10^{21} V/m (Fig. 5a). According to the nuclear drop model and the
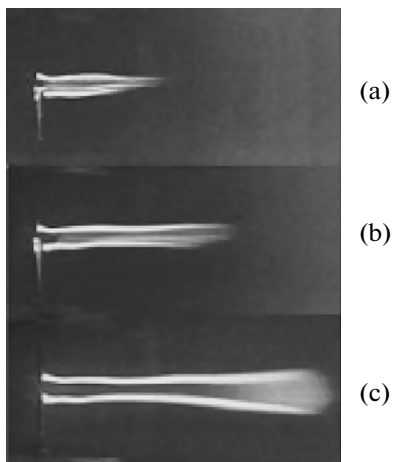
Fig. 4. The appearance of a direct current discharge between the needles in the aerodynamic tube at $M = 6$, $P_0 = 50$ atm, $p = 28$ Torr, and $D_0 = 3$ mm and at different values of the current I and the voltage U (a–c): (a)—$I = 0.2$ A, $\langle U \rangle = 2.45$ kV; (b)—$I = 0.5$ A, $\langle U \rangle = 1.95$ kV; (c)—$I = 1$ A, $\langle U \rangle = 1.7$ kV. The unclosed cylindrical electric filaments with the strata are observed down along the horizontal flow. The needle (the grounded cathode) is at the bottom. The exposition time is 1/60 s [4].

Gauss law, we obtain the following electric field profile in such stationary spherically symmetric jumps (see Fig. 5b) corresponding to the potential barrier $U(r) = \int eE(r)dr \sim r^2$; that is, $U(R) \sim R^2$ for a negatively charged particle with the energy $E_k > 0$ (Fig. 5c). At the electric field strengths $\sim 10^{22}$ V/m, the electric field energy density P_E is already comparable with the mass energy density m_0 in the atomic core with volume V_0 ($P_E = \varepsilon_0 E^2/2 \sim m_0 c^2/V_0$). These are stationary jumps of the electric field or electric potential forming on the boundary of the spherically symmetric charged structures. These electric potential jumps seem to efficiently prevent the neutrons from destruction in the case of β-disintegration focusing the electrons back into the atomic nucleus.

In 1964, Gunn discovered the moving electric field jumps (the space charge layers or the shock waves with violation of neutrality) in semiconductors [11]. They are called the domains of the electric field. Visually observed shock waves with violation of neutrality in gas-discharge plasma were discovered analytically in
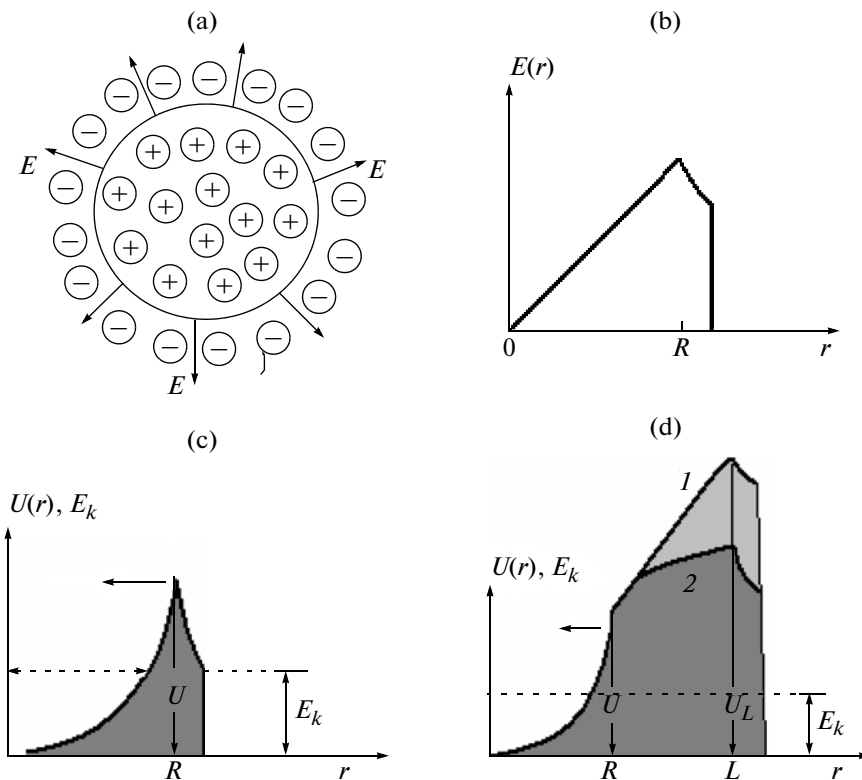
Fig. 5. (a) The model of a plasmoid with radius R as a supra-atom (used in [5–10] to define the physical principle of alloying nanocomposite materials and controlling their properties). (b) The profile with the electric field jump $E(r)$ in the charged spherical structure presented in Fig. 5a. Respectively, the dependences in the form of a jump for the parameter E/N; T_e—the temperature of the electrons ($T_e \sim (E/N)^{2/3}$); P_e—the pressure of the electrons are similar. (c) The potential barrier $U(r)$ for the free negatively charged particles in the electric field jump heating them at the periphery of the charged spherical structure up to energies of $E_k > 0$. (d) The potential barrier $U(r)$ for the free negatively charged particles in the electric field jump heating them at the periphery of the charged spherical structure with length L. The characteristic cross dimension of the potential well is more in this case than the structure's radius and is determine by its length ($\approx L$). Curve 1 corresponds to the symmetry of the surfaces (3D rectangle); curve 2 corresponds to the cylindrical symmetry (3D cylinder).

[12] in 1985 and studied numerically and experimentally in works [1–2, 13–15] (see Fig. 2). Yet, Rutherford [16] was the first to discover the bilayer of the space charge in the atom, or self-condensation of the space charge. In work [17], there is determined the common features in the generation of stationary jumps of space charges (JSC) in atoms, gas-discharge plasma, and white dwarves and neutron stars. It is shown that JSC, as discovered by Rutherford in atoms and the author in 1985 [12] in gas-discharge plasma, are similar to the shock waves discovered by Mach and the magnetic field jumps discovered by Sagdeev [18]. JSC under different conditions are determined both by the nonlinear properties of plasma and the quantum properties of elementary charged particles. Common features for JSC are the violation of neutrality, the generation of substantial electric fields focusing or dissipating the electrons, and changing their de Broglie wavelengths, thus determining the formation of convective cumulative–dissipative (CD) structures and their characteristic dimensions from 10^{-15} m up to 10^8 m and more. The squeezing of plasma by shock waves or electric field jumps with violation of neutrality is studied in this work.

The violation of neutrality in plasmoids is caused by the fact that the electrons are more movable and more quickly leave the plasmoids than massive and slow ions. The ions, uncompensated for by the electrons, form by their charge, distributed in the space, a profile of a synergetic (general) electric field that brings back (blank) the electrons that seem to be free. These very electric field profiles, self-organizing in the medium, are presented in Fig. 5b. These profiles coincide qualitatively with the profiles in an atomic nucleus. Of special note is that the characteristic dimension of the potential well for electrons in all directions is determined by the largest size of the charged structure (Fig. 5d), and the effective volume of confinement or condensation of the electron gas may be $\sim \pi L^3 \gg 4\pi R^3/3$. In such a way it shows up as the synergetic dimensional effect of the electric field of the charged structures in confining the "free" particles with the opposite charge within the region of their action. It seems to follow that the charged structures distributed in the space are more stable and their influence is more far-ranging than the charged structures with the spherical symmetry (Figs. 5c–d). This is a possible reason that, in low-current discharges, there are always formed some planar structures (strata), and then some electric filaments (Figs. 2, 4) or arcs are formed in the discharge. However, it should be remembered that there exist some external factors that considerably determine the self-organization and life activity of the charged structures between the electrodes. Consequently, without a cathode spot, the current through the discharge gap is scanty. Thus, cathode spots, being elliptic plasma structures [19], (Fig. 3) have no less unique cumulative and dissipative properties.

DIMENSIONAL EFFECTS DUE TO THE VIOLATION OF NEUTRALITY

The charged structures function equivalently within all the ranges of the characteristic dimensions due to the generation of an electric field jump at their surface (Fig. 5). The electric field magnitude at the surface of the uniformly charged 3D structure according to the Gauss law

$$E(R) = R\rho/k\varepsilon\varepsilon_0, \tag{1}$$

is determined by the charge density ρ; the size of the positively charged structure R; and the geometric factor $k = 1, 2, 3$ at the plane, cylindrical, and spherical symmetry, respectively (Fig. 5a). At large dimensions R, the peripheral electric fields (Fig. 5b) may be great (even at a negligible density of the uncompensated charge ρ) and their role in the plasma processes may be fundamental [20] as the ionization frequency depends exponentially on the parameter E/N. In this case, the potential barrier $U(r)$ confining the electrons and other negatively charged particles in the potential well (plasmoid) (Fig. 5c, d) grows with the characteristic dimension as R^2 for all kinds of symmetry from the center to the periphery of the charged structure and thus banks (cumulates, focuses) inside itself the free particles with huge kinetic energies ($0 < E_k < U(R) = \rho R^2/2k\varepsilon\varepsilon_0$ for spherically symmetric plasmoids) or with large energies (see Fig. 5d) for the case of cylindrical or plane symmetry of plasmoids, for which the potential well value is determined as $\ln L$ or L, respectively. This is a synergetic (joint) cumulative dimensional effect associated with the particular features of the 3-dimensional charged structures (plasmoids) (Fig. 5b–d). In the case of cylindrical and planar (strata) plasmoids, the volume of focusing the electrons by an electric field and the potential well size are determined by the largest characteristic dimension L (see Fig. 5d). With rotation at polarized plasmoids (Fig. 5a), there appears some magnetic field. Let us specify this Coulomb-dimensional effect for any charged plasmoids; the author of this work seems to be the first to discover it.

THE SQUEEZING OF PLASMOIDS BY ELECTRIC FIELD SHOCK WAVES OR BY THE PRESSURE OF PERIPHERAL ELECTRONS P_E

The Coulomb squeezing of atomic nuclei by negatively charged peripheral electrons or mesons, which appear to stabilize neutrons (the scheme in Fig. 5a), is a problem which has not been elaborated in detail, though the principle of the cumulation of negatively charged particles by the electric field jump back into the atomic nucleus can be diagrammed (see Fig. 5, 6).

The Coulomb static squeezing proposed by the author or physical doping by free electron traps (the scheme in Figs. 5 and 6) is an accepted method in nanotechnologies [5–10], which is now being thoroughly

studied. Physical doping by electron traps makes it possible to control the parameters and properties of nanocomposites. Thanks to the model, in Fig. 5c we can predict and investigate the quantum dimensional effects associated with the resonance polarization capture of electrons into hollow molecules (C_{60}, C_{70}) and nanotubes (polarizable resonators for de Broglie waves of electrons) [5−10]. It is suggested in [6] that the Coulomb squeezing of positively charged structures (the scheme in Fig. 5a) could be performed not only by negatively charged electron traps (for instance, by fullerene endoions) but also by the free electrons themselves. Such squeezing by the electrons of the charged plasma structures according to the scheme in Fig. 5a is in exact accordance with the model of an atom, molecule, supra-atom, or hypermolecule. Dynamic squeezing of the charged 3D structures by a monolayer of high energy sharing electrons results in the generation of the dynamic surface tension round a structure limited by a layer of electrons (a squeezed supra-ion) and the formation of an electric field shock wave converging to the cumulation center and compressing by a layer of electrons the whole ionized gas (see the arrow in Fig. 5c and d) or other plasma even with a slight violation of neutrality. There are no other particles in this layer, only electrons. This model corresponds to the one for atom electron shells. The compression of a supra-atom (plasmoid) will take place until the external pressure of the electrons in the electric field jump is balanced by the pressure of the electrons in the plasmoid compressed by the jump. This scheme explains in detail the stoppage of the gravitational collapse of a white dwarf by the pressure of the compressed degenerating Fermi gas of electrons and the cumulation of the plasma into spherical and cylindrical plasmoids. The work on the radial compression of the charged plasmoid within the gas discharge is eventually done by the external EMF, initially charging the plasmoid. The investigation of such dynamic surface tension or shock waves cumulating plasma in charged plasma structures is carried out in this work. First, this dynamic tension is caused by the pressure of the free external electrons (Figs. 5a, 6) heated by the synergetic electric field of the plasmoid's inner parts charged by a positive charge (Fig. 5b). The strength of the synergetic electric fields is the largest at the periphery, at R (or $\sim L$) from the center of the charged 3D structures (plasma lens) for electrons (Fig. 5b). Accordingly, here is attained the largest average energy of the free electrons captured into a trap, or their temperature T_e; thus, the electron pressure P_e is also maximum. The behavior and characteristic dimensions of the plasma structures are determined by the whole set of convection and diffusion processes going on and prevailing in the charged plasmoids (self-forming energy reservoirs for the kinetic energies of the electrons locked in these traps). Let us next classify these coulomb structures (energy self-organizing bags—traps for energy, charge, and electron mass).
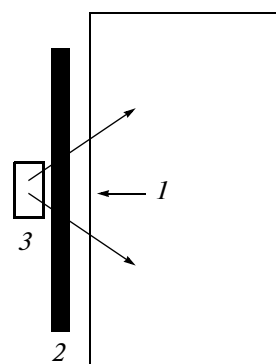

Fig. 6. The diagram of an atom (a quantum star or a coulomb focusing lens) according to Rutherford's investigations [16] and [21]: *1*—the electron shell (nanosize), *2*—the coulomb diaphragm (the coulomb force field compressing the electron De Broglie wave lengths from nanosize up to femtosize—JSC, *3*—the atomic nucleus (femtosize).

Types of Coulomb Structures

According to the information mentioned above, coulomb polarized 4D structures can be the following:

(1) cumulative, i.e., compressed by an electric field jump (Figs. 5 and 6) if the pressure of the peripheral electrons is larger than inside the plasmoid;

(2) dissipative, i.e., scattered by the spatial charge of ions (the bounce of ions from their spatial charge) or if the electron pressure inside is more than the one at the periphery;

(3) quasi-stationary or stationary, i.e., the forces of focusing and dissipation are in equilibrium (Fig. 5a); and

(4) pulsing cumulative-dissipative, i.e., when there are generated two spaced-apart reflecting mirrors (for instance, in magnetic traps) [21].

Some particular features of the behavior of charging pulsing structures show up in the similar functionality in the course of pulsations (focusing and bouncing) of the "excessive" energy in the Kepler generalized 2D problem and the "excessive" mass in the Vysikaylo−Chandrasekhar 3D problem on cumulation and dissipation of de Broglie waves in quantum stars (pulsing accretion of polarizable quantum stars) with mass more than the Chandrasekhar one (~1.46 masses of the sun) [21]. This particularity is the essence of a super powerful repetitively pulsed thermonuclear reactor, which is the most efficient in quantum stars. We consider in part 2 the operation of such a coulomb pulsing thermonuclear reactor as discovered by the author.

CLASSIFICATION OF DISTRIBUTION FUNCTIONS OF FREE ELECTRONS LIMITED BY THE COULOMB POTENTIAL BARRIER IN PLASMA STRUCTURES

Townsend has established that the parameter E/N is the main one in weakly ionized plasma (with the degree of ionization less than 10^{-6}). Here, N is the density of the neutral gas particles. In this case, the function of the electron distribution by the energies is a Boltzmann one, and all the processes of the transfer and origination are determined by the parameter E/N (or E/P, as was noted for the first time by Stoletov in 1889 in *Zhurnale Russkogo Fiziko-Khimicheskogo Obshchestva*, the Journal of the Russian Physico-Chemical Society (the physical part, vol. 21, p. 159). With the increase of the level of ionization ($\alpha_i = n_e/N \sim 10^{-(5-2)}$), the role of maxwellization grows and the function of the electron distribution by the energies becomes a Maxwell one, and the temperature of the free electrons T_e can be used as the main parameter. It is well known that, with a further increase in the degree of the gas ionization and the comparison of the characteristic length of the electron de Broglie wave with the characteristic distance between the free electrons, there takes place the degeneration of the electron gas and it obeys the Fermi−Dirac statistics. Let us estimate the concentration of the electron gas squeezing the plasmoid surface by a dense layer in this case. To excite the glow of air molecules in a normal atmosphere, the average energy of the electrons E_e should be about 1 eV, which corresponds to the d`e Broglie wave length $\lambda_{el} \approx 12.25/E_e^{0.5}$ [Å]= 1.225 nm. Here, the average energy E_e is in eV. In turn, this wave length corresponds to the critical density of the degenerated electron gas $n_{eF} = 1/\lambda_{el}^3 = 5.5 \times 10^{26}$ m^{-3}, or 5.5×10^{20} cm^{-3}. This value is by a factor of 20 more than the air's neutral gas density 2.7×10^{19} cm^{-3}. There emerges the question if there is possible the coulomb self-constriction (coulomb compression, coulomb cumulation of the spatial charge) of the ionized gas by the electric field jump to such densities, i.e., if it is possible that the movement of the coulomb barrier along the arrow to the charged structure's center (see Fig. 5c and d) is caused by the coulomb surface tension affecting the charged plasmoid surface. What EMF is capable of such compression? Such dynamic self-focusing of plasmoids seems to be possible under certain conditions (Fig. 1, 2). Such squeezing occurs in metals and other materials in which a part of the electrons are shared. The concentration of shared electrons free from atomic nuclei but localized near the surface is responsible for the skin effect in semiconductors. There are no other forces besides electromagnetic and inertial ones in condensed media. Gravitation in the mesoworld is negligible.

COULOMB IMPLOSION OF STRUCTURES OF CONDENSED MEDIA BY ELECTRON DE BROGLIE WAVES. CLASSIFICATION OF METASTABLE PLASMOIDS WITH FREE ELECTRONS

According to the de Broglie hypothesis, the particles behave as waves at the characteristic dimensions comparable with their de Broglie wave length. Such behavior is described by quantum mechanics. The mass of electrons is small; thus, the quantum properties of electrons manifest themselves when additionally nucleons and atomic nuclei behave as common particles. The difference of the masses of free electrons and atomic nuclei (the corresponding difference of their characteristic de Broglie wave lengths $\lambda_e \gg \lambda_i$) results in the quantum-mechanical separation of charges by the scheme in Fig. 5a. This quantum-mechanical separation occurs not only at the dimensions of atoms but at the dimensions of any plasmoids with free sharing electrons for which

$$n_e\lambda_e^3 \geq 1, \text{ and } n_i\lambda_i^3 \ll 1. \tag{2}$$

Conditions (2) lead to the quantum-mechanical separation of charges, the heating of electrons in the field of ions or atomic nuclei, and the cooling of positively charged nuclei and leveling of the de Broglie wave lengths of the sharing electrons and positively charged nuclei of the atoms. In the case of common discharges, the formation of charged plasmoids results from the withdrawal of a small part of the electrons from the plasmoids. Now, we can classify the metastable quasi-stationary plasmoids by the density of squeezing (free or sharing inside the plasmoid) electrons (see Fig. 7).

Classic plasmoids
— Boltzmann plasmoids $n_e < 10^{19}$ m^{-3}
— Maxwell plasmoids $n_e > 10^{19}$ m^{-3}

Quantum or Fermi−Dirac plasmoids
— Fermi plasmoids $n_e > 10^{26}$ m^{-3}
— White dwarves
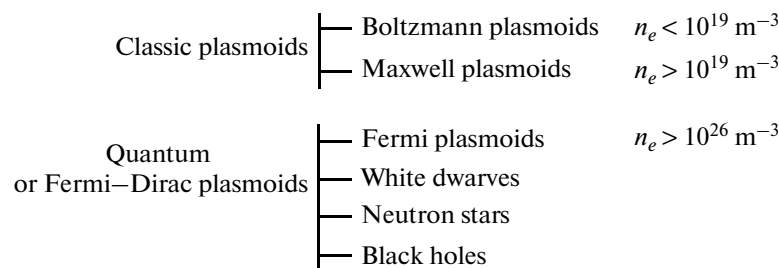— Neutron stars
— Black holes

Fig. 7. The diagram of the classification of metastable plasmoids by the function of the distribution of the electrons confined by the potential barrier with the sharing and free ones inside the coulomb barrier.

The dependence of the hydrogen plasma parameters on the kinetic energy E_e of the monolayer of the electrons squeezing the plasmoid (Fig. 5, a–d)

E_e, eV	λ_e, 10^{-10} m	λ_p, 10^{-10} m	n_e, 10^{30} m^{-3}	$\psi = E_e/E_{p,\,n}$	ρ_H, 10^3 kg/m^3	P_e, GPa
1	12.25		$>5.5 \times 10^{-4}$	1		$>88 \times 10^{-3}$
10	3.9	0.9×10^{-1}	$>1.7 \times 10^{-2}$	1		>28
13.6	3.34	7.6×10^{-2}	2.7×10^{-2}	1	1.7	
200	0.86	2×10^{-2}	1.6	$m_p/m_e = 1836$	10	$>51 \times 10^4$ 5×10^{13} J/m^3
400	0.61	1.4×10^{-2}	4.4	1836		
10^4	1.2×10^{-1}	2.9×10^{-3}	5.8×10^2	1836	10^3	$>9.3 \times 10^8$
10^5	3.7×10^{-2}	9.0×10^{-4}	1.9×10^4	1836		$>3.0 \times 10^{11}$
2.5×10^5	$\lambda_W \sim 2.1 \times 10^{-2}$ White dwarf		1.1×10^5	1836		$>4.4 \times 10^{12}$ 4×10^{21} J/m^3
10^6	$\lambda_W \sim 0.9 \times 10^{-3}$ White dwarf	2.9×10^{-4}	4.2×10^6	$\psi \approx 2m_p c^2/E_e$	2.6×10^6	$>6.7 \times 10^{14}$ 7×10^{26} J/m^3
10^7	$\lambda_M \sim 1.2 \times 10^{-3}$	0.9×10^{-4}	5.8×10^8	188	$\sim 10^9$	$>9.3 \times 10^{19}$ 9×10^{30} J/m^3
10^8	1.2×10^{-4}	2.7×10^{-5}	5.8×10^{11}	18.8	$\sim 10^{13}$	$>9.3 \times 10^{21}$ 9×10^{30} J/m^3
5×10^8	$\lambda_{P.N} \sim 2 \times 10^{-5}$	1.2×10^{-5}	7.2×10^{13}	3.8	$\sim 10^{14}$	$>5.8 \times 10^{24}$
10^9	1.2×10^{-5}	7.3×10^{-6}	5.8×10^{14}	1.9	$\sim 4 \times 10^{15}$	$>9.3 \times 10^{25}$ 9×10^{34} J/m^3
BH	BH	BH	BH	Black hole	$\sim 10^{16}$	
10^{10}	1.2×10^{-6}	1.2×10^{-6}	5.8×10^{17}	1	$\sim 10^{18}$	$>9.3 \times 10^{29}$

The parameters of plasmas squeezed by a monolayer of sharing electrons with kinetic energies E_e and corresponding de Broglie wave lengths λ_e on their surface by the scheme in Fig. 5 are presented in the table. The characteristic lengths of de Broglie waves λ_e at the given energies were calculated according to [16]: $\lambda_e \approx 12.25(1 - 0.489 \times 10^{-6} E_e)/E_e^{0.5}$. E_e is the energy of the electrons squeezing the charged plasmoid in eV. The relationships for the de Broglie wave length for the protons λ_p presented in the table are taken from Table 18 in [16]. In the P_e table, the electron gas pressure or the kinetic energy density in the plasmoid squeezed by a monolayer of high-energy electrons is estimated from below according to the scheme in Fig. 5. With a coulomb potential well, the free electrons (including the degenerated ones) with larger kinetic energy gather in the center of the plasmoid limited by the electric potential jump. According to the table, the Fermi−Dirac plasmoids increase the density of their inner energy (or the pressure P_e) by a factor of more than 300 ($P_e \sim E_e^{5/2}$) with only a tenfold growth of the energy of the electrons squeezing the plasmoid in the case of nonrelativistic electrons. For the relativistic ones, the density of the stored energy due to the coulomb cumulation grows to E_e^4, that is, by 10^4 when E_e increases by a factor of 10. Such relationships follow from our analysis of the energy cumulation in self-organizing energy reservoirs to store the kinetic energy of the electrons free from atomic nuclei and confined by the coulomb potential (Fig. 5c, d). Thus is formed a supra-atom—a charged metastable plasmoid with a focusing coulomb membrane. The huge kinetic energy of the electrons captured by a self-organizing coulomb barrier acts as a squeezing force. In this case, the total energy of the electrons captured and confined by the coulomb barrier is considerably larger than zero (Fig. 5). Such plasma structures are metastable (Fig. 5, c and d) and, with the coulomb membrane broken, can blow up, releasing the enormous kinetic energy (focused before by the membrane) of the confined free electrons. The collapse of quantum metastable stars can be attended by powerful gamma radiation.

According to the table, the plasma cumulation by a shock wave of an electric field, heating the electrons (the jump sweeps the plasma and inside the plasmoid $P_{e\uparrow}$), will cause the intensification of the charge separation and the enhancement of the spatial charge bilayer (Fig. 5) at the surface of any plasmoids, including collapsing stars. The author has examined the coulomb squeezing of stars with only hydrogen plasma. It is not very difficult to consider all the particular features, but the detailed examination of the star spectrum demands tedious computations. Thus, we are going to restrict ourselves to hydrogen plasma and

studying the coulomb squeezing of stars and neglect the transmutation of hydrogen. The positive spatial charge of the whole star efficiently accelerates the electrons, going to its center, and retards the movement of the protons and positively charged ions to the positively charged star center, i.e., it will cool them and the neutrons colliding with them will cool down as well. The diagram of such a heater–cooler leading to a collapse of normal stars (plasma movement according to the arrow in Fig. 5c, d and Fig. 6) into white dwarves and neuron stars is presented in Fig. 6. In this case, the energy should be supplied to the plasmoid (or star) core (see the table, P_e) but not extracted as for normal stars. According to the Gauss law, $E(R) \approx Rn\alpha_{i1}/3\varepsilon_0$. Here, R is the star's radius, n is the average density of the nucleons, and α_{i1} is the degree of violation of neutrality (VN). The obtained results can be substantiated on the basis of the probabilistic approach, as well as from the viewpoint of the deterministic [22] or "Copenhagenian" approaches [16, 23]. In both approaches, the statistically average characteristic dimensions occupied by the localized particles are determined only by their impulse (energy) [16, 22, 23]. An electron with kinetic energy close to zero is situated with equal probability in the whole space; thus, it is more probable that it is out of the plasmoid, which leads to the quantum-mechanical separation of the charge in the plasmoid. Thus, there are no reasons to distinguish these approaches hereafter.

The interrelationship between the average de Broglie wave lengths of the free electrons and protons and the substance density in the cumulative–dissipative (CD) plasmoid structure squeezed by the electrons is illustrated in the table in accordance with works [16, 17, 21]. It follows from the condition of the quasi-neutrality (almost neutrality) of the whole substance with any quantum meso- or macro-CD structure (for instance, ionized by pressure) the approximate equality of the average characteristic quantum-mechanical dimensions of the free sharing electrons (λ_e) and atomic nuclei (λ_N) or their de Broglie waves in this structure with free electrons: $\lambda_e \approx \lambda_N$. If this relation is ruled out through the increase of the average de Broglie wave length for the electrons, the CD structure will force out of itself a part of the spatial electrons due to the gravitation. The generated spatial charge of the positively charged uncompensated nucleons will cool the positively charged atomic nuclei, thus increasing their λ_N. The external synergetic (joint) electric field will heat the forced out electrons (Fig. 5), thus reducing the efficient de Broglie wave length and focusing them to the star's center by the scheme in Fig. 6 and forming a nonequilibrium polarized plasmoid (Fig. 5). The approximate equality of the de Broglie wave's characteristic dimensions for the electrons and atomic nuclei imposes some condition on the characteristic energies of the electrons and atomic nuclei: $E_e \approx \psi E_N$. The parameter $\psi = E_e/E_N$, where E_e is the energy of

the electrons and E_N is the energy of the nucleons, characterizes the relation of the energies of the electrons and nucleons under the condition of the dense substance's quasi-neutrality and is an indicator demonstrating the state of the plasma (equilibrium $\psi = 1$) or nonequilibrium ($\psi \neq 1$) (see the table). In the case of dense hydrogen (and nonrelativistic electron gas), the parameter $\psi = m_p/m_c = 1836$. Only in this case does the pressure of the degenerated electron gas heated in the bilayer (Fig. 6) stop the collapse of a white hydrogen dwarf, but tremendous energy in the star's core (see the table) with density $W_e > 4.4 \times 10^{22}$ J/m^{-3} is necessary for its collapse. The accumulation of the huge inner energy W_e happens due to the electron treatment of the surface of quantum stars by high energy electrons.

PLASMA LENS AND THE 3D ARRANGEMENT IN DISCHARGES

As is shown in [20, 24], the charged plasma 3D structures are a lens focusing the electrons at the bottom and their flow into plasma focuses. These focuses between the charged plasmoids are analogs of the Lagrange libration points L_1 discovered by Euler in the gravitational fields of spaced masses in 1769 and by the author [20, 24] for fields of spaced electric like charges. The flows of electrons are focused in plasma focuses and libration points where the electric field strength becomes correspondingly zero. As a result, the gas glow disappears at these points (Figs. 1–3); i.e., the discharge glow is structured by these libration points. This is the main reason for the origination of the Faraday dark space near the libration point—the Vysikaylo–Euler cumulation between the plasmoids charged by a positive charge (a cathode spot and a positive column). A rough geometric layout to determine the focus or libration point between positively charged plasmoids (a cathode spot and a positive column) is presented in Fig. 3 (photo 5). The dimensions of the focuses within the mode of nanosecond discharges with the electron drift and the gas particle ionization by the direct electron impact being the main processes are calculated analytically in [20, 24]. In the second part of this work, there will be performed the analysis of the studied processes of the cumulation and dissipation of the electron flow in the polarizable plasma structures with the charge distributed in the 3D space. We have carried out the classification of dissipative plasma structures and proved that the formation of dynamic surface tension caused by the electric field's generation, the heating of the electrons in it, and the corresponding electron pressure on the structure's periphery is possible on the charged structure's surface. In this case, the pressure of the peripheral electrons substantially exceeds the pressure of the ions ($P_i (P_e \gg P_i)$), as the ions are efficiently cooled by the neutral gas. The presence of the dynamic surface tension and the asymmetry of the external actions can lead to the formation of cumulative jets wallowing

from the charged cumulative–dissipative structures squeezed by the electron pressure. The jets are formed of the charged high energy particles. These cumulative jets complete a current path between the plasma structures (Figs. 1–3) and are responsible for their 3D structurization in 4D space–time, as well as for the plasmoid pulsations.

As is mentioned in part 2 of this work, there will be for the first time investigated the electron treatment of the surfaces of quantum stars: white and other dwarves and neutron stars with jumps of electric fields near their surface. It is proved that the surface of such quantum structures is lively treated and thus hardened by the high energy electrons. Such quantum structures are hardened through the coulomb squeezing (Fig. 5a). A new mechanism (type) of a thermonuclear reactor at the surface of charged quantum stars, the dense nuclei of normal stars, and planets with a liquid polarized core will be characterized in detail in part 2 on the basis of the performed analysis. The acceleration of electrons up to the energies measured in MeV in synergetic electric fields of the uncompensated charged particles in quantum stars and their transmutation in the near-surface layer with the enormous electric fields into neutrons in reactions with protons is the fundamental principle of the new mechanism of atom transmutation in stars. The tremendous electric synergetic (total) field of all the uncompensated ions (Fig. 5b) heating the electrons up to the energies of ~1 MeV and more at the average values of their de Broglie wave lengths in the near-surface jumps of the charged plasmoids and quantum stars and the cores of normal stars and planets is the catalyst of proton neutralization and the consequent transmutation of chemical elements in these reactions (the inverse β-decay). A supra-atom (Figs. 5a, 6) is thus suggested as a model to characterize quantum stars and the dense cores of planets. This is a possible mechanism of thermonuclear reactions in other plasmoids, such as lightning discharges, jets, blue streams, etc. However, the efficiency of such transmutations of atoms seems to be little there. This model (Figs. 5a, 6) dates back to the model used by Rutherford in his experiments when studying the atomic structure. In the case of ordinary gas-discharge plasmoids, the forms of such charged structures are determined by the discharge parameters. The electric field jumps (shock waves) can both press the structure and sputter it by the space charge of positive ions. 4D structures pulsing in space and time are possible.

DETAILED ELABORATION
OF SOME PROBLEMS AND REVIEW
OF THE PREVIOUS SOLUTIONS

Examining the outer space structures and plasmoids in gas-discharge plasma, it is usually assumed that all these structures are absolutely neutral [20, 24]. In the case of dense stars such as white dwarves and neutron stars, this means approximate equality of the de Broglie wave lengths of the electrons and nucleons and atomic nuclei pointing to the difference of their average kinetic energies by a factor of $(M/m)^{0.5}$ (nonrelativistic case). Otherwise, a part of the electrons free from atomic nuclei forming a Fermi gas or a Fermi liquid with their large average de Broglie wave lengths will be forced out of the structure of a quantum star or a plasmoid. For example, in [25], on pp. 349–350, it is stated that the "separation of charges of both signs is rather disadvantageous in terms of energy due to the appearance of very big electric fields." That is a reason to use the neutral gas model for the simulation of quantum stars. The theory of a neutral medium is further elaborated in work [25] for white dwarves and neutron stars, in which a considerable part of the electrons are sharing ones and form a degenerated Fermi gas or Fermi liquid stopping the star's collapse. Astrophysicists do not investigate why the sharing electrons with little resting masses have an average kinetic energy much greater than large nucleons and ions (their de Broglie wave lengths should be equal in a neutral state). The source (3D heater) warming the electrons and the 3D cooler actively cooling the hot nucleons and transferring their total energy to the electrons are ignored in such a neutral consideration, which is the reason the plasma nonequilibrium in Fermi–Dirac plasmoids (quantum stars) is not examined, and the effect of the degenerated electron gas pressure on the sizes of quantum stars is considered without a detailed study of the powerful process of the energy pumping from nucleons to electrons. Such pumping can result from only the action of enormous (synergetic) electric fields or electric potential (Figs. 5 and 6).

There appears a new conception in [Physics-Uspekhi]. Here, is a statement of one of the votaries of such an approach: "One research team at the Lebedev Moscow Physics Institute with Academician Aleksandr Viktorovich Gurevich as the leader since 1992 proposed, besides objections, their own explanations for both sprites and lightning strokes in general. From this viewpoint, the lightning strokes are governed by the showers of secondary ionized charged particles forced out of air atoms by energetic particles of primary cosmic rays (ambassadors of supernovas; galaxies; and, possibly, mysterious black holes)." The authors and votaries of this conception do not explain the essence of such a notion as the breakdown and how the electrons are accelerated within the breakdown up to energies of 100 keV and more. It should be noted that, with the dimensions of lightning discharges (about hundreds of meters and even kilometers), electrons with energy even more than 2 MeV do not run far (2–4 m). The formation of a plasma channel hundreds of meters long is necessary for them to run in some direction, but no such channel is noticed in this conception or it is hidden by the authors by the term "breakdown." Therefore, in this "conception" based

on the priority of cosmic rays in lightning, the author, unlike the votaries of cosmic rays, assigns the problem of the first electron (the external ionizer, UV radiation, etc.) but not the problem itself of the moving powerful mechanism of discharge and plasma self-condensation at the dimensions of hundreds of meters. The main energy source and the method of focusing its energy in linear, beaded, or globe lightning as a plasma structure charged by a positive charge are related to the problem of the mechanism of the discharge (lightning), as well as the specific way of the electron acceleration up to energies of ~2 MeV and more in the plasmoid, in which there are initially free electrons.

CONCLUSIONS

The assumption of neutrality is often used in the description of gas-discharge plasma and other ones. These assumptions of the absolute neutrality lead to the so called asymptotic paradoxes, which cannot be explained within the limits of quasi (absolute) neutrality. Even a slight violation of neutrality (about $(n_i - n_e)/n_i \sim 10^{-18}$) due to the forcing out of a small part of the electrons from the structures causes the sputtering (bouncing) of the previously cumulating (gravitating) neutral structures [21]. On the other hand, as is proved in this work, the separation of charges results in the generation of the coulomb surface tension squeezing huge plasmoids, including stars with densities up to those of quantum stars (see the table). Can such coulomb surface tension caused by coulomb forces squeezing the plasmoids be applied practically? Undoubtedly, it will be possible in the not so distant future. There fly globe lightning strokes doing only damage. It is high time for such lightings and common ones to do good, as is now useful in the nanoconstruction of the layers of a spatial charge in nanocomposites [7]. A slight violation of neutrality or polarization in the system of plasma structures results in the formation of a system of a plasma lens (strata) [20, 24]. As proved in [20, 24], the finite-dimensional 3D strata focus the electrons into focuses or libration points. These focuses are similar to the Lagrange points L_1 discovered by Euler for two gravitational attractors (for instance, between Jupiter and the Sun) in 1767. The detailed investigation of the dynamics of the self-constriction and cumulation of plasma structures can be evidently applied to free the atmosphere of dust and a number of deleterious substances. Allowance for the neutrality of giant plasmoids may make it possible to explain the quick recession of galaxies in which there are many quantum positively charged stars continuing to cumulate a positive charge. The overwhelming majority of protons in cosmic rays point to their reflection from the normal and quantum stars. It is well known the problem on the Universe's overheating due to the radiation of normal stars. This overheating should happened as the radiation energy of normal stars grows in a sphere by the law

of R^3 and is thrown out of the sphere by the law of R^2. The existence of cumulation of the star radiation energy by the law of R^3 follows from the very fact that we are alive within the radiating Space. The presence in the Space of quantum stars being effective accumulators of the electromagnetic radiation (of any energy and mass) protects us from overheating.

Actual experimental investigations and an analytic study will be considered in part 2 within the framework of the model proposed for polarizable or charged plasmoids.

REFERENCES

1. Babichev, V.N., Vysikaylo, Ph.I., Pis'mennyi, V.D. et al., Experimental Investigation of Ambipolar Drift of Plasma Disturbed by a Bunch of Quick Electrons, *Dokl. Acad. Nauk SSSR. Fiz.*, 1987, vol. 297, no. 4, pp. 833–836.

2. Babichev, V.N., Vysikaylo, Ph.I., Golubev, S.A., Experimental Evidence for the Existence of Jumps of Gas Discharge Plasma Parameters, *Pis'ma Zh. Teor. Fiz.*, 1986, vol. 12, no. 16, pp. 992–995.

3. Vysikaylo, Ph.I., Glova, A.F., Smakotin, M.M., Stationary Glow Discharge in Nitrogen with the Negative Volt-Ampere Characteristic, *Fiz. Plazmy*, 1988, vol. 14, no. 6, pp. 734–736.

4. Vysikaylo, Ph.I., Ershov, A.P., Kuz'min, M.I, Tivkov, A.C., and Chekalin, B.V., Peculiarities of Current Transfer in Discharge in Transversal Supersonic Gas Flow at Formation of Cylindrical Cumulative Structures (Plasmoids), *Fiz. Khim. Kin. Gaz. Din.*, EJ, 2007, vol. 5. http://www.chemphys.edu.ru/pdf/2007-06-21-002.pdf.

5. Vysikaylo, Ph.I., Formation of Fullerene Ion and Coulomb Melting of Fullerites, *Tezisy dokladov Nauchno-prakticheskoi konferentsii "Nanotekhnologii proizvodstvu"* (Proc. Conf. "Nanotechnologies for Industry), Fryazino, 2009, pp. 18–19.

6. Vysikaylo, Ph.I., Physical Fundamentals of Hardening of Materials by Space Charge Layers, *Surf. Eng. Appl. Electrochem.*, 2010, vol. 46, no. 4, pp. 291–298.

7. Vysikaylo, Ph.I., Polarization of Allotropic of Carbon Hollow Forms and its Application in Construction of Nanocomposites, *Tezisy dokladov XXXVIII Mezhdunarodnoi konferentsii po fizike plazmy i upravlyaemomu termoyadernomu sintezu* (Proc. XXXVIII Int. Conf. on Physics of Plasma and controlled thermonuclear fusion), Zvenigorod, 2011, p. 311.

8. Vysikaylo, Ph.I., Cumulation of de Broglie Waves of Electrons. Endoions and Endoelectrons of Fullerenes and Resonances in the Properties of Nanocomposite Materials with the Spatial Charge Layers, *Surf. Eng. Appl. Electrochem.*, 2010, vol. 46, no. 6, pp. 547–557.

9. Vysikaylo, Ph.I., Cumulative Quantum Mechanics and its Application to Construct Nanocomposites, *Tezisy dokladov Vserossiiskoi konferentsii "Fizika nizkotemperaturnoi plazmy"* (Proc. All-Russian Conf. "Physics of Low-Temperature Plasma"), Petrozavodsk, 2011.

10. Vysikaylo, Ph.I., Polarization of Allotropic Carbon Hollow Forms and its Application in Construction of Nanocomposites, *Nanotekhnika*, 2011, vol. 9, no. 1, pp. 19–36.

11. Gunn, J., Gunn Effect, *Usp. Fiz. Nauk*, 1966, vol. 89, no. 1, pp. 147−160.

12. Vysikaylo, Ph.I., Jumps of Parameters of the Nonuniform Collisional Plasma with Current Caused by Violation of Quasi-Neutrality, *Fiz. Plasmy*, 1985, vol. 11, no. 10, pp. 1256−1261.

13. Babichev, V.N., Vysikaylo, Ph.I., Golubev, S.A., Trukhin, S.S., et al., Investigation of Drift Jumps of Gas Discharge Plasma, *Fiz. Plasmy*, 1987, vol. 13, no. 12, pp. 1524—1529.

14. Vysikaylo, Ph.I. and Tsendin, L.D., Sharply Non-Uniform Profiles of Plasma Concentrations in Discharge at High Pressures, *Fiz. Plasmy*, 1987, vol. 12, no. 10, pp. 1206−1210.

15. Vysikaylo, Ph.I. and Trukhin, S.S., Numerical Model of Plasma Column of Longitudinal Discharge Disturbed by the External Ionizer, *Teplofiz. Vys. Temp.*, 1987, vol. 25, no. 3, pp. 597−599.

16. Shpol'skii, E.V., *Atomnaya fizika* (Atomic Physics), Moscow: Fizmatgiz, 1963.

17. Vysikaylo, Ph.I., Self-Organizing Jumps with Spatial Charge in Femto-, Nano-, Meso- and Macrostructures, *Materialy V Vserossiiskoi konferentsii "Fizicheskaya elektronika"* (Proc. V All-Russian Conf. "Physical Electronics"), Makhachkala, 2008, pp. 14−18.

18. Sagdeev, R.Z., Collective Processes and Shock Waves in Rarefied Plasma in *Voprosy teorii plazmy* (Problems of Plasma Theory), Moscow: Atomizdat, 1964, no. 4, pp. 20−80.

19. Kesaev, I.G., *Katodnye processy elektricheskoi dugi* (Cathode Processes in Electric Arc), Moscow: Nauka, 1968.

20. Vysikaylo, Ph.I., The Analytical Calculations of Ionization-Drift Waves (3D-Strata) of Nanosecond Discharges: the Determination of the Cathode Drop in Nanosecond Discharges According to the Number of Visualized Plasma Structures), *Surf. Eng. Appl. Electrochem.*, 2011, vol. 47, no. 2, pp. 139−144.

21. Vysikaylo, Ph.I., Instability of Focusing Mass, *Sbornik trudov Mezhdunarodnoi konferentsii "Transformatsiya voln, kogerentnye struktury i turbulentnosn'"* (Proc. Int. Conf "Transformation of Waves, Coherent Structures and Turbulence"), Moscow, 2009, p. 512.

22. Broglie De, L., *Sootnoshenie neopredelennostei Geizenberga i veroyatnostnaya interpretatsiya volnovoi mekhaniki* (Interrelation of Heisenberg Indeterminacies and Probabilistic Interpretation of Wave Mechanics), Moscow: Mir, 1986.

23. Born, M., *Atomnaya fizika* (Atomic Physics), Moscow: Mir, 1965.

24. Vysikaylo, Ph.I., Points, Lines and Surfaces of Vysikaylo−Euler Libration (Cumulation) in Nonuniform Structures in Plasma with Current, *Tezisy dokladov XXXVII Mezhdunarodnoi konferentsiii po fizike plazmy i UTS* (Proc. XXXVII Int. Conf. on Physics of Plasma and CTNF), Zvenigorod, 2010, p. 311.

25. Landau, L.D. and Lifshits, E.M., *Teoreticheskaya fizika* (Theoretical Physics), vol. 5 of *Statisticheskaya fizika* (Statistical Physics), Moscow: Nauka, 1976.

Machining of Shaped Holes Using Focused Laser Radiation

N. I. Anyakin, M. Nayebi, and V. S. Kovalenko

National Technical University of Ukraine–Kiev Polytechnical Institute,
Laser Technology Research Institute, pr. Pobedy 37, Kiev, 03056 Ukraine
e-mail: anyakin@ukr.net; v.kovalenko@kpi.ua
Received June 23, 2011

Abstract—The process of manufacturing shaped holes in rotating blank parts using focused laser radiation is investigated. It has been revealed that a hole with a specified shape and cross section can be obtained by varying the inclination angle of the blank's rotation axis and the laser machining modes.

INTRODUCTION

Items made from hard-to-machine materials such as natural and artificial diamonds, cubic boron nitride, etc., are widely used in modern industry. Their unique wear resistance and heat resistance make these materials irreplaceable for fabricating metal-cutting tools, different dies, and nozzles. The latter have holes with a complicated cross section (they usually have a tapered input cone, a full cylindrical thread, and a tapered output cone [1–3]), which cannot be formed without applying modern machining techniques. The small sizes of the holes in the dies and their complicated shapes hinder (or even make impossible) their fabrication using smelting and machining or electric discharge treatment due to the high mechanical properties of the blank material, the small sizes, etc. Thus, the only method for fabricating such items is laser machining.

The first investigations in the field of laser technology [3–5] revealed the following:

—the dependence between the cross section of the machined hole (for mono- and multipulse machining) and the irradiation modes (the pulse energy and duration, the focal distance of focusing the optics, its defocusing, etc.);

—the possibility of controlling the size and shape of the cross section of the treated hole by varying the laser machining modes.

The next step in the fabrication of holes and cuts with a specified cross section is the "layer-by-layer" technology of the blank machining [6]. This technique is widely used for treatment of the items from natural and rough diamonds, hard alloys, etc., using focused radiation of Q-switched lasers operated at different harmonics. The authors of [7] propose increasing the depth of the cutting and decreasing the cut's width by using an additional inclination of the blank with respect to the axis of the focused laser radiation.

Deep holes are machined using the method of trepanation according to the "layer-by-layer" removal of the metal's envelope as well [8]. In this case, the focused laser radiation reciprocates along a helical path with the focal plane deepening into the blank's body; it is accomplished with the help of additional scanning of radiation [8] or (during machining of bodies of revolution) by its additional (with simultaneous rotation of the blank) displacement in the longitudinal center plane [1, 2]. For example, when machining dies and nozzles, the blank rotates with the specified speed and the focused laser radiation moves in the longitudinal center plane ensuring the deepening of the focal plane and removing the blank's material layer-by-layer [1, 2]. Naturally, at constant rotary speeds, the displacement of the focusing spot, and the pulse repetition rate, the speed of the machining varies as the laser radiation's axis approaches the rotation axis of the blank; as the result, the coefficient of the spot's overlapping, the radiation energy density, and the thickness of the removed layer increase (see [2]). In their investigations, the authors of [1, 2] do not consider the problems related to the shaping of the "inverse cones" of dies and nozzles and groups of items from one blank. This paper is devoted to the solution of this very problem.

Let us consider the process of drilling holes in a rotating blank. Such a flowsheet process of machining is possible for shaping holes in small-size and small-mass items when it is not necessary to apply special auxiliary systems for the balancing the drive.

During conventional hole machining (without additional displacements of the component and the focusing unit), "hyperbolic" holes can be "instantaneously" shaped by inclining the rotation axis (Fig. 1). In this case, the inclination angle of the hyperbola's asymptote is determined by the angle of the rotation axis's inclination with respect to the axis of the focused laser radiation g, while the position of the apex is determined by the point of the laser radiation axis's
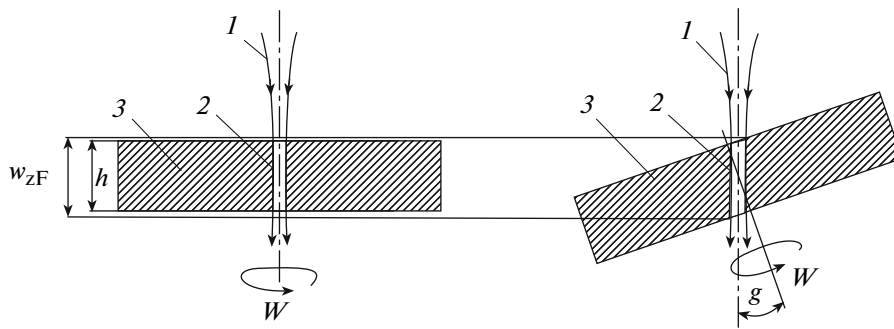
Fig. 1. Schematic of hole drilling in the *h*-thick blank rotating with the speed *w*: (*1*) focused laser beam; (*2*) hole cavity; (*3*) blank; *g* is the inclination angle of the rotation axis
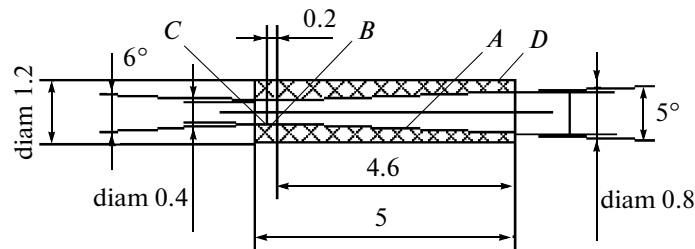

Fig. 2. Nozzle design.

intersection with the rotation axis of the blank. During such a machining procedure, the thickness *h* of the treated item should be comparable with the flange focal distance of the focusing optics w_{zF}.

If *h* is substantially larger than w_{zF}, the shaping of holes becomes much more complicated. By way of example, let us consider the process of fabricating miniature nozzles from synthetic diamond (for the design, see Fig. 2). Since the blanks from synthetic diamond are shapes in the form of 5 mm-high "pellets" with a diameter of up to 7 mm, several ready-made items can be obtained from one blank.

It is known from the general machine-building technology that, when solids of rotation are fabricated by cutting the minimal axis, misalignment of the outer and inner surfaces will be observed in the case when they are fabricated at "one setting," i.e., using one and the same technology. Thus, when fabricating a nozzle at one setting, the following should be cut:

—a tapered lead and a tapered output cones (surfaces *A*, *C*; Fig. 2);

—a cylindrical full thread (surface *B*, Fig. 2);

—a cylindrical outer part (surface *D*, Fig. 2).

Note that, when nozzles are shaped with the help of focused laser radiation and the technology of the "layer-by-layer" removal of the metal envelope is implemented, the earlier-considered (Fig. 1) relative positions of the rotation axis of the blank and that of the focused laser radiation are preserved.
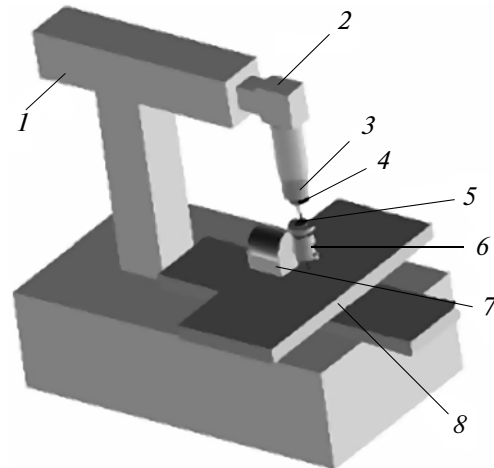

Fig. 3. Schematic of the experimental test bench: (*1*) laser; (*2*) optical unit; (*3*) movable carriage; (*4*) lens; (*5*) component; (*6*) rotary actuator; (*7*) rotator; (*8*) desktop.

EXPERIMENTAL EQUIPMENT AND INVESTIGATION TECHNIQUE

The experiments were staged at the experimental test bench (Fig. 3) of the yttrium-aluminum garnet (YAG) Q-switched laser and the average radiation power operated in the single-mode generation regime up to 20 W (the radiation's wavelength is 1.06 μm). The optical unit consisting of a 4-fold telescopic system, a rotary mirror, and interchangeable lenses (with the
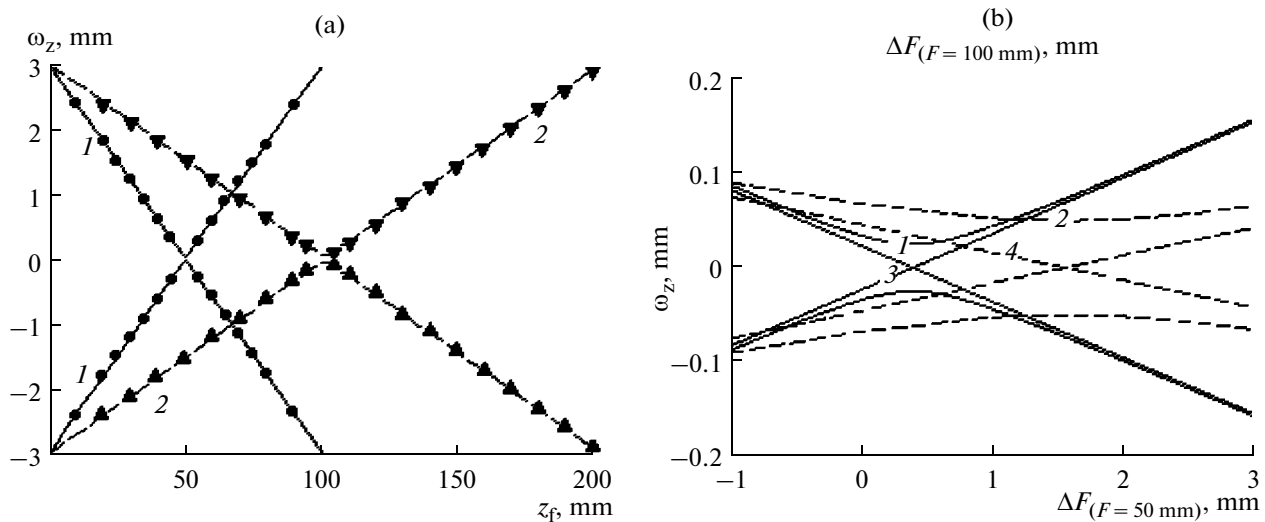
Fig. 4. Measured diameters of the focused laser radiation (a) and the calculated sausages of the caustic surfaces (b) formed by lenses with different focal distances, where ● are the measured diameters of the caustic surface formed by a lens with $F = 50$ mm; ▼ are the measured diameters of the caustic surface formed by a lens with $F = 100$ mm; (*1*) the calculated caustic surface formed by a lens with $F = 50$ mm; (*2*) the calculated caustic surface formed by a lens with $F = 100$ mm; (*3, 4*) asymptotes of the caustic surfaces formed by lenses with $F = 50$ mm and $F = 100$ mm, respectively.

focal distances $F = 100$ mm and $F = 50$ mm) was placed on the path of the beam from the resonator. The lens was fixed in a movable carriage providing its displacement by $+/-$ 50 mm with a 5 μm step. The machined blank was glued to a substrate and mounted in the holder of the 3000 rpm rotary actuator (driven by a dc motor). The rotary actuation was fixed in a rotary fixture mounted on a 2-coordinate desktop (the displacement accuracy is 5 μm). The operation of the laser, the desktop, the lens drive, and the rotary fixture was controlled by a PC.

"Pellets" from synthetic diamond and cubic boron nitride (kibarite) were used as specimens. Three tests were carried out at each experimental point using transverse microsections from the kibarite specimens. The machining results were measured using MMI-4, PMT-3, and MIS-11 microscopes and a profilometer–profilograph.

DISCUSSION OF THE RESULTS

When items are shaped with the help of focused laser radiation, knowledge of the parameters of the caustic surface, i.e., the conditional surface enveloping the flow of the focused laser beam, plays a significant role. The caustic surface of focused single-mode laser radiation represents a rotation hyperboloid with a sausage at a certain distance from the focal plane of the lens. Thus, for the caustic to be unambiguously described, it is necessary to know the laser beam's diameters at least at three points on the beam's axis or at two points with one of them being in the caustic sausage (when the equation for the tangent to the surface enveloping the beam is actually specified) and an arbi-

trary point on its axis. The use of the latter case is rather complicated due to the substantial level of the laser beam's power density at the focusing point and, as a result, of the radiation flow hitting the measuring element. When carrying out the experiment, the diameter of the caustic surface (at the level of $1/\exp^2$) was predetermined at the specified points on the axis of the focused beam using the scanning diaphragm method. Then, the measured values were approximated with the least-squares method using the hyperbola equation as the equation of the correlation between the measured values and the required dependence. Figure 4 shows the measured diameters of the focused laser radiation at different distances from the principle plane of focusing the lenses z_f (their defocusing DF) and the calculated caustic surfaces (with their asymptotes) formed by the lenses with different focal distances.

When analyzing the obtained dependences (shown in Fig. 4), note that, by using this equipment (performing elementary 3-coordinate machining, namely, moving the component over the plane with the gradual deepening of the focal plane of the focusing lens into its body), it is possible to machine deep holes, slots, and cuts with the conical section angle being not less than 3.5° ($a_{F50} = 3.5°$ is the inclination angle of the asymptotes of the caustic surface formed with the lens with $F = 50$ mm) and 1.7° ($a_{F100} = 1.7°$ for the lens with the focal distance of 100 mm).

When the component is placed in the focal plane of the lens with $F = 50$ mm ($DF = 0$), the efficiency of the material removal decreases with an increase in the number of passes (Fig. 5), which is related not only to
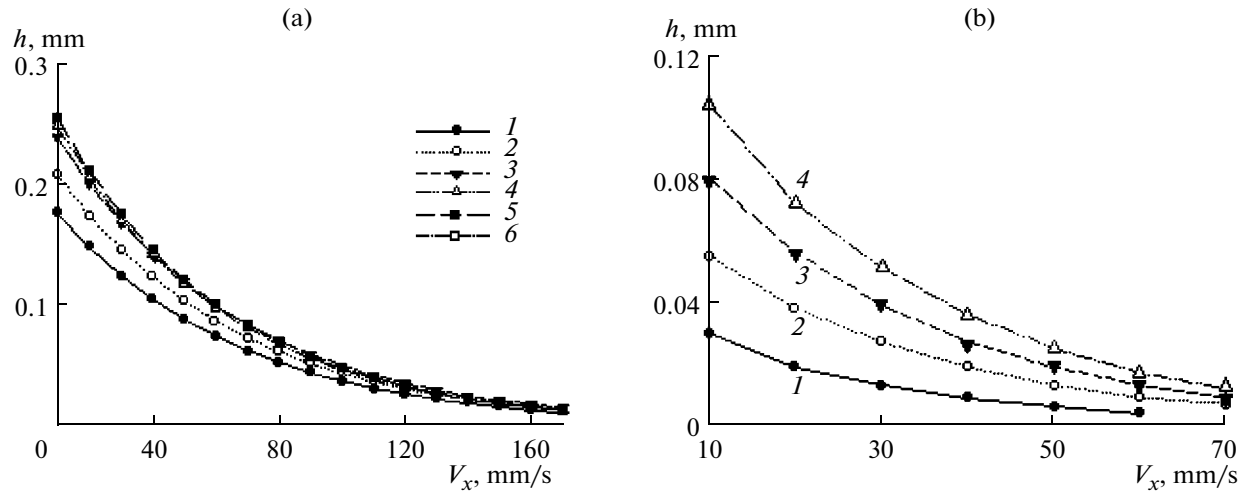
Fig. 5. Depth of a single scribe as a function of the displacement rate of the laser radiation ($P = 18$ W, the modulation frequency is $n = 8$ kHz, $DF = 0$ mm) focused by a lens with $F = 50$ mm (a) and $F = 100$ mm (b) for a different number of passes; *1, 2, 3,..., 6* is the number of passes.
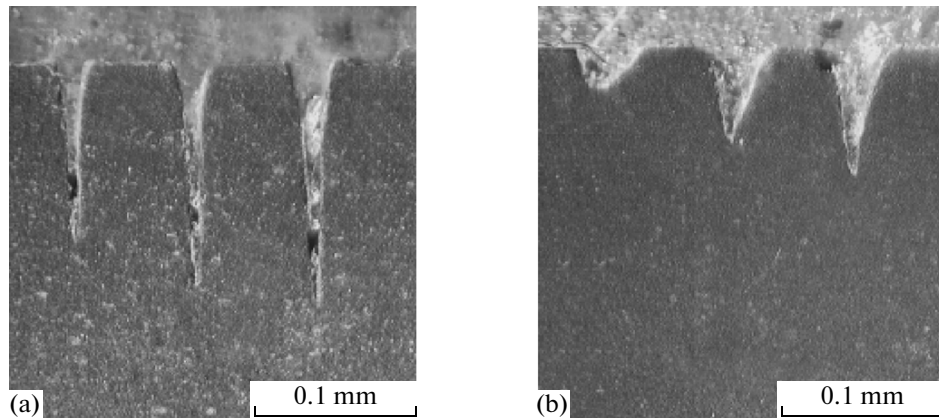

Fig. 6. Cross section of a single scribe in cubic boron nitride (kibarite) during machining with laser radiation ($P = 18$ W, the modulation frequency is $n = 8$ kHz, and $DF = 0$ mm) focused by a lens with $F = 50$ mm (a) and $F = 100$ mm (b) for *1, 2*, and *3* passes of the focused radiation.

the "screening" of the periphery of the focused radiation by the cut walls but also to the increase in the size of the focusing spot due to the properties of the caustic surface (Fig. 4) and the area on which radiation is focused (the cut bottom has a "wedgelike" shape (Fig. 6a). The latter also determines the inclination angle of the generatrix of the machined hole (slot, deepening, etc.) due to a sharp increase in the size of the focusing spot (the spot with the round cross section transforms into an ellipse) taking place when the caustic intersects the machined surface.

When analyzing the dependences shown in Figs. 4 and 5, note that, when the laser radiation is focused by the lens with the focal distance of 100 mm (in the case when $DF = 0$), the observed depth of the laser scribing is almost directly proportional to the number of laser radiation passes over the machined surface (Fig. 5b).

This is related to the flatter caustic surface, the longer sausage of the focused laser radiation (Fig. 4), and the less pronounced "wedge-like" shape of the scribe (Fig. 6b). However, due to the low power density of the focused laser radiation, the efficiency of the performed operation (the amount of the removed material bulk) is substantially lower as compared to the machining accomplished with the lens with a focal distance of 50 mm (Fig. 5a).

Thus, knowing the equations for the caustic surfaces (their asymptotes) and the equations describing the machined component (for the given machining procedure, it is sufficient to circumscribe the nozzle's surface with a set of straight lines) and the dependence of the scribed width and depth on the machining modes, it is possible to determine the law of the displacement of the actuators in the case the nozzle is cut
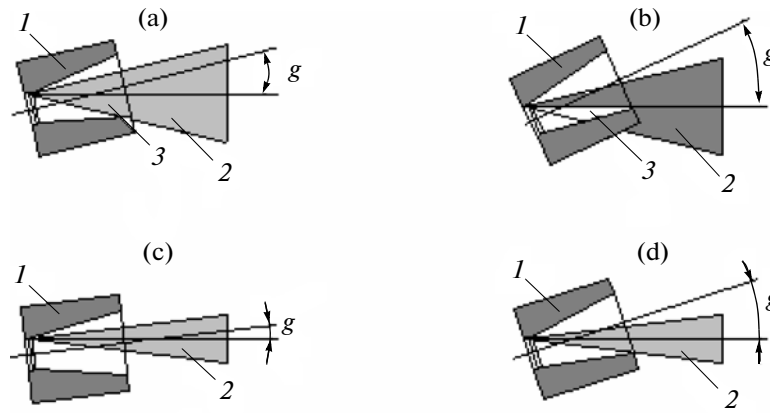
Fig. 7. Machining of a cylindrical section (a, c) and an inverse cone (b, d) of a nozzle with laser radiation focused by a lens with $F = 50$ mm (a, c) and $F = 100$ mm (c, d); (*1*) blank; (*2*) focused laser radiation; (*3*) screened caustic section.
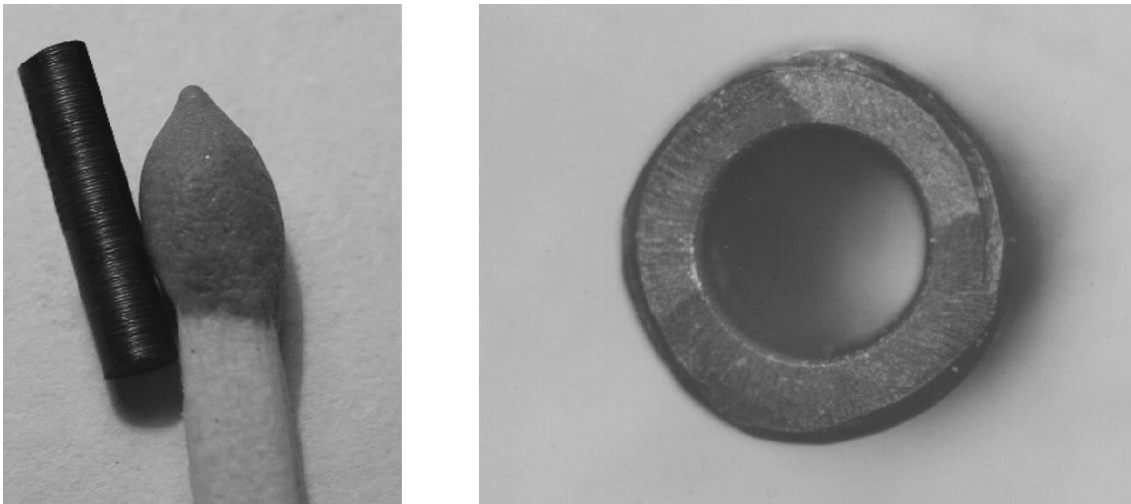

Fig. 8. Physical configuration of a special nozzle (a 5 mm-long cylinder 1.2 mm in diameter, the flow area is 0.4 mm; synthetic diamond) cut out from a pellet.

according to the technique of the "layer-by-layer" removal of the envelope material.

In this case, the absence of the tangency (intersection) of the caustic asymptotes with the machined component's surface is a natural limitation.

Reasoning from the latter, note that the fabrication of nozzles (Fig. 2) with the help of the focused laser radiation with the lens with $F = 50$ mm is inexpedient since the stage of the radiation's screening begins when cutting the lower part of the cylindrical hole (Fig. 7a). In this case, the turning angle of the blank's rotation axis reaches 3.5° (i.e., the wall of the machined surface is parallel to the caustic branch). When an inverse cone is fabricated (the turning angle is $g = 6.5°$), as much as 48% of the laser radiation flow is screened by the outer section of the nozzle (Fig. 7b).

When the laser radiation is focused by the lens with $F = 100$ mm (owing to a flatter caustic), it becomes possible to fabricate this component "at one setting": the inner and the outer nozzle's surface (Fig. 7c and 7d) and cutting several nozzles from one blank. Figure 8 shows the image of a nozzle made from a synthetic diamond.

CONCLUSIONS

When fabricating nozzles by focused laser radiation following the technique of "layer-by-layer" removal of the metal envelope in a rotating blank, the control over the inclination angle of the blank's rotation axis allows fabricating nozzles with a specified cross section and tapered cones and a cylindrical full thread and it is expedient to use focusing optics shaping the caustic surface with asymptotes having the minimal inclination angles.

REFERENCES

1. Cao, F. and Huang, J., Technique of Precise Laser Machining for the Diamond Wire Drawing Dies, *Proc. International Symposium for Electromachining "ISEM-XI"*, Lausanne, 1995, pp. 629–637.

2. Cao, F.G., Zhang, Q.J., and Liu, Y., A New Technology for Laser Drilling of Precise and Micro Diamond Drawing Dies, *Proc. 15th International Symposium on Electromachining*, Pittsburgh, 2007, pp. 405–408.

3. Veiko, V.P., Libenson, M.N., Melyuchev, A.M., et al., *Lazernaya tekhnologiya* (Laser Technology), Moscow: Institut "Elektronika", 1970.

4. Epperson, J.P., Dyer, R.W., and Grziwa, J.C., Laser System Cuts Cost of Drilling Diamond Dies, *Laser Focus*, 1966, no. 10, pp. 26–27.

5. Kovalenko, V.S., Dimensional Machining of Materials with a Photon Beam, *Tekhnol. Organ. Proizvod.*, 1967, no. 4, pp. 101–104.

6. Lasers are Diamond's Best Friend, *Photonics Spectra*, 1992, vol. 26, no. 6, p. 40.

7. Sytenko, I.N. and Mikhin, K.E., New Method for Laser Machining of Diamonds and Superhard Materials, *Proc. VI International Conference "Beam Technologies & Laser Application"*, St. Petersburg, 2009, pp. 365–370.

8. Kovalenko, V.S., Kotlyarov, V.P., Dyatel, V.P., et al., *Spravochnik po tekhnologii lazernoi obrabotki* (Reference Book on Laser Machining), Kovalenko, V.S, Ed., Kiev: Tekhnika, 1978.

9. Leong, K., Drilling with Laser, *Ind. Laser Solutions Manuf.*, 2000, vol. 15, no. 9, pp. 39–45.

Experimental Studies on Bulk Tempering of 34CrNiMo6 Steel[1]

N. Popescu[a], M. Cojocaru[a], and V. Mihailov[b]

[a]*Polytechnica University of Bucharest, 313 Splaiul Independenţei, Bucharest, 060042, România*
[b]*Institute of Applied Physics, Academy of Sciences of Moldova, 5 Academiei, Chişinău, MD-2028, Rep. Moldova*
e-mail: mocojocaru2005@yahoo.co.uk; valentin.mihailov@gmail.com
Received May 05, 2011

Abstract—The class of steels for hardening and tempering, alloyed with chrome, nickel and molybdenum, standardized in Europe (four steel grades), USA (10 grades) and Russia (9 grades) is highly diversified and is especially interesting in the production of machine parts having an extremely large range of dimensions. The heat treatment features of these steels are particularly attractive: high bainitic hardenability and a good temperability etc. The correlation between the hardness achieved after high tempering on products made from these steels, their equivalent diameter and the heat and time parameters of tempering can be explained by means or Jominy samples test for products with equivalent diameters equal to or less than 100 mm, or by the results obtained through the method of simulation of oil cooling (Pavaras–Gheller method) for products with equivalent diameters higher than 100 mm. In this paper, based on experimental results, these correlations are customized for a steel group representative as is 34CrNiMo6.

INTRODUCTION

The studied 34CrNiMo6 steel [1] belongs to the class of steels for quenching and tempering, alloyed with 0.4–2% Cr, 0.5–4% Ni and 0.15%–0.5% Mo, with the carbon content within 0.3–0.45%, standardized in Europe (4 grades), U.S. (10 grades), and Russia (9 grades). These steels are widely used in industry for the manufacture of parts (machine parts) with very different thicknesses ($D_{ech} = 15$–200 mm). The main heat treatment features of these steels are low quenching temperature, high bainitic hardenability and good temperability, due to high proportions of martensite and bainite of the quenched structure. The standardized chemical composition of 34CrNiMo6 steel (SR EN 10083-1:1995) in weight % is:

C	Si	Mn	P	S	Cr	Ni	Mo
0.3–0.38	max 0.40	0.30–0.80	max 0.030	max 0.030	1.30–1.70	1.30–1.70	0.15–0.30

Figure 1 presents the TRC chart and the hardenability band of the 34CrNiMo6 steel confirming its high bainitic hardenability.

MATERIAL AND RESEARCH METHODOLOGY

Samples taken from a ∅40 mm bar, hot rolled and normalized, with the following chemical composition (in weight %) were used:

C	Si	Mn	P	S	Cr	Ni	Mo
0.35	0.31	0.65	0.018	0.022	1.40	1.50	0.16

For the parts with the equivalent diameter $D_{ech} \leq$ 100 mm Jominy samples were used and for the parts with the equivalent diameter between 100 and 180 mm were used samples for oil cooling simulation of cylinders with the equivalent diameters $D_{sim} = 60, 120$ and 180 mm (Fig. 2). The samples taken from the studied steel bars with square section, dimensions □ $20 x R_{sim}$, packed in asbestos with h thickness, dependent on the simulated cylinder diameter, were used accordingly to the table shown below:

R_{sim}, mm	30	60	90
h, mm	6	16	24

The asbestos layer is sealed with steel sheet having the thickness $g = 2$ mm.

[1] The article is published in the original.

C	Si	Mn	P	S	Cr	Ni	Mo	T	t	N
0.35	0.25	0.55	0.025	0.015	1.55	1.55	0.20	830°C	15 min	9

Fig. 2. Simulation of oil quenching of a cylinder with $D_{sim}xL$ dimensions by means of a square section sample with □20x$H = R_{sim}$ dimensions, packed in an asbestos layer with h thickness (the Pavaras–Gheller method).

From the simulation samples quenched in oil, one was kept in the as-quenched state, and three samples were tempered according to the data shown below:

T_{temp}, °C/K	500 (773)	600 (873)	700 (973)
t_{iz}, h	1	1.6	5.0
P_{HJ}	14678	16762	19168

Both for the quenched samples and quenched and tempered samples, the HRC hardness measurements were made. For the frontal quenched sample also a microstructural analysis was made.

Fig. 1. TRC chart (up) and hardenability band (down) of 34CrNiMo6 steel.

EXPERIMENTAL RESULTS ON JOMINY SAMPLES

The hardnesses taken on length of Jominy samples are given in Table 2.

The results shown in Table 2 are also emphasized in Fig. 3.

Figure 4 shows the microstructures obtained at few distances from the cooled end of a Jominy sample and the corresponding hardnesses of these microstruc-

Jominy samples were austenitized at $T_A = 830°C/t_A = 45$ min and frontal quenched; the simulation samples of the cylinders with 60, 120 and 180 mm diameters were cooled in oil at 60°C, with moderate agitation ($H_{rel} = 0.5$). After the frontal quenching one Jominy sample was kept in as-quenched state and five samples were tempered at the temperatures and isothermal maintaining times listed in Table 1.
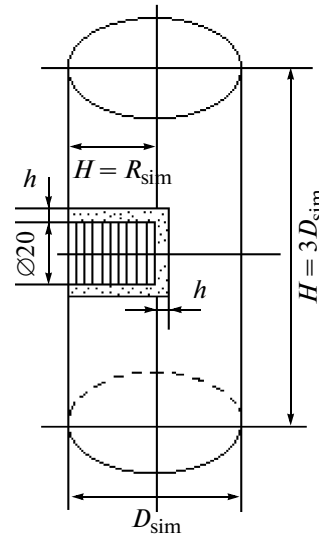
Table 1. The tempering parameters of the frontal quenched Jominy samples

Tempering temperature, °C/K	500/773	550/823	600/873	650/923	700/973
Isothermal maintaining time (t_{iz}), h	1.0	1.6	1.6	5.0	5.0
$\log t_{iz}$	0	0.2	0.2	0.7	0.7
$P_{HJ} = T_{rev}(19 + \log t_{iz})$	14678	15800	16762	18183	19168

Table 2. The hardnesses taken on length of quenched and tempered Jominy samples

d_J, mm / Condition	1.5	3	6	9	12	18	27	36	45
Frontal quenched	55	54	53	52	51.5	50	49	48	47
Tempered 500°C/1 h	46	45	44	42	40.5	39	34	31	28
Tempered 550°C/1.6 h	41.5	40.5	39.5	38	37	35	31	28	25
Tempered 600°C/1.6 h	38	37.5	36	35	34	32	29	26	24
Tempered 650°C/5 h	34	33	32	31	30	28	25.5	23.5	22
Tempered 700°C/5 h	30	29.5	29	28	27	25	23.5	22	21

tures, which are in accordance with the bainitic hardenability specific to steel.

EXPERIMENTAL RESULTS OF THE SIMULATING QUENCHING AND TEMPERING ON SAMPLES WITH SIMULATING DIAMETERS OF 60, 120 AND 180 mm

These results have been obtained through determining the hardness on simulating samples, that had allowed the graphical representation of hardness variation in the cross section of parts with the given diameters (Fig. 5).

Note. Figure 5 also gives the hardness values (black circles) in S; $3/4R$; $1/2R$ and C points in the sample with $D_{sim} = 60$ mm, taken from the diagram that show the connection between these points from the cross section with the distance in the Jominy sample d_J (Fig. 6). These values are close or similar to those experimentally determined on the simulating sample, therefore the simulating method used in this work is available also for diameters larger than 100 mm.

PROCESSING, DISCUSSION AND INTERPRETATION OF EXPERIMENTAL RESULTS DETERMINED ON JOMINY SAMPLES

The experimental results presented in Table 2 and illustrated in Fig. 3 demonstrate that hardness decreases after tempering with the increase of the tem-
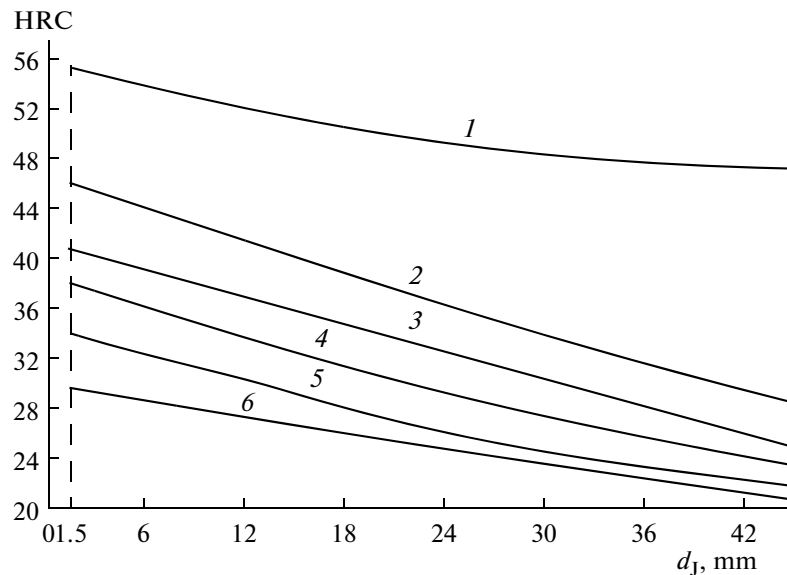

Fig. 3. Hardness variations in the frontal quenched Jominy samples, respectively in the frontal quenched and tempered Jominy samples. *1*—frontal quenched; *2*—tempered 500°C/1 h; *3*—tempered 550°C/1, 6 h; *4*—tempered 600°C/1, 6 h; *5*—tempered 650°C/h; *6*—tempered 700°C/5 h.
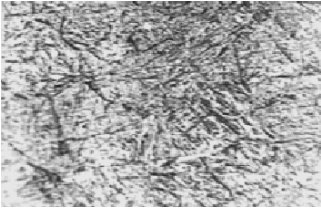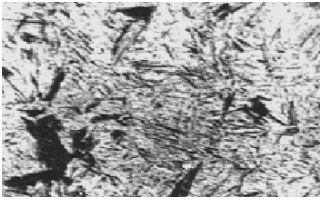
	$d_J = 2.5$ mm	98%M + 2%B	54HRC
	$d_J = 5$ mm	96%M + 4%B	53HRC
	$d_J = 12.5$ mm	92%M + 8%B	51HRC
	$d_J = 30$ mm	75%M + 25%B	48HRC
	$d_J = 45$ mm	50%M + 50%B	47HRC

Fig. 4. Microstructures (nital 2%) and hardnesses in the frontal quenched Jominy sample.

pered parameter P_{HJ} and the distance from the cooled end of the Jominy sample d_J. To process this dependence and determine the mathematical expression of the correlation $HRC_{rev} = f(P_{HJ}; d_J)$, in Fig. 7 were plotted $HRC_{rev} = f(P_{HJ})$ curves at some significant distance from the Jominy sample (d_J = 9, 18, 27, 36 and 45 mm). It is evident from Fig. 7 that these curves are straight lines, in fact, the straight lines having the following general equation:

$$HRC_{Rev} = HRCo - m(P_{HJ} - 14700), \quad (1)$$

in which both the ordinate at the origin (HRCo), and the straight lines slope (m) decrease when increasing

distance d_J. Further mathematical processing has shown that both HRCo and m are linearly dependent on distance d_J (Fig. 8), having concrete equations, as below:

$$HRCo = 45.5 - 0.39d_J, \quad (2)$$

respectively:

$$m = 0.0035 - 0.000043d_J. \quad (3)$$

With these explanations, the general Eq. (1) has the form:

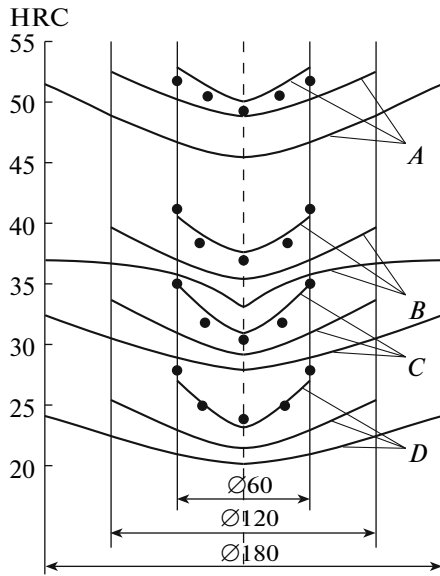$$HRC_{rev} = (45.5 - 0.39d_J) - (0.0035 - 0.000043d_J)(PHJ\text{-}14700), \quad (4)$$

Fig. 5. Hardness variations in the cross-section in the samples of 60, 120 and 180 mm simulation diameters. *A*—oil quenched; *B*—quenched and tempered 500°C/1 h; *C*—quenched and tempered 600°C/1, 6 h; *D*—quenched and tempered 700°C/5 h; ●—experimental data in Jominy samples for *D* = 60 mm.

which can be written in an explicit polynomial form:

$$HRC_{rev} = 97 - 0.0035P_{HJ} - 1.022d_J + 0.000043P_{HJ}d_J. \quad (5)$$

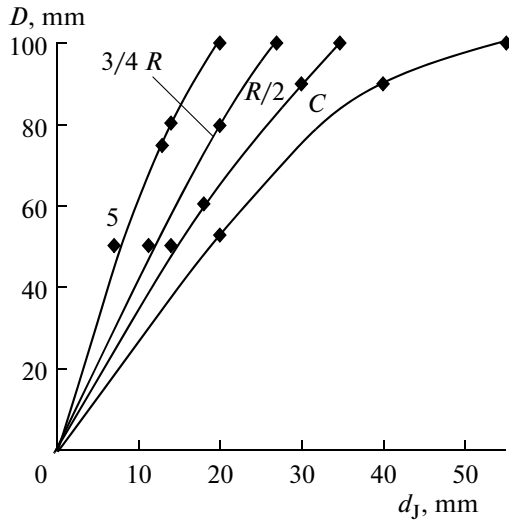From the Eq. (5) results that the hardness of steel 34CrNiMo6 after tempering decreases more rapidly with P_{HJ} tempering parameter, more slowly with the d_J distance and slightly increases with $P_{HJ}xd_J$ product. That product is the result of ongoing changes in the conditions of decomposition reactions of structure hardening during the tempering stage IV, in the sense that the longer the d_J distance, the lower the proportion of martensite, and simultaneously the higher the proportion of bainite (Fig. 9) will be. This phenomenon has two significant effects, respectively:

(a) a decrease of the initial hardness HRCo (Fig. 8, derived from data in Fig. 4);

(b) a decrease of the softening rate, respectively of the slope *m* of the straight lines from Fig. 8, because bainite softens more slowly than martensite.

On the other hand, the tempering parameter directly influences the kinetics of the softening process through high tempering, because the tempering temperature leads to the exponential increase of the softening process rate and the increase of the isothermal tempering time also leads to the parabolic increase of the softening process rate.

PROCESSING AND DISCUSSION OF EXPERIMENTAL RESULTS OBTAINED BY THE METHOD OF SIMULATION OF PARTS WITH THE EQUIVALENT DIAMETER GREATER THAN 100 mm

In the mathematical processing the experimental results obtained on simulation diameters 60, 120 and 180 mm, in the main points of the cross section (*C*, *R*/2 and *S*), in the three values of parameter of tempering (P_{HJ} = 14700, 16800, and 19200) were

Fig. 6. Correlation between the diameter of the piece, *D*, and distance d_J from the end of Jominy sample, cooled to quench the piece in oil 60°C with moderate agitation (*H* = 0.5).
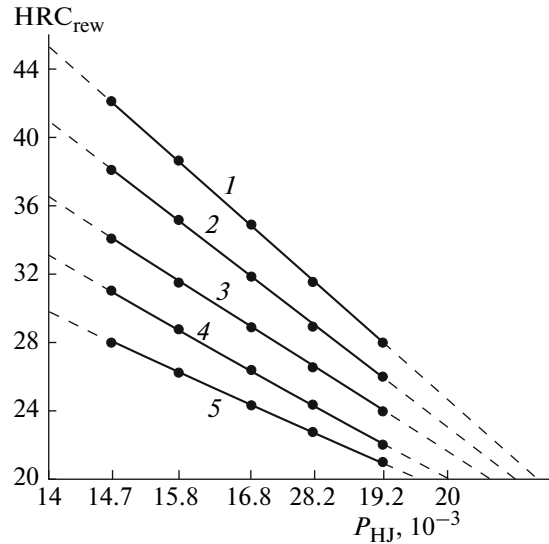

Fig. 7. Variations of hardness after tempering, with the tempered parameter, P_{HJ} and distance from the end of the cooled Jominy sample d_J mm: *1*—9; *2*—18; *3*—27; *4*—36; *5*—45.
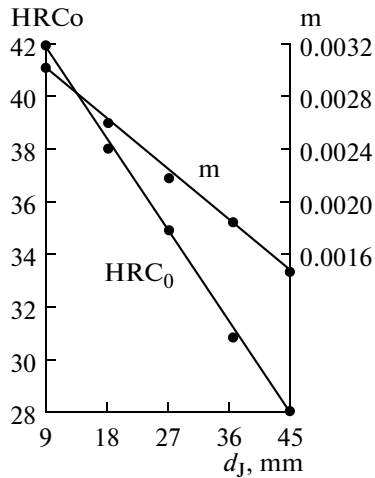
Fig. 8. Dependence of the ordinate at the origin (HRCo) and slope (m) of the straight lines $HRC_{rev} = HRCo - m(P_{HJ} - 14700)$.

used. First, the results plotted as shown in Fig. 10, demonstrate that hardness linearly varies with the tempering parameter and evidenciate that the straight lines slopes are much smaller at larger diameter, and that the points in the cross section are deeper placed from the surface, so the structure contains less martensite.

As the second step the results were mathematically processed, and finally the equation of straight line was determined: $HRC = HRCo - mP_{HJ}$, which has the general expression:

$$HRC = [76 - 0.1D + (25 - 0.001 P_{HJ})r/R] - (0.003 - 0.00004D)P_{HJ}, \quad (6)$$

where: r/R is the coordinate point of the cross section of a machine part with the equivalent diameter $D = 2R$. From Eq. (6) it is found that after tempering hardness is even lower, as the tempered parameter and the part diameter are larger and the corresponding point is placed deeper from the surface (as in Fig. 10).

At the end of this section it should be noted that the results obtained by applying relation (6) lead to linear changes in hardness in the cross section of the part and, as a result, to deviations of up to ±2.5 HRC against to the real situations in which hardness variation in cross-section occurs in accordance with curves having the minimum in the centre section (Fig. 5). With this specification, the simulation method can be applied with satisfactory results in the case of parts with diameters larger than 100 mm, and for the parts with diameters up to 100 mm the method of Jominy samples can be applied.
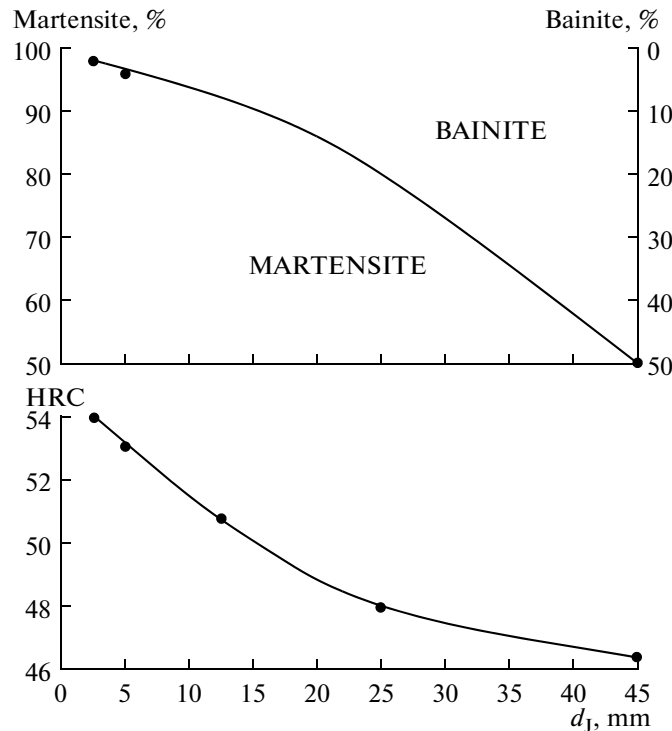

Fig. 9. Variations of the proportions of martensite and bainite (up), hardness (down,) with the distance d_J of Jominy samples of front quenched 34CrNiMo6 steel.
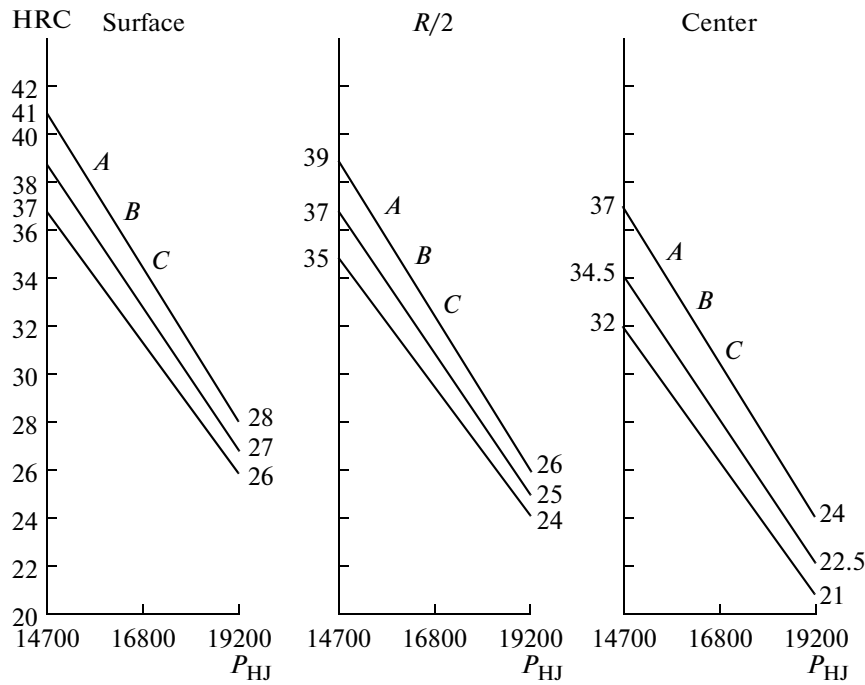
Fig. 10. Variation of hardness after tempering, with the tempered parameter and the diameter of the piece, in the main points of the cross section: A : $D = 60$ mm; B : $D = 120$ mm; C : $D = 180$ mm.
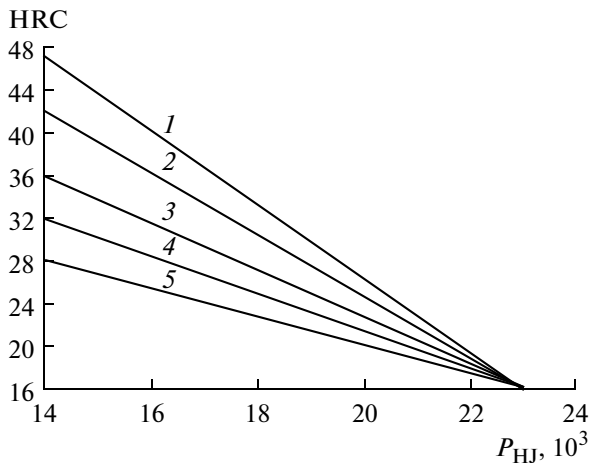
Fig. 11. The dependence of hardness on the P_{HJ} tempering parameter and d_J distance from the end of front quenched Jominy samples of 34CrNiMo6 steel. d_J, mm: *1*—2; *2*—20; *3*—30; *4*—40; *5*—50.

CONCLUSIONS

The experimental research into the bulk tempering of steel 34CrNiMo6 was performed on Jominy and simulation samples. It resulted in the production of two general relationships for the dependence of hardness after tempering on the Hollomon–Jaffe parameter, namely:

$$HRC = 97 - d_J - 0.035 P_{HJ} + 0.000043 P_{HJ} d_J, \quad (7)$$

applicable to parts with $D_{ech} \leq 100$ mm, with an accuracy of ± 1 HRC, also:

$$HRC = [76 - 0.1 D + (25 - 0.001 P_{HJ}) r/R] \\ - (0.003 - 0.00000 D) P_{HJ}, \quad (8)$$

applicable to parts $100 < D_{ech} \leq 180$ mm, with precision ± 2.5 HRC.

Equation (5) is more accurate and leads to graphical presentation of straight beam lines, converging at the point of coordinates ($P_{HJ} = 23000$; HRC = 16), as can be seen from Fig. 11. This graphical result evidences that the point of convergence would be the highest tempering at the softest structure, consisting of polyhedral ferrite and globular carbides with a very small degree of dispersion.

REFERENCES

1. Standard of steel SR EN 10083-1:1995.

A New Single Bath for the Electrodeposition of NiFe/Cu Multilayers Exhibiting Giant Magnetoresistance Behavior[1]

S. Esmaili and M. E. Bahrololoom

Department of Materials Science and Engineering, School of Engineering, Shiraz University, Zand Blvd., Shiraz, Iran
e-mail: esmaili@shirazu.ac.ir, esmaili_sitra@yahoo.com
Received May 25, 2011

Abstract—A new single bath for the electrodeposition of ultrathin NiFe/Cu multilayers was developed and magnetoresistance measurements were conducted. Complementary methods such as scanning electron microscopy (SEM), x-ray diffraction (XRD) and transmission electron microscopy (TEM) were used to characterize the multilayers. Magnetoresistance measurements indicated that the multilayers grown from this new bath exhibited a giant magnetoresistance (GMR) behavior.

INTRODUCTION

Since the discovery of giant magnetoresistance (GMR) in 1988 [1], multilayered structures consisting of ferromagnetic layers separated by a nonmagnetic spacer layer have been studied worldwide. Among different choices, the material combination of permalloy/copper (denoted by Py/Cu) has raised great interest regarding its application potential as magnetoresistance read heads in the new generation of magnetic recording storage devices [2]. Several papers have been published on the GMR effect of deposited NiFe/Cu multilayers grown by ion-beam [3], magnetron sputtering [4], face to face sputtering [5] and vacuum evaporation technique [6]. These techniques have the advantages of a high control of film growth and a pure material can be easily obtained but they inevitably require high vacuum and/or temperatures. However, electrodeposition exhibits advantages of low cost, simplicity and ease of production [7].

A great deal of research has been performed on the investigation of the magnetic behavior of Py/Cu multilayers deposited by physical methods after Parkin [8] found that saturation magnetoresistance values at 300 K of these multilayers exceeds 16% for saturation fields of only 600 Oe. Nakatani et al. [3] observed oscillatory magnetoresistance changes with copper thickness for NiFe/Cu multilayers formed by ion beam sputtering and a GMR of 19% was reported. Urbaniak et al. [9] investigated the GMR effect and magnetization reversal processes of Py/Cu multilayer obtained by face-to-face sputtering. It was shown that for such multilayers a high field sensitivity of GMR effect and negligible hysteresis can be found for a low number of Py layers. Heitmann et al. [10] reported that the Py/Cu multilayers, grown by magnetron sput-

tering, consisting of alternating blocks of first and second anti-ferromagnetic coupling maximum can display a GMR ratio up to 20%. Fulthorpe [11] determined the structural changes that occur during the annealing of Py/Cu multilayers grown by the same method. Luo et al. [12] also grew Py/Cu multilayers by magnetron sputtering and applied reflection anomalous fine structure analysis to find a strained permalloy layer at the Py/Cu interface. In 2005, Ene et al. [13] analyzed the sputtered NiFe/Cu multilayer stacks by atom probe tomography and studied annealing effects which degrade the GMR ratio. Ai et al. [2] investigated the microstructure nanomechanical behavior of Py/Cu magnetic multilayers deposited by a DC magnetron sputtering system.

Research in this area is still in progress; however, few papers addressing the electrodeposition of NiFe/Cu multilayers have been published to the date. In 1994, Chang and Romankiw [14] demonstrated that it was possible to electroplate thin layers of NiFe/Cu onto an N-doped (111)-oriented Si wafer from a single solution, but GMR studies were not performed. To the best knowledge of the authors, so far two groups have reported the GMR of electrodeposited NiFe/Cu multilayers apart from studies on nanowires: The first results of GMR in electrodeposited NiFeCu/Cu multilayers was presented by Attenborough et al. [15] in 1995. This group used a single electrolyte based upon the electrolyte used by Romankiw and Olsen [14]. A GMR of 1.4% was reported for $[NiFeCu_{(2\,nm)}/Cu_{(2.5\,nm)}]_{200}$. The MR curves were quite sharply peaked but they did not saturate even with an applied field of 8 kOe which suggested that some regions of the film layers were antiferromagnetically coupled. The copper content within the magnetic layers was estimated to be 9%. One year later Chassaing et al. [16] reported a magnetoresistance value of 2% at

---

Table 1. Electrolytes compositions

Electrolyte	$NiSO_4$	$FeSO_4$	$CuSO_4$	Saccharin	Sodium Dodecyl Sulphate (SDS)	Boric acid
Chang solution	0.2 M	0.002 M	0.002 M	2 (g/L)	0.02 (g/L)	–
New solution	0.4 M	0.004 M	0.01 M	–	–	0.2 M

2 kOe for $[NiFe_{(3\ nm)}/Cu_{(15\ nm)}]_{30}$ at 77 K. Such magnetic couplings were observed for a copper layer thickness ranging between 1.5 and 3.5 nm. For thinner magnetic layers no coupling was observed. Tokarz et al. [17] have also electrodeposited NiFe/Cu multilayers by a single bath technique. A columnar structure deposit with column diameter in the range from 10 to 30 nm was observed. The line scans acquired using energy dispersive spectra confirmed the layered structure of the deposit, but pointed towards the possibility of intermixing of species from alternating sublayers. No magnetic and magnetotransport data were reported.

In the present research, the solution proposed by Chang and Romankiw [14] was used and multilayers were deposited, characterized and magnetoresistance (MR) measurements were taken and studied. Since the MR results were not satisfactory, the solution was modified and a new solution was introduced. The concentration of the metal salts was adjusted and additives which proved to be deleterious for the GMR of electrodeposited multilayers [18] were omitted so as to obtain a giant magnetoresistance behavior. Multilayers deposited from this new solution were characterized and GMR measurements were made. GMR behavior was observed from the NiFe/Cu multilayers deposited from this new solution.

EXPERIMENTAL SAMPLE PREPARATION

Electrodeposition was performed using a potentiostat, model Auto Lab Equipment (PGSTATX, BSTR10A) equipped with a general purpose electrochemical system (GPES) software. The computer-controlled potentiostat was used to monitor the entire electrochemical process. Experiments were conducted in the potentiostatic mode for both layers. Two solutions were prepared which were based on the early work of Chang and Romankiw [14], although one of the solutions was used after some modifications. Compositions are given in Table 1, respectively. Analytical-grade (Merck) reagents and distilled water was used. Electrodeposition was carried out in a standard three-electrode cell with a saturated calomel electrode (SCE) as the reference electrode. The counter electrode was a platinum wire. Since copper is one of the most noble metals, it requires only a small negative potential for reduction to occur, whereas nickel and iron (less noble metals) require a much higher potential [15]. Therefore, the deposition potentials were chosen to be—2.5 V for the NiFe layer and—0.4 V for

the Cu layer, measured relative to a SCE as close as possible to the cathode surface, to minimize the ohmic potential drop in the electrolyte. The computer controlled potentiostat was adjusting these two potentials. A Pt foil counter electrode was placed directly opposite the working electrode substrate. Electrodeposition from Chang's solution was carried out at 40°C, whereas deposition from the new solution was performed at room temperature with no stirring.

MORPHOLOGICAL INVESTIGATIONS

An Oxford Instrument Stereoscan 120 scanning electron microscope (SEM) and a transmission electron microscope (TEM) operating at an accelerating voltage of 200 keV (0.23 nm resolution) were used for morphological studies. Cu foils, (200) oriented and 2 cm^2 in area, were used as substrates. Thick multilayers were electrodeposited from both solutions under the same conditions and compared. In order to perform the high resolution transmission electron microscopy study, the samples were polished mechanically and then thinned by means of Ar$^+$ bombardment to achieve the appropriate thickness, which allows electrons to pass through the sample (around 100 nm). The samples were then mounted on a copper holder.

LOW ANGLE X-RAY DIFFRACTION (LAXRD)

Low angle x-ray diffraction (LAXRD) was used to investigate the structure of the deposits using a Phillips X' pert Pro X-ray diffractometer (Cu $K_{\alpha 1}$ radiation, $\lambda = 0.15405$ nm) by scanning in the $2\theta = 40°–60°$ range with 0.01 steps at a grazing angle of 5°. Glasses sputtered with 100 nm gold, 2 cm^2 in area, were used as substrates for the LAXRD studies.

MAGNETORESISTANCE MEASUREMENTS (MR)

Multilayers prepared for magnetotransport measurements were deposited onto Si(100)/Cr(5 nm)/Cu(20 nm). The Cr adhesive layer and the Cu seed layer were prepared by evaporation on the Si wafer. The magnetoresistance was measured on 2 mm wide strips at room temperature with the four-point-in-line method in magnetic fields between −8 kOe and +8 kOe in the field-in-plane/current-in-plane geometry. Both the longitudinal magnetoresistance (LMR, field parallel to current) and the transverse magnetoresistance (TMR, field perpendicular to current) components were mea-

sured. The following formula was used for calculating the magnetoresistance ratio: $R/R_0 = (R_H - R_0)/R_0$ where R_H is the resistance in a magnetic field H and R_0 is the resistance value of the magnetoresistance peak around zero field. The shunt effect of the substrate was not corrected. Table 2 presents the number of the prepared specimens along with the characterization techniques and experiments carried out on each specimen.

RESULTS AND DISCUSSION

Cross-sectional scanning electron microscopy (SEM) images of sample 1 are shown in Fig. 1. In each SEM image the brighter regions are NiFe while the darker ones are Cu layers. A total of 4 periods (8 continuous layers, 4 of Cu and NiFe each) are visible. The Cu layers have an average thickness of 500 nm while that of NiFe, 1 µm. The SEM investigations confirm the periodical formation of the multilayers from Chang's solution deposited onto the copper substrate.

Figure 2 shows the room-temperature magnetoresistance curves for samples 2, 3 and 4 grown from Chang's solution. As seen, all samples show anisotropic magnetoresistance (AMR) instead of giant magnetoresistance (GMR) i.e. the deposit exhibits ferromagnetic behavior similar to that of bulk NiFe. Positive LMR and negative TMR components are obtained with an AMR = LMR − TMR value amounting to some 1%.

In order to investigate the reason of the absence of GMR behavior from these samples, cross sectional transmission electron microscopy images were taken. The modulated structure of NiFe/Cu multilayers with thin bilayer thickness prepared from Chang's solution is shown in Fig. 3. Transmission electron microscopy (TEM) results show that there are some ordered regions which are very small. The bilayers thickness also seems to vary too much. Additionally, the orientation of the stripes is rather random, while in a real multilayer one should see a dominant layer plane which is roughly perpendicular to the growth direction. Therefore, these pictures are in accord with the MR proper-

Table 2. Characterization of specimens

Specimen no.	Electrolyte	No. of bilayers	Characterization techniques
1	Chang	4	SEM, LAXRD
2	Chang	50	MR
3	Chang	100	MR, TEM
4	Chang	150	MR
5	New	5	SEM, LAXRD
6	New	50	MR
7	New	100	MR
8	New	150	MR

ties, namely, the lack of the laminar structure and the occurrence of the AMR.

To modify Chang's bath, all components that were taken from the classical experience of the plating industry, i.e. sodium saccharin and sodium dodecyl sulfate, were omitted. These components serve as stress relievers and brighteners for decorative plating but at the same time decrease the crystallite size drastically. As a result, the growth of continuous and even layers will become less and less likely. This could be one reason why samples 2, 3 and 4 did not show any GMR. The typical additives used as surfactants such as sodium dodecyl sulfate (SDS), sulfur organic compounds such as saccharin, both known as levelers, stress relievers and brighteners are harmful for the formation of the layer structure and result in the loss of GMR [18]. On the other hand, saccharin is known to decrease the crystallite size. The decrease in the crystallite size always leads to the increase in resistivity, simply because the electrons are frequently scattered at the grain boundaries where the atomic ordering is imperfect. Since the MR ratio is referred to the zero-field resistivity, a drastic increase in the latter quantity leads to a decrease in the MR ratio to the same extent. In addition, the concentrations of the metal salts were changed. The Ni^{2+} ion concentration was raised to 0.4 mol/L while the Fe^{2+} ion concentration was increased to 0.004 mol/L. The concentration of the Cu^{2+} ion was very small in Chang's bath, therefore it
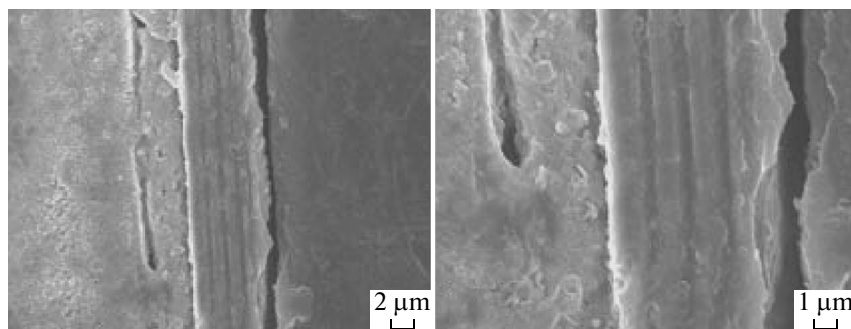
Fig. 1. SEM micrographs of sample 1 showing the 4 bilayers of [NiFe/Cu]$_4$ deposited from Chang's solution. NiFe layers are the brighter bands while Cu layers are the darker ones.
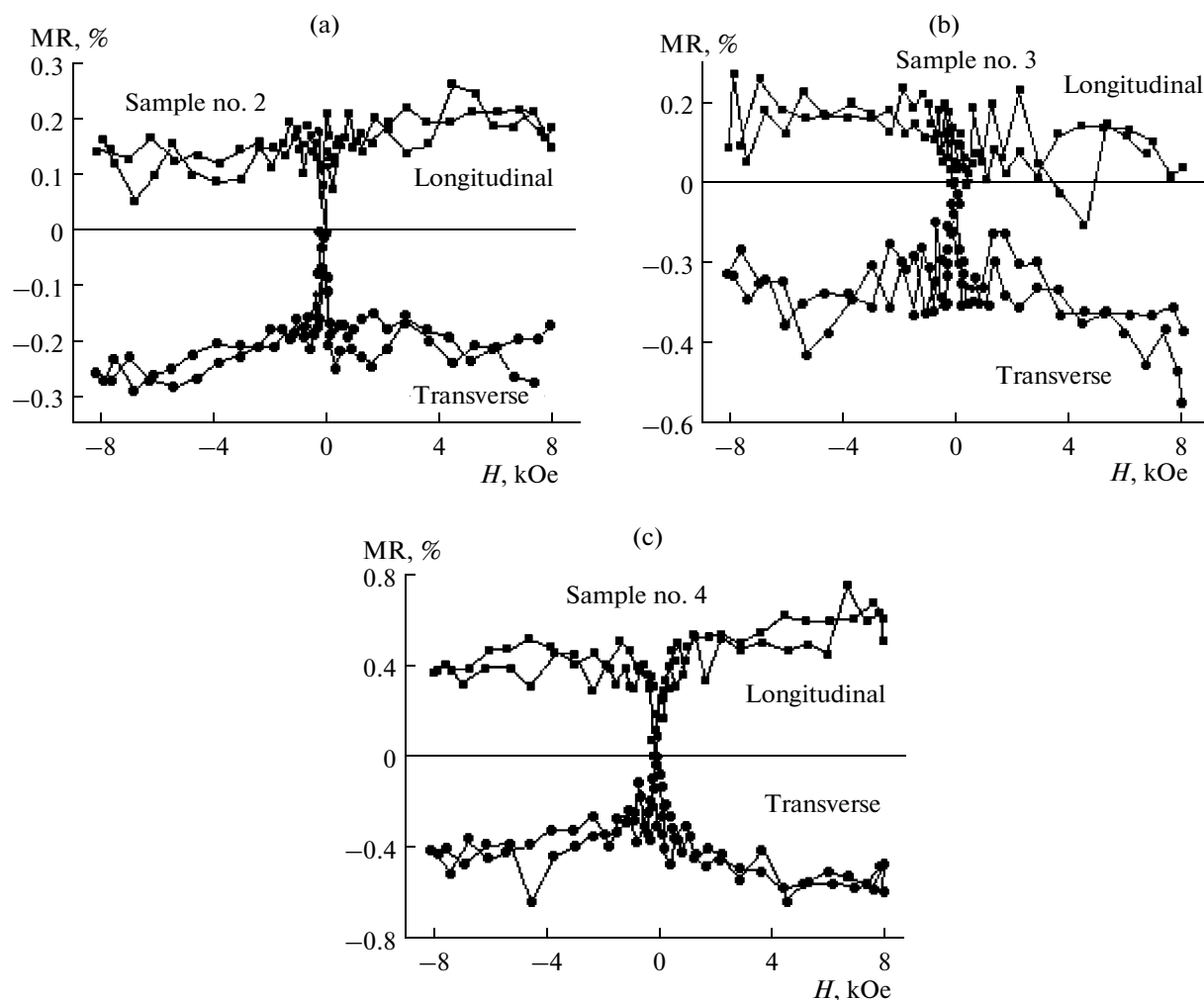
Fig. 2. Longitudinal (LMR) and transverse (TMR) components of the magnetoresistance saturation for samples deposited from Chang's solution: (a) sample 2, (b) sample 3, and (c) sample 4.
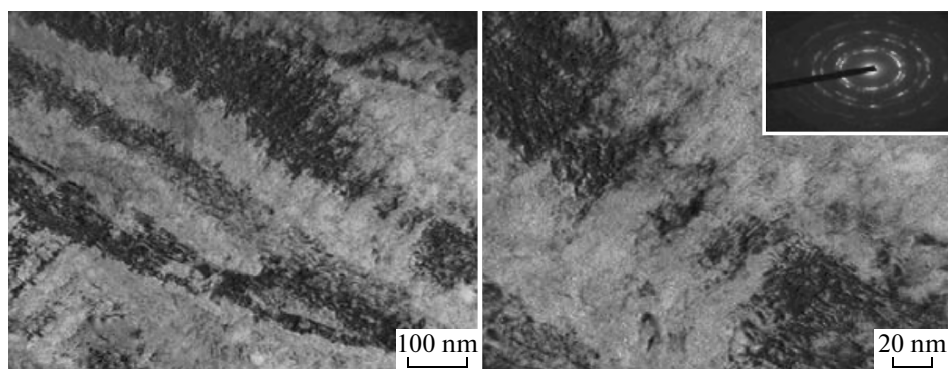
Fig. 3. Cross sectional transmission electron microscopy image of NiFe/Cu multilayers of sample 3 made from Chang's solution.

was increased to 0.01 mol/L. Apart from the metal salts, 0.2 mol/L boric acid was also used. Boric acid is known to buffer the pH, help prolong the plating bath life, and produce more uniform deposits [19]. The preliminary experiments showed that the rest potential of the magnetic layer is rather close to −0.65 V vs. SCE. Nevertheless, the dissolution of the NiFe layer at −0.4 V is not very fast, so even at this potential the mis-estimation of the layer thicknesses due to the Fe to Cu exchange is negligible.
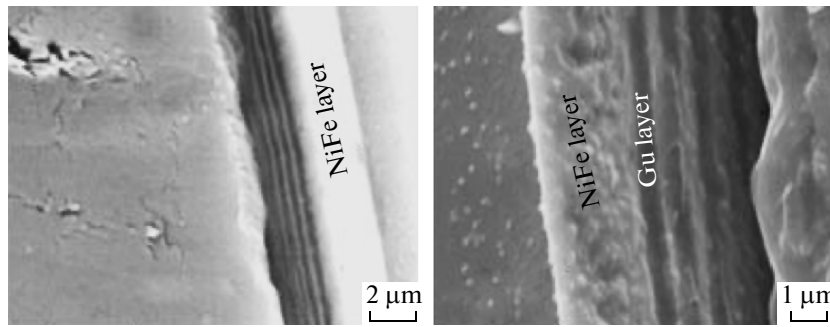
Fig. 4. SEM micrographs of sample 5 containing five bilayers of [NiFe/Cu]₅ multilayers deposited from the modified solution. A thick NiFe layer separates the multilayer region from the substrate.
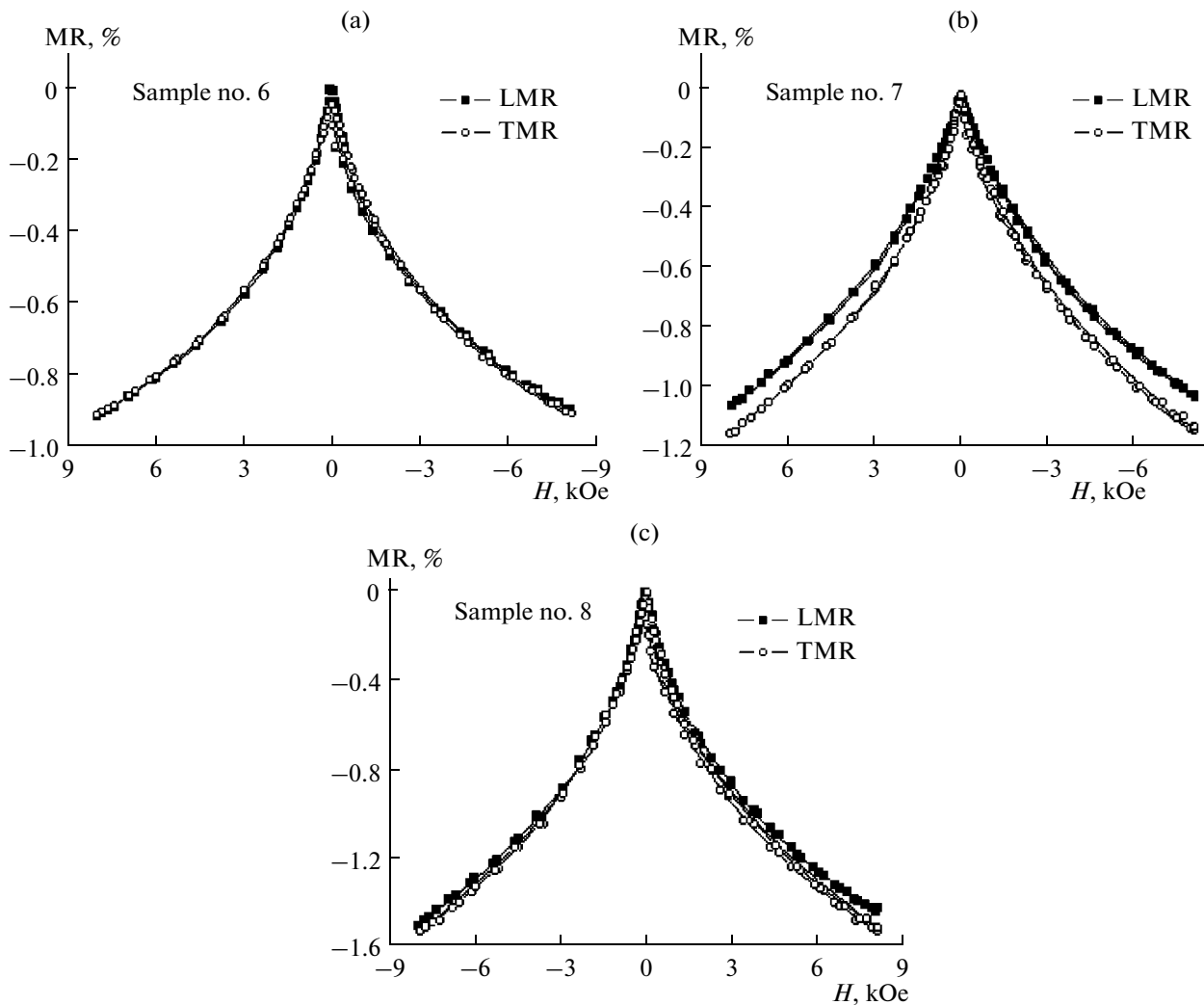
Fig. 5. Magnetoresistances measured at room temperature for samples 7, 8 and 9. (a) $[NiFe_{(3\ nm)}/Cu_{(1.2\ nm)}]_{50}$, (b) $[NiFe_{(3\ nm)}/Cu_{(1.2\ nm)}]_{100}$, (c) $[NiFe_{(3\ nm)}/Cu_{(1.2\ nm)}]_{150}$.

The SEM micrographs taken from thick deposits of multilayers electrodeposited from the new solution are shown in Fig. 4. A thick NiFe layer was deposited first which indicates that the NiFe layers are the brighter bands with an average thickness of 450 nm and the darker bands are the Cu layers with a nominal thickness of 480 nm.

Figure 5 shows the results of GMR measurements for samples 6, 7 and 8. The GMR effect is very evident. All samples exhibit a superparamagnetic (SPM)—the
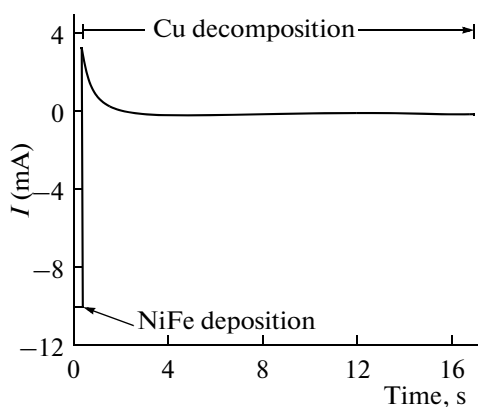
Fig. 6. Typical current-time response of one cycle during the pulse potential deposition of sample 8.
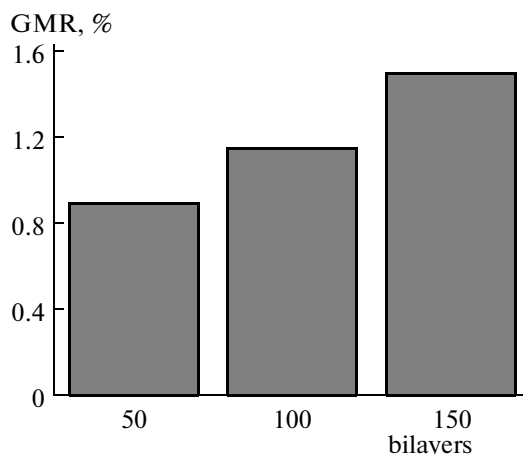
Fig. 7. Dependence of number of layers on GMR ratio.
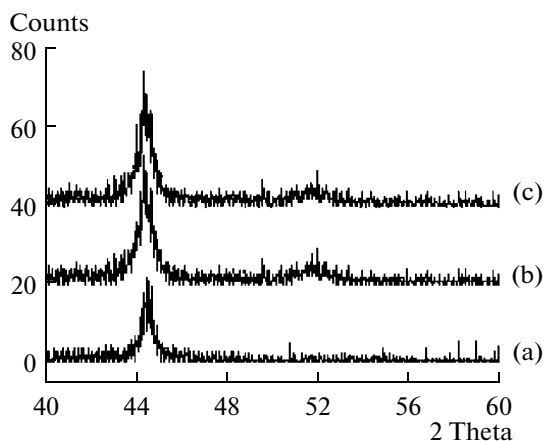
Fig. 8. LAXRD of (a) glass substrate sputtered with a 100 nm-Au layer, (b) sample 1, [NiFe/Cu]$_4$ multilayers deposited from Chang's solution on the latter substrate, (c) sample 5, [NiFe/Cu]$_5$ deposited from the modified solution on the latter substrate.

so-called magnetically isolated islands within the magnetic layers [18, 20]—character which is shown by the slow saturation. The effect is not very large. The SPM character of the GMR curves tells that the magnetic layer is either fragmented or quite rich in Cu and there is some element segregation.

The reason of the SPM character found in these samples could also be explained in Fig. 6 which shows the typical current-time response during the pulse potential deposition of sample 8. A very large anodic transient at the beginning of the Cu pulse is depicted which means that there is a significant dissolution at the beginning of the pulse until the Cu layer fully covers the surface. The dissolution of the magnetic layer contributes to both the interface roughening and the fragmentation of the magnetic layer. To overcome this problem, the Cu deposition potential should be chosen more negative.

Figure 7 shows the effect of the number of layers on the GMR effect exhibited by this modified solution. As the number of layers increases, the system exhibits a larger amount of GMR. This effect is caused by a decreased contribution of the outer boundary scattering to conducting processes and a higher number of magnetic-nonmagnetic interfaces within the electron mean free path. In other words, increasing the amount of interfacial material increases the magnitude of the GMR.

The low angle X-ray diffraction (LAXRD) patterns of samples 1 and 5 (Fig. 8) reveal the dominant orientations of the Cu and NiFe layers to be (111) and (200) respectively. No multilayer satellites were observed in the thick layers studied, which is either the indication of a non-coherent growth of the subsequent layers or that of the undulated interfaces. The occurrence of satellite peaks is expected around the main multilayer peak, if there exists any, but in the absence of such peaks the lack of the satellite is a very natural feature of the diffractograms [21].

Further studies on this electrolyte are currently taking place in order to optimize and increase the GMR effect achieved from this bath and to obtain further structural information on the multilayers, transmission electron microscopic studies are planned to be performed.

CONCLUSIONS

NiFe/Cu multilayers were electrodeposited by a single bath technique in the potentiostatic mode. No GMR behavior was observed using the electrolyte suggested by previous researchers, therefore the solution was modified by omitting harmful additives and changing the concentrations of the chemicals and a new electrolyte was introduced. The multilayers deposited from this electrolyte exhibited a GMR ratio up to 1.5%. GMR effect was more pronounced in samples containing higher number of bilayers. Struc-

tural studies pointed towards a (111) orientation in the copper layers and a dominant (200) orientation for the NiFe layers. The inferior GMR characteristics of electrodeposited multilayers as compared to physically deposited multilayers can be ascribed to microstructural features leading to the appearance of SPM regions, pinholes in the spacer layers and not sufficiently perfect interfaces.

ACKNOWLEDGMENTS

REFERENCES

1. Baibich, M.N., Broto, J.M., Fert, A., Nguyen Van-Dau, F., Petroff, F., Etienne, P., Creuzet, G., Friederich, A., and Chazelas, J., Giant Magnetoresistance of (001)Fe/(001)Cr Magnetic Superlattices, *Phys. Rev. Lett.*, 1988, vol. 61, pp. 2472–2475.

2. Ai, J., Gao, Y., Yang, G., and Pan, F., Micro-Structure, Nano-Property and Nano-Tribological Behaviour of the Permalloy/Copper Multilayers, *Surf. Coat. Tech.*, 2007, vol. 201, pp. 5988–5993.

3. Nakatani, R., Dei, R., Kobayashi, T., and Sugita, Y., Giant Magnetoresistance in NiFe/Cu Multilayers Formed by Ion Beam Sputtering, *IEEE T. Magn.*, 1992, vol. 28, pp. 2668–2670.

4. Meyer, D.C. and Paufler, P., Coherency and Lattice Spacings of Textured Py/Cu Multilayers as Revealed by X-ray Diffraction, *J. Alloys Compd.*, 2000, vol. 298, pp. 42–46.

5. Luciniski, T., Stobiecki, F., Elefant, D., Eckert, D., Reiss, G., Szymanski, B., Dubowik, J., Schmidt, M., Rohrmann, H., and Roell, K., The Influence of Sublayer Thickness on GMR and Magnetization Reversal in Py/Cu Multilayers, *J. Magn. Magn. Mater.*, vol., 174, pp. 192–202.

6. Neamtu, J., Volmer, M., and Coraci, A., Magnetoresistive Properties and Microstructure of NiFe Thin Films and NiFe(t)/Cu(s)/NiFe(t) Multilayer Films, *Thin Solid Films*, 1999, vols. 343–344, pp. 218–221.

7. Miyake, T., Kume, M., Yamaguchi, K., Amalnerkar, D.P., and Minoura, H., Electrodeposition of Cu/Ni-P Multilayers by a Single Bath, *Thin Solid Films*, 2001, vol. 397, pp. 83–89.

8. Parkin, S.S.P., Oscillations in Giant Magnetoresistance and Antiferromagnetic Coupling in $[Ni_{81}Fe_{19}/Cu]_N$ Multilayers, *Appl. Phys. Lett.*, 1992, vol. 60, pp. 512–514.

9. Urbaniak, M., Lucinski, T., and Stobiecki, F., High Sensitivity GMR with Small Hysteresis in Ni-Fe/Cu Multilayers, *J. Magn. Magn. Mater.*, 1998, vol. 190, pp. 187–192.

10. Heitmann, S., Hutten, A., Hempel, T., Scheper, W., and Reiss, G., Enhanced GMR Amplitude and Temperature Stability of Cu/Py Combination Multilayers, *J. Magn. Magn. Mater.*, 2001, vols. 226–230, pp. 1752–1754.

11. Fulthorpe, D., Hase, T.P.A., Tanner, B.K., Marrows, C.H., and Hickey, B.J., Oscillations in Giant Magnetoresistance and Antiferromagnetic Coupling in $Ni_{81}Fe_{19}/Cu$ Multilayers, *J. Magn. Magn. Mater.*, 2001, vols. 226–230, pp. 1733–1734.

12. Luo, G.M., Mai, Z.H., Hase, T.P.A., Fulthorpe, B.D., Tanner, B.K., Marrows, C.H., and Hickey, B.J., X-Ray Reflection Anomalous Fine Structure Analysis of the Stability of Py/Cu Multilayers, *J. Magn. Magn. Mater.*, 2001, vols. 226–230, pp. 1728–1729.

13. Ene, C.B., Schmitz, G., Kirchheim, R., and Hutten, A., Stability and Thermal Reaction of GMR NiFe/Cu Thin Films, *Acta Mater.*, 2005, vol. 53, pp. 3383–3393.

14. Chang, J.W. and Romankiw, L.T., Electrodeposited Superlattices for CoFe/Cu and NiFe/Cu on *n*-Type (111) Si Single Crystal Wafers, *Elec. Soc. Proc. Ser.*, 1994, vol. [PV 94-6], pp. 223–232.

15. Attenborough, K., Hart, R., Lane, S.J., Alper, M., and Schwarzacher, W., Magnetoresistance in Electrodeposited Ni–Fe–Cu/Cu Multilayers, *J. Magn. Magn. Mater.*, 1995, vol. 148, pp. 335–336.

16. Chassaing, E., Nallet, P., and Trichet, M.F., Electrodeposition of $Cu/Fe_{20}Ni_{80}$ Magnetic Multilayers, *J. Electrochem. Soc.*, 1996, vol. 143, pp. L98–L100.

17. Tokarz, A., Wieczorek, P., Lis, A.K., and Morgiel, J., Microstructure of Electrodeposited NiFe/Cu Multilayers, *J. Microsc.*, 2010, vol. 237, pp. 456–460.

18. Bakonyi, I. and Peter, L., Electrodeposited Multilayer Films with Giant Magnetoresistance (GMR): Progress and Problems, *Prog. Mater. Sci.*, 2010, vols. 55–3, pp. 107–245.

19. Cheung, C., Palumbo, G., and Erb, U., Synthesis of Nanocrstalline Permalloy by Electrodeposition, *Scripta Metall. Mater.*, 1994, vol. 31, no. 6, pp. 735–740.

20. Peter, L., Padar, J., Toth, E., Cziraki, A., Soki, P., Pogany, L., and Bakonyi, I., Electrodeposition of Co–Ni–Cu/Cu Multilayers, *Electrochim. Acta*, 2007, vol. 52, pp. 3813–3821.

21. Garcia-Torres, J., Peter, L., Revesz, A., Pogany, L., and Bakonyi, I., Preparation and Giant Magnetoresistance of Electrodeposited Co–Ag/Ag Multilayers, *Thin Solid Films*, 2009, vol. 517, pp. 6081–6090.

Some Peculiar Features of Electric Separation

F. P. Grosu, M. K. Bologa, V. I. Leu, and Al. M. Bologa

Institute of Applied Physics, Academy of Sciences of Moldova, ul. Akademiei 5, Chisinau, MD-2028 Republic of Moldova
e-mail: mbologa@phys.asm.md
Received July 5, 2011

Abstract—The most characteristic features of the processes of electrical filtration of ideal and low-conducting dielectric fluids are considered. It is noted that, in liquid dielectrics in highly inhomogeneous electric fields, phenomena similar to those at corona discharge in gases with all its consequences are observed. The processes of electrical purification (separation) are interpreted in terms of a corona discharge. In particular, the electric charging of dispersed particles and their transport to the "electrode–collector" are considered. The threshold phenomena at electric separation such as the appearance and disappearance of the separation effect are treated from the standpoint of a corona discharge as well. Two concepts, namely, the screening of an external electric field by the field's spatial electric charge and the ohmic resistance of the layer of dispersed particles deposited on the collector are discussed. Both approaches lead to identical results. To clarify the above-mentioned theoretical concepts and to work out recommendations for the modernization and efficient use of electrical separation, further studies of the experimental time–current characteristics of the process of the separation are needed.

INTRODUCTION

The problems of the separation of heterogeneous systems, in particular, dielectric ones, such as suspensions, emulsions, aerosols, etc., are undoubtedly topical. It is difficult to imagine any domain of science, engineering, the chemical industry, food manufacturing, medical ones, and so on in which the questions connected with separation do not arise. For this reason, regular international symposiums are held including conferences [1].

A lot of methods to separate heterogeneous systems, for instance, centrifugation, particle deposition, mechanical filtration, and chemical possibilities, exist. Yet, the methods of separation with the help of electric fields appear to be rather original. They were used at some production enterprises even in the 1950s to clean smoke from combustion material microparticles (carbon black, aerosols, etc.) entering the atmosphere and contaminating it. Works [2–4] are interesting from this point of view and are directly devoted to the questions of electric filtration of the air and other gases.

The physics of electrical cleaning (EC) methods used in gas electric filters is based on the phenomenon of a corona discharge. Among the multitude of peculiar features of this type of gas discharges [5–7], we note those ones that are of direct relevance to the problems under consideration. We first note that this discharge type is typical for nonuniform electric fields, when there is possible the strong local ionization of the medium within a limited space area between the electrodes producing the field. At a sufficient voltage between the electrodes, this can occur in the vicinity of electrodes with little geometric curvature (thin wires, needles, etc.), in which the medium is strongly ionized and is also characterized by a slight glow in the case of gases. This rather narrow area with a size of about the electrode's curvature radius is referred to as a "corona" layer or simply a corona. Beyond this layer, in the so-called peripheral area of the corona, there appears a region of the electrically charged medium with a charge of some spatial density ρ of the corona electrode's sign. Under the action of the Coulomb force $\mathbf{f} = \rho\mathbf{E}$, the medium is put in macroscopic motion. Thus, another peculiar feature of a corona discharge is the fact that it is always accompanied by hydrodynamic phenomena known under the name of electrohydrodynamic (EHD) ones, or simply as the "electric" wind (EW).

The peculiar features mentioned are also specific for the electric cleaning process as a whole as the dispersed particles, which should be removed from the gas, entering the spatial charge area are charged acquiring some electric charge q. Under the action of the Coulomb force $\mathbf{F} \equiv q\mathbf{E}$ and, partially, at the expense of the EHD flow ($\mathbf{f} = \rho\mathbf{E}$), these particles are whirled to the opposite electrode being at the same time a collector to gather them [2–4]. This is a brief explanation of the principle of operation of an electric filter for gases.

The considered phenomena are also observed in outline in liquid dielectrics in which an "electric wind" occurs too [8–10], and this is especially remarkable. Generally, the presence of EHD phenom-

ena at electric discharges in one or another system of electrodes points clearly to the fact that, in these discharges, the charges of some electric polarity prevail substantially over the ones of another polarity. Indeed, the general formula for the electric current density has the form

$$\mathbf{j} = \sigma\mathbf{E} \equiv (k^+\rho^+ + k^-\rho^-)\mathbf{E} \approx k(\rho^+ + \rho^-)\mathbf{E}, \qquad (1)$$

where σ is the specific conductivity, and $k^{\pm}$ is the mobilities of the ions of the corresponding sign. On the assumption of their equality, we obtain approximate equation (1). On the other hand, the excess density of the spatial charges is

$$\rho = \rho^+ - \rho^- \qquad (2)$$

If, for example, $\rho^+/\rho^- \gg 1$, then, for a purely coulomb EHD force, we obtain a simple formula,

$$\mathbf{f} = \rho\mathbf{E} = \mathbf{j}/k, \qquad (3)$$

with $\rho \approx \rho^+$. The spatial density of the charges ρ and the mobility ratio k in formula (3) always correspond to the sign of the corona electrode.

This approach uniting formulas (1)–(3) and describing EHD phenomena in the cases of both gases and liquids is collectively called "unipolar" conduction [11]. Note that these formulas conform to binary electric systems containing two types of current carriers, and they are still valid for multicomponent systems too if by $k^{\pm}$ and $\rho^{\pm}$ are meant the effective values determined by the following equations [12]:

$$k^+ \equiv \frac{\sum_i k_i^+ \rho_i^+}{\sum_i \rho_i^+}; \quad k^- \equiv \frac{\sum_i k_i^- \rho_i^-}{\sum_i \rho_i^-};$$

$$\rho^+ \equiv \sum_i \rho_i^+; \quad \rho^- \equiv \sum_i \rho_i^-. \qquad (4)$$

OTHER PHYSICAL FEATURES OF EC AND DISCUSSION

In principle, electric separation is also possible in the electric fields of a parallel-plate capacitor, i.e., under the conditions of a uniform electric field and the absence of a corona discharge. Electrolysis, when some substance plates out on the electrodes as a result of separation, is such a typical case. However, this occurs in conducting media (electrolytes) but not in dielectric ones, which are under consideration here. In the last case, due to the "charging–recharging" on the capacitor plates, there might take place some phase separation, which should be extremely inefficient as the surface charging of particles, i.e., contact charging, might happen. The corona discharge case is fundamentally distinguished by the fact that the electric charging of particles takes place in a comparatively

large space occupied by the spatial charge as it involves a much greater number of charged particles. There should also be remembered the transport role of the electric wind.

Thus, the usage of a "corona" (current) in electric filters is their key point. This is precisely why one of the main characteristic properties of an electric filter is the "ampere–time" one along with the determined characteristic "particle concentration–time." Besides, a similar situation is observed in the case of electrolysis, when it is the current that plays the decisive role in the process. It is clear according to the Faraday law that the mass transfer is unambiguously associated with the charge transfer, and such happens in the case of electric separation. Unfortunately, this problem has not received proper attention, and, in most works dedicated to electric cleaning, the voltage U on the filter is usually presented without any data on the dependence of the residual concentration of the dispersed particles on the electric current strength as the main electric parameter. The experimental data demonstrating the absence of the separation effect until an electric current appears in the working cell's circuit, though the voltage on the cell is not zero, show that the current strength should be the crucial factor of the electric separation process [13].

It counts in favor of the current conception of electric separation that the investigators of [14], as well as the authors of this work [13], intentionally made notches ("scratches") on the wires with comparatively big diameters (~1 mm) coated with enamel insulation and serving as electrodes in electrofilters to cause an electric discharge on them. The discharge naturally had a corona character as those notches were very small.

The fact that there is a voltage threshold ($U > U_{\mathrm{cr}} => j \neq 0$) at which the EC process begins and that is evidently at the same time the threshold of the corona discharge inception is one more particular feature of electric separation. In order to reveal other particular qualities of EC, let us examine some typical experimental characteristics of the dispersed medium concentrations $\varphi(t)$ at different voltages as presented in Fig. 1 according to the data of [13].

In accordance with the theoretical concepts concerning the relaxation processes, in particular concerning the "ampere–second" characteristics of the electric discharge in dielectric liquids under the conditions of a parallel-plate capacitor field [15], it might be expected that the curves in Fig. 1 should follow a simple exponent [16]:

$$\varphi(t) = \varphi_0 \exp(-\alpha t), \qquad (5)$$

where φ_0 is the initial concentration, and α is the relaxation process decrement depending on the voltage and other factors. Relationship (5) is not fulfilled. It is seen from the fact that, at big times ($t \to \infty$), the concentration does not tend to zero, as follows from
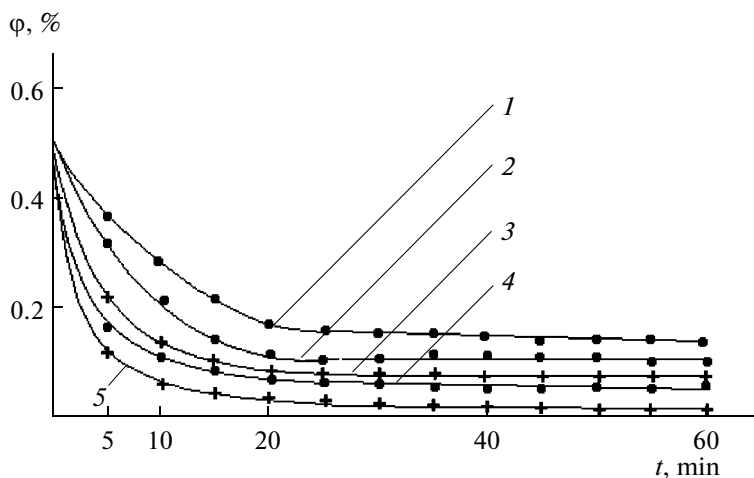
Fig. 1. The residual concentration the versus treatment time for a sunflower oil—waxes suspension (0.5%; U, 10^3 V): *1*—9; *2*—15; *3*—18; *4*—20; *5*—23.

(5), but to some nonzero constant. This is clearly seen from Fig. 1.

This noncompliance can be easily remedied by introducing the limited concentration $\varphi_\infty \equiv \varphi(t)|_{t \to \infty} = \text{const} \neq 0$ by the formula

$$\varphi(t) = \varphi_\infty + (\varphi_0 - \varphi_\infty)\exp(-\alpha t). \qquad (6)$$

However, though this formula satisfies both the initial condition and the condition at infinity, it is not adequate, which is well seen in Fig. 1 showing that the "critical" durations t_c of the cleaning process are about 30, 35, 40, 45, and 50 min for voltages of 9, 15, 18, 20, and 23 kV, respectively. At a time exceeding the mentioned one, the concentrations simply remain constant at the minimum level. Note that it is not a case of asymptotes but of horizontal secants: $-\varphi(t) = \varphi_\infty$ at $t > t_c$. This means that we are dealing with another peculiar feature, which is interesting mainly due to its unexpectedness: it turns out there is a threshold not only at the start of the EC process at $U > U_c$ but also a threshold of its finishing at the time $t = t_c$, after which the separation stops.

Prior to considering the ascertained "threshold" effects, note some peculiarities of the influence of the particle conductivity σ_1 on the process of the electric separation. It is precisely determined experimentally that dielectric particles of wax with very little specific conductivity in sunflower oil (Fig. 1), moving to the "electrode—collector" and reaching it, deposit on it, forming an adherent layer of a heterocharge, i.e., a charge with its sign opposite to that of the electrode. It is easy to verify this through the commutation of the high voltage polarity on the electrofilter, resulting in the immediate repulsion of the deposited particles from the collector. Thus, the above-mentioned fact is confirmed.

In principle, the same also occurs in the case of semiconducting particles (chrome oxide, Cr_2O_3) or conducting (carbonic) ones [17]. The only difference is that the particles at the collector are gathered not in the form of a layer but a "cloud" filling the labyrinths of the "electrodes—collectors," which are also called traps. Such a behavior of semiconducting and conducting particles is explained by their partial recharging on the electrodes.

In both cases, pure liquid is removed by the flow from the space outside the traps, and the filter itself is flushed after each cycle of cleaning. At the end of the cleaning before flushing the electrofilter, some voltage with the opposite polarity in relation to the working voltage sign is applied to it; thereupon, there takes place the quick repulsion of the particles from the traps and the following evacuation by the washing flow.

ON THE THEORY OF THRESHOLD PHENOMENA AT EC FROM DIELECTRIC PARTICLES

In our opinion, the existence of the threshold of electric separation of some heterogeneous system at any voltage on an electrofilter should be regarded as the main question among the most important ones concerning the subjects at hand. We try to answer this question while restricting ourselves to the case of dielectric particles.

On the basis of the above-mentioned particular features of a corona discharge and some electric separation regularities caused by it, we point out three main explaining factors. The first is the screening action of the spatial charges attendant to the whole EC process. The screening can cause such a decrease of the field strength in the corona area that the corona may "go out," thus resulting in the disappearance of

the process itself. Second, the layer deposited on the "electrode–collector" with an electric resistance sufficient to lead to the same drop of the field strength in the corona area as the screening by the spatial charge acts as factor limiting the external field in the case of dielectric (nonconducting) particles. Finally, the small size of the particles is a particular factor that is difficult to eliminate. It is established that the smaller the size of the dispersed particles, the more difficult it is to remove them. This question, calling for a special examination, is not considered in this work; we focus our attention on the first two factors limiting the electrocleaning.

Fig. 2. Designed model of an electrofilter.

THE EFFECT OF THE ELECTRIC FIELD SCREENING BY THE SPATIAL CHARGE FIELD

Knowing that there is some charged layer, we can understand the reason for the reduction of the cleaning effect. This happens due to the screening of the external electric field by that layer. The observed sudden stop of the separation effect could be explained now by the corona character of the electric charge. Indeed, assume that some critical strength E_c of the discharge onset in the liquid corresponds to the critical voltage U_c. Now, in the course of obtaining the $\varphi^*(t)$ curve, naturally, at some voltage, $U > U_c$. Consequently, $E > E_c$. With time, with the charged particles being accumulated on the collector at the fixed applied voltage U, the field strength near the corona points will drop because of the screening effect. The discharge current will simultaneously decrease, but the reduction of the field strength is important here. When the strength decreasing from the initial value $E_0 > E_c$ reaches the critical E_c, the discharge will go out, as well as the process of the particle charging and of the separation itself, as has been already noted.

In the simplest model [18] under our consideration, we assume that the deposited layer is uniform and the charge density in it is constant and equal to ρ_1 according to Fig. 2. There is the second layer beyond this layer, which is also assumed to be uniform, with the spatial density being ρ_2 with the same charge signs as the sign of the "corona" electrode (in our case, it is negative). Naturally, ρ_2 will decrease with time due to the reduction in the concentration of the dispersed charged particles beyond the ξ-layer, and, up to the end of the cleaning process, this charge can be in a first approximation neglected in comparison with ρ_1. Then, according to Gauss's theorem, the screening strength can be estimated by the formula

$$E_1(x > \xi) = \frac{1}{2\varepsilon_1}\rho_1\xi, \tag{7}$$

where ξ is the layer's thickness, and the index "1" refers to the layer's characteristics. Considering that
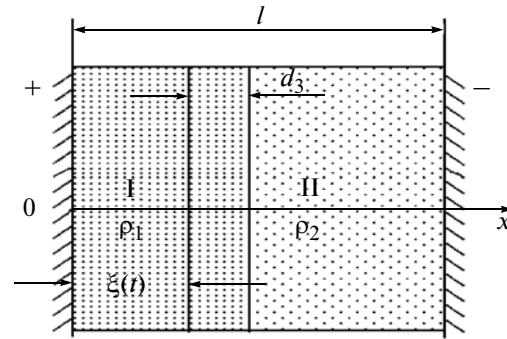
$\rho_1 < 0$, we see that this charge causes the reduction of the field within the corona area. As the right member of (7) grows with time due to the increase of ρ_1, because of the possible compaction of the particles and the increase in the layer thickness ξ, the screening can turn out to be efficient enough up to the values of the strength equal to the critical E_c. Indeed, let us estimate numerically the right part of equation (1). We obtain

$$E_1 \sim \frac{1}{\varepsilon_1}|\rho_1|\xi \sim \frac{1}{\varepsilon_1}|\mathbf{j}\nabla\tau_1|\xi \sim \frac{1}{\varepsilon_1}j\frac{\tau_1}{\xi}\xi \sim \frac{j}{\sigma_1} \le E_0,$$

i.e., the strength E_1 is not more than the initial E_0, but it may have the same order of magnitude, which supports the data mentioned above.

Assume the total strength in the vicinity of the corona electrode to be equal to the initial E_0 except for the screening one (7). Then, the condition of the separation existence is

$$E = E_0 - \frac{|\rho_1|\xi}{2\varepsilon_1} > E_c. \tag{8}$$

From this formula, we find the limiting thickness ξ_{mE} of the deposited particle layer determined by the initial strength and density of the charges:

$$\xi < \frac{2\varepsilon_1(E_0 - E_c)}{|\rho_1|} \equiv \xi_{mE}. \tag{9}$$

The involved strength E_0 is determined by the working voltage U on the electrofilter, which is evidently directly proportional to this quantity: $E_0 \sim U$. Thus, the more the voltage U is, the more the critical thickness of the layer is and, consequently, the less the residual minimum concentration φ_∞ is. It follows from (9) that the quantity ξ_{mE} is the greatest layer thickness that should be expected in the course of electric cleaning at the given voltage (strength) on the electrofilter. The quantity ξ_{mE} should not be confused with the maximum quantity ξ_m determined by the whole mass of the dispersed particles in the liquid under the con-

dition of their complete deposition into the layer (see below, the second formula in (10)). Apparently, owing to the ideality of the last condition, it is always $\xi_{mE} < \xi_m$.

The maximum treatment time t_c after which the phase separation process stops can be calculated from the formula for the dependence of the layer's thickness on the time [18]:

$$\xi(t) = \frac{1 - \exp(-\lambda t)}{1 - \nu \exp(-\lambda t)}\xi_m, \quad \xi_m \cong \varphi_0 l/(\gamma_1^*), \quad (10)$$

where ξ_m is the maximum layer thickness (at $t \to \infty$), which is given by the second formula in (10) at little initial concentrations φ_0; l is the distance between the electrodes of the plate type; $\gamma_1^* \equiv \gamma_1/\gamma$; γ_1 is the density of the particle substance; and γ is the medium density ($\gamma_1^* \sim 1$). The other parameters are determined by the following formulas:

$$\nu \equiv A\varphi_0/E_0; \quad \lambda \equiv bqE_0(1 - \nu)/l;$$
$$A = -\rho_1 l/\varepsilon_2. \quad (11)$$

Exponentiating formula (10), we obtain an expression for the critical time t_c that is the minimum time necessary for the EC process:

$$t > t_c \equiv \frac{1}{\lambda}\ln\frac{1 - \nu B}{1 - B}; \quad B \equiv \frac{2\varepsilon_1(E_0 - E_c)}{|\rho_1|\xi_m} \equiv \frac{\xi_{mE}}{\xi_m}; \quad (12)$$
$$b = 1/(6\pi\eta a),$$

where B is the mobility of the particles according to Stokes law, η is the dynamic viscosity, and a is the radius of the particles (the same for all the particles). Here is the numerical estimation of the cleaning process duration t_c with the following data: cleaning by 80 percent, i.e., $B = \xi_{mE}/\xi_m = 0.8$; $\nu = 1.2$; and $\lambda = 0.05$ min^{-1} [18]. By the first formula of (12), we obtain $t_c \approx 29$ min, which corresponds to the experimental data [18].

OHMIC CONCEPTION

The presented observations concerning the threshold phenomena have an "electrostatic" character in the sense that no allowance was made for the presence of currents through the filter and the focus was maintained on the charge formation. Now, we consider this very question from the viewpoint of Ohm's law while noting that the disappearance of the electroseparation effect makes possible an explanation not directly involving the charge formation processes.

Really, averaging the density of the electric currents $j_1 = j_2 \equiv j$ by layers "1" and "2" with allowance for $E_1 = -d\varphi_1/dx$ and $E_2 = -d\varphi_2/dx$, we obtain

$$\int_0^\xi \bar{\sigma}_1 d\varphi_1 = \bar{\sigma}_1\varphi_1\big|_0^\xi = \bar{\sigma}_1[\varphi_1(\xi) - \varphi_1(0)]$$
$$= \bar{\sigma}_1 U_1 = j\xi;$$

$$\int_\xi^l \bar{\sigma}_2 d\varphi_2 = \bar{\sigma}_2\varphi_2\big|_\xi^l = \bar{\sigma}_2[\varphi_2(l) - \varphi_2(\xi)]$$
$$= \bar{\sigma}_2 U_2 = j(1 - \xi).$$

Thus, as $j_1 = j_2$, we have

$$\bar{\sigma}_1 U_1(l - \xi) = \bar{\sigma}_2 U_2\xi, \quad (13)$$

where $\bar{\sigma}_1$, $\bar{\sigma}_2$ are some average values in the first ($x \in [0; \xi)$) and second ($x \in (\xi; l]$) intervals in which there are the drops of voltages U_1 and U_2. Let us find them by setting one more equation up according to which the sum of the voltages should be equal to the given total voltage U on the electrofilter:

$$U_1 + U_2 = U. \quad (14)$$

From system (13), (14) we find

$$U_1 = \frac{\bar{\sigma}_2 U}{\bar{\sigma}_2\xi + \bar{\sigma}_1(l - \xi)};$$
$$U_2 = \frac{\bar{\sigma}_1 U}{\bar{\sigma}_2\xi + \bar{\sigma}_1(l - \xi)}(l - \xi), \quad (15)$$

and the corresponding average strengths of the fields in the sections are

$$\bar{E}_1 = \frac{U_1}{\xi} = \frac{\bar{\sigma}_2 U}{\bar{\sigma}_2\xi + \bar{\sigma}_1(l - \xi)};$$
$$\bar{E}_2 = \frac{U_2}{l - \xi} = \frac{\bar{\sigma}_1 U}{\bar{\sigma}_2\xi + \bar{\sigma}_1(l - \xi)}. \quad (16)$$

These are the direct Ohm's law derived relations, and it is noteworthy that they are correct irrespectively of the presence or absence of the medium electrization, or the charge densities ρ_1 and ρ_2 being zero or not. At first, it may be strange, but there is nothing strange at all, as the averaged specific conductivities $\bar{\sigma}_1$ and $\bar{\sigma}_2$ tacitly consider these charges. At $\rho_1 = 0$ and $\rho_2 = 0$, we would simply automatically have $\bar{\sigma}_1 = \sigma_1$ and $\bar{\sigma}_2 = \sigma_2$.

In the context of the explanation of threshold phenomena, the most interesting is the field strength in the second zone where the particles are charged.

Denoting the relation $\bar{\sigma}_1/\bar{\sigma}_2 \equiv \mu$ in view of $l \gg \xi$, formula (16) for E_2 becomes

$$E_2 = \frac{\mu U}{\xi + \mu l} = \frac{\mu}{\xi_* + \mu}\frac{U}{l}, \qquad (17)$$

where $\xi_* \equiv \xi/l$ is the relative thickness of the layer. Assuming for sunflower oil [13] $\bar{\sigma}_2 \sim 10^{-9}$ Ohm^{-1} m^{-1} and for the wax layer $\bar{\sigma}_1 \sim 10^{-13}$ Ohm^{-1} m^{-1}, we obtain $\mu \sim 10^{-4}$. Now, $\xi \approx \xi_m \approx \varphi_0 l \approx 5 \times 10^{-3} l$. Then, by (17), the strength E_2 in the corona area decreases by 50 times in comparison with $(U/l) \approx E_0$, that is, by one−two orders of magnitude. It seems to be sufficient for the corona discharge to disappear, amounting to the screening of the external field (behind the "ξ-layer"). This is the reason for the threshold disappearance of the corona discharge and of the process of the electric separation itself.

Thus, the threshold value of the electric field strength at which the electric cleaning process starts is explained by the presence of the threshold of the electric discharge itself (at $E = E_c$). As any EC process begins from some supercritical strength $E_0 - E_c$ (see formula (9)), after this process finishes, due to the reasons mentioned above, the drop in the strength from E_0 to E_c with the retention of the initial voltage U happens. The transition $E_0 \rightarrow E_c$ takes place because of the screening of the field E_0 at the expense of the electric charges of the ξ-layer or, equally, because of the sharp growth of this layer's resistance. Most likely, the joint action of both factors takes place.

CONCLUSIONS

Let us remark in conclusion that variable electric fields can be in principle used in electric filters if the time of the electric relaxation of the particles is considerably less than the period of the oscillation of the external electric field in order that the particle charge can change its electric sign during one half-period of the field oscillation. However, for a number of reasons, variable fields are more rarely used in electrofilters than stationary ones. The nonregular phase displacements of the external field and the processes of electric charging of the particles with different physical parameters is one of these reasons.

REFERENCES

1. Bologa, M.K., Grosu, F.P., and Leu, V.I., Separation of Dielectric Liquids from Mechanical Impurities in a Direct Electric Field, *Proc. 2nd European Conf. on Filtration and Separation*, Compiegne, 2006.

2. Kaptsov, N.A., *Koronnyi razryad i ego primenenie v elektrofil'trakh*, (Corona Discharge and its Application in Electrofilters), Moscow: OGIZ, 1947.

3. Nesterov, S.R., The Effect of Electric Wind on Gas Cleaning in Electrofilters. Review of National and Foreign Literature, *NIIOGAZ*, Moscow, 1968, p. 42.

4. Levitov, V.I., Rashodov, I.K., Tkachenko, V.I., et al., *Dymovye elektrofil'try* (Smoke Electrofilters), Moscow: Energiya, 1980.

5. Lyob, L., *Osnovnye protsessy elektricheskikh razryadov v gazakh* (Main Processes of Electric Discharges in Gases), Moscow: Fizmatgiz, 1950.

6. Kaptsov, N.A., *Elektricheskie yavleniya v gazakh i vakuume* (Electric Phenomena in Gases and Vacuum), Moscow: Gostekhizdat, 1950.

7. Vereshchagin, I.P., Levitov, V.I., Mirzabekyan, G.Z., and Pashin, M., *Osnovy elektrodinamiki dispersnykh sistem* (Foundations of Electrodynamics of Dispersed Systems), Moscow: Energiya, 1974.

8. Petrichenko, N.A., Electric Wind in Insulating Liquids, *Cand. Sci. (Phys.-Math.) Dissertation*, Leningrad, 1973.

9. Ostroumov, G.A. and Petrichenko, N.A., Electric Wind in Insulating Liquids, *Elektron. Obrab. Mater.*, 1974, no. 6, pp. 37−39.

10. Bologa, M.K., Grosu, F.P. and Kozhukhar, I.A., *Elektrokonvektsiya i teploobmen* (Electroconvection and Heat Transfer), Kishinev: Shtiintsa, 1977.

11. Grosu, F.P., Thermoelectroconvective Phenomena and their Applied Aspects, *Dr. Sci. (Eng.) Dissertation*, Kishinev, 2009.

12. Grosu, F.P. and Bologa, M.K., On Bipolar Structures of Spatial Charge in Weakly Conducting Dielectric Liquid in the External Electrostatic Field, *Elektr. Obrab. Mater.*, 2007, vol. 43, no. 1, pp. 47−51.

13. Bologa, M.K., Kozhukar, I.A., Grosu, F.P., and Leu, V.I., Investigation of Process of Dielectric Liquid Cleaning from Mechanical Impurity in Stationary Electric Field, *Elektron. Obrab. Mater.*, 2001, no. 5, pp. 34−39.

14. Bologa, M.K., Potemkina, T.A., and Beril, I.I., Electrodehydration of Water-Sunflower Oil Emulsion, *Elektron. Obrab. Mater.*, 1986, no. 2, pp. 63−66.

15. Skanavi, G.I., Physics of Dielectrics (Weak Fields), Moscow: GIITL, 1958.

16. Bologa, M.K., Kozhukhar, I.A., Grosu, F.P., and Leu, V.I., Relaxation Processes in Filters, *Sbornik trudov Mezhdunarodnoi nauchnoi konferentsii "Sovremennye problemy elektrofiziki i elektrodinamiki zhidkikh dielektrikov"* (Proc. Int. Conf. "Modern Problems of Electrophysics and Electrodynamics of Liquid Dielectrics), St. Petersburg, 2000, pp. 210−213.

17. Leu, V.I., Electric Cleaning of Transformer Oil from Mechanical Impurity in Stationary Electric Field, *Elektron. Obrab. Mater.*, 2002, no. 5, pp. 55−59.

18. Grosu, F.P., Bologa, M.K., Kozhukhar, I.A., and Leu, V.I., On theory of Cleaning Dielectric liquids from Mechanical Impurity in Stationary Electric Field, *Elektron. Obrab. Mater.*, 2001, no. 6, pp. 35−40.

Spectroscopy of the Dielectric Parameters of ZnO-Based Varistors

F. Kharirchi[a], Sh. M. Gasanli[b], Sh. M. Azizova[b], and Dzh. Dzh. Khalilov[b]

[a]Islamic Azad University, South Tehran Branch, Tehran, Iran
[b]Institute of Physics, National Academy of Sciences of Azerbaijan, pr. Dzhavida 33, Baku, AZ-1143 Republic of Azerbaijan
e-mail: hasanli_sh@rambler.ru
Received May 20, 2011

Abstract—The spectroscopy of the dielectric parameters of ZnO-based varistors is studied. An analysis of the data on the temperature and frequency dependence of the electric conductivity shows that variable-range hopping conductivity between the localized states near the Fermi level can be implemented in the varistors.

INTRODUCTION

In studying the transport properties of heterogeneous materials, an important role is assigned to the analysis of the dispersion of the dielectric parameters of the material (dielectric permittivity, dielectric loss, etc.); the frequency dependences of the effective values of the dielectric permittivity and dielectric loss coefficient are sensitive to the ratio between the electrophysical parameters of the dispersed phase and the matrix, as well as to the shape of the inclusions and their orientation in the external electric field. Despite the broad scope of the applications in various fields of physics and chemistry [1–6], the theoretical studies of the dispersion of the dielectric permittivity of heterogeneous media are constrained for a number of reasons, among which we should mention the following. First, the analytical calculations of the effective parameters of multicomponent systems, which are of independent significance and make up an integral part of the theory of dispersion in heterogeneous dielectrics, are a separate complicated mathematical problem, which can be solved only in specific cases. Second, in studying the multicomponent materials, the quantity of the parameters and dimensionless numbers that characterize the behavior of the system's heterogeneities in an alternating electric field increases; in addition to the parameters that determine the geometrical structure of composites and the electroconductive and dielectric properties of the components, we must examine the frequency parameters and characteristic times correlated with each phase of the system. All this complicates the study of the electric spectroscopy of heterogeneous materials.

In the opinion of many authors, the main polarization mechanism for heterogeneous matrix media is the Maxwell–Wagner polarization [1, 2]. This is a macroscopic, or, as it is also called, surface polarization (in the literature, there are also the terms interlayer, space-charge, interfacial polarization, etc.). It is associated with the formation of charged surface layers, which arise from the motion of free charges within the individual phases of a composite material under the action of an external alternating electric field at the interface of heterogeneous media.

The Maxwell–Wagner polarization is of the orientation polarization type, because the inclusions within which the charge carriers (CCs) move behave like macroscopic objects with induced dipoles. In fact, in the calculations of an electric field outside spherical bodies and cylindrical inclusions with a circular cross section, the field is represented as an infinite sum of induced dipoles [3, 4]. The relaxation processes in these systems are described in terms of the Debye classical theory [7]. This is also confirmed by the configuration of the Cole–Cole diagram, which, in the case of a low concentration of cylindrical inclusions with a circular cross section, in accordance with the Debye equations, has the shape of a semicircle.

Note that the frequency dependence of the dielectric parameters, namely, the components of the complex dielectric permittivity, is a characteristic of the material and is determined for each substance not only by the properties of the molecules of the material but also by the presence and composition of the impurities.

In this study, we carried out an experimental investigation of the dielectric spectra of ZnO-based varistors.

EXPERIMENTAL AND DISCUSSION

To prepare the varistors, a ceramic charge with the composition (mol %) of $96.5\ \mathrm{ZnO} + 0.5\ \mathrm{Bi_2O_3} + 0.5\ \mathrm{Co_3O_4} + 0.5\ \mathrm{MnO_2} + 0.5\ \mathrm{B_2O_3} + 1\ \mathrm{Sb_2O_3} + 0.5\ \mathrm{ZrO_2}$ in an amount of 100 g is weighed and crushed in a ball mill to a particle size of 60 μm and less. Then, this mixture is used to prepare granules, which are compressed under a 40-ton force to derive samples in the form of washers with a height of 10 mm and a diameter of 20 mm. After that, the samples are placed in an
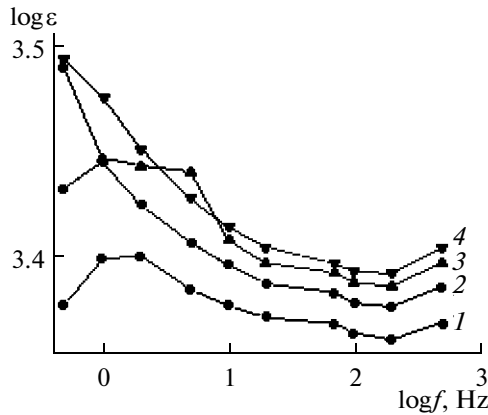
Fig. 1. Frequency dependence of the imaginary part of the dielectric permittivity: (*1*) 317, (*2*) 341, (*3*) 373, and (*4*) 390 K.
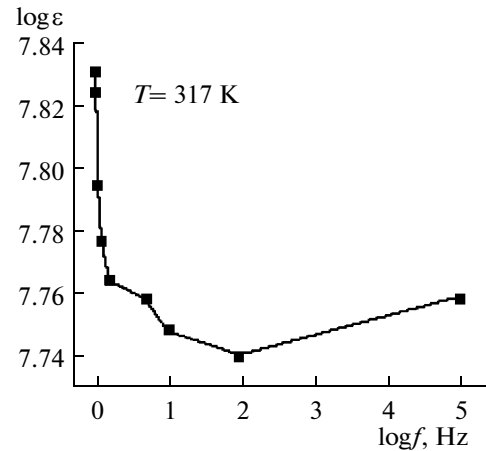

Fig. 2. Frequency dependence of the real part of the dielectric permittivity.

electric furnace to perform the synthesis: the heating to a temperature of 900°C is carried out at a rate of 150°C/h, while to a temperature of 1250°C, at a rate of 200°C/h. The synthesis of the compressed washers occurs in the ambient air, and the annealing of the washers at a temperature of 1200°C is carried out for 2 h. After turning off the furnace, the samples are cooled for 7–8 h.

The synthesized cylindrical samples (washers) are ground and polished on both sides, and then a thin layer (3–4 mm) of aluminum is coated on these surfaces via vacuum deposition in order to obtain an electric contact.

Measurements of the capacitance, resistance, and dielectric loss were carried out using E7-20 digital immittance meters (at frequencies of 10^2–10^6 Hz) in the a temperature range of 300–450 K. A measuring voltage of 1 V was applied across the sample. A bridge provided the automatic selection of the pattern of the reactivity of the equivalent circuit of the samples under study; the accuracy of the measurement of ε and D was 3 and 5%, respectively.

The values of the real and imaginary parts of the dielectric permittivity (ε' and ε''), as well as the electric conductivity in the studied samples, were determined from the results of the measurements of the capacitance C and the dielectric loss D using the following formulas:

$$C = \frac{\varepsilon \varepsilon_0 S}{d}, \tag{1}$$

$$\varepsilon' = \frac{\varepsilon}{\sqrt{1 + D^2}}, \tag{2}$$

$$\varepsilon'' = \frac{\varepsilon}{\sqrt{1 + D^2}} D, \tag{3}$$

$$\sigma = 2\pi f \varepsilon'' D, \tag{4}$$

where D is the dielectric loss; ε' is the real part of the dielectric permittivity; ε'' is the imaginary part of the

dielectric permittivity; C is the capacitor capacitance, pF; $\varepsilon_0 = 8.85 \times 10^{-12}$ F/m; S is the contact area, m²; and d is the sample thickness, m.

The calculation results are shown in Figs. 1, 2, and 4. Figure 1 depicts the frequency dependences of the imaginary part of the dielectric permittivity ε'' at different temperatures. It is evident that the pattern of the variation of ε'' as a function of the frequency exhibits a relaxation behavior, which is shown in the monotonic decrease in ε'' with increasing frequency for all the measured temperatures. This pattern of variation corresponds to the dipole and migration polarizations. Since an increase in the temperature leads to a decrease in the relaxation time of the dipoles, i.e., to an increase in their mobility, the dielectric constant value increases. The decrease in ε' and ε'' versus the frequency is explained by the lag of the dipoles and the decrease in the number of particles involved in the polarization. At the same time, it is evident from Fig. 4 that, in the low-frequency range, the electric conductivity monotonically increases and then dramatically enhances with the increasing frequency. In addition, the electric conductivity σ varies according to the law $\sigma \approx f^{0.8}$. The resulting dependence of $\sigma \approx f^{0.8}$ is indicative of the hopping charge transfer between the localized states near the Fermi level [8]. Note that, at the temperatures under study, the dependence $\sigma = F(f)$ exhibits the same behavior.

Figure 3 shows the frequency dependence of the dielectric loss for the ZnO-based varistors. It is evident from the dependences that the values of the dielectric loss D decrease by a factor of 50 as the frequency increases from 100 Hz to 1 MHz.

The presence of two mechanisms of charge transfer can be clearly seen from the Cole–Cole diagrams (Fig. 5), where the relaxation part is represented by a circular arc, and the low-frequency part is represented by almost a straight line segment. The observed deviations of the diagrams $\varepsilon'' = f(\varepsilon')$ from circles in the
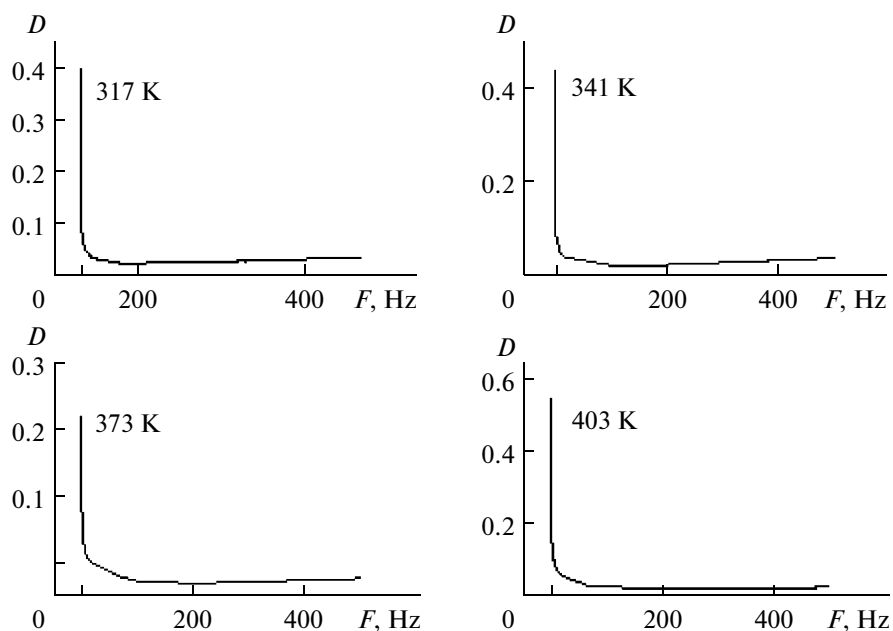
Fig. 3. Frequency dependence of the dielectric loss.

region of high frequency values are apparently caused by the presence of a whole set of relaxation times (as well as the contribution of the reach-through the conductivity in the low-frequency range).

The experimental points of the $\sigma(T)$ curve are well fitted to a straight line in the Mott coordinates [8] (Fig. 6). In this case, the expression for the conductivity is as follows:

$$\sigma(T) = \sigma_0/T^{1/2}\exp\{-(T_0/T)^{1/4}\}. \qquad (5)$$

Here, the parameter T_0 is determined through the formula

$$T_0 = \lambda a^3/kg(E_f), \qquad (6)$$

where λ is the dimensionless constant with a value of $\sim$16 [5], and k is the Boltzmann coefficient (J/K).

The coefficient σ_0 is the conductivity of the varistor at the inverse temperature $1/T$ tending to zero; it is found from the expression

$$\sigma_0 = e^2 a^2 \nu_{ph} g(E_v), \qquad (7)$$
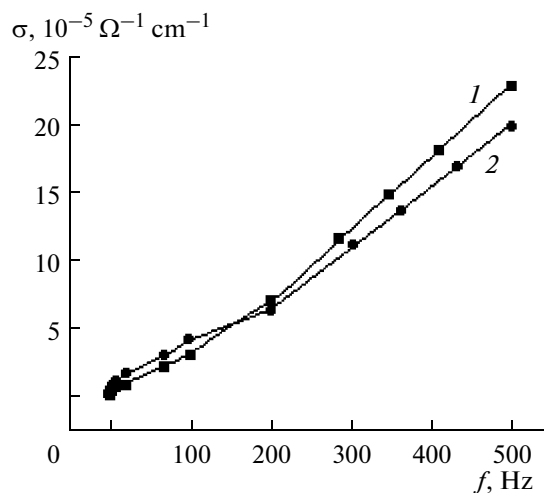
Fig. 4. Frequency dependence of the conductivity: (*1*) 317 and (*2*) 403 K.
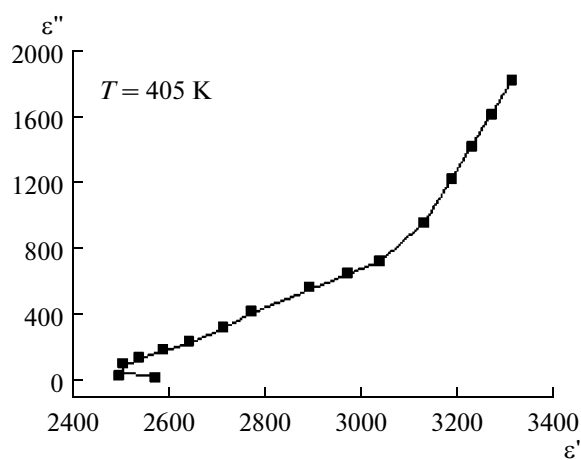
Fig. 5. Cole–Cole diagram at $T = 405$ K.
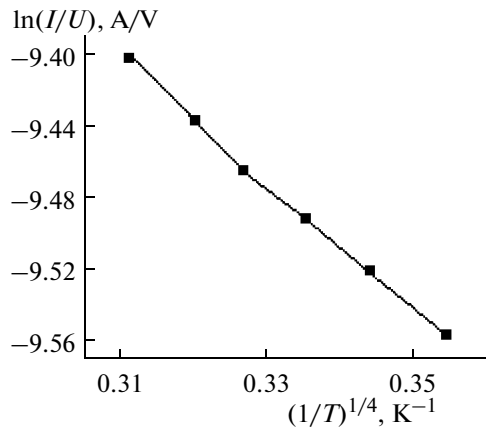
Fig. 6. $\ln I/U–(1/T)^{1/4}$ dependence in the ZnO ceramics.

where $a = 1/a$ is the localization radius, m; $g(E_v)$ is the density of the states near the Fermi level, m^{-3}; and ν_{ph} is the phonon frequency, Hz.

To determine the parameter σ_0, we use the extrapolation of the linear function $\ln[\sigma/T^{1/2}]$ from $T^{1/4}$ to the point of intersection with respect to the value of T_0. The running of this dependence in the temperature range of $T = 300–330$ K indicates that the charge transfer in the varistors under study occurs via the variable-range hopping conductivity of electrons between the localized states lying in a narrow energy band near the Fermi level. These states can be generated in the varistor by extended defects, i.e., grain boundaries and dislocations.

A specific feature of the hopping conductivity mechanism is the low mobility of CCs; it is characterized by the CC transfer through weakly overlapped tails of the wave functions of the neighboring acceptor levels.

In terms of the model under discussion, the average CC hopping distance R between the localized states near the Fermi level for a given temperature T is found from the expression [8]

$$R = 3/8(a)(T_0/T)^{1/4}. \qquad (8)$$

The above equation suggests that a decrease in the temperature leads to an increase in the value of the parameter R. In addition, the rapid emptying of the localized states in the band gap occurs, and a significant role in the conductivity process is played by

the carrier hopping between individual impurity levels without activation into the conduction band. This results in an increase in the probability of CC hopping to spatially more distant but energetically closer localization centers, which is responsible for the decrease in the hopping activation energy.

In this case, the value of the energy spread of the localized states is defined through the formula

$$\Delta E = \frac{3}{2\pi R^3 g(E_F)}, \qquad (9)$$

and the trap density value of a measurement is found from the equation

$$N_t = g\{E_v\}\Delta E, \qquad (10)$$

where N_t is the trap density.

The values of the parameters that characterize the hopping electron transfer in the dark mode of measurement are listed in the table. In the respective calculations, the density of the localized states $g(E_f)$ was determined through formula (6); for the localization radius, we took the value of $a = 16$ Å by analogy with the data for amorphous semiconductors [8].

Thus, the analysis of the temperature and frequency dispersion of the electric conductivity shows that variable-range hopping conductivity between the localized states near the Fermi level can be implemented in the varistors.

REFERENCES

1. Emets, Yu.P., Dielectric Dispersion of Three- and Four-Component Matrix Media, *Tech. Phys.*, 2003, vol. 48, no. 3, pp. 317–328.

2. Turik, S.A., Chernobabov, A.I., Turik, A.V., and Radchenko, G.S., Disordered Heterogeneous Systems: an Insulator–Conductor Transition, Issledovano v Rossii. http://zhurnal.ape.relarn.ru/articles/2004/191.pdf

3. Turik, A.V. and Radchenko, G.S., Maxwell–Wagner Relaxation in Piezoactive Media, *J. Phys. D: Appl. Phys.*, 2002, vol. 35, no. 11, pp. 1188–1192.

4. Oreshkin, P.T., *Fizika poluprovodnikov i dielektrikov* (Physics of Semiconductors and Dielectrics), Moscow: Vysshaya Shkola, 1977.

5. Matsuoka, M., Nonohmic Properties of Zinc Oxide Ceramics, *Jpn. J. Appl. Phys., Part 1*, 1971, vol. 10, no. 6, pp. 736–746.

6. Souza, F.L., Gomes, J.W., Bueno, P.R., et al., Effect of Addition of ZnO Seeds on the Electrical Properties of ZnO Based Varistors, *Mater. Chem. Phys.*, 2003, vol. 80, pp. 512–516.

7. Debye, P., *Polyarnye molekuly* (Polar Molecules), Moscow: Gos. Nauchno-Tekh. Izd., 1931.

8. Mott, N.F. and Davis, E.A., *Electronic Processes in Non-Crystalline Materials*, Oxford: Clarendon, 1971.

Some parameters of zinc oxide varistors

Parameters	$T = 317$K	$T = 403$K
$g(E_v)$ eV^{-1} cm^{-3}	4×10^{18}	8×10^{18}
R, AÅ	80	35.4
N_t, cm^{-3}	2.8×10^{17}	4.2×10^{17}
ΔE, meV	70	50

Calculation of the Elemental Composition of Thin Films Deposited by Magnetron Sputtering of Mosaic Targets

D. A. Golosov, S. N. Melnikov, and A. P. Dostanko

Institution of Education of the Belarussian State University of Informatics and Radioelectronics,
ul. Brovki 6, Minsk, 220013 Belarus
e-mail: dmgolosov@gmail.com
Received June 9, 2011

Abstract—A model of the process of magnetron sputtering that allows the prediction of the composition of the films deposited using sputtering of mosaic targets with the arbitrary location of the inserts for axial magnetron sputtering systems (MSS) is proposed. The model is based on the integration of the sputtered flows from each point of the sputtering zone, and it takes into account the sputtering yields and the electron-ion emission of the material of the base and inserts. The curve of the distribution of the discharge current density is approximated using the third central moment in the double Gaussian distribution, which makes it possible to use real parameters of the sputtering zone and the discharge current of the magnetron. This allows the fairly accurate mathematical description of the distribution of the ion current density. To verify the proposed model, experimental studies on depositing thin film using magnetron sputtering of Ti/Zr and Ti/Zr/Pb mosaic targets were carried out. The model's error does not exeed 10%.

INTRODUCTION

The technological needs of the market have considerably increased the interest in obtaining thin film with specific electrophysical, optical, mechanical, and heat- and rust-proof properties. At present, the coatings represent single-layer nanocrystalline composites; the properties of films are modifiable in thickness or complex multilayer heterostructures based on superlattices and gradient structures [1, 2]. These are mainly complex multicomponent compounds based on oxides, nitrides, or carbides. They are dielectrics that are difficult to sputter. Traditionally, the method of RF magnetron sputtering is used to deposit multicomponent thin films [3, 4]. This method allows the sputtering of multicomponent dielectric targets. Its comparatively low productivity, costly RF power sources, and complex scaling are disadvantages, which substantially reduce its possibility of industrial application.

The method of reactive sputtering is more promising in this relation. This method maintains all the advantages of magnetron sputtering (the high deposition rate of film, the low temperature of the substrate, the simplicity of the construction, etc.). It allows for the films to be easily deposited using targets manufactured with relative ease. Three main methods of magnetron sputtering are currently used to deposit multicomponent thin films, namely, multitarget sputtering, individual sputtering of each of the components, and sputtering of mosaic targets. The method for the sputtering of alloy targets yields good results in the case when the obtaining of an alloy or a mix of required elements is possible [5, 6]. The composition of the deposited layers almost repeats the concentrations of elements of the initial target. However, in a number of cases, the composition of the deposited layers comprises different materials with low mutual solubility or great difference in melting temperatures. Here, it is next to impossible to obtain the targets of a required composition. Good results are yielded by multitarget sputtering in this case [7, 8]. Several sputtering devices are used in this method to obtain multicomponent films with each element being deposited by a separate magnetron. The multitarget sputtering makes it possible to accurately control the elemental composition of the deposited films, and films with different compositions can be obtained by varying the current or the discharge capacity of each of the magnetrons. However, this method almost cannot be used owing to its complexity at industrial facilities.

One recent tendency in developing the method of magnetron sputtering for depositing multicomponent thin films is the use of so-called composite or mosaic targets, i.e., targets that consist of a matrix of one metal with inserts of other metals [9]. Multicomponent films with any quantity and content of elements using a single magnetron can be obtained by this method. The advantage of the method for magnetron sputtering of mosaic targets is particularly evident in the cases when the films to be obtained comprise elements with low mutual solubility or a great difference in melting temperatures. The disadvantage of the

above method is the complexity of selecting the size and quantity of the inserts for creating the required concentration and uniform distribution of the elements in the deposited film, since the rate of sputtering the substrate and inserts depends on a few factors (the distribution of the ion current density, the coefficient of sputtering of an element, the energy of the ions, etc.). Practice shows that to reach the required ratio between the elements in the deposited film, a number of experiments on sputtering of the mosaic target are needed followed by the correction of the sizes of the inserts according to the results of the elemental analysis of the deposited films. This method of selection is fairly costly (in particular, when rare materials are used in the target) and time-consuming. In this case, computer simulating allows a considerable reduction of the time and cost of the engineering and elimination of certain errors.

This work is thus aimed at developing a model of sputtering mosaic targets that allows determining the sizes and location of the inserts for the correction of the composition of the deposited multicomponent film.

1. DESCRIPTION OF THE MODEL

The mosaic target consists of a base (main matrix) formed of material A and mosaic inserts from material B, which are located in this base (Fig. 1). The inserts are uniformly located along the radius of the maximal erosion of the target. The size and quantity of the inserts depend on the required content of material B in the deposited film. The target is mostly manufactured so that the entire area of the inserts falls into the zone of sputtering. Material A is characterized with the relative atomic mass A_A, density ρ_A, sputtering yield Y_A, and coefficient of ion-electron emission γ_A. Material B is specified with the relative atomic mass A_B, density ρ_B, sputtering yield Y_B, and coefficient of ion-electron emission γ_B.

The model is constructed for the case of axial magnetron with a planar target. The following allowances are to be accepted for the model's construction, namely, (1) the sputtered atoms have a directed motion and are distributed through the space according to the cosine law, (2) the sputtered atoms do not collide either with each other or with the atoms of the working gas (i.e., the thermalization effect of the sputtered flow is absent), and (3) the sputtered atoms are condensated at the point of hitting the substrate. Moreover, the distribution of the current density in the discharge zone of the axial magnetron is assumed to depend only on the radius of the sputtering r_1 and is independent of the type of sputtered material.
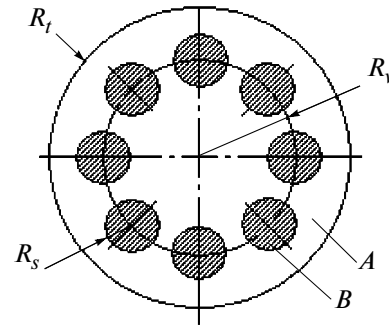
Fig. 1. Geometrical model of the target: A is the base of the target, B are the inserts, R_t is the radius of the target, R_s is the radius of the inserts, and R_v is the radius of the location of the inserts.

The number of sputtered target atoms per unit of time from a certain site of the target can be calculated according to the formula

$$\nu_x(r_1) = Y_x \frac{j_i(r_1)}{e}, \tag{1}$$

where Y_x is the sputtering yield by ions of Ar atoms of the substrate material or that of the inserts; e is the electron charge; and $j_i(r_1)$ is the density of the ion current on the target surface at the radius r_1, which can be calculated using the formula

$$j_i(r_1) = \frac{j_t(r_1)}{1 + \gamma_x}, \tag{2}$$

where $j_t(r_1)$ is the current density at the r_1 radius, and γ_x is the coefficient of the ion-electron emission of the base or the insert materials. The sputtering rate of the target with respect to the thickness is

$$\upsilon_x(r_1) = \frac{\nu_x(r_1)A_x}{N_A e \rho_x}, \tag{3}$$

where A_x is the atomic mass of the sputtered material, ρ_x is the material density, and N_A is Avogadro constant $N_A = 6.022 \times 10^{23}$ mol^{-1}. Using (4) and (5), the sputtering rate with respect to the thickness can be written as

$$\upsilon_x(r_1) = Y_x \frac{j_t(r_1)A_x}{N_A e \rho_x(1 + \gamma_x)}. \tag{4}$$

It is noteworthy that the effective sputtering yield of the target material (which depends on the distribution of the bombarding ion energy) might preferably be used for the calculations of the sputtering rate [10].

The distribution of the discharge current density $j_i(r_1)$ can be calculated using the Particle-in-cell Monte Carlo technique of simulation of the motion kinetics. (PIC-MC) [11−13]. However, this substantially complicates the model and can be used for precision calculations if needed. In our case, the curve of the distribution of the discharge current density was

Fig. 2. Calculation results for the discharge current density distribution (*a*) and normalized profile of the target erosion area for magnetron MAC-80 (*b*)
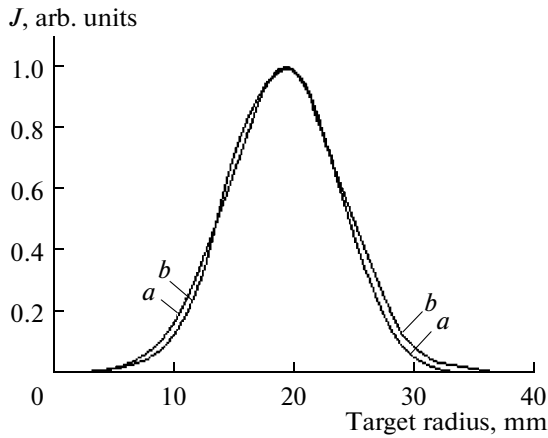
approximated using the third central moment in the double Gaussian distribution with various dispersions at the left and right shoulders of the distribution. This distribution uses real parameters of the zone of distribution and the magnetron discharge current; it allows for the fairly accurate mathematical description of the distribution of the ion current density. Due to applying this simulation method, the profile of the ion current density distribution in the discharge zone is preset analytically according to the formula

$$j_t(r_1) = \frac{I_t}{\pi(R_{max} + R_{min})} \frac{f(r_1)}{\int\limits_0^\infty f(r_1)dr_1}, \quad (5)$$

where I_t is the magnetron discharge current; R_{min} and R_{max} are the minimum and maximum radii of the target erosion zone; and $f(r_1)$ is the function of the distribution in the form of a double semi-Gaussian

$$f(r_1) = \begin{cases} \dfrac{1}{\sqrt{2\pi}\sigma} \exp\left[-\dfrac{(r_1 - \overline{R})^2}{2\sigma_1^2}\right] & \text{for} \quad r_1 \le \overline{R}; \\[4mm] \dfrac{1}{\sqrt{2\pi}\sigma} \exp\left[-\dfrac{(r_1 - \overline{R})^2}{2\sigma_2^2}\right] & \text{for} \quad r_1 > \overline{R}; \end{cases} \quad (6)$$

$$\sigma_1 = \frac{\overline{R} - R_{min}}{3}, \quad \sigma_2 = \frac{R_{max} - \overline{R}}{3}, \quad \sigma = \frac{R_{max} - R_{min}}{6},$$

where $\overline{R}$ is the radius of the maximum target erosion. Moreover, the function of the distribution must satisfy

the relation

$$\int\limits_{-\infty}^{\infty} j_t(r_1)dr_1 = I_t. \quad (7)$$

Figure 2 shows the results of the calculation of the profiles of the ion current density distribution using the double Gaussian for approximation (curve *a*). For comparison, Fig. 2 (curve *b*) presents the normalized profile of the erosion zone of a MAC-80 magnetron. Since the discharge current density is proportional to the sputtering rate on the target material [14], it can be inferred that the above method of approximation using the third central moment in the double Gaussian distribution makes it possible to describe mathematically the discharge current distribution in the MSS zone with high accuracy.

In order to determine the film deposition rate on the substrate, we shall use the integration technique for the sputtered flow at each point of the zone of sputtering. In our case, the substrate is parallel to the target's plane; therefore, the model of the sputtering process will be constructed for the case when the angle of sputtering equals that of the condensation, i.e., $\phi = \varphi$. The rate of the film deposition at the substrate's point at a distance of x_2 from the axis of the magnetron can be calculated by the formula

$$F(x_2) = \frac{1}{\pi} \int\limits_{R_{min}}^{R_{max}} \int\limits_0^{2\pi} \frac{\nu(r_1)r_1\cos^2\varphi(x_2, r_1, \alpha)}{L^2(x_2, r_1, \alpha)} dr_1 d\alpha, \quad (8)$$

where α is the azimuth angle, φ is the angle of sputtering (condensation), and L is the distance from the point of the sputtering to the point of the condensation.

To define the contribution of the rate of the deposition from the base and inserts, two methods of calculation can be used; i.e., (1) the part of a circle that is occupied by the inserts is determined at every radius of the sputtering zone, while the insert sputtering rate is considered to be proportional to the ratio between the length of the circle and the summarized length of the inserts; (2) the position of the inserts is set analytically using the equation.

The first method is easier for the calculation. Here, the sputtering zone is divided into three sites (Fig. 3), namely, site I is from R_{min} till R_{min1} and site III is from R_{max1} till R_{max}, where only the substrate material is present, and site II is from R_{min1} till R_{max1}, where the circle of the current radius crosses the inserts. At every radius of site II of the sputtering zone, the part of the length of the circle is determined that is occupied by the inserts of material *B*:

$$M(r_1) = n\frac{\sqrt{R_v^2 - (R_s - r_1)^2}}{\pi r_1}, \quad (9)$$

where n is the number of inserts, R_v is the radius of an insert, and R_s is the radius of the location of the centers of the inserts.

The deposition rate of the base's material from sites I and III $F_1(x_2)$ and $F_1(x_2)$ is calculated using (8) taking into account the limits of the integrations from R_{min} to R_{min1} for site I and from R_{max1} to R_{max} for site III. At site II where the inserts are located, part of the circle $M(r_1)$ is occupied by the inserts. The rate of the base's material deposition will be

$$F_2(x_2)$$
$$= \frac{1}{\pi} \int_{R_{min1}}^{R_{max1}} \int_0^{2\pi} \frac{v_0(r_1)r_1(1 - M(r_1))\cos^2\varphi(x_2, r_1, \alpha)}{L^2(x_2, r_1, \alpha)} dr_1 d\alpha, \tag{10}$$

where v_0 is the sputtering rate of the base. The overall deposition rate of the base's material can be calculated as the sum of the deposition rates from all three sites of the target:

$$F_0(x_2) = F_1(x_2) + F_2(x_2) + F_3(x_2). \tag{11}$$

The deposition rate of the inserts' material can be calculated using the formula

$$F_v(x_2)$$
$$= \frac{1}{\pi} \int_{R_{min1}}^{R_{max1}} \int_0^{2\pi} \frac{v_v(r_1)r_1 M(r_1)\cos^2\varphi(x_2, r_1, \alpha)}{L^2(x_2, r_1, \alpha)} dr_1 d\alpha, \tag{12}$$

where v_v is the sputtering rate of the inserts.

The percentage composition of the inserts' material in the deposited film is calculated as

$$T(x_2)\% = \frac{F_v(x_2) \times 100}{F_0(x_2) + F_v(x_2)}. \tag{13}$$

The thickness deposition rate of the component film was determined as the sum of the deposition rates of the base's and inserts' materials:

$$V(x_2) = F_0(x_2)\frac{A_0}{N_A\rho_0} + F_v(x_2)\frac{A_v}{N_A\rho_v}, \tag{14}$$

where A_0, ρ_0, A_v, ρ_v are the atomic mass and density of the base's and inserts' materials, relatively.

The presented method makes it possible to calculate the composition and the deposition rate of the film at the sputtering of the target, which consists of an arbitrary number of cylindrical inserts from various elements. However, it is impossible to use it in determining the nonuniformity of the distribution of the element concentrations at a small target–substrate distance, when the effects of the predominant deposition of an insert's material at the substrate's site (which is located opposite to the insert) starts to act. In this case, more preferable is the method when the
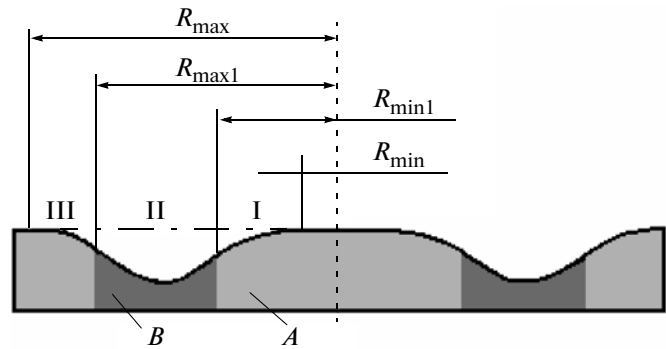
Fig. 3. Sputtering area of the mosaic target.

location of the inserts is preset analytically by the equation

$$(x_1 - x_k)^2 + (y_1 - y_k)^2 < R_v^2, \tag{15}$$

where x_k and y_k are the coordinates of the k-th insert, and x_1 and y_1 are the current coordinates. In the process of integration, it is determined whether the current coordinate belongs to the substrate or the inserts, and, depending on the sputtered material, the contribution of the substrate's or inserts' deposition to the rate is summarized.

EXPERIMENTAL

In order to verify the proposed model, studies were performed on sputtering Ti–Zr (Fig. 4a) and Ti–Zr–Pb (Fig. 5) mosaic targets. The Ti–Zr mosaic target was a 5-mm-thick Ti base (99. 95% pure) with $\varnothing$ 80 mm; eight cylindrical Zr inserts with $\varnothing$ 13 mm were pressed into it. The inserts were uniformly distributed along the 42.5-mm diameter. The Ti–Zr–Pb mosaic target consisted of a 5-mm-thick Ti base (99.95% pure) with $\varnothing$ 80 mm; four 12-mm-diameter zirconium and four 10.5-mm-diameter lead inserts were pressed into it. The inserts were uniformly distributed along the 42.5-mm diameter.

A scheme of the experimental device for the thin film deposition using the method of magnetron sputtering of mosaic targets is shown in Fig. 6. The chamber of a VU-2MP vacuum device was equipped with a MAC-80 magnetron and an hall current ion source. The ion source was used for the preliminary ion cleaning of the substrate's surfaces.

The substrates were Si (100%). They were fixed on a substrate holder and were successively brought into the zones of cleaning and deposition. The distance magnetron's target-substrate was 85 mm at the magnetron's axis.

The chamber of the vacuum device was pumped out to a residual pressure of 2×10^{-3} Pa, and the ion cleaning of the substrates was carried out. To do this, Ar was supplied into the assisting stage of the ion

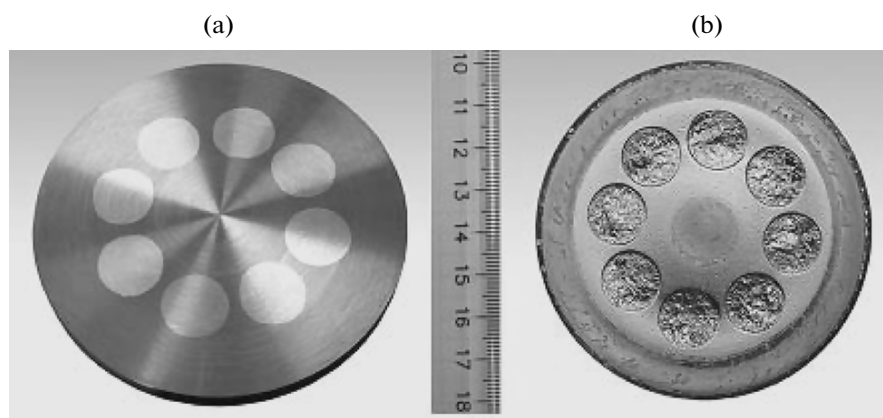**Fig. 4.** Outward appearance of the Ti–Zr mosaic target prior to (a) and after the sputtering (b).

source up to a working pressure of 2.0×10^{-2} Pa ($Q_{Ar} = 25$ sccm). The time of the cleaning, the energy of the ions, and the discharge current in all the experiments were constant and equaled 3 min, 500 eV, and 70 mA, respectively.

Then, the preliminary cleaning of the target surface was done. In this case, the substrates were taken away from the sputtering zone. Ar was supplied into the gas-distribution system of the magnetron. The Ar flow into the chamber was $Q_{Ar} = 65$ sccm, and it was controlled by an RRG-1 mass flow control. The target was cleaned in the power stabilization mode $P_t = 500$ V. Here, the discharge voltage was $U_t = 400-500$ V and the discharge current was $I_t = 1.1-1.25$ A; the time of the target's cleaning was 4 min.

The sputtering of mosaic targets was performed using the method of magnetron sputtering in the discharge current stabilization mode. The Ar flow into the chamber during the sputtering of the Ti–Zr and Ti–Zr–Pb targets was 50 and 65 sccm. The time of the deposition was 10 min. The sputtering of the Ti–Zr target was performed under the following conditions: the discharge current was $I_t = 3.0$ A and the discharge voltage was $U_t = 445$ V. During the sputtering of the

Fig. 5. Outward appearance of the Ti–Zr–Pb mosaic target.

Ti–Zr–Pb target, the target voltage was $U_t = 402$ V and the discharge current was $I_t = 1.0$ A.

The distribution of the thickness of the deposited layers was determined by a POI-08 optical interferometric profilometer. The elemental composition of the deposited films was analyzed using X-ray fluorescence analysis (XRF) using an ED-200 fluorescence spectrometer (Oxford).

RESULTS AND DISCUSSION

The deposition rate distribution and the composition of the deposited films during the magnetron sputtering of the Ti–Zr mosaic target were analyzed. It was detected that, owing to the difference in the rates of base and inserts of the depletion the inserts or the base get ruined (Fig. 4b). These processes can affect the changing of the ratio of the elements in the deposited film in the process of the target's use.

Figure 7a shows the results of measuring the distribution of the thickness of the deposited film during the magnetron sputtering of a Ti–Zr mosaic target. The deposition rate at the magnetron's axis was 0.46 nm/s. The obtained profile is almost the same as the profiles of the deposition rate of single-components targets. For comparison, Fig. 7 (curve *b*) shows the results of simulation of the thickness distribution profile of the Ti–Zr film. The following parameters of the target were used for the calculation: an 80-mm-diameter Ti base, the sputtering yield $- Y_{Ti} = 0.26$ (0.5 with 500 eV), the density $- r_{Ti} = 4.54$ g/cm^3, 13-mm-diameter Zr inserts, their number $-$ 8 units (sputtering yield $Y_{Zr} = 0.3$ (0.63 with 500 eV), the density $- r_{Ti} = 6.50$ g/cm^3). The inserts were located along a 42.5-mm diameter.

The parameters of the sputtering zone were as follows: $R_{min} = 4.5$ mm, $\bar{R} = 19.5$ mm, and $R_{max} = 32.6$ mm. The discharge current was $I_t = 3.0$ A, and the deposition time was 10 min. The target–substrate distance was 85 mm. As is seen, the calculated profile
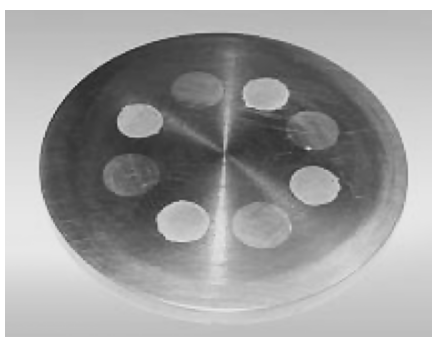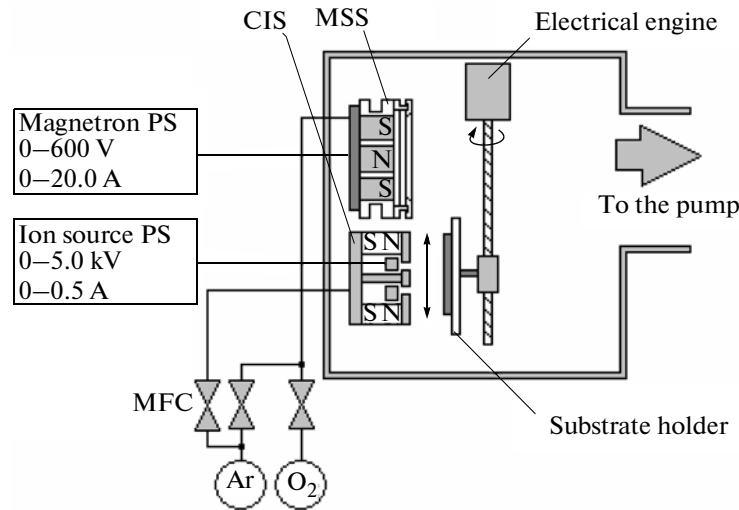
Fig. 6. Scheme of the experimental device for sputtering mosaic targets using the method of magnetron sputtering: CIS is the ion source for cleaning; MSS is the magnetron sputtering system; MFC is the mass flow control.

almost coincided with the experimental data. Figure 8 shows the results of the simulation of the deposition rate distribution of Ti and Zr. The following concentrations of the elements in the deposited film were obtained (Fig. 8), at %: Ti was 39.04 and Zr was 60.96, which, as a result of the recalculation for the weight percents, gave the following content, wt %: Ti was 25.5 and Zr was 74.85. The measurements of the elemental composition of the deposited films using the method of X-ray fluorescence analysis showed that the Ti composition was 73,42 at % and that of Zr was 26.3 at % in the deposited film. The results of the simulation show that the distribution of the elements at a distance of 85 mm from the target's surface is highly uniform across the substrate's area

Examining the results of the model's verification, we found that the model's error is not more than 10% when a two-component target is calculated.

The study of the deposition rate's distribution and the ultimate composition of the deposited films at the magnetron sputtering of a Ti–Zr–Pb mosaic target were carried out. The measured results for the deposited film thickness at the magnetron sputtering of a Ti–Zr–Pb mosaic target are presented in Fig. 9 (curve *a*). The deposition rate in the magnetron axis was 1.55 nm/s. The results of the simulation of the deposited film's thickness at the Ti–Zr–Pb mosaic target's sputtering are presented in Fig. 9 (curve *b*).

The following target parameters were used in the calculations: the Ti base diameter—80 mm; the Zr

Fig. 7. The distribution profile of the deposited film thickness for the case of magnetron sputtering of the Ti–Zr mosaic target: *a* − measurement results, *b* − simulation results.

Fig. 8. Calculated deposition rate distributions of elements during Ti–Zr mosaic target sputtering: *a* − Ti deposition rate, *b* − Zr deposition rate.

Fig. 9. Distribution profiles of the deposited film thickness for the case of magnetron sputtering of Ti–Zr–Pb mosaic target: a – measurement results, b – simulation results.

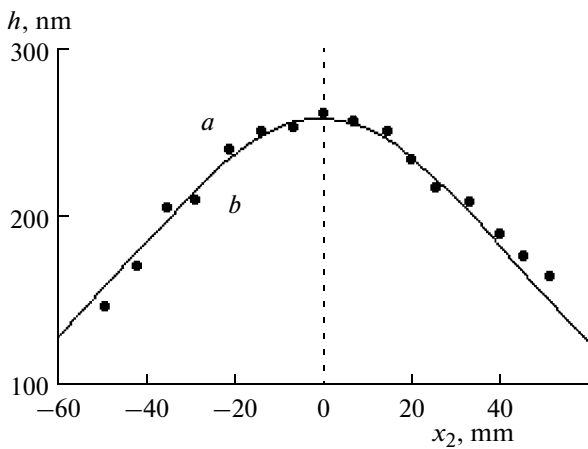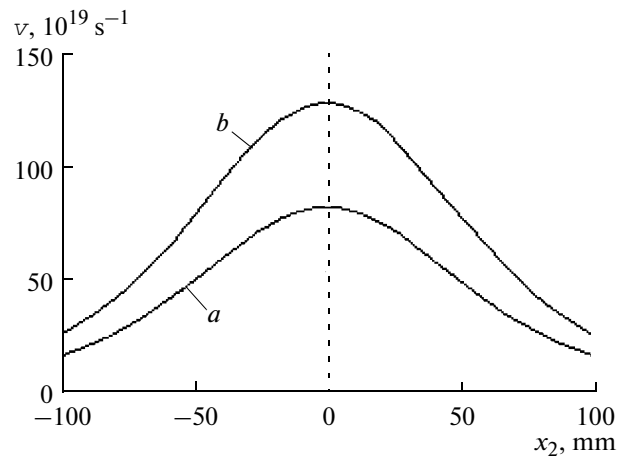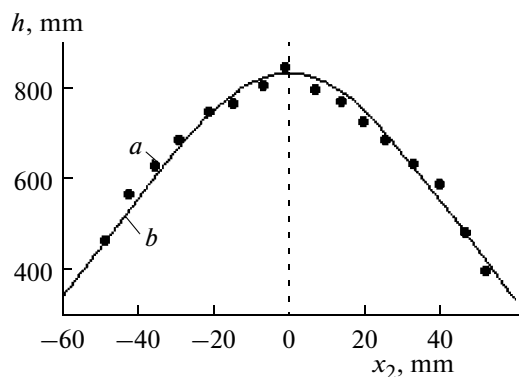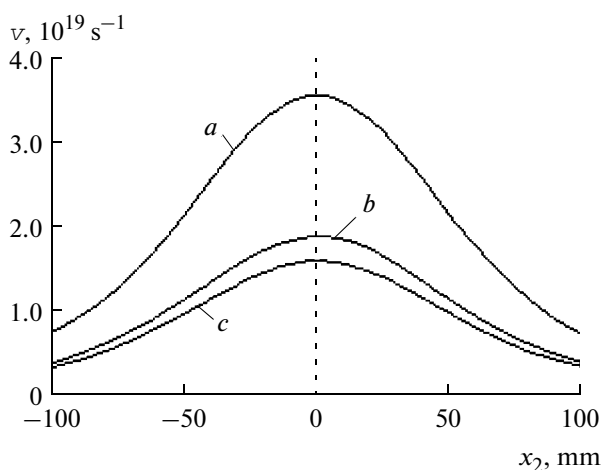**Fig. 10.** Simulation results for deposition rate distributions of elements during Ti–Zr–Pb mosaic target sputtering: a – Ti deposition rate, b – Zr deposition rate, c – Pb deposition rate.

inserts diameter—12 mm, the number—4 pieces; and the Pb inserts diameter—10.5 mm, the number—4 pieces. The insertion blocks are placed in a diameter of 42.5 mm. The following initial data were used in the calculations for the Pb insertion blocks: the atomic mass A_{Pb} = 207.2 a.m.u., the density ρ_{Pb} = 11.34 g/cm³, and the sputtering yieldt Y_{Pb} = 0.32 (2.3 at 500 eV). The discharge current was I_t = 1.0 A, and the deposition time was 10 min. The rest of the features of the materials and the parameters of the sputtering area are presented above. The calculated profile of the deposition rate distribution agrees well enough with the experimental data.

The results of the simulation of the deposition rate distribution in the case of the Ti–Zr–Pb mosaic target sputtering are presented in Fig. 10. The following concentration of the elements in the film has been calculated in at %: Ti—50.7, Zr—26.71, Pb—22.58. In

terms of the weight percentage, the content is the following in wt %: Ti—25.43, Zr—25.53, Pb—49.035. The examination of the applied layers by X-ray fluorescence analysis has shown that the deposited film produced through the method of magnetron sputtering of a Ti–Zr–Pb mosaic target contains the following elements in wt %: Ti—25.25, Zr—26.30, Pb—48.45. As is seen, for the three-component target, the simulation error is also less than 10%; this fact permits one to use the proposed models to predict the concentrations of elements in the deposited film when array targets are sputtered.

The composition of $PbZr_{0.54}Ti_{0.46}O_3$ is assumed to be the best one to form ferroelectric thin films with a perovskite structure. The relation of the materials in the deposited film should be Pb : Zr : Ti is 1 : 0.54 : 0.46. This is Pb/Ti = 2.174, Zr/Ti = 1.174 in relation to Ti. The X-ray analysis results show the relation of the elements in the deposited film as Pb/Ti = 0.44, Zr/Ti = 1.23. As is seen, in the case of sputtering the Ti–Zr–Pb array target, a substantial deficit of lead is observed. According to the simulation results, the sputtering yield of Pb turned to be much smaller than the tabular value: Y_{Pb} = 0.32 (the tabular value is Y_{Pb} =2.3 at 500 eV). This fact seems to be associated with the formation of a film on the surface of the inserts as a result of the interaction of Pb with the residual atmosphere and the high thermalization of the lead atoms.

CONCLUSIONS

A model simulating the process of magnetron sputtering of mosaic targets is proposed. This model allows one to predict the ultimate composition of the deposited films when compound targets with cylindrical insertion blocks are sputtered by axial magnetron sputtering systems.

Experimental investigations of the deposition of thin films by the method of magnetron sputtering of Ti/Zr and Ti/Zr/Pb mosaic targets were carried out to verify the proposed model. The analysis of the results shows that the simulation error is not more than 10%, so it is possible to use the proposed models in order to predict the concentrations of the elements in the deposited film when mosaic targets are sputtered. It is established on the basis of the simulation results that, when calculating the sputtering rate, one should consider the thermalization of the sputtered atoms and use the effective coefficient of the target material's sputtering depending on the distribution of the energy of the bombarding ions.

REFERENCES

1. Musil, J., Hard and Superhard Nanocomposite Coatings, *Surf. Coat. Technol.*, 2000, vol. 125, pp. 322–330.
2. Yang, Q., Zhao, L.R., McKellar, R., and Patnaik, P.C., Microstructure and Mechanical Properties of Multi-

Constituent Superlattice Coatings, *Vacuum*, 2006, vol. 81, pp. 101−105.

3. Youl-Moon Sung and Hee-Je Kim, Sputter Deposition and Surface Treatment of TiO_2 Films for Dye-Sensitized Solar Cells Using Reactive RF Plasma, *Thin Solid Films*, 2007, vol. 515, pp. 4996−4999.

4. Huidong Tanga, Shouhong Tana, Zhengren Huanga, Shaoming Donga, and Dongliang Jiang, Surface Morphology of a-SIC Coatings Deposited by RF Magnetron Sputtering, *Surf. Coat. Technol.*, 2005, vol. 197, pp. 161−167.

5. Jia-Ming Ye, Yu-Pin Lin, Yueh-Ting Yang, Jing-Tang Chang, and Ju-Liang He, Electrochromic Properties of Ni(V)Ox Films Deposited Via Reactive Magnetron Sputtering with a 8V−92Ni Alloy Target, *Thin Solid Films*, 2010, vol. 59, pp. 1578−1582.

6. Hui-Wen Chang, Ping-Kang Huang, Andrew Davison, Jien-Wei Yeh, Chun-Huei Tsau, and Chih-Chao Yang, Nitride Films Deposited from an Equimolar Al−Cr−Mo−Si−Ti Alloy Target by Reactive Direct Current Magnetron Sputtering, *Thin Solid Films*, 2008, vol. 516, pp. 6402−6408.

7. Vidyarthi, V.S., Lin, W.-M., Suchaneck, G., Gerlach, G., Thiele, C., and Hoffmann, V., Plasma Emission Controlled Multi-Target Reactive Sputtering for in-situ Crystallized Pb(Zr, Ti)O₃ Thin Films on 6" Si-wafers, *Thin Solid Films*, 2007, vol. 515, pp. 3547−3553.

8. Suchaneck, G., Lin, W.-M., Vidyarthi, V.S., and Gerlach,G., Hartung Multi-Target Reactive Sputtering − a Promising Technology for Large-Area Pb(Zr, Ti)O₃ Thin Film Deposition, *J. Europ. Ceram. Soc.*, 2007, vol. 27, pp. 3789−3792.

9. Nakano, J., Miyazaki, H., Kimura, T., Goto, T., and Zhang S., Thermal Conductivity of Yttrium-Stabilized Zirconium Thin Films Prepared by Magnetron Sputtering, *J. Ceram. Soc. Jpn.*, 2004, vol. 112, pp. 908−911.

10. Czekaj, D., Goranchev, B., and Hollmann, E.K., Incident Ion Energy Spectrum and Target Sputtering Rate in DC Planar Magnetron, *Vacuum*, 1991, vol. 42, nos. 1−2, pp. 43−45.

11. Kusumoto, Y. and Iwata, K., Numerical Study of the Characteristics of Erosion in Magnetron Sputtering, *Vacuum*, 2004, vol. 74, pp. 359−365.

12. Nanbu, K. and Kondo, S., Analysis of Three-Dimensional DC Magnetron Discharge by the Particle-in-Cell/Monte Carlo Method, *J. Appl. Phys.*, 1997, vol. 36, no. 1, pp. 4808−4814.

13. Nanbu, K., Segawa, S., and Kondo, S., Self-Consistent Particle Simulation of Three-Dimensional Magnetron Discharge, *Vacuum*, 1996, vol. 47, pp. 1013−1016.

14. Golosov, D.A., Melnikov, S.N., Kundas, S.P., and Dostanko, A.P., Prediction of Target Erosion in Magnetron Sputtering Systems, *Prob. Fiz. Mat. Tekh.*, 2010, vol. 2, no. 3, pp. 62−67.

Accumulation of Hydrogen Peroxide at the Long-Term Effect of an Atmosphere Pressure Glow Discharge on Electrolyte Solutions

L. A. Kuz'micheva, Yu. V. Titova, and A. I. Maksimov

Institute of Solution Chemistry, Russian Academy of Sciences,
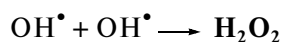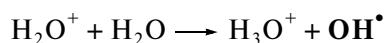*ul. Akademicheskaya 1, Ivanovo, 153045 Russia*
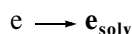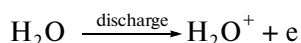*e-mail: jvt@isc-ras.ru*
Received June 30, 2011

Abstract—The kinetic characteristics of the hydrogen peroxide accumulation at the long-term effect of an atmospheric pressure glow discharge on aqueous solutions of electrolytes have been obtained. The initial rates of the H_2O_2 generation and the primary yields are calculated using the straight line portions of the kinetic characteristics. It is found that the times of reaching a steady hydrogen peroxide concentration (or its maximum) are rather long (about several hours). The $OH^\bullet$ yield has been estimated, and the initial yield of hydrogen peroxide and its effective lifetime have been calculated using the kinetic relationship obtained for a glow discharge–water system.

DOI: 10.3103/S1068375512010103

INTRODUCTION

An atmospheric pressure glow discharge with an electrolyte cathode is an efficient instrument to initiate a set of chemical reactions in a liquid phase. When a discharge affects an electrolyte solution, the solution's surface directly contacting with the plasma (the cathode glow area) is subjected to bombardment by positive ions from the plasma zone. The ion bombardment causes the dissociation and ionization of water molecules and the appearance of primary active particles such as atomic hydrogen, hydroxyl radicals, and solvated electrons in the cathode glow region [1].

$$H_2O \xrightarrow{\text{discharge}} OH^\bullet + H^\bullet$$

$$H_2O \xrightarrow{\text{discharge}} H_2O^+ + e$$

$$e \longrightarrow e_{solv}$$

$$H_2O^+ + H_2O \longrightarrow H_3O^+ + OH^\bullet$$

$$OH^\bullet + OH^\bullet \longrightarrow H_2O_2$$
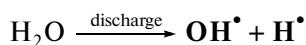
Hydrogen peroxide is one of the main durable oxidizing agents formed at the glow discharge effect on aqueous solutions of electrolytes. The accumulation of H_2O_2 was studied in [2, 3, 4, 5]. Our previous investigations [6, 7] have shown that the yield of hydrogen peroxide is in the range from 0.5 to 9 molecules/ion depending on the experiment conditions (with the current from 10 to 40 mA and the volume of the solution under treatment from 80 to 500 mL). The time of the plasma treatment of the electrolyte solutions was not more than 120 minutes. At the same time, it might be expected that a stationary state will be attained at the long-term effect of a gas discharge on aqueous solutions. This question can be answered after further research of hydrogen peroxide accumulation for a long time, which is the purpose of this work.

EXPERIMENTAL

The basic diagram of the experimental setup and the cell to investigate the effect of the atmospheric pressure glow discharge on the electrolyte solutions are presented in [8].

The experiments on the H_2O_2 accumulation under the effect of an atmospheric pressure glow discharge were carried out in distilled water, aqueous solutions of sodium sulfate, sodium hydroxide, and nitric acid with a concentration of 0.01 mol/L. The volume of the solution treated was 100 mL. The discharge current was 10 mA, Mo and Cu cathodes was used, and the distance between the anode and the solution surface was ~2 mm. The cell was placed into a bath with water in order to avoid superheating with the working solution temperature being not more than 45°C.

The concentration of H_2O_2 was determined spectrophotometrically ($\lambda = 254$ nm) using a UV-V is spectrophotometer (Agilent 8453) and controlled by iodometric titration routinely with the addition of ammonium molibdate as a selective catalyst of the reaction between the hydrogen peroxide and iodide ions [9].

$C_{H_2O_2}$, mol/L
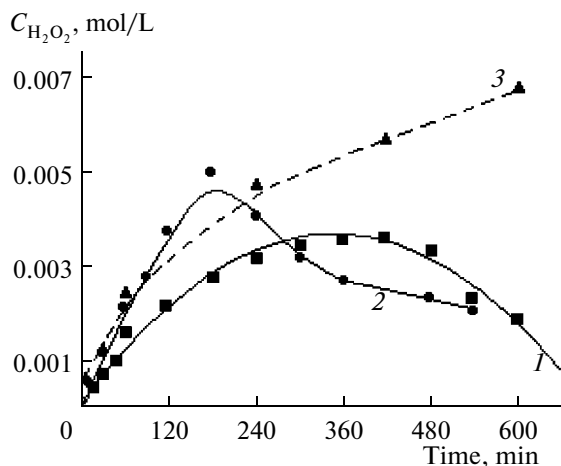
Fig. 1. The hydrogen peroxide accumulation under the effect of a glow discharge in the solutions of nitric acid (*1*), sodium hydroxide (*2*), and sodium sulfate (*3*); the cathode—Mo.

$C_{H_2O_2}$, mol/L
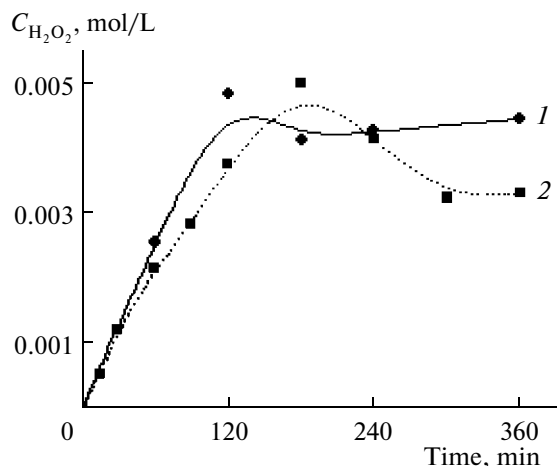
Fig. 2. The H_2O_2 accumulation in a sodium hydroxide solution under the effect of a glow discharge using copper (*1*) and molybdenum (*2*) cathodes.

RESULTS AND DISCUSSION

The type of kinetic curve for the hydrogen peroxide accumulation corresponding to that predicted by a simple model has been obtained in the experiments with distilled water as the initial electrolyte [10].

The kinetic characteristics of the H_2O_2 accumulation in the solutions of nitric acid, sodium hydroxide, and sodium sulfate are shown in Fig. 3.

As it seen from Fig. 1, some peaks are observed in the kinetic characteristics in acidic and alkaline media with the trends of the kinetic curves being different: the initial yield of H_2O_2 in the alkaline medium is twice as much as the similar parameter in the acid medium (see Table 1). Peaks in the kinetic characteristics were previously observed in a 0.1 M solution of potassium chloride [6]. Only a gradual decrease of the initial rate of the hydrogen peroxide generation was observed in the case of the sodium sulfate solution; the experiment duration seems to be insufficient.

If the kinetic characteristics of the hydrogen peroxide disintegration processes in the course of the gas-discharge action do not change, the product accumulation curve should smoothly tend to the limit. The appearance of some extremes in the kinetic characteristics can be caused by the accumulation in the solution of some component catalyzing the disintegration of H_2O_2. Two components that can catalyze the disintegration of hydrogen peroxide—nitric acid (and the change in the medium pH) [11] and ions entering the solution with the cathode sputtering [12]—can be accumulated in the plasma–solution system under consideration.

Nitric acid appears in the solution under the effect of a discharge as a result of the air nitrogen oxidation in the plasma area. At the same time, there are no peaks in the case of distilled water and sodium nitrate.

Our data do not allow us to reach an unambiguous conclusion concerning the role of the ions coming from the cathode. Indeed, a molybdenum cathode was used in all the cases mentioned above. Molybdenum ions are efficient catalysts of hydrogen peroxide disintegration [13]. However, in not all the cases we observed peaks in the kinetic curves. The kinetic curves of the hydrogen peroxide accumulation when molybdenum and copper anodes are used are depicted in Fig. 2. Copper ions are less efficient for catalyzing the process of hydrogen peroxide disintegration than molybdenum ions, yet the kinetic curves are rather close in both cases.

Experiments with NaOH solutions with different concentrations were carried out to determine the

$C_{H_2O_2}$, mol/L

Fig. 3. Kinetic characteristics of the hydrogen peroxide accumulation in NaOH solutions with different concentrations: *1*—0.001 M, *2*—0.01 M, and *3*—0.05 M (the cathode was copper).

Characteristics of the hydrogen peroxide accumulation under the effect of the atmospheric pressure glow discharge with a liquid cathode

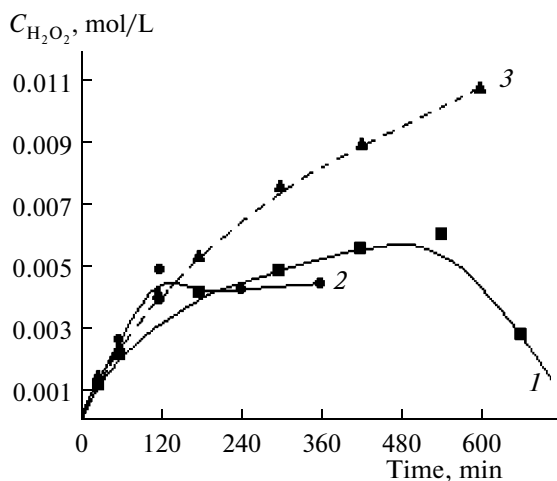| Experimental conditions	Time of attainment of the maximum H_2O_2 concentration, min	The value of the maximum H_2O_2 concentration, mol/L	Initial rate of H_2O_2 formation, mol/L^{-1}s^{-1}	Primary H_2O_2 yield, molecules/ion
H_2O Dist., Mo—cathode	240	0.0035	8.04×10^{-7}	0.77
Na_2SO_4, 0.01 M, Mo—cathode	(600)*	(0.007)*	6.95×10^{-7}	0.67
HNO_3, 0.01 M, Mo—cathode	360	0.004	2.5×10^{-7}	0.24
NaOH, 0.01 M, Mo—cathode	180	0.005	4.79×10^{-7}	0.46
NaOH, 0.01 M, Cu—cathode	120	0.0048	6.71×10^{-7}	0.65
NaOH, 0.001 M, Cu—cathode	540	0.006	6.92×10^{-7}	0.67
NaOH, 0.1 M, Cu—cathode	(600)*	(0.011)	7.17×10^{-7}	0.69

Note: (The values are not extreme ones; the maximum values of the H_2O_2 concentration obtained in the course of the experiment.

effect of the pH on the kinetic curves for the H_2O_2 accumulation with the qualitative composition of the solutions being the same. The kinetic characteristics for hydrogen peroxide accumulation in sodium hydroxide solutions presented in Fig. 3 show that, in this case too, there is no unambiguous answer to the question. It seems necessary to carry out experiments with insoluble electrodes in some inert gas atmosphere with a controlled ion composition of the solution to properly determine the mechanism of the generation and disintegration of hydrogen peroxide in plasma–solution systems.

It has been shown above that a simple kinetic curve shape corresponding to our model [10] is observed only in the case of the plasma treatment of distilled water.

The initial rates of the hydrogen peroxide generation (according to the straight line portion of the kinetic curve), the OH radical yield, and the initial H_2O_2 yield have been calculated from the obtained experimental data. The hydrogen peroxide yield according to the current was calculated using the following equation:

$$f = \frac{R_0 V N_A}{(N_A/F)I},$$

where R_0 is the rate of the hydrogen peroxide formation at the initial time moment, mol/Ls; V is the volume of the treated solution, L; N_A is Avogadro constant, 6.02×10^{23} mol^{-1}; I is the current strength, A; and F is the Faraday constant, 9.46×10^4 mol/charge.

In the case of a discharge with distilled water, these quantities are as follows:

(1) The yield of hydroxyl radicals was 5.0 radicals/ion.

(2) The primary yield of H_2O_2 calculated using the initial linear portion of the kinetic characteristics was ~0.8 molecules/ion, and the initial rate of the hydrogen peroxide formation was 8×10^{-7} mol/L^{-1}s^{-1}.

(3) The effective lifetime of the hydrogen peroxide was estimated as $\approx 7 \times 10^3$ s.

The experimental data on the time of the attainment and the values of the largest oxygen peroxide concentration in the solutions of electrolytes are presented in table.

The tabulated data show that the setting times for the H_2O_2 stationary concentration (or the times of the maximum H_2O_2 concentration) are rather long for the mentioned solution (about some hours).

REFERENCES

1. Pikaev, A.K., Kabakchi, S.A., and Makarov, I.E., *Vysokotemperaturnyi radioliz vody i vodnykh rastvorov* (High Temperature Radiolysis of Water and Aqueous Solutions), Moscow: Energoatomizdat, 1988.

2. Ivannikov, A.A., Lelevkin, V.M., Tokarev, A.V., and Yudanov, V.A., The Effect of the Atmosphere Pressure Glow Discharge on Water, *Khim. Vys. Energii*, 2003, vol. 37, no. 2, pp. 148–151.

3. Sunka, P., Babicky, V., Clupek, M., Lukes, P., et al., Study of Wastewater Treatment by Radicals Using DC and Pulsed Corona Discharge over Water, *Plasma Sources Sci. Technol.*, 1999, no. 8, pp. 258–261.

4. Lukes, P., Appleton, A.T., and Locke, B.R., Hydrogen Peroxide and Ozone Formation in Hybrid Gas–Liquid

Electrical Discharge Reactors, *Acta Phys. Slov.*, 2004, vol. 54, pp. 135−139.

5. Maksimov, A.I. and Khlyustova, A.V., Physical Chemistry of Plasma-Solution Systems, *Khim. Vys. Energii*, 2009, vol. 43, no. 3, pp. 195−201.

6. Kuz'michyova, L.A., Maksimov, A.I., and Titova, Yu. V., Formation of Hydrogen Peroxide under the Action of Atmosphere Pressure Glow Discharge on Aqueous Solutions of Electrolytes, *Elektron. Obrab. Mater.*, 2004, vol. 40, no. 4, pp. 57−61.

7. Maksimov, A.I., Kuz'michyova, L.A., Khlyustova, A.V., Titova, Yu.V., and Dydykin, M.G., The Role of Transport Processes of Solution Components to Plasma Zone in Chemical Reactions, Initiated by Glow Discharge in Electrolyte Solutions, *Mendeleev Commun.*, 2007 no. 5, pp. 1−3.

8. Kuz'michyova, L.A., Titova, Yu.V., and Maksimov, A.I., Study of the Effect of Atmosphere Pressure Surface Discharge on Electrolyte Solution, *Elektron. Obrab. Mater.*, 2008, vol. 44, no. 2, pp. 106−109.

9. Skug, D. and West, D., *Osnovy analiticheskoi khimii* (Foundations of Analytical Chemistry), vol. I, Moscow: Mir, 1979.

10. Kuz'michyova, L.A., Titova, Yu.V., and Maksimov, A.I., Yields of Hydroxyl-Radicals and Hydrogen Peroxide in the System of Glow Discharge with Liquid Cathode, *Elektron. Obrab. Mater.*, 2011, vol. 47, no. 6, pp. 45−47.

11. Kuz'michyova, L.A., Titova, Yu.V., and Maksimov, A.I., The Effect of Gas-Phase Processes Initiated by Glow Discharge on the Properties of Electrolyte Solutions, *Elektron. Obrab. Mater.*, 2006, vol. 42, no. 3, pp. 148−152.

12. Balantseva, E.V., Antina, E.V., Titova, Yu.V., and Maksimov, A.I., *Sbornik trudov IV Mezhdunarodnogo simpoziuma po teoreticheskoi i prikladnoi plasmokhimii* (Proc. IV Int. Symposium on Theoretical and Applied Plasma Chemistry), Ivanovo, 2005, vol. 1, pp. 252−254.

13. Shumb, W.C, Satterfield, C.N, and Wentworth, R.L., *Perekis' vodoroda* (Hydrogen Peroxide), Moscow: Inostrannaya Literatura, 1958, pp. 373−429.

Non-Traditional Machining Processes by Means of Velocity Shear Instability in Plasma[1]

R. K. Tyagi[a], K. K. Srivastava[a], and R. S. Pandey[b]

[a] *Department of Mechanical Engineering, Birla Institute of Technology Mesra Ranchi, Jharkhand, India,*

[b] *Department of Applied Physics, Amity School of Engineering and Technology, Amity University Utter Pradesh, Noida, India*

e-mail: tyagi_rk1@rediffmail.com

Received June 18, 2011; in final form, November 01, 2011

Abstract—The material removal within different machining process can be performed in distinct modalities. One of the modality is based on the effect of impact phenomenon. In this paper theoretical model of non-traditional machining process based on impact phenomenon is discussed. The material is removed from the surface due to the impact of ions. The velocity of ions is equal to the velocity at which the electrostatic ion-cyclotron instability driven by parallel flow velocity shear generated by massive ions takes place. The main ways for the material removal as consequence of the impact phenomenon are the microcracking, microcutting, melting and vaporizing of small quantities from the work-piece surface layer.

INTRODUCTION

Machining concerns the modification of the workpiece on the shape, on the dimensions, on the outward view and eventually on the material constitution, to obtain the product with certain qualities. There are two machining processes, one is the traditional machining process and second is the non-traditional machining process. In traditional machining process we can find two modalities, which are the big pressure exerted between the tool and the workpiece, or the chemical reaction into the work medium [1].

In non-traditional machining process there is one modality, which is the impact phenomenon. This impact phenomenon can be classified into two ways [1].

When there is a temporary contact of some particle with workpiece material. The dimension of macroparticles being some tenths of millimeter; such particles are used with abrasive jet machining, water jet machining, ultrasonic machining [2–4].

When impact phenomenon is occurs due to subatomic particle with the workpiece surface layer. Subatomic particles include ions, electrons, the photons, and sometimes, just the concrete atoms. Such particles are used within the electrical discharge machining, the plasma beam machining, the ion beam machining, the electron beam machining [2, 3].

If the impact is generated by subatomic microparticles, the main effect derives from the change of the kinetic energy into thermal energy. The kinetic energy of the microparticles directed to the workpiece surface. It is clear that not all this energy is transformed in

thermal energy, a part of the kinetic energy being necessary for the afterward motion of the particles. Due to their small dimensions, the electrons could initially penetrate a thin surface layer, without to obtain significant effect from the point of view of the machining method. If the electrons energy is high enough to continue their trajectories at depths higher than the dimension defined by the Shenland's relation, the electrons are able to transfer their kinetic energy to the atomic structures (atoms, molecules) of the workpiece material. This means that the amplitude of the atomic structures oscillations round to their equilibrium positions increase and this fact is materialized by the increasing of the temperature. If the temperature is high enough, a so-called thermal source appears and the workpiece solid material is transformed in melted material or even in vapors [5].

The micro-scale movable mechanical pin joints, springs, gears, sliders, sealed cavities, and many other mechanical and optical components have been fabricated using surface micromachining of poly-silicon. The analog devices have commercialized such as ADXL-50, a 50 g accelerometer that was developed using surface micromachining for activating air-bag deployment. Texas Instruments' Digital Micro-mirror Device is also based on surface micromachining [6].

In particular, a micro-manufacturing refers to the fabrication of products or components where the dimensions of at least one feature are in the micrometer range. Similarly, nano-manufacturing refers to the production of devices where some of the dimensions are in the nanometer range. A broad range of technologies exists for micro- and nano-manufacturing, and the physical principles implemented in them are very

---

[1] The article is published in the original.

diverse. Several researchers have proposed classification schemes to categories' these technologies. For example, Masuzawa [7] focused on micromachining processes and classified them according to the implemented machining phenomena. Madou [8] categorized the micro-fabrication techniques as traditional or non-traditional methods and lithographic and non-lithographic methods. Perhaps the most widespread classification is that by Brinksmeter et al. [9].

OBJECTIVE

The objective of this study is to find out the effect of magnetic field, electric field and its inhomoge-neity on the metal removal from surface due to the impact of subatomic particles such as ions by using theoretical calculations. Note that the main consequences of the impact phenomena are the generation of craters on the workpiece surface, as consequence of the energy dissipation and development of heat, small quantities of the workpiece material are melted, vaporized and ejected out of the workpiece.

GENERATION OF VELOCITY SHEAR INSTABILITY

We consider plasma in which the massive heavy positive ions are produced due to ionization of K^+ and light electrons are produced from SF_6^-. Fully ionized and collisionless potassium plasma is produced by contact ionization of potassium atoms (K) sprayed onto a tungsten (W) plate. The machine is equipped to produce or to control magnetic field-aligned K^+ flow and its velocity shear including the following features [10].

The plate W for K^+ production (positive ion source) is concentrically segmented.

Another W plate to supply thermionic electrons (the electron source) is mounted at the opposite end of chamber column.

A mesh grid (stainless steel) negatively biased with respect to grounded vacuum chamber is situated in front of the positive ion source.

The generation and control of the parallel velocity shear are achieved by individually biasing each segment of the segmented ion source i.e. a difference between voltages applied between two conjunctive segments. The generation of parallel velocity shear instability can be ensured by the electrostatic energy analyzer and with the laser induced florescence diagnostic technique [11]. The negative ions are produced by introducing sulphur hexafluoride (SF_6) gas into the potassium plasma [12, 13]. An SF_6 molecule has a great electron attachment cross-section for the electron energies less than 1 eV [14]. Due to this production of negative and positive ions in different layers which have shear of velocity and density gradient in respective layer. The velocity shear instability is generated as it is shown in Fig. 1.

MACHINING PROCESSES BY USING IONS

A kinetic energy of the moving particles is transmitted to workpiece material: really, the substantial part of the kinetic energy transforms in thermal energy. Thus, the oscillation amplitude of atomic structure increases. The insignificant increase of this amplitude means that a temperature will increase. If the increase of the oscillation amplitude is larger, then some structural changes occur in the workpiece material. Hereafter, if the oscillation amplitude exceeds a certain value then there is possibility for some structures to leave the place, so that process of melting or vaporizing occurs. The material from the work surface can be removed by circulation of the work liquid [1].

MATHEMATICAL MODEL

The ions/electrons must have enough energy to go through the distance up to the workpiece and to penetrate into the workpiece surface layer. Since the ions are the electrical charges, their trajectories and velocities are influenced by electric and magnetic field. Using the results by Tyagi et al. [15], it is easy obtained the expression for the group velocity of electrostatic ion-cyclotron wave in the laboratory reference system assuming small perturbations of the electric field E_1, magnetic field B_1 and distribution function f_{s1}. For the perturbed values of the electric and magnetic fields the harmonic dependence as exp i(kr-ωt) are assumed.

Now the ion's velocity v (assuming it to be equal the group velocity of wave, i.e. as $\partial \omega_r / \partial k$, and using the expression for the real frequency ω_r of the wave incident on the workpiece surface according to equation (15) from Tyagi et al. [15]) can be written as:

$$\frac{\overline{\omega'}}{\Omega_i} = -\frac{b_1}{2a_1}\left[1 \pm \sqrt{\left(1 - \frac{4a_1 c_1}{b_1^2}\right)}\right], \qquad (1)$$

where:

$$a_1 = a_2\left(\frac{\Omega_i}{k_\parallel \alpha_\parallel}\right)^2, \quad b_1 = \frac{\Omega_i}{k_\parallel \alpha_{\parallel i}} b_2 - \frac{2k_\perp \Delta'}{k_\parallel^2 \alpha_{\parallel i}^2} a_2 \Omega_i,$$

$$a_2 = \frac{\eta_e}{\eta_i}\frac{T_{\perp i}}{T_{\parallel i}} + \frac{T_{\perp i}}{T_{\parallel i}} - \Gamma_n(\mu_i)\frac{T_{\perp i}}{T_{\parallel i}}, \quad b_2 = \frac{\Gamma_n(\mu_i)k_\perp}{2k_\parallel}\varepsilon_n \rho_i$$

$$\times \frac{\alpha_{\perp i}}{\alpha_{\parallel i}} - \frac{\Gamma_n(\mu_i)k_\perp}{2k_\parallel} - \frac{\Gamma_n(\mu_i)k_\perp n\Omega_i}{2k_\parallel^2 \alpha_{\parallel i}},$$

$$c_1 = \frac{\Gamma_n(\mu_i)T_{\perp i}}{2T_{\parallel i}}\left(1 - \frac{k_\perp}{k_\parallel}A_i\right) - \frac{b_2 k_\perp \Delta'}{k_\parallel \alpha_{\parallel i}} + \frac{k_\perp^2 \Delta'^2}{k_\parallel^2 \alpha_{\parallel i}^2},$$

$$\eta_i = 1 - \frac{\overline{E_i'}(x)}{4\Omega_i^2}, \quad \eta_e = 1 - \frac{\overline{E_e'}(x)}{4\Omega_e^2}, \quad \overline{\omega'} = \overline{\omega} - n\Omega_i,$$
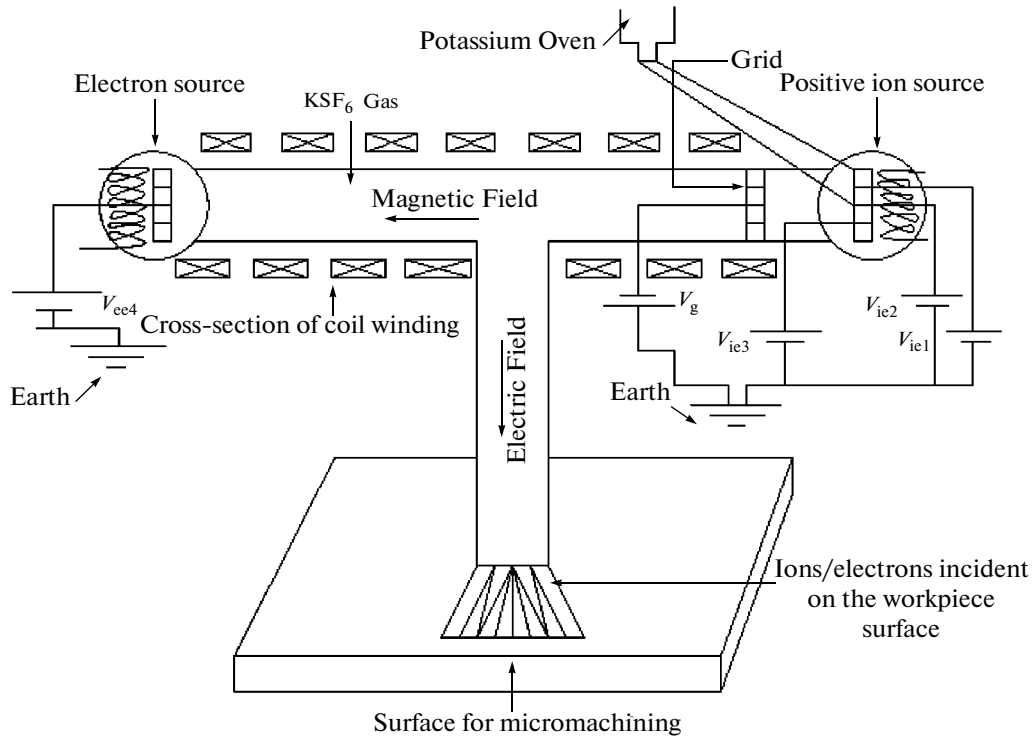
Fig. 1. The model of micromachining process (V_{ie} and V_{ee} are the bias voltages applied to the positive ion source and electron source, respectively. V_g is the grid bias voltage.)

$$\bar{E}(x) = \frac{e_s E(x)}{m_s}, \quad E(x) = E_0\left(1 - \frac{x^2}{a^2}\right),$$

$$\Omega_s = \frac{e_s B_0}{m_s}, \quad \alpha_{\perp s} = \left(\frac{2k_B T_{\perp s}}{m_s}\right)^{1/2}, \quad \alpha_{\parallel s} = \left(\frac{2k_B T_{\parallel s}}{m_s}\right)^{1/2},$$

$$\xi = \frac{\bar{\omega} - (n+p)\Omega_s - k_\perp \Delta'}{k_\parallel \alpha_{\parallel s}}, \quad \Delta' = \frac{\partial \Delta}{\partial t},$$

$$\Delta = \frac{\bar{E}(x)t}{\Omega_s}\left[1 + \frac{E''(x)}{E(x)}\frac{1}{4}\left(\frac{v_\perp}{\Omega_s}\right)^2 \cdots\right],$$

$$A_s = \frac{1}{\Omega_s}\frac{\delta v_{oz}(x)}{\delta x}, \quad \varepsilon_n = \frac{\delta \ln n_0(x)}{\delta x}, \quad A_T = \frac{\alpha_{\perp s}^2}{\alpha_{\parallel s}^2} - 1,$$

$$\bar{\omega} = \omega - k_\parallel v_{oz}(x),$$

$$\Gamma_n(\mu_s) = \exp(-\mu_s)I_n(\mu_s), \quad \mu_s = \frac{k_\perp^2 \rho_i^2}{2},$$

$$(s = i, e).$$

Here $\mathbf{E}(x)$ is the inhomogeneous DC electric field, and it is perpendicular to the external magnetic field $\mathbf{B}_0$, which is parallel to ion flow. The detailed description of all variables, which used in the given model, is considered in [15].

The dimensionless real frequency and ion's velocity have been calculated by computer technique with the help of equation (1) for inhomogeneous DC electric field. For inhomogeneous DC electric field the condition $x/a \le 1$ has been taken.

The kinetic energy of the charged particle under action of voltage U determines as:

$$eU = \frac{m v^2}{2}. \tag{2}$$

Evidently, the metal removal rate is dependent versus generated voltage U, which defines the depth of ion penetration in the workpiece material. The thickness of this surface layer is defined by the Shenland's relation [5]:

$$\delta = 2.2 \times 10^{-12}\frac{U^2}{\rho} \text{ [cm]}, \tag{3}$$

where ρ is the workpiece material density, in g/cm^3 and U is the acceleration voltage, in V.

RESULTS AND DISCUSSION

In this mathematical model of machining processes the experimental data [16, 17] are used. We show the solution of the equation (1), (2) and (3) using parameters may be representative of laboratory by Kim, Merlino [18] and Rosenberg, Merlino [19]. We

Fig. 2. The variation of ion penetration versus $k_\perp \rho_i$ with other fixed parameters: $A_i = 0.5$, $T_e/T_i = 2$, $E_0 = 16$ V/m, $x/a = 0,2$, $\theta = 88.5°$, $A_T = 1.5$, $\varepsilon_n \rho_i = 0.2$, $k_\perp/k_\parallel = \tan(\theta)$, the density of metal $= 3000$ kg/m^3. *1*—Series 1, $B_0 = 0.11$ T; *2*—Series 2, $B_0 = 0.14$ T; *3*—Series 3, $B_0 = 0.17$ T.

Fig. 3. The variation of ion penetration versus $k_\perp \rho_i$ with other fixed parameters: $A_i = 0.5$, $T_e/T_i = 2$, $B_0 = 0.14$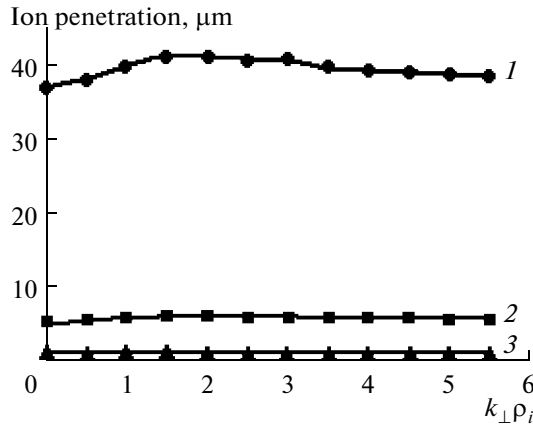 T, $x/a = 0.2$, $\theta = 88.5°$, $A_T = 1.5$, $\varepsilon_n \rho_i = 0.2$, $k_\perp/k_\parallel = \tan(\theta)$, the density of metal $= 3000$ kg/m^3. *1*—$E_0 = 12$ V/m; *2*—$E_0 = 16$ V/m; *3*—$E_0 = 20$ V/m.

consider the plasma in which the heavy positive ions are produced due to ionization of K$^+$ and light electrons are produced from SF$_6^-$. We have assumed that electron-ion temperature ratio T_e/T_i is 2. It is further assumed that the plasma is immersed in a magnetic field whose strength varies from 0.11 T to 0.17 T and inhomogeneous DC electric field with strength from 12 V/m to 20 V/m, so that the given fields are perpendicular. In this case for the positive ions the gyro-radius is $\rho \sim 0.095$ cm and the temperature anisotropy is $A_T = T_i/T_{\parallel i} - 1 = 1.5$ with density gradient $n_i = 0.2$. In this case we would accept that for the heavy positive ions the electrostatic ion-cyclotron instability could become excited by the parallel velocity shear with scale length from $A_i = 0.5$ to $A_i = 0.55$.

Figure 2 shows the variation of ion penetration in the metallic surface (μm) versus $k_\perp \rho_i$ for different values of the magnetic field strength B_0 with other fixed parameters listed in figure caption. The ion penetration decreases with increasing of the magnetic field strength. Due to the change of the magnetic field the gyro-frequency changes, therefore the magnetic field strength is a useful parameter for the machining processes. The maximum value of ion penetration is 41 μm when the value of magnetic field is 0.11 T and the minimum value is 0.137 μm for 0.17 T with other fixed parameters listed in the figure caption.

Figure 3 shows the variation of ion penetration versus $k_\perp \rho_i$ for various values of inhomogeneous DC electric field. The real frequency increases with increasing the value of electric field. In general, this has a stabilizing effect owing to resonant and non-resonant interactions affecting the real frequency. The maximum ion penetration is 14 μm, when the value of inhomogeneous DC electric field is 20 V/m and the

minimum value is 2 μm for 12 V/m with other fixed parameters listed in the figure caption.

Figure 4 shows the variation of ion penetration versus $k_\perp \rho_i$ for various values of inhomogeneity (x/a) in DC electric field and other parameters being fixed. The ion penetration decreases at increasing the value x/a. For inhomogeneity of the DC electric field the condition $x/a < 1$ is taken. Herewith x/a shows the destabilizing effect on the wave incident on the workpiece surface.

If the potential difference U has a value corresponding to voltage applied usually within the electrical discharge machining (for example, $U = 70$ V), one can notice that the depth of electron's penetration is insig-
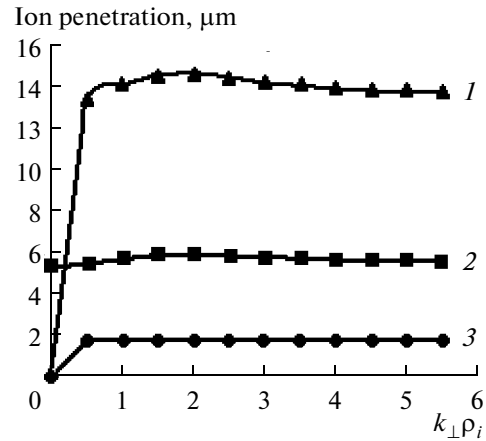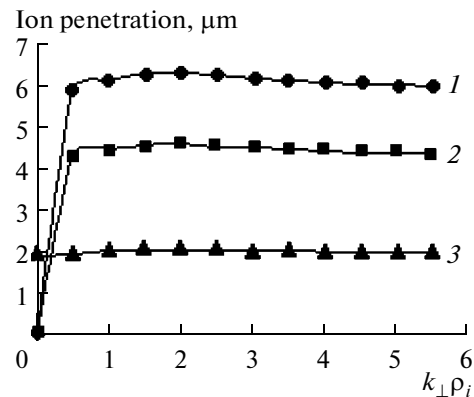

Fig. 4. The variation of ion penetration versus $k_\perp \rho_i$ with other fixed parameters: $A_i = 0.5$, $T_e/T_i = 2$, $B_0 = 0.14$ T, $E_0 = 16$ V/m, $\theta = 88.5°$, $A_T = 1.5$, $\varepsilon_n \rho_i = 0.2$, $k_\perp/k_\parallel = \tan(\theta)$, the density of metal $= 3000$ kg/m^3. *1*—$x/a = 0.1$; *2*—$x/a = 0.4$; $x/a = 0.7$.

nificantly small ($\delta = 1.381 \times 10^{-9}$ cm). But if the potential difference is $U = 5000-200000$ V, then the depth of electron's penetration in the surface layer of the metallic workpiece is much more ($\delta = 7.05 \times 10^{-8}-1.128 \times 10^{-2}$ cm). After the penetration of the electrons through the layer of depth δ, the electron's energy is dissipated and as a consequence the temperature of workpiece material increases up to the vaporizing and melting temperatures, so that the micro-explosions are produced and the small quantities of the workpiece material are ejected and the small craters are generated [20].

The theoretical results obtained from the given mathematical model are found out within the range of experimental result [20].

CONCLUSIONS

This paper describes the mathematical model for the micromachining process. This shows the flexibility of using the magnetic field, electric field and its inhomogeneity for control of ion penetration into metallic surface. It has been shown that under the parameters considered, the maximum value of ion penetration is 41 μm (at value of the magnetic field 0.11 T, voltage 16 V and inhomogeneity 0.2). Moreover, the theoretical results show that the ion penetration increases with corresponding decrease of the magnetic field value and inhomogeneity in the DC electric field and by increasing of the DC electric field value.

ACKNOWLEDGMENTS

REFERENCES

1. Slătineanu, L., Coteaţă, M., Dodun, O., Iosub, A., and Apetrei, L., Impact Phenomenon in the Case of Some Non-traditional Machining Processes, *Int. J. Mater. Form.*, 2008, vol. 1, no. 1, 1391−1394.

2. Hashish, M., Material Properties in Abrasive-waterjet Machining, *Transactions of the ASME: Journal of Engineering for Industry*, 1995, vol. 117, no. 4, pp. 578−583.

3. Cheng, K., Abrasive Micromachining and Microgrinding, in *Micromachining of Engineering Materials*, McGeough, J.A., Ed., New York-Basel: Marcel Dekker Inc., 2002, pp. 85−90.

4. Marinescu, N.I., Nanu, D., Lăcătuş, E., Popa, L., Marinescu, R.D., and Savastru, R., *Machining Processes with Beams and Jets*, [in Romanian], Bucureşti: Institutul Naţional de Optoelectronică (INOE), 2000.

5. Slătineanu, L., Dodun, O., Coteaţă, M., Gonçalves-Coelho, A.M., Beşliu, I., and Pop, N., Machining Methods Based on the Impact Effects, *International Journal of Modern Manufacturing Technologies*, 2009, vol. 1, no. 1, pp. 83−88.

6. Roy, S. and Mehregany, M., Fabrication of Electrostatic Nickel Microrelays by Nickel Surface Micromachining, *IEEE Proceedings of the 8th Annual International Workshop on Micro Electro Mechanical Systems*, Amsterdam, The Netherlands, 29 January−2 February, 1995, pp. 353−358.

7. Masuzawa, T., State-of-the-Art on Micromachining, *CIRP Annals—Manufacturing Technology*, 2000, vol. 49, no. 2, pp. 473−488.

8. Madou, M.J., *Fundamentals of Microfabrication: The Science of Miniaturization*, 2nd edition, Boca Raton, FL: CRC Press, 2002.

9. Brinksmeier, E., Riemer, O., and Stern, R., Machining of Precision Parts and Microstructures, *Proceedings of the 10th International Conference on Precision Engineering (ICPE)*, Yokohama, Japan, 18−20 July, 2001, pp. 3−11.

10. Kaneko, T., Odaka, Y., Tada, E., and Hatakeyama, R., Generation and Control of Field-aligned Flow Velocity Shear in a Fully Ionized Collisionless Plasma, *Review of Scientific Instruments*, 2002, vol. 73, no. 12, pp. 4218−4222.

11. Reynolds, E.W., Kaneko, T., Koepke, M.E., and Hatakeyama, R., Laser-induced-fluorescence Characterization of Velocity Shear in a Magnetized Plasma Column Produced by a Segmented Q-machine Source, *Phys. Plasmas*, 2005, vol. 12, no. 7, p. 072103 [6 pages].

12. Wong, A.Y., Mamas, D.L., and Arnush, D., Negative Ion Plasmas, *Phys. Fluids*, 1975, vol. 18, no. 11, pp. 1489−1493.

13. Sato, N., Production of Negative Ion Plasmas in a Q Machine, *Plasma Sources Science and Technology*, 1994, vol. 3, no. 3, pp. 395−399.

14. Liu, X., Xiao, D., Wang, Y., and Zhang, Z., Monte Carlo Simulation of Electron Swarms Parameters in c-C_4F_8/CF_4 Gas Mixtures, *Journal of Shanghai Jiaotong University (Science)*, 2008, vol. 13, no. 4, pp. 443−447.

15. Tyagi, R.K., Srivastava, K.K., and Pandey, R.S., Analysis of Electrostatic Ion-cyclotron Instability Driven by Parallel Flow Velocity Shear, *Surface Engineering and Applied Electrochemistry*, 2011, vol. 47, no. 4, pp. 370−377.

16. Tse, H.C., Man, H.C., and Yue, T.M., Effect of Magnetic Field on Plasma Control During CO_2 Laser Welding, *Optics and Lasers Technology*, 1999, vol. 31, no. 5, pp. 363−368.

17. Ichiki, R., Kaneko, T., Hayashi, K., Tamura, S., and Hatakeyama, H., Parallel-velocity-shear-modified Drift Wave in Negative Ion Plasmas, *Plasma Physics and Controlled Fusion*, 2009, vol. 51, no. 3, p. 035011 [11 pages].

18. Kim, S.-H. and Merlino, R.L., Electron Attachment to C_7F_{14} and SF_6 in a Thermally Ionized Potassium Plasma, *Phys. Rev. E*, 2007, vol. 76, no. 3, p. 035401(R) [4 pages].

19. Rosenberg, M. and Merlino, R.L., Instability of Higher Harmonic Electrostatic Ion Cyclotron Waves in a Negative Ion Plasma, *Journal of Plasma Physics*, 2009, vol. 75, no. 04, pp. 495−508.

20. Slătineanu, L., Coteaţă, M., Dodun, O., Anton, D., Munteanu, A., and Ilii, S.M., Impact Phenomena During Electrical Discharge Machining, *Proceedings of the 3rd International Conference on Manufacturing Engineering (ICMEN)*, Chalkidiki, Greece, 1−3 October, 2008, pp. 193−198.

Pressure-Induced Change in the Order of the Phase Transition in Lead Titanate: Structural Aspects

S. G. Jabarov[a, b], **D. P. Kozlenko**[a], **S. E. Kichanov**[a], **A. I. Mamedov**[b], **R. Z. Mehdieva**[b], **E. V. Lukin**[a], **B. N. Savenko**[a], **and C. Lathe**[c]

[a]*Joint Institute for Nuclear Research, ul. Joliot-Curie 6, Dubna, 141980 Russia*
[b]*Institute of Physics, National Academy of Sciences of Azerbaijan, pr. Javid 33, Baku, AZ-1143 Republic of Azerbaijan*
[c]*Helmholtz Center Potsdam, Telegrafenberg, Potsdam, 14407 Germany*
e-mail: sakin@jinr.ru

Received September 12, 2011; in final form, October 26, 2011

Abstract—The crystal structure of lead titanate $PbTiO_3$ have been studied by energy-dispersive X-ray diffraction under pressures of 0–4 GPa in the temperature range of 300–950 K. At a temperature of $T = 747$ K, a structural phase transition from a ferroelectric tetragonal phase to a paraelectric cubic phase is observed. The application of pressure leads to a significant decrease in the phase transition temperature; under pressures of $P \sim 2$ GPa, the type of the phase transition changes from the first to second order. In the low pressure range, the baric coefficient value is $dTc/dP = -20(3)$ K/GPa; under pressures above 2 GPa, it increases up to $-113(5)$ K/GPa.

DOI: 10.3103/S1068375512010048

INTRODUCTION

Compounds with a perovskite structure exhibit a variety of interesting physical phenomena: ferroelectricity, pyroelectric effects, piezoelectricity, and structural and magnetic phase transitions [1, 2]; the study of these phenomena is one of the most urgent problems of modern condensed matter physics. In addition, these materials are widely used in modern electronics; this necessitates a careful study of their crystal structure and physical properties.

Lead titanate $PbTiO_3$ is one of the well known and most studied ferroelectrics with a perovskite structure [3, 4]. $PbTiO_3$ has a high ferroelectric–paraelectric phase transition temperature T_C [5, 6]; the relative simplicity of the crystal structure makes it a convenient model object for the construction of theoretical models of the ferroelectric state in ionic crystals [7–9]. The ferroelectric effect in lead titanate is a result of the distortions of the oxygen octahedra in the tetragonal crystal structure with respective changes in the positions of the oxygen and titanium atoms [10]. An increase in the temperature T_C to 763 K leads to a ferroelectric–paraelectric structural phase transition, which is associated with the transition from a tetragonal phase to a cubic phase with space group $Pm\overline{3}m$ [11–13]. It is a first-order phase transition [10].

The structural changes in lead titanate under a high pressure were studied at a fixed temperature by means of X-ray diffraction [7, 8, 14]. The exposure to a high pressure leads to a significant decrease in the Curie temperature; at $P \sim 11$ GPa, a second-order ferroelectric–paraelectric transition is found in $PbTiO_3$ at room temperature [7, 8]. The authors of [7] assume that the phase diagram of lead titanate comprises a critical point at which the type of the phase transition changes from the first to second order. To study the structural mechanisms of the change in the order of the phase transition and the instability of the ferroelectric phase under high pressures, we studied the crystal structure of the $PbTiO_3$ compound by energy-dispersive X-ray diffraction in a pressure range of 0–4 GPa at temperatures of 300–950 K.

EXPERIMENTAL

Ceramic samples of lead titanate $PbTiO_3$ were prepared from PbO and Ti_2O_5 oxides using the standard solid-state reaction technique with additional oxygen lancing in platinum crucibles. The synthesis was carried out in two stages: at a temperature of 1073 K for 1 day and at a temperature of 1273 K for 12 h with intermediate crushing and compression molding into tablets.

The experiments on energy-dispersive X-ray diffraction under high pressures up to 4.0 GPa in a temperature range of 300–950 K were carried out using an MAX80 high-pressure hydraulic press [15], which operated at beamline F2.1 of a DORIS-III source (HASYLAB, DESY; Hamburg, Germany). A sample was placed into a cylindrical container made of boron nitride; the upper part of the container was filled with

Intensity, rel. units
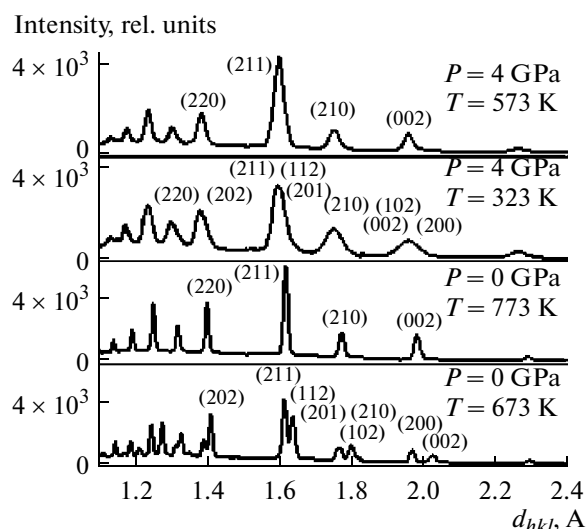
Fig. 1. Energy-dispersive X-ray diffraction pattern regions of $PbTiO_3$ obtained under a normal pressure at temperatures of 673 and 773 K (bottom) and under a high pressure of $P = 4.0$ GPa at temperatures of 573 and 323 K (top).

the sample, and the lower part was filled with NaCl for calibrating the pressure. The sample was heated by means of a graphite heater, and the temperature was controlled using a thermocouple. The energy-dispersive diffraction patterns were recorded using a germanium semiconductor detector with a resolution of 153 eV at an energy of 5.9 keV and with a resolution of 500 eV at 122 keV with a total averaged resolution of $\Delta d/d \approx 1\%$. The fixed Bragg angle of the detector in the

experiment was 9.093°, and the exposure time was ~5 min.

The diffraction patterns were processed using Full-Prof software [16], which is based on the standard Rietveld method [17].

RESULTS AND DISCUSSION

The X-ray diffraction patterns of lead titanate obtained at high pressures and temperatures are shown in Fig. 1. Under normal pressure, in the temperature range of 300−747 K, the diffraction patterns correspond to the tetragonal crystal structure with symmetry $P4mm$ [6]. The unit cell parameters for this phase under normal conditions were $a = 3.903(6)$ Å and $c = 4.145(4)$ Å, which is in good agreement with the previous results [6, 11, 14]. At a temperature of $T_C = 747$ K, we observed changes in the diffraction patterns (Fig. 1) corresponding to a structural transition into the cubic phase of $PbTiO_3$. The calculated value of the unit cell parameter for the cubic phase was $a = 3.971(3)$ Å (at $T = 747$ K).

The temperature dependence of the unit cell parameters of $PbTiO_3$ under normal and high pressures is shown in Fig. 2. To interpolate them, we used linear functions for the paraelectric cubic phase and second-order polynomials for the ferroelectric tetragonal phase.

The pressure dependence of the relative volume of the unit cell for the tetragonal and cubic phases of $PbTiO_3$ at temperatures of 300 and 773 K is shown in
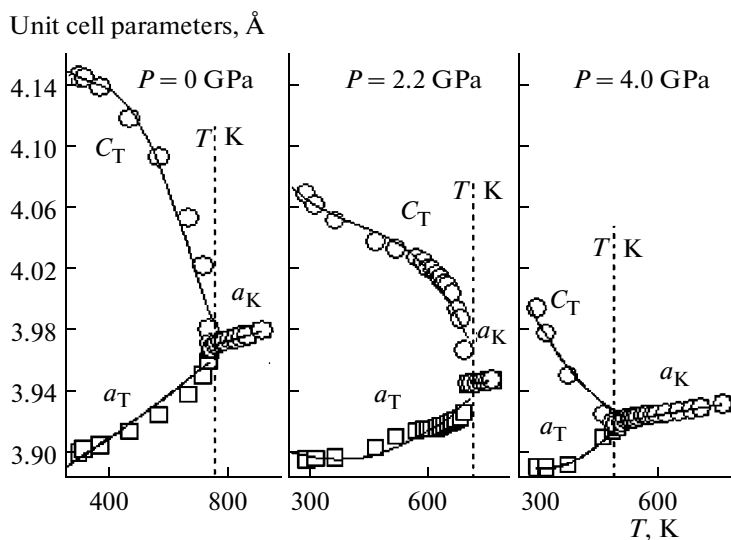
Fig. 2. Temperature dependences of the unit cell parameters of the tetragonal and cubic phases of lead titanate under normal, and high (2.2 GPa and 4.0 GPa) pressures. The solid lines show the interpolation of the experimental data by linear functions and second-order polynomials.
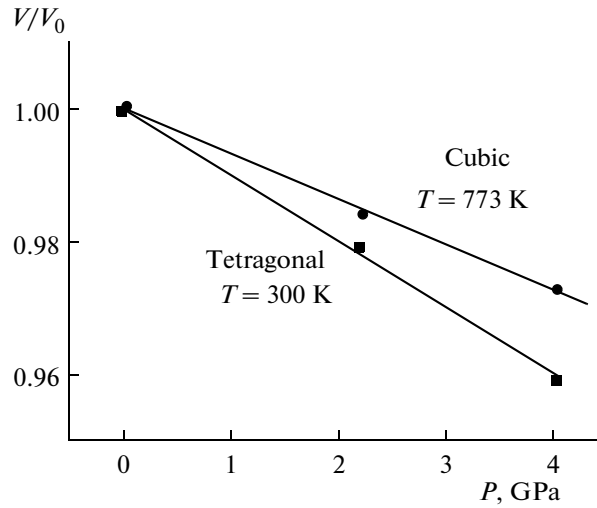
Fig. 3. Pressure dependence of the relative volume of the unit cell of $PbTiO_3$ for the tetragonal (at room temperature) and cubic phases (at $T = 773$ K). The solid lines are the interpolation of the experimental data by the Birch−Murnaghan equation.
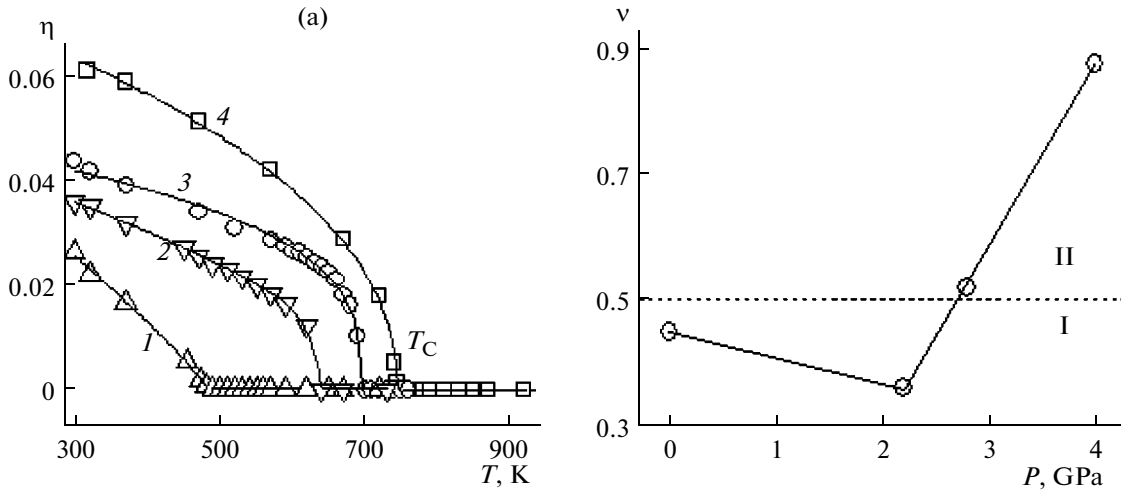
Fig. 4. (a) Temperature dependence of the spontaneous stress η at different pressures P, GPa: (*1*) 4.0, (*2*) 2.8, (*3*) 2.2, and (*4*) 0. The experimental data were interpolated by the equation from [22]. (b) Baric dependence of the exponent ν.

Fig. 3. The experimental data were interpolated by the third-order Birch−Murnaghan equation of state [18]:

$$P = 3/2 B_0 (x^{-7/3} - x^{-5/3}) \times [1 + 3/4(B' - 4)(x^{-2/3} - 1)], \tag{1}$$

where $x = V/V_0$ is the relative unit cell volume; V_0 is the unit cell volume at $P = 0$; and B_0 and B' are the bulk modulus ($B_0 = -V(dP/dV)_T$) and its derivative with respect to the pressure ($B' = (dB_0/dP)_T$), respectively. The resulting values were $B_0 = 90(8)$ GPa for the tetragonal phase and $B_0 = 138(9)$ GPa for the cubic phase of $PbTiO_3$.

It was found in [19] that the squared value of the spontaneous polarization P_s is directly proportional to the value of the spontaneous stress $\eta = c/a - 1$ for the tetragonal phase of lead titanate; according to the Landau theory of phase transitions [20, 21], it is an order parameter whose value depends on the order of the phase transition. Experimental data on the temperature dependence of the spontaneous stress for different pressures were analyzed by using the following function: $\eta(T) = A(T_C - T)^\nu$ [22], where T_C is the Curie temperature, ν is the above-mentioned order parameter, and A is the scale coefficient (Fig. 4a). Under a high pressure, an increase in the exponent ν
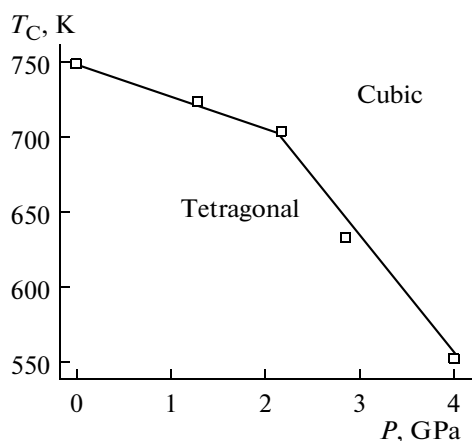
Fig. 5. Pressure dependence of the ferroelectric–paraelectric phase transition temperature T_C in PbTiO$_3$. The solid line shows the linear interpolation of the experimental data.

of the function is observed (Fig. 4b); it is this that indicates the change in the order of the phase transition from the first to second [21]. The change in the order of the phase transition leads to a change in the baric behavior of the Curie point T_C (Fig. 5). It is evident that the critical point in the phase diagram at which a break of the baric behavior of T_C is observed corresponds to a pressure of $P \sim 2.5$ GPa and a temperature of $T \sim 720$ K. In the low-pressure range, the baric coefficient's value is $dTc/dP = -20(3)$ K/GPa; under pressures above 2 GPa, it increases to $-113(5)$ K/GPa.

CONCLUSIONS

It is found in this study that a high pressure leads to a significant decrease in the temperature of the transition from the tetragonal ferroelectric phase to the cubic paraelectric phase; in addition, in the low-pressure range, the baric coefficient is $dTc/dP = -20(3)$ K/GPa; under pressures of $P > 2$ GPa, this coefficient increases to $-113(5)$ K/GPa. This can be attributed to the change in the order of the ferroelectric–paraelectric phase transition from the first to second under a high pressure, as is evidenced by the change in the behavior of the temperature dependence of the spontaneous stress under a high pressure.

ACKNOWLEDGMENTS

REFERENCES

1. Rabe, K.M., Ahn, Ch.H., and Triscone, J.-M., *Physics of Ferroelectrics: A Modern Perspective*, Berlin: Springer, 2007.

2. Topolov, V.Yu. and Bowen, Ch.R., *Electromechanical Properties in Composites Based on Ferroelectrics*, London: Springer, 2009.

3. Lines, M. and Glass, A., *Principles and Applications of Ferroelectrics and Related Materials*, Oxford: Clarendon, 1977.

4. Jona, F. and Shirane, G., *Ferroelectric Crystals*, Oxford: Pergamon, 1962.

5. Shirane, D., Hoshino, S., and Suzuki, K., X-Ray Study of the Phase Transition in Lead Titanate, *Phys. Rev.*, 1950, vol. 80, pp. 1105–1106.

6. Shirane, G., Pepinsky, R., and Frazer, B.C., X-ray and Neutron Diffraction Study of Ferroelectric PbTiO$_3$, *Acta Crystallogr.*, 1956, vol. 9, pp. 131–140.

7. Ramirez, R., Lapena, M.F., and Gonzalo, J.A., Pressure Dependence of Free-Energy Expansion Coefficient in PbTiO3 and BaTiO$_3$ and Tricritical-Point Behavior, *Phys. Rev. B: Condens. Matter*, 1990, vol. 42, no. 4, pp. 2604–2606.

8. Samara, G.A., Pressure and Temperature Dependence of the Dielectric Properties and Phase Transitions of the Ferroelectric Perovskites: PbTiO$_3$ and BaTiO$_3$, *Ferroelectrics*, 1971, vol. 2, pp. 277–289.

9. Jaouen, N., Dhaussy, A.C., Itie, J.P., Rogalev, A., Marinel, S., and Joly, Y., High-Pressure Dependent Ferroelectric Phase Transition in Lead Titanate, *Phys. Rev. B: Condens. Matter*, 2007, vol. 75, p. 224115.

10. Sani, A., Hanfland, M., and Levy, D., The Equation of State of PbTiO$_3$ up to 37 GPa: a Synchrotron X-Ray Powder Diffraction Study, *J. Phys.: Condens. Matter*, 2002, vol. 14, pp. 10601–10604.

11. Sani, A., Hanfland, M., and Levy, D., Pressure and Temperature Dependence of the Ferroelectric–Paraelectric Phase Transition in PbTiO$_3$, *J. Solid State Chem.*, 2002, vol. 167, no. 2, pp. 446–452.

12. Gavrilyachenko, V.G., Komarov, V.D., Leiderman, A.V., and Fesenko, E.G., Size Effect in Isometric PbTiO$_3$ Crystals, *Fiz. Tverd. Tela*, 1998, vol. 40, no. 8, pp. 1546–1547.

13. Glazer, A.M. and Mabud, S.A., Powder Profile Refinement of Lead Zirconate Titanate at Several Temperatures: II. Pure PbTiO$_3$, *Acta Crystallogr., Sect. B: Struct. Crystallogr. Cryst. Chem.*, 1978, vol. 34, pp. 1065–1070.

14. Dzhabarov, S.G., Kichanov, S.E., Kozlenko, D.P., Mamedov, A.I., Lukin, E.V., Savenko, B.N., and Late, K., Structural Changes in PbTiO$_3$ at High Pressure and Temperature, *Sbornik trudov 45-ya shkola PIYaF RAN po fizike kondensirovannogo sostoyaniya* (Proc. 45th School on Condensed Matter Physics of Konstantinov Inst. Nuclear Phys., St. Petersburg, Russ. Acad. Sci.), Gatchina, 2011, p. 35.

15. Zinn, P., Lauterjung, J., Wirth, R., and Hinze, E., Kinetic and Microstructural Studies of the Crystallisation

of Coesite from Quartz at High Pressure, *Z. Kristallogr.*, 1997, vol. 212, pp. 691−698.

16. Rodriguez-Carvajal, J., Recent Advances in Magnetic Structure Determination by Neutron Powder Diffraction, *Physica B (Amsterdam)*, 1993, vol. 192, pp. 55−69.

17. Rietveld, H.M., Line Profiles of Neutron Powder-Diffraction Peaks for Structure Refinement, *Acta Crystallogr.*, 1967, vol. 22, pp. 151−152.

18. Birch, F.J., Equation of State and Thermodynamic Parameters of NaCl to 300 kbar in the High-Temperature Domain, *J. Geophys. Res.*, 1986, vol. 91, pp. 4949−4954.

19. Qi, T., Grinberg, I., and Rappe, A.M., Correlations between Tetragonality, Polarization, and Ionic Displacement in $PbTiO_3$-Derived Ferroelectric Perovskite Solid Solutions, *Phys. Rev. B: Condens. Matter*, 2010, vol. 82, pp. 134113.

20. Dove, M.T., Theory of Displacive Phase Transitions in Minerals, *Am. Mineral.*, 1997, vol. 82, pp. 213−244.

21. Aleksandrov, K.S., Anistratov, A.T., Beznosikov, B.V., and Fedoseeva, N.V., *Fazovye perekhody v kristallakh galoidnykh soedinenii ABX3* (Phase Transitions in ABX3 Halide Crystals), Novosibirsk: Nauka, 1981.

22. Singh, S.P., Ranjan, R., Senyshyn, A., Trots, D., and Boysen, H., Structural Phase Transition Study of the Morphotropic Phase Boundary Compositions of $Na_{0.5}Bi_{0.5}TiO_3-PbTiO_3$, *J. Phys.: Condens. Matter*, 2009, vol. 21, pp. 375902.

New Methods of the Improvement of Metal Corrosion Resistance through Surface Impregnation with Anode Electrolyte Heating

V. V. Parshutin, E. A. Pasinkovskii, A. M. Paramonov, A. V. Koval', and N. V. Chernysheva

Institute of Applied Physics, Academy of Sciences of Moldova, ul. Akademiei 5, Chisinau, MD 2028 Republic of Moldova
e-mail: vlad.parshutin40@mail.ru
Received June 27, 2011

Abstract—It is shown that the use of the electrolyte composition developed in this work allows one to reduce by almost twice the carbon content in the surface layer of steel 45 and, with the introduction of an additional operation after the electrolytic heating (oxidation in an aqueous solution of caustic soda with a concentration of $50-100$ g/L), to reduce the corrosion rate almost by a factor of two. It is also established that processing in another electrolyte formulated in the course of the research leads to the reduction of the corrosion rate of electrolytic iron coverings by more than 2 times.

INTRODUCTION

The wear resistance and corrosion resistance of parts are foremost determined by the properties of the surface layers or the adjacent ones. Hence, the metallurgical fabrication of an alloy with such features is not always necessary. It is easier to produce through various methods a conversion surface layer with some prescribed parameters. In this case, it is suitable to use such a process as surface impregnation with anode electrolyte heating [1–5].

It is well known [6] that the presence of carbon in steel increases the metal corrosion rate due to the carbide phase. The surface decarburization of steel removes its active nuclei and raises the metal corrosion resistance. The anode surface impregnation in an electrolyte is one of the decarburization methods.

When electrotechnical steel containing 0.35 wt % of carbon is processed in an aqueous 15% solution of Na_2CO_3 at a voltage of 175 V, a current density of $3-5$ A/cm^2, a temperature of $700 \pm 20°C$ or $885 \pm 15°C$, and with an exposure time of 180 s, in total, the carbon content is reduced by half at a depth of up to 0.2 mm [7]. However, a fivefold growth of the carbon content not favoring the reduction of the metal corrosion rate is observed on the steel surface itself. In addition, the erosion and thermal damage cause local corrosion, and some developed pitting appears here and there.

By decarburizing steel through anode surface impregnation in an aqueous solution of ammonia chloride (NH_4Cl) at a voltage of 180 V, a current density of 1 A/cm^2, and a sample temperature of 650°C, it is possible to reduce the carbon content in the boundary layer by $28-62\%$. The part was cooled in the electrolyte or in the air. Along with the decarburization of the metal surface, there took place its enrichment with

nitrogen due to the high temperature surface oxidation in the vapors of the aqueous electrolyte solution. However, in this case, the decarburization of the surface and its nitriding are not always sufficient, and the oxide film produced due to the heat hardening is not thick and its continuity is inefficient.

Electrolytic metal coatings are used as ornamental ones (implementing corrosion proof components) and to reduce the worn surfaces of machine parts [9]. The iron deposited electrolytically has a higher hardness than steel produced through metallurgic methods. Ironing is a special coating and is mostly used to restore the dimensions of the worn parts of machine tools and agricultural machines. Iron deposits are also used when brazing hard-face plates. However, these coatings do not possess any protective–decorative features, their corrosion resistance is not high, and the electrolytic iron oxidizes in a wet air atmosphere. They try to improve the corrosion resistance of the coatings through the electrolytic deposition of a layer of zinc or nickel. However, this method complicates the engineering process, as it is necessary to use an additional bath and power supply, and greatly prolongs the period of the preparatory and finishing works. Besides improving the corrosion resistance, this method often causes the deterioration of the physical and mechanical properties of the electrolytic deposits.

Other methods [10, 11] to improve the corrosion resistance of iron coatings—alloying by copper, cobalt, manganese, or nickel and using many-component electrolytes—are known. However, these methods do not ensure the product resistance in some media and often cause the deterioration of the physical and mechanical features of the deposits.

The corrosion resistance of coatings is improved through the surface impregnation of a part's surface at

Table 1. The influence of the treatment type on the anode dissolution currents in a 0.05 Na_2SO_4 solution

Treatment method	I_a, A/m² at $\varphi = -0.1$ V	I_a, A/m² at $\varphi = 0.1$ V
Untreated	168	308
In electrolyte I	65.2	290
In electrolyte II	31.4	46.7
With additional oxidation in a caustic-soda solution (50 g/l)	19.8	21.5
With additional oxidation in a caustic-soda solution (75 g/l)	9.7	14.9
With additional oxidation in a caustic-soda solution (100 g/l)	8.1	11.2

the anode process of electrolytic heating in aqueous solutions containing nitrogen compounds (weight %): (1) NH_4Cl—10 and NH_4OH—5; (2) NH_4Cl—11 and NH_4OH_3—11 [1]. The cooling is performed in the electrolyte after the current is switched off or in the air. The surface layer is enriched with nitrogen; there are formed nitrides and an oxide film due to the high temperature oxidation of the surface in the vapors of the aqueous electrolyte solution. However, the nitride layer is nonuniform and has an insufficient depth; the oxide film is not thick with inefficient continuity decreasing the corrosion resistance of the metal surface.

This work is devoted to the development of some ways to improve the physical–mechanical properties and corrosion resistance of electroplated coatings and steel surfaces.

EXPERIMENTAL

The specimens of steel 45 (Its composition (weight %) is as follows: C—0.42–0.5, Cr—0.25, Ni—0.25, Mn—0.5–08, Si—0.17–0.37, P—0.035, and the rest is iron.) 15 mm in diameter and 10 mm in height were subjected to surface impregnation in electrolytes. The process of the steel decarburization and the formation of a continuous oxide film was carried out in a known [8] electrolyte containing ammonia chloride (NH_4Cl—50 g/L; electrolyte I) and in the developed electrolyte (g/L): NH_4Cl, 50; hydroxylamine NH_2OH, 0.05–0.1; hydrozinechloride N_2H_4HCl, 0.1–1.0; and the rest is water (electrolyte II). The part is connected to the current source anode with the voltage between the electrodes of 220 V, a current density of 2 A/cm², and a run time of up to 5 min. On completing the electrolytic heating, in the first case, the part was cooled in the electrolyte. In the second case, the live specimen was taken out of the bath, the current was switched off, and the part was immediately put into a hardening medium (a caustic soda solution with a concentration of 50–100 g/L) until its temperature became the same to perform additional oxidation of the treated surface.

Electroplated coatings were deposited from the ironing chloride electrolyte containing Fe(II) chloride ($FeCl_2 \cdot 4H_2O$; 400 g/L) and a salt acid (HCl) up to

pH = 1.0–1.2. A plate of mild steel served as the anode. To produce a coating with a high adhesion to the base, the specimens on dressing, defatted by soda lime, and washing by water were subjected to anode treatment in an ironing electrolyte with an anode current density of $i_a = 50$–60 A/dm² and a temperature of 60°C for 1 min with the following washing in hot water at 60°C. The deposition was carried out at the cathode current density of $i_k = 10$ A/dm². On completing the deposition process, the specimens were washed in hot water.

The anode surface impregnation of the specimens with the electroplated coatings was carried out in a known salmiac–ammonia–nitrate electrolyte [2] containing the following (weight %): NH_4Cl—11, NH_4NO_3—11 (electrolyte III). It was also carried out in the developed electrolyte containing the following (g/L): ammonia chloride NH_4Cl—75, ammonium nitrate NH_4NO_3—50, sodium nitrite $NaNO_2$—15, and carbamide $CO(NH_2)2$—15 (electrolyte IV). To oxidize the specimen surface, we previously [3] used some additional treatment, namely, heat hardening in a sodium nitrite solution with a concentration of 20–30 g/L. However, in this case, we introduced it into the electrolyte itself, and the specimen was hardened directly in the electrolyte. The voltage on the electrodes was 200 V, the current density was 2.5 A/cm², and the exposure time was 5 minutes.

The corrosion behavior was determined by the corrosion rate, as well as by the potentiodynamic polarization curves (4 mV/s) and by the values of the anode dissolution currents taken with the help of a potentiostat (PI-50-1.1) in a 0.05 M solution of Na_2SO_4. The steady potentials were measured in a standard cell with respect to the chloride silver electrode and then were converted to the normal hydrogen scale. The modified layer microhardness was estimated using a PMT-3 device with a load of 0.2H. The carbon content was determined with the help of a chemical test and X-ray microanalysis.

RESULTS AND DISCUSSION

The tests have shown (Tables 1 and 2) that the surface impregnation of steel in electrolyte II containing NH_2Cl, NH_2OH, and $N_2H_4 \cdot HCl$ and the additional

Table 2. Influence of the type of treatment and the duration of treatment in a 0.05 M Na_2SO_4 solution on the content of carbon in the surface layer, the surface microhardness, and the rate of corrosion of the samples

Electrolyte	Method of cooling	Microhardness H_μ, MPa	Content of C, weight %	Corrosion rate k, g/(m² day)		
				8 h	24 h	72 h
I	in electrolyte	5600	0.28	25.4	8.3	5.8
II	in electrolyte	5900	0.16	18.1	5.8	3.2
	in caustic soda 75 g/l	5990	–	10.3	4.1	2.4

Table 3. The values of the corrosion potential cor, the anode current density i_a, and the rate of corrosion k in testing (in 0.05 M Na_2SO_4) the samples of steel 45 subjected to different types of treatment: the numerator is electrolyte III, the denominator is suggested electrolyte IV

Sample	φ_{cor}, V	i_a, mA/cm² at $\varphi = +0.3$ V	Corrosion rate k, g/(m² day)		
			8 h	24 h	72 h
Steel without a coating and thermal treatment	−0.440	34.07	26.0	16.0	10.4
Steel without a coating, nitrided	−0.073/−0.026	8.02/5.1	17.1/14.2	8.3/7.2	4.3/2.7
Ironed steel, unnitrided	+0.100/+0.150	20.2	21.01	12.4	8.2
Ironed steel and nitrided	+0.255/+0.310	6.15/2.7	13.6/9.2	5.3/3.1	6.3/4.2

hardening in the caustic soda solution decreases the anode dissolution currents in comparison with the known electrolyte I containing 50 g/L of NH_4Cl with a potential of $\phi = -0.1$ V (with the caustic soda concentration of 75 g/L) by factors of 2.1 and 3.38 and at $\phi = 0.1$ V, by factors of 6.2 and 13.5–25.9 with the carbon content in the boundary layer being nearly halved
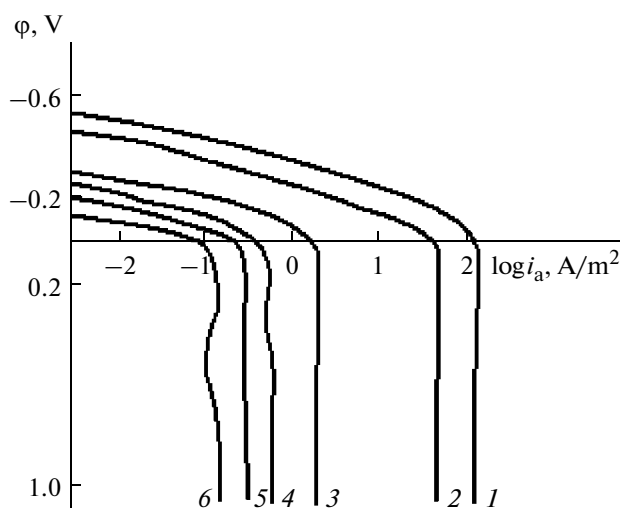
Polarization curves in a 0.05 M Na_2SO_4 solution for steel 45: untreated (*1*), ironed untreated (*2*), treated in electrolyte I (*3*) and in electrolyte II (*4*), subjected to an additional treatment in an NaOH solution with 100 g/L (*5*), and ironed and treated in electrolyte IV (*6*).

and the microhardness growing from 5600 up to 5900–5990 MPa. The latter testifies to the increase of the nitride layer. The corrosion rate reduces after 8 hours of tests by 1.4–2.5 times; after 24 hours, by 1.4–2 times; and after 72 hours, by 1.8–2.4 times. It is seen that the greatest reduction of the corrosion rate is observed in the case of the oxidation in the caustic soda solution with a higher concentration. However, there is no expected result when a concentration less than 50 g/L is used, and, with a concentration of more than 100 g/L, the corrosion resistance of the conversion coatings hardly grows, but it becomes more dangerous for maintenance workers.

The tests show (Table 3) that the electrolytic coatings have a larger corrosion resistance in comparison with steel due to the absence of electrochemically active iron carbide. In this case, the anode dissolution currents reduce from 34.07 down to 20.2 A/cm², the corrosion potential is ennobled by 340 mV, and the corrosion rate, for example, after 8 hours of tests, decreases from 26.0 to 21.01 g/m² day.

The treatment in the proposed electrolyte IV results in some ennoblement of the steel corrosion potential from −0.073 to −0.026 V as compared with electrolyte III, the reduction of the anode dissolution currents from 8.02 to 5.1 A/cm², and a decrease in the corrosion rate after 8 hours of tests from 17.1 to 14.2 g/m² day with the surface microhardness growth from 4120 to 5500 mPa indicating the generation of a larger amount of nitrides in the boundary layer as compared to known electrolyte III.

The surface impregnation of electrolytic iron coatings in the proposed electrolyte IV in comparison with electrolyte III ennobles the potential from +0.255 to +0.310 mV, reduces the anode dissolution currents by a factor of nearly 3 from 6.15 to 2.7 mA/cm^2, and decreases the corrosion rate after 24 hours of tests from 5.3 to 3.1 g/m^2 day. This occurs owing to the great amount of nitrides generated in the boundary layer of the specimen and the more continuous and dense oxide film formed on the specimen in the course of the hardening.

The examination of the potentiodynamic polarization curves shows that untreated steel 45 dissolves the most rapidly (curve *1*). The steel coated by electrolytic iron dissolves considerably slower (curve *2*). However, the surface impregnation even in the known electrolyte (electrolyte I) results in the decrease in the currents by nearly two orders of magnitude (curve *3*), and the treatment in the proposed electrolyte (electrolyte II) additionally decreases the currents by not less than 5 times (curve *4*). If, after the surface impregnation of the steel in electrolyte II, it is subjected to additional oxidation in the caustic soda solution with a concentration of 100 g/l, then the currents decrease even more (curve *5*). The minimum currents are attained on the steel after ironing and surface impregnation in proposed electrolyte IV (curve *6*).

CONCLUSIONS

Thus, new methods to improve the corrosion resistance of steels and electroplated coatings through surface impregnation in the course of anode electrolytic heating have been developed allowing one to increase it substantially for machine parts, tools, and industrial equipment and to increase their endurance.

REFERENCES

1. Revenko, V.G., Parshutin, V.V., Shkurpelo, A.I., et al., Corrosive and Electrochemical Behavior of Steel 40X after Different Variants of Nitriding, *Zashch. Met.*, 2003, vol. 39, no. 1, pp. 53−56.
2. Parshutin, V.V., Revenko, V.G., Pasinkovskii, E.A., et al., The Effect of Nitrogen Input Method on Electrochemical, Corrosive Behavior and Physico-Mechanical Properties of the Modified Surface of Steels, *Elektron. Obrab. Mater.*, 2004, vol. 40, no. 4, pp. 14−33.
3. Parshutin, V.V. and Pasinkovskii, E.A., Improvement of Corrosion Resistance of Steels by Surface Impregnation in Electrolytes, *Elektron. Obrab. Mater.*, 2007, vol. 43, no. 6, pp. 26−28.
4. Parshutin, V., Pasinkovskii, E., Agafii, V, Koval', A., Methods of Corrosion Resistance Increasing of Iron-Based Electroplates, *Corr. Anticor. Protec.*, 2009, no. 1, pp. 51−59.
5. Parshutin, V.V., Pasinkovskii, E.A., Paramonov, A.M., et al., The Effect of Surface Impregnation on Physico-Chemical Properties of Modified Surfaces of Steels, *Trudy GOSNITI,* 2010, vol. 105, pp. 180−185.
6. Parshutin, V.V., Corrosive and Electrochemical Behavior of Pseudoalloys on the Basis of Tungsten and their Components, *Surf. Eng. Appl. Electrochem.*, 2008, vol. 44, no. 6, pp. 446−461.
7. Frantsenyuk, I.V., Anagorskii, L.A., et al., USSR Inventor's Certificate no. 502 963.
8. Zemskii, S.V., Belkin, P.N., Pasinkovskii, E.A., et al., USSR Inventor's Certificate no. 968 761.
9. Petrov, Yu.N., Gur'yanov, G.V., Babanova, Zh.I., et al., *Elektroliticheskoe osazhdenie zheleza* (Electrolytic Deposition of Iron), Kishinev: Shtiintsa, 1990.
10. Sidel'nikova, S.P., Electrodeposition of Iron−Manganese Alloy from Fluorsilicate Electrolyte, *Elektron. Obrab. Mater.*, 1999, no. 3, pp. 10−16.
11. Revenko, V.G., Parshutin, V.V., Kozlova, T.V., et al., Production of Iron−Copper Electrolytic Alloys, *Elektron. Obrab. Mater.*, 1992, no. 4, pp. 18−22.

Annealing of Radiation-Induced Defects in Silicon

G. P. Gaidar

Institute for Nuclear Research, National Academy of Sciences of Ukraine, pr. Nauki 47, Kiev, 03680 Ukraine
e-mail: gaydar@kinr.kiev.ua
Received May 13, 2011

Abstract—Annealing of the main radiation defects in silicon (A-centers, E-centers, and divacancies, etc.) is theoretically described on the basis of the experimental data obtained by many authors. The parameters that characterize this process (the activation energies and frequency factors) have been ascertained, and various mechanisms and reactions that determine the conditions for the annealing of the defects were proposed.

INTRODUCTION

In order to restore the electrophysical properties of semiconductor materials and facilities on their basis that were irradiated with nuclear particles, annealing of the radiation-induced defects (RD) is commonly used. As a rule, annealing is defined as the irreversible thermal dissociation of defects. In a broader sense, annealing includes the following processes: the thermal dissociation of a defect, the motion of the defect as an integral unit towards drains, the separation of one of the components of a defect and the irreversible drift to a drain, and the joining of one component of a Frenkel pair with the existing defect.

The ultimate purpose of the research of the defect annealing is to establish the activation energy of the process of annealing and the frequency of the mobile defect hopping to the drain, as well as to reveal the possible reactions of the interaction between the mobile and stable defects at certain temperatures. The annihilation of defects can be sometimes determined if the pre-exponential multiplier (ν_0) in $\nu = \nu_0 \exp\left(-\dfrac{u_b}{kT}\right)$ is known, where u_b is the potential barrier that the diffusing particle overcomes, and ν is the average hopping frequency of a particle.

In silicon, the annealing of simple RDs is studied most extensively; these defects are formed during the interaction of vacancies and interstitial silicon atoms with the atoms of the background and alloying impurities that are present in crystals.

A vacancy–oxygen complex (A-center, VO) is found to be one of the major radiation-induced defects in Si; it introduces an acceptor level $E_c - 0.17$ eV into the forbidden zone [1, 2]. When an oxygen atom captures a vacancy, it shifts and locates almost at a vacant point without replacing the substituted position entirely. It is shifted from the center of a tetrahedral substitutional position in the $\langle 100 \rangle$ direction and it binds with two silicon atoms to form Si–O$_i$–Si. An A-center is commonly annealed at 600 K with activation energy of 1.3 eV [3]. During the annealing, it is supposed to migrate through the crystal as an integral unit and be captured by other defects to form more complicated centers of oxygen multivacancies of the $V_2O_2(Si-P2)$ or $V_3O(Si-P4)$ types. However, the electric activity of these defects has started to be extensively studied just recently due to the need of enhancing the radiation stability of nuclear radiation detectors. The energy levels of the oxygen vacancy complexes are assumed to be located near the center of the forbidden zone.

The authors of [4] proved that the intensity of the 835-cm^{-1} infrared absorption band diminishes during the annealing of A-centers with an activation energy of 1.3 eV in the temperature range of $(300-400)°$C. The infrared zones of 830 and 877 cm^{-1} are relevant to the absorption by the VO$_i$-centers, which are in neutral and negatively charged states, correspondingly. The effect of annealing on the intensity of these bands and the appearance of an 889 cm^{-1} band during the annealing of the 830 cm^{-1} band were studied. These bands were observed in silicon grown by the Czochralski technique (Cz) after electron irradiation with an energy of 2 MeV and a dose of 1×10^8 e$^-$/cm^{-2}. Isothermal annealing was studied in the temperature region of $300-350°$C. The intensity of the 889 cm^{-1} band increased with the activation energy $E_a = 1.86$ eV and the frequency factor $\nu = 6 \times 10^{11}$ s^{-1}.

The usual energy of 1.86 eV is considered as the energy of activation for the A-center migration to drains (atoms O$_i$). This migration process is probably the partial dissociation of an A-center and consists of three successive processes, i.e., the dissociation of an A-center into V and O$_i$ (where O$_i$ returns to the inter-

stitial position); the vacancy migration; and O_i hopping into a new position, which the vacancy will occupy. Such a representation makes it possible to determine the value of the barrier of the capture of the A-center by a drain, which is 0.36 eV [5].

According to [6], the decrease in the intensity of the band at 830 cm^{-1} with activation energy of 2.27 eV and the frequency factor $\nu = 1.6 \times 10^{15}$ s^{-1} is also attributed to the motion of an A-center with a capture of O_i. However, the decrease of the band's intensity in the temperature range of 600−670 K is nothing but the complete dissociation of an A-center, i.e., $VO_i \rightarrow V + O_i$.

An increase in the dose of γ-quants enhances the annealing temperature of the A-center from 250 to 375°C (at this temperature, the concentration of the defects decreases by 50%, and it is referred to as the annealing temperature).

Divacancies (V_2) are annealed by diffusion in a crystal as an integral unit with the activation energy of ~1.3 eV and a frequency factor of ~10^{13} s^{-1} [8]. Three stages in the annealing of the divacancy were observed in the temperature ranges of 100−200°C with $E_a = 1.0$ eV, 200−300°C with $E_a = 1.3$ eV, and 300−500°C with $E_a = 1.5$ eV [9]. This was attributed to the different positions of the divacancies in the cluster nucleus: in the region of a spatial charge (RSC), and in the conducting Si matrix. The authors of [10] assume that, since the divacancies are stationary at 150°C, their annealing can be ascribed to recombination with the mobile interstitial atoms.

Earlier, Watkins and Corbett showed that divacancies can diffuse for great distances without dissociation, since the binding energy between two vacancies is ≥1.6 eV [8]. The difference in the energies of formation of 1.75 eV of V_2^0 and $2V_1^0$ is in good agreement with the given value of the divacancy dissociation [11]. The high energy of the binding between the two vacancies in the divacancy made it possible for the authors of [12] using annealing at 200°C to transform the level of vacancies $E_V + 0.19$ eV into the donor level $E_V + 0.24$ eV owing to the divacancy's modification by interstitial oxygen with the formation of a V_2O complex in p-Si. A similar annealing at 220−300°C was performed in oxidized n-Si that was grown using the method of a crucibleless floating zone (FZ): ($n_0 = (3-5) \times 10^{12}$ cm^{-3}, $N_0 = (10^{16}-10^{17})$ cm^{-3}) [13]. After irradiation with 7 MeV protons and a 1-hour annealing at 300°C (after the positions of the peaks stabilized), the divacancy position in the forbidden zone of n-Si changed from $E_c - 0.43$ to $E_c - 0.47$ eV. The latter was assigned to the V_2O complex. It was determined in [13] that V_2O is annealed in the temperature region of 325−350°C, which is close to that of V_2O annealing in n- and p-Si at 300−350 °C [14].

Watkins and Corbett [8] observed that the divacancy annealing temperature shifted towards lower temperatures with an increase in the oxygen concentration. The temperature of the annealing of divacancies (220−270)°C is somewhat lower than that of annealing of A-centers. It depends on the relationship of the concentrations of C and O impurities in silicon, as well as on the conditions of irradiation and annealing. The presence of sodium in Cz−Si⟨Na⟩ shifts the stage of A-center annealing in the region of (150−225)°C [15]. Germanium in silicon has no effect on the formation and on the annealing of A-center [16]. The presence of Ge in silicon increases the concentration of interstitial defects. Annealing of the latter results from heating Si⟨Ge⟩ specimens to 200°C. Annealing of regular silicon irradiated with fast neutrons at this temperature exhibits an increase in the concentration of divacancies, which is well-known from the literature. This increase is caused by the annealing of the defects (V_3 and V_4) of a cluster. The annealing of Si⟨Ge⟩ after neutron irradiation, on the contrary, leads to an abrupt decrease in the concentration of the divacancies and can be conditioned by the increase of the probability of the reaction of V_2 and I, which is the reason for the decrease in the concentration of V_2.

A donor-vacancy complex (E-center) is found to be annealed in the temperature range of (80−250)°C depending on the charge state, the kind of annealing dopant (P, As, or Sb), and the tetrahedral covalent radius of the dopant atom. The activation energy of annealing in neutral E-centers $E_a = (0.94 - 1.46)$ eV depends linearly on the covalent radius (r), $E_a = (15r - 0.7)$ eV [17]. A change of the neutral charge state for a single negative state increases the activation energy of the annealing by ~0.3 eV [18]. In n-Si doped with phosphor, depending on the charge state of a defect, the value of the energy of annealing is 0.94 eV provided that the E-center is in a neutral charge state, and it is 1.25 eV if the charge state is negative. The mechanism of annealing of E-centers in silicon have not been determined precisely yet, but both migration and dissociation of them are found to be possible [19].

A boron-vacancy complex (B-V) is unstable at room temperature according to the EPR data [20]. The electric measurements show that the level of $E_V + 0.45$ eV is annealed at a temperature of (360−500) K; however, its activation energy is low; i.e., $E_a = (0.42 \pm 0.05)$ eV [21]. Taking into account the value of the pre-exponential frequency multiplier $\nu_0 = (10^3 - 10^4)$ s^{-1} [17], the long-path migration of these RDs prior to capture by drains can be considered to be the most probable phenomenon in the annealing.

Unlike the V-group dopants of Mendeleev's table, those of the III and IV groups can interact not only with the primary vacancies but also with interstitial the Si atoms that are generated by the radiation. The interaction of the interstitial Si atoms with such dopants is reduced to the formation of a bound spatial configuration followed by further displacement of impurities

Table 1. Parameters of annealing of radiation-induced defects in silicon

Radiation-induced defects	Activation energy, eV	Temperature range of annealing, K	Hopping frequency, c^{-1}	Energy position, eV	References
V^0	0.33 ± 0.03	150–180	10^{11}		[22]
$V^=$	0.18 ± 0.02	60–80	10^8		[23]
$V^= \rightarrow V^{\cdot}$	0.27	90–120	1.2×10^9	$E_c - 0.09$	[24]
$H\,(0.13)^+$	0.32 ± 0.02	150–220	1.6×10^6	$E_v + 0.13$	[25]
$H\,(0.13)^0$	0.45 ± 0.04	200–250		$E_v + 0.13$	[25]
I^-	0.4	140–180			[26]
I^0	1.5	540–600		$E_c - 0.4$	[27]
I^+	0.85	370–420			[27]
I_2^+ (Si-P6)	0.6 ± 0.2	400–420	$\approx 10^8$		[28]
I_2^+ (Si-B3)		700–750			[29]
$V_2^{+(-)}$	1.3	473–573	10^{13}	$u_b = 0.056$ eV*	[8]
C_i	0.71	300;(300–350)	4×10^8	$E_c - 0.12;$ $(E_v + 0.28)$	[30]; [24]; [31]
B_i	0.60	250–300			[32]
VO_i	1.3	600;(523–623)	10^8	$E_c - 0.17$	[1]; [2]
VB		250–280			[20]
VGe		200–240			
V_2O		573–623			[14]
V_2I	0.7 ± 0.1	225–250	10^{12}		[33]
V_2		440–500		$E_c - 0.39$	
V_2O_2		623–683			[14]
C_iC_s	1.08 ± 0.03	453–513			[34]; [35]
$C_iP_s^{-/0/+}$	$1.1 \pm 0.1;$ $u_b = 0.3$ eV**	310–350	9.1×10^{12}	$E_v + 0.48;$ $E_c - 0.38$	[36]
C_iO_i		623–723		$E_v + 0.48 \pm 0.01$	[37]
PV^-	0.94	130–170		$E_c - 0.47$	[17]
P^+V^{2-}	1.25				[18]

Notes: * —the barrier of reorientation C_{2n} of the symmetry in D_{3d} for $V_2^{+(-)}$;

** —the barrier which equals the binding energies of C_i and P_s.

(with sizes less than a tetrahedral silicon radius) from the nodes into the interstitial positions. Depending on the impurity's type, the introduced atoms are annealed in the temperature range of 250–450 K. The annealing of the introduced impurity atoms is accompanied by the formation of complexes (C_iC_s, C_iC_i, and C_iP_s, etc.) that are more stable thermally. The annealing parameters of these and other RDs in accordance with [1, 2, 8, 14, 17, 18, 20, 22–37] are listed in Table 1.

A great number of scientific works that we have analyzed showed that the RD annealing in silicon has been studied just partially up to now. Moreover, the temperature of the RD annealing is determined, though the annealing process itself is almost not described, and when it is, only two mechanisms are primarily considered, i.e., the migration towards drains or the dissociation of the defect. In addition, most of the works that study annealing are entirely experimental. Only [38] offers a theory of annealing of complex defects, which are conventionally subdivided into small and large ones. In this context, the main purposes of this work are (1) to perform the theoretic description of the annealing of simple RDs in silicon based on the experimental data obtained by different

authors, (2) to determine the relevant parameters of the annealing (the activation energy and frequency factor), (3) to propose reactions (if possible) that might explain the mechanisms of the annealing, and (4) to consolidate the obtained information after having analyzed the great data array on RDs annealing that is currently available from the printed materials.

RESULTS AND DISCUSSION

When the concentration of defects in solids exceeds the equilibrium level, these defects are found to interact under certain conditions not only with each other but with the background impurities too, thus decreasing the free energy of a crystal. The modification that the solid substance's properties undergo owing to the presence of radiation-induced defects depends on the time during which the interaction reaction occurs between the defects [39]. For example, in p-Si, it takes $\sim 10^{-2}$ s for silicon vacancies and interstitial oxygen to interact to form stable A-centers at 300 K. In n-Si, this process is much faster due to the lower activation energy of a negatively charged vacancy, and it ends in $\sim 10^{-7}$ s.

The easiest way to describe the annealing of the defects is to use equations similar to those that are used in chemical kinetics. The accumulation or disappearance of the P concentration of the defects due to annealing of the first order can be determined through the rate constants K:

$$\frac{dP^i}{dt} + K_i(P^i - P_m^i) = 0, \quad \frac{dP^j}{dt} = -K_j P^j. \quad (1)$$

Usually, the rate constant $K_{i,j} = A^{i,j} \exp(-E_a^{i,j}/kT)$, where $A^{i,j}$ are the frequency factors; $E_a^{i,j}$ is the activation energy of the process; k is the Boltzmann constant; T is the absolute temperature; and i, j denote the number of accumulation and annealing channels of the defects, respectively. The vacancy-type defects are annealed during annihilation together with the mobile interstitial defects, whose migration energy depends on their charge state [23]. It is noteworthy that using kinetics of the first order is justified in the case when the concentration of drains is at least an order higher than that of the radiation-induced defects [1]. Having integrated Eq. (1) and summed up various channels of annealing or accumulation of defects, we obtain

$$P(T) = \sum_{j=1}^{k} P_0^j \exp\left[-A^j t \exp(-E_a^j/kT)\right]$$

$$+ \sum_{i=1}^{m} P_m^i \exp\left[1 - \exp(-A^j t \exp(-E_a^i/kT))\right] - \sum_{l=1}^{n} P_{00}^l. \quad (2)$$

The last term P_{00}^j indicates that the annealing has not finished. Here, j denotes different channels of annealing the defects (e.g., owing to annihilation together with an interstitial atom (di-interstitial sites), capturing to a drain, dissociation of the defect, and changing of the energy and frequency factor of annealing the defect under the condition of its reorientation); P_0^j is the share of annealing of the concentration of the defects in the j-method; P_m^i is the share of accumulation of the concentration of the defects in the i-method, e.g., due to dissociation of another defect by low temperature annealing; and t is the time of the annealing. The formation of a more stable defect is possible, for example, owing to annealing of another defect. Interstitial silicon atoms that are mobile at room temperature can anneal not only A-centers but also divacancies.

According to [2], a series of annealing processes of radiation-induced simple defects (E-centers, A-centers, and divacancies, as well as the centers that include carbon) that were described based on the experimental data of different authors [6, 14, 15, 19, 40–48], along with the obtained results (the calculated activation energies and frequency factors and the proposed annealing reactions), are listed in Table 2.

The energy of the reorientation of the **E-center** [22] coincides with the activation energy of the annealing (0.94 eV). The binding energy of the P–V complex exceeds it by (0.2–0.3) eV. Therefore, during the annealing, an E-center can migrate towards drains as an integral unit. This is also testified to by the frequency factor of the annealing (Table 2). However, annealing with an activation energy of 0.91 eV was observed in [40]. This points to the fact that E-centers can be annealed owing to annihilation with an interstitial silicon atom [49], and their concentration can grow due to the capture of a vacancy by a phosphor atom during the dissociation of Frenkel pairs [19] in the temperature region of (20–70)°C. The analysis of [19] showed that the $C_s C_s$ defect is formed during the annealing of the $C_i C_s$ defects at annihilation with a vacancy. The $C_s C_s$ defect has a level of $E_c - 0.2$ eV in the forbidden band of silicon. In [47], the growth of a $C_i C_s$ defect and its annealing along the band of 7819.7 cm^{-1} were registered. The analysis showed that the growth of the $C_i C_s$ defect was caused by C_i ($E_m = 0.77$ eV) migration, while its annealing resulted from the dissociation of $C_i C_s$ ($E_a = 1.7$ eV). There was not even the slightest hint that $C_i C_s$ annealing might occur due to a vacancy capture by a $C_i C_s$ defect. Therefore, annealing curve *3* (Fig. 1, [19]) cannot confirm that the annealing occurred according to the reaction $C_i C_s + V \rightarrow C_s C_s$, since, in $C_i C_s$, even C_i is partially located in a node. Therefore, E-centers are not annealed due to dissociation into P and V but rather by moving towards drains, where oxygen atoms O_i are found to be. Here, annealing curve *3* (Fig. 1, [19]) can also be reliably described using the migration of inter-
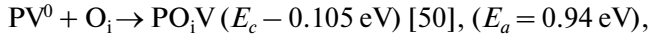
Table 2. Annealing of the radiation defects in silicon. The calculation of the activation energy and frequency factor is performed in the scope of the theory of reactions based on the available experimental data

Defects (levels)	T, K (annealing)	Activation energy E_a, eV	Frequency factor ν, s^{-1}	Annealing reactions	Notes	References
PV (E_c–0.47)	350–390	0.94	1.5×10^8– 1.8×10^9	$PV^0 + I^- \to P_s$	PV^0	[40], [19], [15]
	390–430	1.25	1.3×10^9	$PV^- + I^- \to P_s$	PV^-	[19]
	290–350	0.8 ($D_0 = 0.04$)	1×10^9 ($r = 4 \times 10^{-6}$)	$P^+ + V^- \to PV$	V^-	[19]
	333	0.91	1.34×10^{10}	$P^+V^- + I^- \to P^+$	I^-	[40]
VO$_i$ (12 μm)	300–350	0.74	$(0.7–1.5) \times 10^7$	$VO_i + I_2 \to O_i + I$ ($N_{VOi} = 3 \times 10^{17}$ cm^{-3})	I_2^0	[15], [41]
	400–450	0.91	$(1–3) \times 10^7$	$VO_i + I \to O_i$	I^-	[41]
	450–510	1.3	$(0.5–1) \times 10^{10}$	$\overleftarrow{VO}_i + I \to O_i$	+0.4 eV	[41]
	510–570	1.1	$(2–7) \times 10^8$	$\overleftarrow{VO}_i + I_2 \to O_i + I$	+0.4 eV	[41]
	570–630	1.86 ($D_0 = 416$)	5×10^{11}– 5×10^{14} ($r = 1.5 \times 10^7$)	$VO_i + O_i \to VO_{2i}$ ($N_{Oi} = 7 \times 10^{17}$ cm^{-3})	O_i drain	[15], [41]
VO$_i$ (E_c–0.17)	600–670	2.27	$(0.3–3) \times 10^{15}$	$VO_i \to V + O_i$	dissociation	[15], [6]
	500–550	1.7	1×10^{12}	$VO_i + O_{2i} \to VO_{3i}$	O_{2i}– diffusion	[41]
	300–360	0.8 ($D_0 = 1.5 \times 10^{-3}$)	7×10^8 ($r = 1.5 \times 10^{-7}$)	$O_i + V \to VO_i$	V^-	[15]
VO$_i$I (E_c–0.204)	320–400	0.74	7×10^6	$VO_iI + I_2 \to I + O_iI$	I_2^0	[42]
	420–500	0.91	1×10^7	$VO_iI + I \to O_iI$	I^-	[42]
	500–540	1.86 ($D_0 = 312$)	6×10^{14} ($r = 2 \times 10^{-7}$)	$VO_iI + O_i \to O_{2i}$	O_i drain	[42]
	540–610	2.27	4×10^{15}	$VO_iI \to O_i$	dissociation	[42]
	360–430	1.3	10^{13}	$\overleftarrow{VO}_i + I \to VO_iI$	+0.4 eV	[43]
V$_2$ (E_c–0.261) (E_c–0.43)	280–360	0.4	$(2–3.5) \times 10^2$	$V_2^0 + I^= \to Si + V^-$	$I^=$ (E_c–0.37)	[42], [44]
	360–470	0.74	$(1–3) \times 10^5$	$V_2^0 + I_2^0 \to 2Si$	I_2^0 (E_c–0,315)	[42], [44]
$V_2^{-/0}$	470–520	1.1	9×10^7		V_2^0 migration into a cluster	[42]
$V_2^{=/-}$	470–520	1.3	4.5×10^9		V_2^- migration into a cluster	[42]
V$_2$ (E_c–0.42)	600–630	2.5	2.5×10^{17}	$V_2O \to V_2 + O_i$		[44]

Table 2. (Contd.)

Defects (levels)	T, K (annealing)	Activation energy E_a, eV	Frequency factor ν, s^{-1}	Annealing reactions	Notes	References
V_2C	433	0.4	1×10^3	$V_2C^0 + I^= \rightarrow C_s$		[45]
	433	0.74	1.5×10^6	$V_2C^0 + I_2^0 \rightarrow C_i$		[45]
	350–370	1.1	2×10^{12}	$V_2C \rightarrow V_2 + C_i$	V_2C^0	[15]
	450–520	1.3	2×10^{12}	"	migration	[15]
	450–520	1.5	2×10^{12}	"	V_2C^-	[15], [45]
V_2CO (E_V+0.28)	280–340	0.6	5.5×10^6	$V_2CO + I_2^0 \rightarrow VO_i + C_i$	$E_v + 0.35$ (VO_i)	[46]
	340–370	1.1	3.7×10^{12}	$V_2^+CO \rightarrow V_2O + C_i$	at drains	[46]
growth V_2C^+	370–450	0.91	1×10^8	$I + C_s \rightarrow C_iC_i + V_2 \rightarrow V_2C$		[15]
(E_V+0.20)	280–310	0.6	2×10^7	$V_2C + I_2^+ \rightarrow C_i$		[46]
	340–380	1.1	3×10^{12}	$V_2C \rightarrow V_2 + C_i$	at drains	[46]
C_iC_s 7819.7 cm^{-1} (E_c−0.15) 7819.7cm^{-1} 865.7 cm^{-1} 7819.7 cm^{-1}	320–370	0.87	2×10^9	$C_i + C_s \rightarrow C_iC_s$	Si (Sn)	[47]
	370–420	0.77	$(3–8) \times 10^7$	$C_i + C_s \rightarrow C_iC_s$	Si, Si (Na)	[15], [46]
	450–500	1.7	1.5×10^{14}	$C_iC_s + V_2 \rightarrow C_sC_s + V$	dissociation	[47]
	330–370	0.87 ($D_0 = 2.1 \times 10^{-3}$)	1.5×10^9 ($r = 2.1 \times 10^{-3}$)	$C_i + O_i \rightarrow C_iO_i$	diffusion	[47]
	320–370	0.87 ($D_0 = 2.47 \times 10^{-3}$)	2×10^9 ($r = 2.3 \times 10^{-7}$)	$C_i + C_s \rightarrow C_iC_s$	diffusion	[47]
$C_iC_s^+$ (E_V+0.09)	290–380	0.77	4.8×10^7	$C_i + C_s \rightarrow C_iC_s^+$ ($E_V + 0.09$)		[46]
C_iO_i 865.7 cm^{-1}	475–515	2.53	$D_0 = 0.13$; $r = 1.3 \times 10^6$ $U_b = 1.27$ eV	$C_sO_i \rightarrow C_iO_iV$	change of configuration	[47]
I_{Si} (E_c−0.36)	333	0.91	4×10^{11}	I^- in interstitial sites	drains	[40]
	333	1.0	9×10^{11}	I^- dumbbell	drains	[40]
I_{Si} (E_c−0.37)		0.4	6.5×10^2	$I^=$	drains	[42]
I_2^+ (EPR) Si-B3	480–550	1.5	2.5×10^{11}	$I^0 + I^0 \rightarrow I_2^+$	I^0 (E_V+0.42)	[48]
	550–630	1.5	2.0×10^{10}	$I_2^+ + I^0 \rightarrow I_3$	I_2^+ (E_V+0.45)	[48]
	630–680	1.86	3×10^{11}	$I_2^+ + VO_i^0 \rightarrow O_i + I$	A-center migration	[48]
	680–770	2.27	3×10^{12}	$I_2^+ \rightarrow I^0 + I^0$	dissociation	[48]
V_2O (EPR)	400–490	0.8	3×10^5	$VO_i + V \rightarrow V_2O$	p-, n-Si	[14]
	500–570	1.3 ($D_0 = 4.2 \times 10^{-4}$ cm^2/s)	1×10^9 ($r = 1.6 \times 10^{-7}$ cm)	$V_2 + O_i \rightarrow V_2O$	n-Si	[14]
	570–620	2.5 ($D_0 = 0.13$ cm^2/s)	3×10^{17} ($r = 0.3$ cm)	$V_2O \rightarrow V_2 + O_i$; ($U_b = 0.74$ eV)	p-, n-Si	[14]

stitial silicon atoms I ($E_m = 0.91$ eV) and di-interstitial sites I_2 ($E_m = 0.74$ eV) [49]. The annealing of E-centers can thus be described by the reaction

$PV^0 + O_i \rightarrow PO_iV$ ($E_c - 0.105$ eV) [50], ($E_a = 0.94$ eV),

and the appearance of the level of ($E_c - 0.204$ eV) as

$O_iV + I \rightarrow O_iVI$ ($E_c - 0.204$ eV) [42], ($E_a = 0.91$ eV),

$PO_iV + I_2 \rightarrow P_i + O_iVI$ ($E_c - 0.204$ eV), ($E_a = 0.74$ eV).
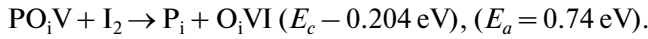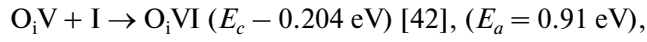
The authors of [42] assume that the level ($E_c - 0.204$ eV) is the acceptor level of an A-center; however, most likely, it is an A-center modified by an interstitial silicon atom. Presently, two models are proposed for an A-center. The first model, which was generally accepted from the beginning of the development of radiation physics, describes an A-center as an acceptor-type defect with a level close to $E_c - 0.17$ eV in silicon. Another model was proposed in [51] based on the results of magnetospectroscopic analyses where an A-center is an amphoteric defect with the acceptor and donor levels being close to $E_c - 0.17$ and $E_c - 0.76$ eV, respectively. Relying on the DLTS measurements, the authors of [52] connected the donor level $E_V + 0.38$ eV with a C−VO complex. According to the model of the modification of the donor and acceptor levels of radiation-induced defects by the background impurities of C_i and O_i types, it was shown in [53] that the interstitial carbon increases the energy of the acceptor levels in the forbidden silicon zone and decreases the energy of the donor levels by 0.035 eV. Therefore, the donor level of an A-center of silicon is assumed to be (0/+) $E_V + 0.415$ eV.

Suppose that the annealing of E-centers is limited by their diffusion onto A-centers [4], interstitial oxygen, or other drains. Then, according to the theory of reactions that are limited by diffusion [54], the rate constant can be written as

$$K_{E - O_i} = 4\pi r_{E - O_i} D, \qquad (3)$$

where $r_{E - O_i}$ is the radius of the interaction between the O_i and E-centers, and D is the diffusion coefficient of a defect to the drains. Let the drains in the specimen with volume $V \cong 1$ occupy the atomic volume with radius R. Then,

$$R = \left(\frac{3}{4\pi N_{O_i}}\right)^{1/2}, \qquad (4)$$

where N_{O_i} is the concentration of drains per a unit of the specimen's bulk.

The average distance between the O_i atoms is $d = \sqrt{2}R$, and the average distance that E-centers are supposed to cover to attain the drains (O_i) is $L = d/\sqrt{2}$. Hence, the average distance of the diffusion of an E-center to a drain equals the radius of the atomic volume drain. Then, in the case of the Markov process $L = \sqrt{Dt}$,

$$D = \frac{1}{t}\left(\frac{3}{4\pi N_{O_i}}\right)^{2/3}, \qquad (5)$$

where t is the time of the annealing. Regardless of the statistically uniform introduction of vacancies under the electron irradiation of silicon, the distribution of E-centers is determined by the distribution of phosphor atoms.

Then, the time constant of the annealing (τ) equals

$$\tau^{-1} = 4\pi D_0 r_{E - O_i} \exp\left(-\frac{E_m}{kT}\right), \qquad (6)$$

where D_0 is the frequency multiplier, and E_m is the energy of the migration of the defect to the drains.

The condition of the linear character of the change of the value of $N_{O_i}/N_{E - O_i}$ on a semilogarithmic scale shows that the annealing of E-centers depending on the temperature or time of the annealing can be represented as the following equation:

$$N_E = N_E^0 \exp\left(-t4\pi r_{E - O_i} D_0 N_{O_i} \exp\left(-\frac{E_m}{kT}\right)\right). \qquad (7)$$

A consistent theory of diffusion-controlled reactions in solids was elaborated by Waite [55]. As a variant, he considered the case when a quasi-chemical interaction occurs between atoms with different coefficients of diffusion in a solid. In our case, only one of the components of the interacting pairs is mobile.

If the hopping frequency (ν) of the mobile defect is known, the frequency multiplier D_0 can be estimated using the formula $D_0 = (2a^2\nu)/3\pi$. Here, $a = 5.43$ Å is the silicon lattice constant. If the mobile defect hopping frequencies cannot be determined but the concentration of drains is known, the frequency multiplier (D_0) can be found using (5), since $D = D_0\exp(-E_a/kT)$ both in the case of isochronous annealing at temperature of half the defect annealing and in the case of isothermal annealing at the moment of 50% annealing of defects. The annealing activation energy was taken equal to the activation energy of the mobile defect diffusion. In so doing, the defect was assumed to cover the average distance R provided that the rate of its disappearing is maximal.

In the framework of the aforementioned developed conceptions, taking into account (2) and using the experimental data obtained by the authors of [14, 15, 19, 40, 41, 47], we estimated the capture radius (R) of the mobile radiation-induced defects onto such drains as the interstitial oxygen and on-site carbon at an appropriate temperature. The results of the calculations are in Table 3.

The radii of the capture of the radiation-induced defects (vacancies, divacancies, and A-centers, etc.)

Table 3. Annealing of intrinsic radiation-induced defects in silicon limited by diffusion

Reactions	Concentration of capture centers, cm^{-3}	D_0, cm/s	E_a, eV	$R \times 10^8$, cm	T_{anneal}, K	References
$V_2 + O_i \rightarrow V_2O$	10^{18}; O_i	4.19×10^{-4}	1.3	16	500–570	[14]
$V + O_i \rightarrow VO$	8×10^{17}; O_i	1.5×10^{-3}	0.8	15	300–350	[15]
$VO + O_i \rightarrow VO_{2i}$	8×10^{17}; O_i	4.16×10^2	1.86	15	500–550	[15]
$C_i + O_i \rightarrow CO$	6×10^{17}; O_i	1.17×10^{-3}	0.87	17	320–380	[47]
$C_i + C_s \rightarrow C_iC_s$,	2.9×10^{17}; C_s	2.53×10^{-3}	0.87	23	320–380	[47]
$V^- + P^+ \rightarrow PV$	5×10^{14}; P	8.6×10^{-2}	0.8	180	300–350	[19]
$PV^0 + O_i \rightarrow PVO$	9×10^{17}; O_i	3.82×10^{-1}	0.94	15	333	[40]
$PV^0 + O_i \rightarrow PVO$	7×10^{17}; O_i	1.06×10^{-4}	0.94	16	350–450	[15]
$I + VO \rightarrow O_i$	2.81×10^{17}; VO	3.9×10^{-5}	0.91	22	400–450	[41]
$I_2 + VO \rightarrow O_i + I$	3.5×10^{17}; VO	1.67×10^{-4}	0.74	20.3	290–360	[41]
$O_{2i} + VO_i \rightarrow VO_{3i}$	2.24×10^{17}; VO	1.5	1.7	23.7	530–570	[41]
$I + \overleftarrow{VO} \rightarrow O_i$	2.57×10^{17}; VO	6.93×10^{-3}	1.3	22.5	470–530	[41]

by an interstitial oxygen and an on-site carbon fall within the limits of 3 to 4 lattice constants of silicon. The radius of capture of interstitial carbon (C_i) by the on-site carbon (23 Å) exceeds that of oxygen (17 Å). The radii of the vacancy capture by interstitial oxygen ($R = 15$ Å) and by a phosphor atom ($R = 180$ Å) were also found. Table 3 lists the calculated values for the activation energy of annealing V_2, VO, C_i, PV, I, I_2, which agree well with similar experimental values obtained by other authors.

The authors of [19] observed annealing of E-centers in n-Si that was grown using zone melting in vacuum. The oxygen concentration in the specimens according to the optical measurements was <10^{15} cm^{-3}. Therefore, the main mechanism of E-centers' annealing in such specimens is assumed to be annihiltion with interstitial silicon atoms according to the reaction $(P^+V^-)^0 + I^- \rightarrow P^+ (E_a^{\Gamma} = 0.85$ eV), and the barrier for the annihilation is 0.09 eV. The barrier grows to 0.4 eV provided that the E-center is in the negative charge state.

The coefficient of diffusion of an E-center onto drains (O_i atoms) can be estimated using (5) provided that the oxygen concentration is high. The energy of reorientation of an E-center (PV), which equals the activation energy of the annealing, allows the pre-exponential factor of the diffusion coefficient of an E-center to be estimated. The radius of the capture of an E-center by interstitial oxygen in n-Si was evaluated using (7). The annealing parameters are presented in Table 3. The average temperature values of the annealing (for 50% annealing) during isochronous annealing and the time of the annealing (50% anneal-

ing) during isothermal annealing were used. The activation energy of the annealing was supposed to equal the activation energy of the diffusion of the mobile defect.

In the annealing of **A-centers**, both interstitial atoms and di-interstitial sites of silicon participate. An A-center has six possible orientations in a silicon lattice. The results of the linear compression show that the energy of the atomic reorientation of an A-center is 0.38 eV [4], and this reorientation can occur at room temperature. Therefore, if the atomic reorientation of an A-center occurs during annihilation with interstitial silicon atoms, the energy of annealing of an A-center will be 1.1 or 1.3 eV depending on whether the A-center interacts with an interstitial site or an interstitial silicon atom, correspondingly. However, an A-center needs high energy (1.86 eV) to migrate through the crystal [6]. The calculations using (7) and the data of [15] showed (Table 3) that the radius of the capture of an A-center by an interstitial oxygen atom is 15 Å. Table 3 shows that the radius of a vacancy capture by interstitial oxygen is also 15 Å during the formation of an A-center. It seems that, with an A-center ($E_c - 0.204$ eV) being modified by an interstitial silicon atom (the same as for a nonorientable divacancy), it fails to be atomically reoriented.
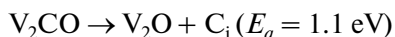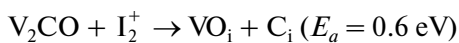
Therefore, though the modified A-center can be annealed during annihilation with interstitial silicon atoms, the stages of annealing with 1.1 and 1.3 eV are not observed (Table 2). The modified A-center migrates with an activation energy of 1.86 eV and dissociates with an energy of 2.27 eV, the same as for a regular A-center. The authors of [6] claim that the

motion of O_i monitors the annealing mechanism of VO_i centers.

Data on the annealing of **divacancies** ($E_c - 0.261$ eV) and ($E_c - 0.43$ eV) based on the data obtained in [42] on annealing of n-Si ($n_0 = (2-4) \times 10^{14}$ cm^{-3}) that was irradiated with α-particles of ^{241}Am with energy of 5.48 MeV are presented in Table 2. Although the annealing of $V_2^{=}$ and V_2^{-} in the region of $(470-520)$ K was detected in the same n-Si specimen, the activation energies of their annealing are different. The annealing of divacancies depends not only on their charge state but rather on the presence of a distortion in the zones of the energy in clusters.
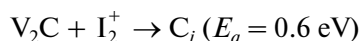
It is natural to assume that, at 500 K, the divacancies are mobile, and their coefficient of diffusion depends on the charge state of the divacancy. In the absence of electric fields generated by clusters, the migration energies of divacancies towards drains are V_2^{-} ($E_a = 1.1$ eV) and V_2^{0} ($E_a = 1.5$ eV). Provided that a divacancy changes its charge state during the migration to drains, the energy of migration is $E_a = 1.3$ eV. The vacancies that are modified by carbon (V_2C) behave similarly. Divacancies may annihilate both with interstitial atoms and di-interstitials of silicon with activation energies of 0.4 and 0.74 eV, respectively. The charge state of the interstitial atom is assumed to be then double negative ($E_c - 0.37$ eV) (Table 1, [53]). Table 1 [53] also shows that a CO-modified divacancy has a donor level of $E_v + 0.28$ eV, the same as interstitial carbon (C_i) in p-silicon. Therefore, the kinetics of the accumulation of a bistable defect C_iC_s (Table 2) are precisely described by the energy of migration of C_i in p-Si ($p_0 = 2.4 \times 10^{15}$ cm^{-3}): $E_a = 0.77$ eV, $\nu = 4.8 \times 10^{7}$ s^{-1} [46]. The annealing of defects with levels $E_v + 0.28$ eV and $E_v + 0.20$ eV showed that they are annealed with activation energies of $E_a = 0.6$ and $E_a = 1.1$ eV. A 70% annealing of the defect $E_v + 0.28$ eV yields precisely the defect C_iC_s ($E_v + 0.09$ eV). The di-interstitial silicon atoms I_2^{+} are found to migrate in the lattice of p-Si with energy of $E_m = (0.6 \pm 0.2)$ eV, and energy of 1.1 eV is typical for the migration of divacancies [28]. Hence, the following pattern of reactions during annealing of the levels of defects (Table 2) can be offered:

$$E_v + 0.28 \text{ eV}$$

$$V_2CO + I_2^{+} \rightarrow VO_i + C_i \ (E_a = 0.6 \text{ eV})$$

$$V_2CO \rightarrow V_2O + C_i \ (E_a = 1.1 \text{ eV})$$

and

$$E_v + 0.20 \text{ eV}$$

$$V_2C + I_2^{+} \rightarrow C_i \ (E_a = 0.6 \text{ eV})$$

$$V_2C \rightarrow V_2 + C_i \ (E_a = 1.1 \text{ eV}).$$

It is possible that the divacancies V_2CO and V_2C do not dissociate during their migration towards drains, as was suggested above.

The energy of migration of interstitial carbon (C_i) in the presence of a deformation in silicon that is created by tin atoms increases to $E_m = 0.87$ eV [47]. The C_iC_s annealing, as well as its dissociation, is doubtful. The reason for the doubts is that the second stage of accumulation of C_iO_i cannot be described as C_i joining O_i. The energy of annealing is much higher than the energy of migration of carbon C_i, which would join O_i. Generally, C_iC_s is annealed in the region of $(450-500)$ K, i.e., in the temperature region of migration of divacancies to drains. Moreover, C_iC_s is in the neutral charge state, when the carbon atoms occupy the node positions, and the silicon atom is bound between them. Hence, the divacancy annihilates with the silicon atom according to the following reaction: $C_iC_s^{0} + V_2 \rightarrow C_sC_s + V$. Since the barrier for the annihilation I with V_2 is 0.4 eV [56], and the energy of migration of the divacancy is ~1.3 eV, the activation energy of annealing the $C_iC_s^{0}$ of a bistable defect will equal $E_a = 1.7$ eV, which was precisely observed when describing the annealing of a $C_iC_s^{0}$ defect [47]. Therefore, to describe the second stage of increasing the concentration of the C_iO_i defects, we shall assume that the O_i atom will extrude C_s to the node position according to the reaction of $C_sO_i \rightarrow C_iO_i + V$. Since in this situation the oxygen atom (O_i) must not migrate through the lattice (the C_sO_i concentration in silicon is fairly high), the O_i atom must overcome the barrier $E_a/2$ for this reaction to occur. Then, in the scope of the theory of the reactions limited by diffusion, using (7), the effective radius of the capture R_{ef} can be determined if the barrier for the reaction is absent. However, as the barrier exists and the radius of the capture of the C_i atom by the free oxygen (O_i) according to Table 3 is 17 Å, it can be determined as ([56], p. 234)

$$R_{ef} = R_0 \exp\left(-\frac{U_b}{kT}\right), \tag{8}$$

where U_b is the barrier of the interaction between C_s and O_i, and R_0 is the radius of the capture of C_i by an O_i atom if the barrier is absent.

Annealing of silicon at $(200-250)°C$ decreases the free oxygen (O_i); however, annealing of the vacancy-type defects by the capture of interstitial defects occurs usually up to 200°C, and, in the region of $(200-250)°C$, the divacancies move to drains. In addition, if C_i appeared during the dissociation of C_iC_s, the growth of C_iO_i would occur with energy of 0.77 eV (annealing of C_i), rather than with ≥2.5 eV.

Annealing in the temperature region of $(250-350)$ K of level ($E_c - 0.37$ eV) [42], which according to (Table 1,

[53]) is related to an interstitial silicon atom $I^{=/-}$, really occurs with activation energy of $E_a = 0.4$ eV. Isothermal annealing at 333 K [40] showed that the interstitial silicon atom in a negative charge state can be in two configurations (dumbbell and interstitial site); thus, its activation energy of annealing can be different (1.0 and 0.91 eV, correspondingly, Table 2).

The energy of migration of I_2^0 in a zero charge state was $E_m = 0.42$ eV [57], and, in an I_2^+-positive charge state, it was $E_m = (0.6 \pm 0.2)$ eV [28]. However, there is a more thermally stable configuration of I_2^+ (Si-B3). The analysis of the annealing and the increase of the concentration of Si-B3 [48] showed that the energy of the formation and annealing of I_2^+ occurs with activation energy of $E_a = 1.5$ eV, which is known to belong to the energy of migration of I^0. Therefore, the energy of migration of Si-B3 is assumed to be >1.5 eV. Its two other energies of annealing ($E_m = 1.86$ and 2.27 eV) have been detected also for annealing of A-centers. Therefore, it would appear reasonable that it is not an A-center that moves to drains but rather the energy of migration of I_2^+ (Si-B3) is $E_m = 1.86$ eV, and its dissociation at $E_0 = 2.27$ eV leads to annealing of A-centers and, probably, other defects as well.

The annealing and growth of V_2O defects in n- and p-Si [14] can be described using the reactions presented in Table 2. Vacancies in n- and p-Si are captured by A-centers with the energy of migration of the vacancies of $E_m = 0.8$ eV [49]. The capture of divacancies for interstitial oxygen with V_2O formation occurs with the energy of migration of the divacancies $E_m = 1.3$ eV in n-Si only. The radius of the capture of a divacancy by an interstitial oxygen atom was determined to be $R = 16$ Å (Table 3) using (7). Annealing of V_2O in n- and p-Si occurs with an activation energy that equals the energy of migration of interstitial oxygen, and, according to (8), the energy of the barrier for the dissociation of $V_2O \rightarrow V_2 + O_i$ is $U_b = 0.74$ eV.

CONCLUSIONS

Annealing of the known radiation-induced defects in silicon (E-centers, A-centers, divacancies, carbon-containing centers, etc.) is described theoretically based on the experimental data that were obtained by many authors. The current material on RD annealing in Si is consolidated to a certain extent. The appropriate parameters of annealing of the main defects (the activation energy and frequency factor) are determined, and various mechanisms and reactions that accompany the RD annealing are proposed. The capture radius of mobile radiation-induced defects (V, C_i, V_2, and A-centers) by interstitial oxygen is found to be in the limits from 3 to 4 silicon lattice constants. The radius of the capture of interstitial carbon (C_i) by node carbon (23 Å) is found to be larger than by oxygen (17 Å). The radii of the vacancy capture by interstitial oxygen ($R = 15$ Å) and phosphor atoms ($R = 180$ Å) were defined, which determines the rate of introduction of A- and E-centers into n-Si.

REFERENCES

1. Young, R.C and Coreli, J.C., Photoconductivity Studies of Radiation Induced Defects in Silicon, *Phys. Rev. B*, 1972, vol. 5, no. 4, pp. 1455–1467.
2. Sonder, E. and Templeton, L.C., Gamma Irradiation of Silicon. I. Levels in n-Type Material Containing Oxygen, *J. Appl. Phys.*, 1960, vol. 31, no. 7, pp. 1279–1286.
3. Bemski, G. and Augustyniak, W.M., Annealing of Electron Bombardment Damage in Silicon Crystals, *Phys. Rev.*, 1957, vol. 108, no. 3, pp. 645–648.
4. Corbett, J.W., Walkins, G.D., Chrenko, R.M., and McDonald, R.S., Defects in Irradiated Silicon. II. Infrared Absorption of the Si–A Center, *Phys. Rev.*, 1961, vol. 121, no. 4, pp. 1015–1022.
5. Varentsov, M.D., Gaidar, G.P., Dolgolenko, A.P., and Litovchenko, P.G., Effect of Radiation and Annealing on Thermal Stability of Radiation-Induced Defects in Silicon, *Vopr. At. Nauki Tekh., Ser.: Fiz. Radiats. Povrezhdenii Radiats. Materialoved.* 2010, no. 5, pp. 27–35.
6. Svensson, B.G. and Lindstrom, J.L., Kinetic Study of the 830- and 889-cm^{-1} Infrared Bands During Annealing of Irradiated Silicon, *Phys. Rev. B*, 1986, vol. 34, no. 12, pp. 8709–8717.
7. Tanaka, T. and Inuishi, J., Hall Effect Measurement of Radiation Damage and Annealing in Si, *J. Phys. Soc. Jpn*, 1969, vol. 19, no. 2, pp. 167–174.
8. Watkins, G.D. and Corbett, J.W., Defects in Irradiated Silicon: Electron Paramagnetic Resonance of Divacancy, *Phys. Rev.*, 1965, vol. 138, no. 2A, pp. A543–A544.
9. Antonova, I.V., Vasil'ev, A.V., Panov, V.I., and Shaimeev, S.E., Peculiarities of Annealing of Divacancies in Silicon with Disordered Regions, *Fiz. Tekh. Poluprovodn.*, 1989, vol. 23, no. 6, pp. 1076–1079.
10. Poirier, R., Avalos, V., Dannefaer, S., Schiettekatte, F., and Roorda, S., Divacancies in Proton Irradiated Silicon: Comparison of Annealing Mechanisms Studied with Infrared Spectroscopy and Positron Annihilation, *Nucl. Instrum. Methods Phys. Res., Sect. B*, 2003, vol. 206, pp. 85–89.
11. Hwang, G.S. and Goddard III, W.A., Diffusion and Dissociation of Neutral Divacancies in Crystalline Silicon, *Phys. Rev. B*, 2002, vol. 65, no. 23, p. 233205-3.
12. Trauwaert, M.A., Vanhellemont, J., Maes, H.E., Van Bavel, A.M., Langouche, G., and Clauws, P., Low-Temperature Anneal of the Divacancy in p-Type Silicon: A Transformation from V_2 to V_xO_y Complexes, *Appl. Phys. Lett.*, 1995, vol. 66, no. 22, pp. 3056–3057.
13. Monakhov, E.V., Avset, B.S., Hallen, A., and Svensson, B.G., Formation of a Double Acceptor Center During Divacancy Annealing in Low-Doped High-Purity Oxygenated Si, *Phys. Rev. B*, 2002, vol. 65, no. 23, p. 233207-4.

14. Lee, Y.H. and Corbet, J.W., ERP Studies of Defects in Electron-Irradiated Silicon: A Triplet State of Vacancy-Oxygen Complexes, *Phys. Rev. B*, 1976, vol. 13, no. 6, pp. 2653−2666.

15. Zastavnoy, A.V. and Korol, V.M., Radiation Defects in Silicon Doped with Lithium and Sodium, *Phys. Status Solidi A*, 1989, vol. 113, pp. 277−283.

16. Ital'yantsev, A.G., Kurbakov, A.I., Mordkovich, V.N., Rubinova, E.E., Temper, E.M., and Trunov, V.A., Effect of Neutron Irradiation and Annealing on Properties of Silicon Doped with Germanium, *Fiz. Tekh. Poluprovodn.*, 1988, vol. 22, no. 5, pp. 834−838.

17. Emtsev, V.V. and Mashovets, T.V., *Primesi i tochechnye defekty v poluprovodnikakh* (Impurities and Point Defects in Semiconductors), Moscow: Radio i Svyaz', 1981.

18. Kimerling, L.C., DeAngelis, H.M., and Carnes, C.P., Annealing of Electron Irradiated Si, *Phys. Rev. B*, 1971, vol. 3, no. 2, pp. 427−432.

19. Medvedeva, I.F., Murin, L.I., and Markevich, V.P., Otzhig kompleksov vakansiya-fosfor v obluchennykh kristallakh Si (Annealing of Complexes Vacancy-Phosphor in Irradiated Silicon Crystals), *Trudy 4-oi Mezhdunarodnoi konferentsii po problemam vzaimodeistviya izluchenii s tverdym telom* (Proc. 4th Int. Conf. on Interraction of Radiations with a Solid), Minsk, Belarus, 2001, pp. 183−185.

20. Watkins, G.D., EPR of a Trapped Vacancy in Boron-Doped Silicon, *Phys. Rev. B*, 1976, vol. 13, no. 6, pp. 2511−2518.

21. Mukashev, B.N., Kolodin, L.G., Nusupov, K.Kh., Kinetics of Annealing of Radiation-Induced Defects in *p*-Silicon at Temperarures of 150-300 K, *Fiz. Tekh. Poluprovodn.*, 1978, vol. 12, no. 6, pp. 1174−1178.

22. Watkins, G.D., *Radiation Damage in Semiconductors* (Int. Conf. on the Physics of Semiconductors, Royaumont, 1964), Baruch, P., Ed., Paris: Dunod Cie, 1965, vol. 3, pp. 97−113 (Proc. Symp. on Radiation Damage in Semiconductors, Royaumont, July 1964).

23. Watkins, G.D., *Radiation Damage in Semiconductors* (Int. Conf. on the Physics of Semiconductors), Vook, F.L., Ed., New York: Plenum Press Inc., 1968, pp. 67−81.

24. Kimerling, L.C., Blood, P., and Gibson, W.M., Defect States in Proton-Bombarded Silicon at *T* < 300 K, *Proc. Int. Conf. on Defects and Radiation Effects in Semiconductors* (1978), Bristol−London: Inst. of Phys., 1979, no. 46, pp. 273−280.

25. Watkins, G.D., Troxell, J.R., and Chatterjel, A.P., Vacancies and Interstitials in Silicon, *Proc. Int. Conf. on Defects and Radiation Effects in Semiconductors* (1978), Bristol−London: Inst. of Phys., 1979, no. 46, pp. 16−30.

26. Seeger, A., Investigation of Point Defects in Silicon and Germanium by Non-Irradiation Techniques, in *Radiation Effects in Semiconductors*, London-New York-Paris: Gordon and Breach Sci. Publisher, 1971, pp. 29−38.

27. Seeger, A., Foll, H., and Frank, W., Self-Interstitials, Vacancies and their Clusters in Silicon and Germanium, *Proc. Int. Conf. on Radiation Effects in Semiconductors* (Dubrovnic, 1976), Bristol−London: Inst. of Phys., 1977, pp. 12−29.

28. Lee, Y.H., Gerasimenko, N.N., and Corbett, J.W., EPR Study of Neutron-Irradiated Sililcon: A positive Charge State of the ⟨100⟩ Split Di-interstitial, *Phys. Rev. B*, 1976, vol. 14, no. 10, pp. 4506−4520.

29. Daily, D.F., New EPR Spectra in Irradiated Silicon, *J. Appl. Phys.*, 1971, vol. 42, no. 2, pp. 864−865.

30. Kimerling, L.C., Defect States in Electron Bombarded Silicon: Capacitance Transient Analyses, *Proc. Int. Conf. on Radiation Effects in Semiconductors* (1976), Bristol−London: Inst. of Phys., no. 31, 1977, pp. 221−230

31. Lee, Y.H., Cheng, L.J., Gerson, J.D., Mooney, P.M., and Corbett, J.W., Carbon Interstitial in Electron Irradiated Silicon, *Solid State Commun.*, 1977, vol. 21, no. 1, pp. 109−111.

32. Watkins, G.D., Defect in Irradiated Silicon: EPR and Electron Nuclear Double Resonanse of Interstitial Boron, *Phys. Rev. B*, 1975, vol. 12, no. 12, pp. 5824−5839.

33. Watkins, G.D., EPR Studies of the Lattice Vacancy and Low-Temperature Damage Processes in Silicon, *Proc. Int. Conf. on Lattice Defects in Semiconductors*, Bristol−London: Inst. of Phys., 1975, no. 23, pp. 1−22.

34. Boyarkina, N.I. and Smagulova, S.A., Temperature Dependence of Annealing of Di-Carbon in Irradiated *n*-Si on Oxygen Concentration in Crystal, *Fiz. Tekh. Poluprovodn.*, 2004, vol. 38, no. 5, pp. 513−515.

35. Asom, M.T., Benton, J.L., Sauer, R., and Kimerling, L.C., Interstitial Defect Reactions in Silicon, *Appl. Phys. Lett.*, 1987, vol. 51, no. 4, pp. 256−258.

36. Zhan, X.D. and Watkins, G.D., Electron Paramagnetic Resonance of Multistable Interstitial-Carbon-Substitutional-Group-V-Atom Pairs in Silicon, *Phys. Rev. B*, 1993, vol. 47, no. 11, pp. 6363−6380.

37. Komarov, B.A., Medvedeva, I.F., Murin, L.I., Gusakov, V.E., Kuchinskii, P.V., and Lindstrom, J.L., DLTS Spectroscopy of Complexes Radiation Defect-Residual Impurity in Silicon), *Trudy IV mezhdunarod. Konferentsii po vzaimodeistviyu izluchenii s tverdym telom* (Proc. 4th Int. Conf. on Interaction of Radiations with a Solid), Minsk, Belarus, 2011, pp. 161−163.

38. Baranov, A.I., Gerasimenko, N.N., Dvurechenskii, A.V., and Smirnov, L.S., Annealing of Large Vacancy Clusters, *Fiz. Tekh. Poluprodn.*, 1974, vol. 11, no. 1, pp. 92−99.

39. Gregory, B.L. and Sander, H.H., Transient Annealing of Defects in Irradiated Silicon Devices, *Proc. IEEE*, 1970, vol. 58, no. 9, pp. 1328−1341.

40. Moll, M., Fretwurst, E., Kuhnke, M., and Lindstrom, G., Relation between Microscopic Defects and Macroscopic Changes in Silicon Detector Properties after Hadrons Irradiation, *Nucl. Instrum. Methods Phys. Res. B*, 2002, vol. 186, no. (1−4), pp. 100−110.

41. Whan, R.E., Oxygen-Defect Complexes in Neutron-Irradiated Silicon. *J. Appl. Phys.*, 1966, vol. 37, no. 9, pp. 3378−3382.

42. Asghar, M., Zafar, Iqbai M., and Zafar, N., Characterization of Deep Levels Introduced by Alpha Radiation in n-Type Silicon, *J. Appl. Phys.*, 1993, vol. 73, no. 8, pp. 3698−3708.

43. Lugakov, P.F. and Luk'yanitsa, V.V., Interaction of Defects of Vacancy and Interstitial Types during

Annealing of Irradiated *n*-Si, *Fiz. Tekh. Poluprovodn.*, 1983, vol. 17, no. 1, pp. 166—168.

44. Moll, M., Feick, H., Fretwurst, E., Lindstrom, G., and Schutze, C., Comparison of Defects Produced by Fast Neutrons and ^{60}Co Gammas in High-Resistivity Silicon Detector Using Deep-Level Transient Spectroscopy, *Nucl. Instrum. Methods Phys. Res., Sect. A,* 1997, vol. 388, no. 3, pp. 335—339.

45. Poirier, R., Avalos, V., Dannefaer, S., Schiettekatte, F., Roorda, S., and Misra, S.K., Divacancies in Proton Irradiated Silicon: Variation of EPR Signal with Annealing Time, *Phys. B*, 2003, vols. 340—342, pp. 752—755.

46. Song, L.W., Zhan, X.D., Benson, B.W., and Watkins, G.D., Bistable Interstitial-Carbon-Substitutional-Carbon Pair in Silicon, *Phys. Rev. B*, 1990, vol. 42, no. 9, pp. 5765—5783.

47. Khirunenko, L.I., Kobzar', O.A., Pomozov, Yu.V., Sosnin, M.G., and Tripachko, N.A., Effect of Tin on Reactions Occurring in the Presence of Interstitial Carbon in Irradiated Silicon, *Fiz. Tekh. Poluprovodn.*, 2003, vol. 37, no. 3, pp. 304—309.

48. Brower, K.L., EPR of a ⟨001⟩ Si Interstitial Complex in Irradiated Silicon, *Phys. Rev. B*, 1976, vol. 14, no. 3, pp. 872—883.

49. Varentsov, M.D., Gaidar, G.P., Dolgolenko, A.P., and Litovchenko, P.G., Radiation Hardness of Germanium-Doped Silicon with High Concentration of Free Oxygen, *Yaderna Fizika ta Energetika*, 2006, no. 1(17), pp. 60—66.

50. Jellison, G.E., Jr. Transient Capacitance Studies of an Electron Trap at $E_C - E_T = 0.105$ eV in Phosphorus-Doped Silicon, *J. Appl. Phys.*, 1982, vol. 53, no. 8, pp. 5715—5719.

51. Frens, A.M., Bennebroek, M.T., Zakrzewski, A., Schmidt, J., Chen, W.M., Janzen, E., Lindstrom, J.L., and Monemar, B., Observation of Rapid Direct Charge Transfer between Deep Defects in Silicon, *Phys. Rev. Lett.*, 1994, vol. 72, no. 18, pp. 2939—2942.

52. Mooney, P.M., Cheng, L.J., Suli, M., Gerson, J.D., and Corbett, J.W., Defect Energy Levels in Boron-Doped Silicon Irradiated with 1-MeV Electrons, *Phys. Rev. B*, 1977, vol. 15, no. 8, pp. 3836—3843.

53. Dolgolenko, A.P., Litovchenko, P.G., Varentsov, M.D., Gaidar, G.P, and Litovchenko, A.P., Particularities of the Formation of Radiation Defects in Silicon with Low and High Concentration of Oxygen, *Phys. Status Solidi B,* 2006, vol. 243, no. 8, pp. 1842—1852.

54. Vasil'ev, A.V., Annealing of Divacancies in Silicon Irradiated by Fast Neutrons, *Fiz. Tech. Poluprovod.*, 1986, vol. 20, no. 3, pp. 561—564.

55. Waite, T.R., Theoretical Treatment of the Kinetics of Diffusion-Limited Reactions, *Phys. Rev.*, 1957, vol. 107, no. 2, pp. 463—470.

56. Vinetskii, V.L. and Kholodar', G.A., *Radiatsionnaya fizika poluprovodnikov* (Radiation Physics of Semiconductors), Kiev: Naukova Dumka, 1979.

57. Dolgolenko, A.P., Varentsov, M.D., Gaidar, G.P, Litovchenko, P.G., The Rate of Introduction of Defects Depending on the Dose of Irradiation of *p*-Si by Fast Neutrons of Reactor, *Yaderna Fizika ta Energetika*, 2007, no. 2(20), pp. 89—96.

Energy Transformation in Water and Oxygen-Containing Electrolytes

K. D. Pershina[a], V. V. Kokhanenko[b], L. N. Masliuk[b], and K. A. Kazdobin[b]

[a]*Vernadsky Taurida National University, pr. Vernadskogo 4, Simferopol, 95007 Ukraine*
[b]*Vernadsky Institute of General and Inorganic Chemistry, National Academy of Sciences of Ukraine,*
pr. Paladina 32/34, Kiev, 03142 Ukraine
e-mail: kazdobin@ionc.kiev.ua
Received June 30, 2011; in final form, August 10, 2011

Abstract—The conductivity of distilled water and dilute electrolyte solutions in the presence and absence of dissolved oxygen is studied. It is found that the circuit can be implemented with equal probability as a capacitive circuit with physically different current carriers and as an inductive circuit in water and dilute aqueous solutions of oxygen-containing electrolytes. The occurrence of an inductive resistance is caused by the presence of particles with intrinsic magnetic moment, i.e., reactive oxygen species. The frequency ranges of possible pulse energy transformation in an electrochemical system that contains oxygenated water are shown. In the absence of oxygen, this circuit is not implemented.

Oxygenated water serves as a reaction medium for most natural redox transformations. Therefore, the charge transfer in a water—oxygen system and the conductivity mechanism in it are a subject of undoubted interest. The required information can be obtained via studying the behavior of water and electrolytes in an electromagnetic field that simulates the field of the earth using the electrochemical impedance spectroscopy method [1].

All the known studies of the electroconductive properties of ultrapure water were carried out without determining the conductivity mechanisms; they were a priori considered to be relay-race [2, 3]. The impedance spectroscopy method was used in an attempt to construct a simple equivalent circuit of the structure of an electric double layer (DL) at the electrode—water interface in terms of the Gouy—Chapman and Stern models [2]. The high-precision measurement of the electroconductivity of ultrapure water in the range of $0-100°C$ was performed in order to clarify the role of the conductivity of the hydroxyl ion at high temperatures [3]. The measurements served as the basis for calculating the fundamental properties of the water (the ion mobility, density, and ionization constants).

Modern methods revealed the heterogeneous state of water (clusters) in which long-range order elements are preserved in the structure above the melting point [4—12]. Heterogeneous structures are recorded in the temperature range of the existence of wildlife (0—35°C) and can lead to "soft" local changes of the water properties via speeding up or slowing down the biological and other natural processes. Since the mechanisms of cluster formation are not completely clear, some attempts of their quantum-chemical modeling have been made [13—15]. In addition, the possibilities of an energy gain during the formation of supramolecular structures were shown. Of particular interest are the calculations [15] that point to a nonmonotonic increase in the total dipole moment of oxygen-containing clusters with an increase in their size in the range of $10 > n > 50$ formula units.

Heterogeneous entities must have a significant effect on the mechanism of water conductivity owing to the possibility of damping the charge in a quasi-crystalline backbone, i.e., on the long-range order elements above the melting point or in another supramolecular structure [9, 13]. This property makes pure water significantly different from the electrolyte solutions that mostly contain short-range order structures that arise from the solvation of ions [1].

Charge transfer and the formation of redox couples are the basis for any process of energy conversion. However, in all theoretical and experimental studies, water is considered as an inert medium that is not involved in the electrode processes. Previously a hypothesis of a complex proton—electron mechanism of conductivity of oxygen-containing water was advanced [16]. Therefore, the study of the accumulation and transformation of energy under conditions of redox reactions at the electrode—water interface in pure water, a dilute electrolyte, and in oxygen-containing water is the subject of this study.

EXPERIMENTAL

For the studies, we used distilled water that underwent degassing via long-term boiling (for 2.5—3 h) with a reflux condenser made of teflon. Hot water having a temperature of 80—85°C was placed into a sealed measuring cell, in which it was cooled to $20 \pm 2°C$.

After that, the water was oxygenated via bubbling for 2−3 h using an intermediate container with 0.1 M NaOH to trap the carbon dioxide. The content of oxygen in the water and electrolytes was controlled using the Winkler method [17].

The 0.1 M KCl and 0.01 M Na_2SO_4 electrolytes were prepared from special purity grade reagents.

The effect of an electromagnetic field was measured in tubes with a diameter of 15 mm and a length of 160 mm, which had 500 turns of 0.15 PEL copper wire outside a polyvinylchloride or glass frame (Fig. 1). Platinum electrodes were mounted into the ends of the tube. An alternating voltage with an amplitude of 18.75 V and a frequency of 50 Hz was applied across the winding. The resulting response was measured in the tube using a UT-30C high-resistance voltmeter (Uni-Trend, Hong Cong) with an input impedance of no less than 10 mΩ. The measurement error was ±0.5%.

The electric conductivity of the solutions was determined from measurements of the impedance spectra. They were carried out using an Autolab-30 electrochemical module (Ekochemie BV, Netherlands) equipped with a Frequency Response Analyzer (FRA) module. The samples were placed into the cell with platinum electrodes with an area of 4 cm^2 at a distance of 1 cm. The measurements were performed according to a standard procedure in the frequency range of 0.001 Hz to 1.0 MHz with a single pulse amplitude of ±5 mV. The module was controlled using Autolab 4.7 software with the subsequent processing using the Zview 2.0 software package via the complex amplitude method. The graphic data are presented without conversion to specific values because of the operating conditions of the ZView 2.0 computation package.

RESULTS AND DISCUSSION

The data on the conductivity of the oxygen-containing and degassed water, which were derived from the measurement at a commonly used frequency of 3 kHz, show significant differences in values: in the presence of oxygen, the water conductivity increases by several orders of magnitude unlike the electrolyte solutions (Table 1).
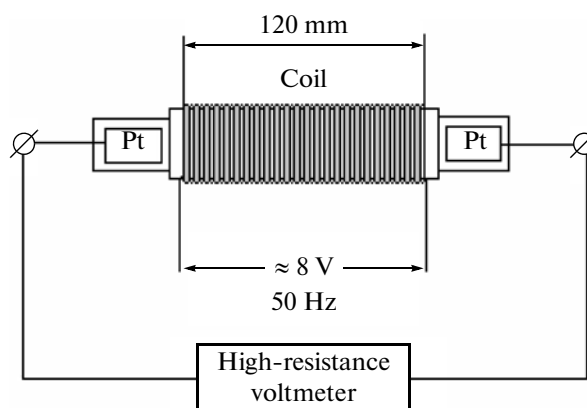

Fig. 1. Scheme of the experiment in an electromagnetic field.

The table shows that the oxygen content in the dilute electrolytes differs slightly. Hence, the conductivity of the systems is determined by their structural features.

The impedance spectra and the equivalent circuit parameters of solutions of strong electrolytes (0.1 M KCl and 0.01 M Na_2SO_4) are shown in Fig. 2. They suggest that Faradic charge transfer, which is described by the classical theory of electric conductivity, is observed in the solution of 0.1 M KCl [19]. The spectrum is represented by a straight line with a negative value of the complex impedance. The negative value of the imaginary number is determined through the equation

$$Z = -j/\omega C = -jX_C. \qquad (1)$$

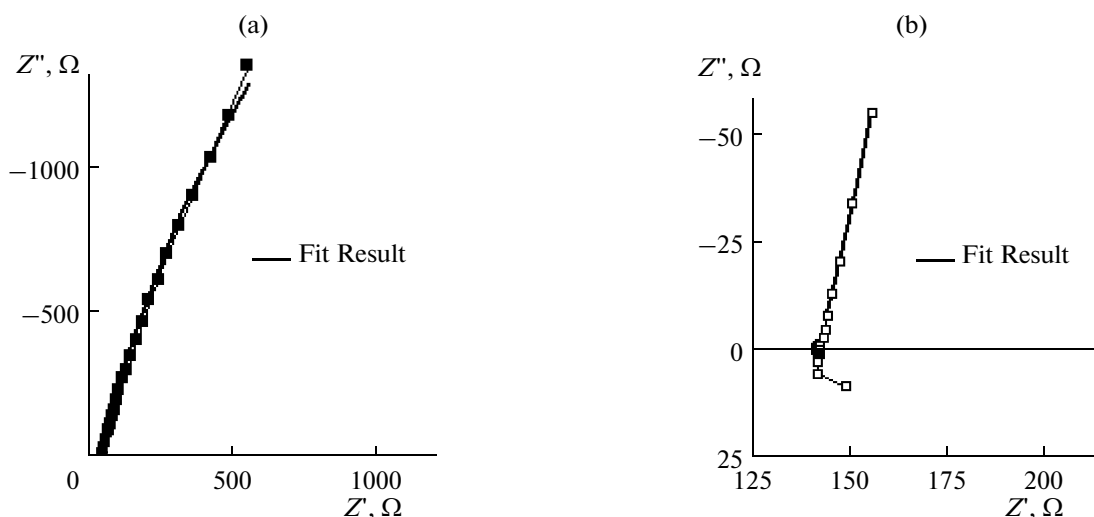In this case, the equivalent circuit is a capacitive circuit (Fig. 2a).

The equivalent circuit for the oxygen-containing solution of Na_2SO_4 is much more complicated; this is attributed to the specific features of the electrode reactions of oxygen-containing anions. In this case, a positive value is described through the following equation:

$$Z = j\omega L = jX_L. \qquad (2)$$

Therefore, the equivalent circuit corresponds to an inductive circuit. The presence of both positive and negative values of the imaginary part of the impedance shows that the circuit can be both capacitive and

Table 1. Values of the electric conductivity χ of the studied objects measured at 3 kHz

Component	χ, S/cm	Reference data	Content of O_2, mL/L
Distilled water + O_2	1.64×10^{-4}		9.0
Degassed distilled water	7.33×10^{-8}	5.56×10^{-8} [3]	−
0.01 M aqueous solution of Na_2SO_4 pH 6.5	3×10^{-3}	1.0×10^{-4} [18]	9.0
0.1 M aqueous solution of KCl pH 6.8	9.98×10^{-3}	12.88×10^{-3} [18]	8.6

(a)

(b)

Element	Resistance, Ω	Error, %	Resistivity, Ω/cm^2
R_1	45, 46	0.023	11.36
CPE1-T	1.33×10^{-4}	0.4	0.333×10^{-4}
CPE1-P	0.843	0.1	0.211
R_2	9988	3.04	2497

Element	Resistance, Ω	Error, %	Resistivity, Ω/cm^2
R_1	142.5	0.049	35.625
CPE1-T	1.9×10^{-4}	1.342	4.75×10^{-5}
CPE1-P	0.846	0.272	0.212
L_1	2.337×10^{-6}	7.201	5.843×10^{-7}
R_2	17.62	15.16	4.405

Fig. 2. Impedance spectra of the 0.1 M KCl and 0.01 M Na_2SO_4 solutions and their equivalent circuits.

inductive. In this case, at zero values of the imaginary impedance, the equal probability is implemented (Fig. 2b):

$$-jX_C = jX_L. \qquad (3)$$

The equivalent circuit of the sodium sulfate solution, which simultaneously contains capacitive and inductive resistance, gave the best agreement with the experimental data. The occurrence of an inductive resistance is possible if the system comprises particles with an intrinsic magnetic moment. These particles

Table 2. Parameters of equivalent circuits for (*1*) oxygen-free and (*2*) oxygenated bidistilled water

Parameter	Resistivity 1, Ω/cm^2	Resistivity 2, Ω/cm^2
L	-3.9×10^{-4}	-2.8×10^{-5}
R	30.5×10^2	-1.8×10^4
CPE-T	29.0×10^{-6}	28.8×10^{-7}
CPE-P	16.2×10^{-2}	7.5×10^{-4}

can include the reactive oxygen species resulting from the electrode reaction.

Since sodium sulfate is an indifferent electrolyte, water is the main participant in the formation of these reactive species. The impedance spectra derived for pure water (Fig. 3) have no positive imaginary part of the impedance; however, in a certain range, they are at its zero mark, which also suggests the equiprobable implementation of the above described equivalent circuits. This occurs in the case of oxygenated water (Fig. 3b). In the case of degassed water, the equivalent circuit is most similar to an oscillatory circuit.

The parameters of the impedance spectra of distilled water in the presence and absence of dissolved oxygen are shown in Fig. 3 and Table 2.

For oxygen-free bidistilled water (Fig. 2a), the spectrum is similar to the electrolytes with deviations in the high-frequency region, whereas the spectrum of oxygen-containing water (Fig. 2b) comprises a significant contribution of inductive resistance [20]. The data of Table 2 suggest that its value varies from
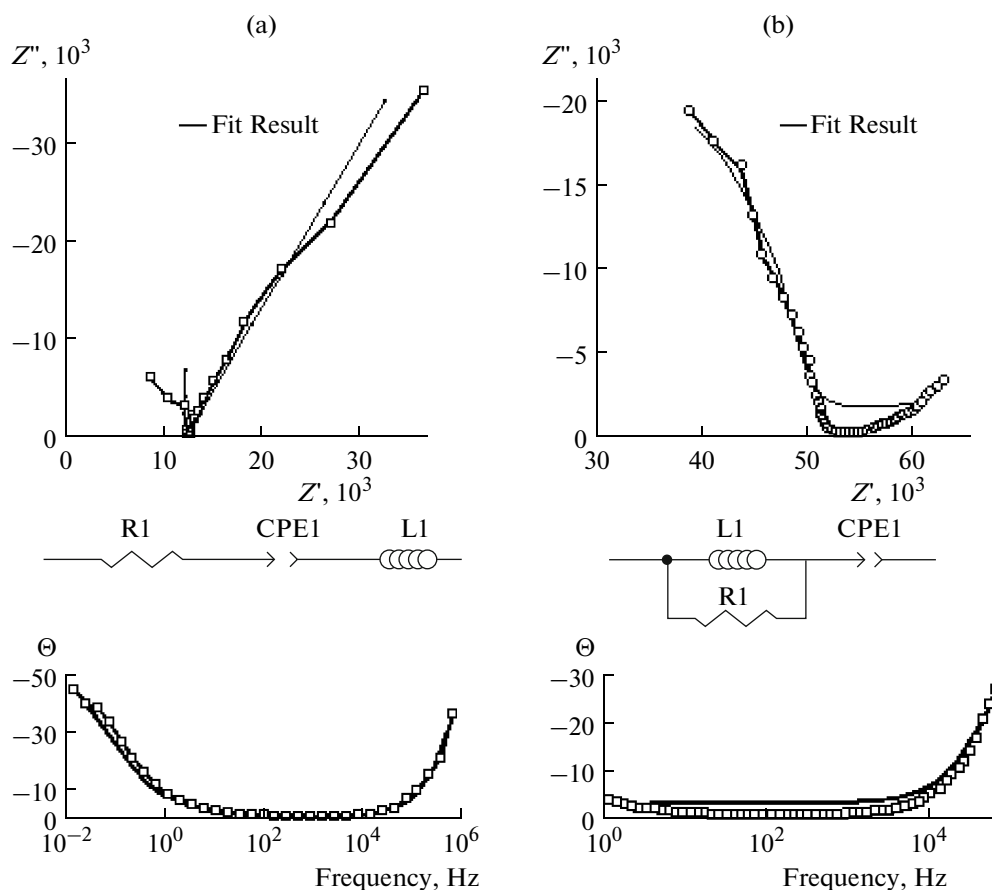
Fig. 3. Impedance spectra and equivalent circuits for (a) oxygen-free and (b) oxygenated bidistilled water.

-15.6×10^{-4} to -1.13×10^6 Ω. These significant differences can be attributed to the structural features of the water. The analysis of the phase angle shift (Fig. 3) revealed a considerable shift of the phase angle to the negative region in both the low-frequency and high-frequency ranges in the case of water without oxygen. In the oxygen-containing water, a phase angle shift is not observed in a fairly wide frequency range. In accordance with equation (4), this is indicative of the equiprobable participation of the inductive and capacitive components of the mpedance:

$$\tan\Theta = (X_L - X_C)/R, \qquad (4)$$

where R is the active resistance, and $R \neq 0$.

The absence of the components that form the diffuse region of the EDL in pure water and the introduction of an electrochemically active gas, i.e., oxygen, in it have led to the necessity of modeling fundamentally new equivalent circuits. Since the molecule of oxygen and its reactive species exhibit magnetic properties, their presence in the reaction chamber can cause self-induction currents. To take into account the specificity of the structure of the near-electrode layer during the anodic evolution of oxygen, we introduced an inductive resistance into the composition of the equiv-

alent circuit of the process [21–24]. This model, which contains two time constants, can adequately describe the evolution of oxygen/ozone on an inert β-PbO$_2$ electrode in the absence of diffusion control. The model takes into account the uncompensated resistance of the solution R_Ω, the EDL capacitance in the form of a constant phase element (CPE$_1$ (C_{dl})), the charge transfer resistance R_{ct}, the adsorption pseudocapacitance of the reaction intermediates CPE$_2$ (C_{dl}), and the resistance of the adsorbed intermediates R_{ads}.

The introduction of an inductive resistance into the circuit was caused by its manifestation in the high-frequency range of the impedance spectrum [22, 25–27].

However, having introduced an inductive resistance into a fairly cumbersome equivalent circuit, the authors of [25] did not take it into account in the calculations; they assumed that it would not have an effect on the formation of active oxidizing agents with the participation of water, although the presence of oxygen and ozone, which exhibit magnetic properties, must necessarily change the equivalent circuit of the electric conductivity in the near-electrode space. This statement is based on the fact that the surface polar molecules give a pronounced anisotropic response to
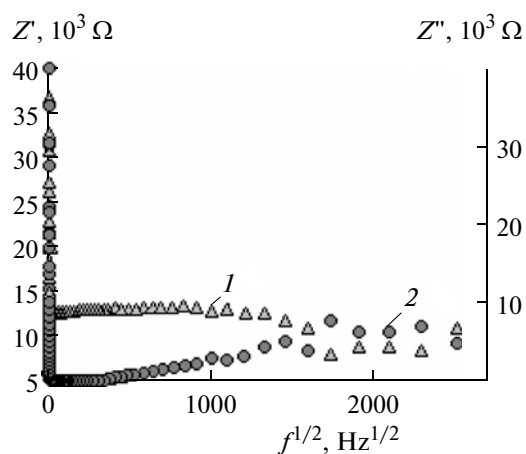
Fig. 4. Frequency dependence of the active and reactive components of the impedance for oxygen-free water: (*1*) $f^{1/2}$ vs. Z' Ω and (*2*) $f^{1/2}$ vs. Z'' Ω.

the applied electric field and mostly form dipole orientations parallel to the surface [28]. In particular, in water, these effects take place because of the occurrence of a spontaneous asymmetry of hydrogen bonds in water clusters, which results from a change in their configuration. It is these effects that determine the polarization properties of water at the interface, including the conditions of the imposition of an external electromagnetic field [29].

The experimental data for the dependences of the real and imaginary parts of the impedance on the frequency of the oxygenated and degassed distilled water are shown in Figs. 4 and 5. It should be noted that the experimental data for the oxygenated water are similar to the results obtained by Grasso [2].

It is noteworthy that the appearance of oxygen in the water leads to a change in the frequency range by
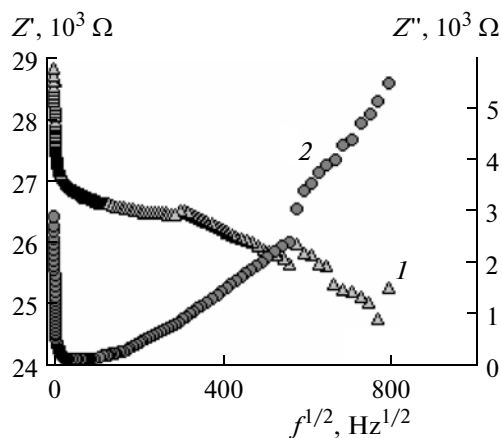
an order of magnitude (Fig. 5) with respect to the oxygen-free water (Fig. 4). For the oxygen-free water, this model is valid up to frequencies of 0.25 MHz (Fig. 4).

To substantiate the introduction of a CPE into the circuit in the studied systems, we considered the possible processes at the electrode–solution interface under the conditions of a low-amplitude alternating current being applied. In this case, only the electroactive regions of the electrode's surface are involved into the electrochemical reaction rather than the entire surface. As this takes place, the following processes occur: (i) the charging of the EDL capacitance, (ii) the charge transfer owing to one or more electrochemical reactions, (iii) the spatial separation of the charges owing to the diffusion in the solution's volume, and (iv) the charging of the capacitance owing to the specific adsorption of the solution's components or the electrode reaction products. The two last-mentioned processes are functions of the temperature and pressure. Therefore, the properties of a CPE (a double-layer capacitor without an insulator interlayer) depend on these two parameters. The CPE that is formed at the interface of physically different current carriers [30] can indicate the occurrence of several nonequilibrium flows for example, in the presence of intermediates of electrochemical reactions involving oxygen [31, 32]. In this case, the active oxygen-containing intermediate products form a region of spatial (volume) charge separation similar to semiconductors irradiated with high-energy electron fluxes [33].

The CPE-T parameter is responsible for the spatial separation of the charges owing to the diffusion in the solution's volume; CPE-P is responsible for the charging of the capacitance owing to the specific adsorption of the solution's components or the electrode reaction products.
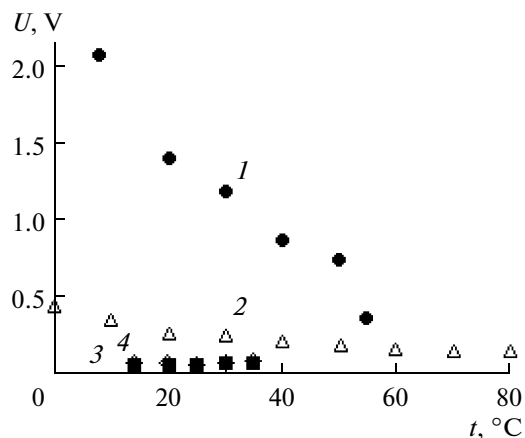

Fig. 5. Frequency dependence of the active and reactive components of the impedance for oxygen-containing water: (*1*) $f^{1/2}$ vs. Z' Ω and (*2*) $f^{1/2}$ vs. Z'' Ω.

Fig. 6. Variation in the alternating voltage response in a solenoid: (*1*) bidistilled water, polyvinylchloride frame; (*1*) bidistilled water, glass frame; (*3*, *4*) 0.1 M KCl and 0.01 M Na$_2$SO$_4$, respectively, glass frame.
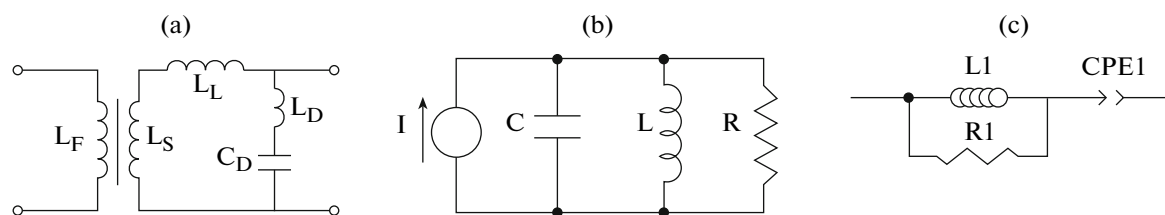
Fig. 7. Equivalent circuits of (a) a pulse transformer with distributed capacitance, (b) a Laplace pulse transformer [19], and (c) an electrochemical system with oxygen-containing water (the secondary winding of the transformer).

The dependence of the amplitude of the current on the amplitude of the EDL is similar to Ohm's law, in which the role of the resistance is played by the impedance of the electrochemical circuit under study. It comprises capacitive and inductive resistances in the presence of these elements in the circuit. The resulting numerical values of the inductive and capacitive resistances adequately describe the behavior of oxygen-containing distilled water if we assume that, in accordance with the model (Fig. 3b), in a molecular cluster of water with oxygen, a stable defect region arises and forms a "capacitor and solenoid" system, and the solenoid core is oxygen.

The presence of an inductive resistance in water systems is the subject of debate [34]. In order to directly confirm the differences in the behavior of water and a dilute electrolyte, we carried out an experiment on the transmission of an electromagnetic field through the systems under study. The measurement data are shown in Fig. 6.

In a fairly wide temperature range, in the presence of an electromagnetic field in water, an increase in the temperature leads to a gradual decrease in the voltage response, which disappears only at a temperature of $60°C$. However, this phenomenon is not observed in the electrolyte solutions (Fig. 6, curves *3–4*). Thus, we can assume that oxygen-containing pure water has a stable eigenstructure capable of holding the reactive oxygen species and forming a kind of microsolenoids.

The variation in the response values is apparently attributed to the different wettability of the materials: polyvinylchloride is hydrophobic, and glass is hydrophilic. In this case, the additional losses are caused by the formation of an EDL on the surface of the glass, which results from the specific adsorption of water.

A comparative analysis of the equivalent circuits of the pulse transformers (Fig. 7) revealed a correlation between the elements of the model circuit of oxygen-containing water and equivalent circuits of pulse transformers, which suggests that, in the frequency ranges with a negative value of the phase angle shift, pulse energy transformation is possible in an electrochemical system that contains water saturated with oxygen. In the absence of oxygen, this circuit is not implemented.

CONCLUSIONS

The presence of both positive and negative values of the imaginary part of the impedance indicates that the circuit can be implemented with equal probability as a capacitive circuit (a double-layer capacitor without an insulator interlayer) with physically different current carriers and as an inductive circuit in water and dilute aqueous solutions of oxygen-containing electrolytes.

The occurrence of an inductive reactance is possible if the system contains particles with an intrinsic magnetic moment. These particles can include reactive oxygen species.

It is experimentally found that oxygen-containing pure water has a stable eigenstructure capable of holding the reactive oxygen species.

It is shown that pulse energy transformation can take place in an electrochemical system that contains oxygenated water in the frequency ranges with a negative value of the phase angle shift. In the absence of oxygen, this circuit is not implemented.

REFERENCES

1. Bard, A.J. and Faulkner, L.R., *Electrochemical Methods: Fundamentals and Applications*, New York: Wiley, 2001.

2. Grasso, F., Musumeci, F., and Triglia, A., Impedance Spectroscopy of Pure Water, *Il Nuovo Cimento*, 1990, vol. 12, pp. 1117−1131.

3. Light, T.S., Licht, S., Bevilacqua, A.C., and Morashc, K.R., The Fundamental Conductivity and Resistivity of Water, *Electrochem. Solid-State Lett.*, 2005, vol. 8, no. 1, pp. E16−E19.

4. Bresme, F., Lervik, A., Bedeaux, D., and Kjelstrup, S., Water Polarization under Thermal Gradients, *Phys. Rev. Lett.*, 2008, vol. 101, no. 2, p. 020602.

5. Zwier, T.S., The Structure of Protonated Water Clusters, *Science*, 2004, vol. 304, pp. 1119−1121.

6. Miyazaki, M., Fujii, A., Ebata, T., and Mikami, N., Infrared Spectroscopic Evidence for Protonated Water Clusters Forming Nanoscale Cages, *Science*, 2004, vol. 304, pp. 1134−1136.

7. Sedlák, M., Large-Scale Supramolecular Structure in Solutions of Low Molar Mass Compounds and Mixtures of Liquids: I. Light Scattering Characterization, *J. Phys. Chem. B*, 2006, vol. 110, no. 9, pp. 4329−4339.

8. Sedlák, M., Large-Scale Supramolecular Structure in Solutions of Low Molar Mass Compounds and Mix-

tures of Liquids: II. Kinetics of the Formation and Long-Time Stability, *J. Phys. Chem. B*, 2006, vol. 110, no. 9, pp. 4339–4347.

9. Syroeshkin, A.V., Smirnov, A.N., Goncharuk, V.V., et al., Water as a Heterogeneous Structure, Issledovano v Rossii. http://zhurnal.ape.relarn.ru/articles/2006/088.pdf.

10. Goncharuk, V.V., Smirnov, V.N., Syroyeshkin, A.V., and Malyarenko, V.V., Clusters and Gigantic Heterophase Water Clusters, *J. Water Chem. Technol.*, 2007, vol. 29, pp. 3–17.

11. Goncharuk, V.V., Orehova, E.A., and Malyarenko, V.V., Clusters and Gigantic Heterophase Water Clusters, *J. Water Chem. Technol.*, 2008, vol. 30, pp. 136–152.

12. Demangeat, J-L., *NMR Water Proton Relaxation in Unheated and Heated Ultrahigh Aqueous Dilutions of Histamine: Evidence for an Air-Dependent Supramolecular Organization of Water, J. Mol. Liq.*, 2009, vol. 144, pp. 32–41.

13. Domrachev, G.A., Selivanovskii, D.A., Domracheva, E.A., et al., The Role of Neutral Defects in the Structure of Liquid Water, *Zh. Strukt. Khim,* 2004, vol. 45, no. 4, pp. 670–677.

14. Sediki, A., Lebsir, F., Martiny, L., Dauchez, M., and Krallafa, A., Ab Initio Investigation of the Topology and Properties of Three-Dimensional Clusters of Water $(H_2O)_n$, *Food Chem.*, 2008, vol. 106, pp. 1476–1484.

15. Galashev, A.E., Chukanov, V.N., and Galasheva, O.A., Dielectric Characteristics of $O_2(H_2O)_i$ and $(O_2)_2(H_2O)_i$ Clusters: Computer-Aided Experiment, *Colloid J.*, 2006, vol. 68, no. 2, pp. 131–136.

16. Pershina, K.D. and Kazdobin, K.A., Conductivity of Water Media as an Alternative of Electronic and Ionic Transfer, *J. Water Chem. Technol.*, 2008, vol. 30, no. 6, pp. 358–367.

17. Knowles, G. and Lowden, G.F., Methods for Detecting the End-Point in the Titration of Iodine with Thiosulphate, *Analyst,* 1953, vol. 78, no. 924, pp. 159–164.

18. *Spravochnik po elektrokhimii* (Handbook of Electrochemistry), Sukhotin, A.M., Ed., Leningrad: Khimiya, 1981.

19. Grafov, B.M. and Ukshe, E.A., *Elektrokhimicheskie tsepi peremennogo toka* (Alternating-Current Electrochemical Circuits), Moscow: Nauka, 1973.

20. Frish, S.E. and Timoreva, A.V., *Kurs obshchei fiziki* (A Course in General Physics), Moscow: Fizmatgiz, 1962, vol. 2, p. 516.

21. Ho, J.C.K., Tremiliosi-Filho, G., Simpraga, R., and Conway, B.E., Structure Influence on Electrocatalysis and Adsorption of Intermediates in the Anodic O_2 Evolution at Dimorphic α- and β-PbO_2, *J. Electroanal. Chem.*, 1994, vol. 366, 147–162.

22. Bisquert, J., Randriamahazaka, H., and Garcia-Belmonte, G., Inductive Behavior by Charge-Transfer and Relaxation in Solid-State Electrochemistry, *Electrochim. Acta*, 2005, vol. 51, pp. 627–640.

23. Francoa, D.V., Da Silva, L.M., Wilson, F.J., and Boodts, J.F.C., Influence of the Electrolyte Composition on the Kinetics of the Oxygen Evolution Reaction and Ozone Production Processes, *J. Braz. Chem. Soc.*, 2006, vol. 17, no. 4, pp. 746–757.

24. Alves, V.A., Da Silva, L.A., and Boodts, J.F.C., Surface Characterization of $IrO_2/TiO_2/CeO_2$ Oxide Electrodes and Faradaic Impedance Investigation of the Oxygen Evolution Reaction from Alkaline Solution, *Electrochim. Acta*, 1998, vol. 44, pp. 1525–1534.

25. Da Silva, L.M., De Faria, L.A., and Boodts, J.F.C., Electrochemical Impedance Spectroscopic (EIS) Investigation of the Deactivation Mechanism, Surface and Electrocatalytic Properties of $Ti/RuO_2(x)$ + $Co_3O_4(1-x)$ Electrodes, *J. Electroanal. Chem.*, 2002, vol. 532, pp. 141–150.

26. Qian, S.Y., Conway, B.E., and Jerkiewicz, G., Comparative Effects of Adsorbed S-Species on H Sorption into Pd from UPD and OPD H: a Kinetic Analysis, *Int. J. Hydrogen Energy*, 2000, vol. 25, pp. 539–550.

27. Macdonald, J.R., *Impedance Spectroscopy*, New York: Wiley, 1987.

28. Bratko, D., Daub, C.D., and Luzar, A., Water-Mediated Ordering of Nanoparticles in an Electric Field, *Faraday Discuss.*, 2009, vol. 141, pp. 31–39.

29. Skúlason, E., Karlberg, G.S., Rossmeisl, J., et al., Density Functional Theory Calculations for the Hydrogen Evolution Reaction in an Electrochemical Double Layer on the Pt(111) Electrode, *Phys. Chem. Chem. Phys.*,2007, vol. 9, pp. 3241–3250.

30. Pleskov, Yu.V., Synthetic Diamond in Electrochemistry, *Usp. Khim.*, 1999, vol. 68, no. 5, pp. 416–429.

31. Kompan, M.E., Kuznetsov, V.P., and Malyshkin, V.G., Nonlinear Impedance of Solid-State Energy-Storage Ionisters, *Tech. Phys.*, 2010, vol. 55, no. 5, pp. 692–698.

32. Elkin, V.V., Marshakov, A.I., Rybkina, A.A., and Maleeva, M.A., Interpretation of the Impedance Comprising Negative Capacitance and Constant Phase Elements on Iron Electrode in Weakly Acidic Media, *Russ. J. Electrochem.*, 2011, vol. 47, no. 2, pp. 136–146.

33. Poklonski, N.A., Gorbachuk, N.I., Shpakovski, S.V., and Wieck, A., Equivalent Circuit of Silicon Diodes Subjected to High-Fluence Electron Irradiation, *Tech. Phys.*, 2010, vol. 55, no. 10, pp. 1463–1471.

34. Inductance in Electrochemistry. http://www.consultrsr.com/resources/eis/index.htm.

SHORT COMMUNICATIONS

Anomalous Electrodeposition of Co–W Coatings from a Citrate Electrolyte due to the Formation of Multinuclear Heterometallic Complexes in the Solution

S. S. Belevskii, S. P. Yushchenko, and A. I. Dikusar

Institute of Applied Physics, Academy of Sciences of Moldova, ul. Akademiei 5, Chisinau, MD 2028 Republic of Moldova
e-mail: dikusar@phys.asm.md
Received November 10, 2011

Abstract—It is shown that the anomalous electrodeposition of Co–W coatings in a citrate electrolyte occurs as a result of the formation in the bulk of the solution of multinuclear heterometallic complexes with their structure (composition) defined by the solution and near-electrode layer pH values.

The induced codeposition of iron group metals with refractory metals (W, Mo, Re) falls into the category of so-called "anomalous" electrodeposition, as the refractory metals cannot be electrodeposited alone from their aqueous solutions. However, in the case of electrodeposition from solutions containing salts of the iron group metals (Fe, Co, Ni), their codeposition in the form of alloys having a high content of a refractory metal and possessing some unique physicomechanical properties occurs [1]. However, the mechanism of this process is not completely understood [2–4].

We need here the most important answer to the question whether the alloy is produced due to electrodeposition from the corresponding heterometallic complex that is formed directly in the electrolyte [4] or it is the consequence of reduction from the intermediate which contains a metal from the iron group and a refractory metal and is generated through the electrochemical reaction (see, for instance, [2, 3]).

In order to find the answer to this question by the example of a citrate electrolyte to produce Co–W alloys, its gel-chromatographic separation into components with different molecular masses has been carried out (see also [5]).

The electrolytes containing (mol/L) $CoSO_4$ (0.2), Na_2WO_4 (0.2), H_3BO_3 (0.65), citric acid (0.04), and sodium citrate (0.25) and characterized by different pH values from 5 to 8 were suggested to undergo separation.

The results of the performed experiments show that the examined electrolyte to produce CoW alloys contains no elementary substances (components used in the course of its preparation). The electrolyte is a mixture of complex compounds.

In some cases, water was used as an eluent in gel-chromatographic separation; in other cases, it was a buffer mixture consisting of all the components of the electrolyte with the same concentrations except for Na_2WO_4 and $CoSO_4$. This approach allowed us to carry out the chromatography in two modes: at a large excess of the citrate ion (favors the "completion" by citrate ions of complex compounds contained by the electrolyte to complexes with larger molecular mass) and, correspondingly, at its absence, when only the disintegration of unstable complex compounds of the electrolyte is possible because of their dissociation.

Using vitamin B12 as a compound etalon with a certain molecular mass (1355 g/mol), the increase in the molecular mass of the complexes taking place at the excess of the citrate ion, and resulting in the formation of complexes with molecular masses of much more than 1355 g/mol was shown. Without any citrate ions in the eluent, the molecular mass of the complex compounds produced during gel-chromatographic separation was smaller than this value.

The more detailed chromatographic study with the use of water as an eluent has shown that the increase in the electrolyte pH (from 5.0 to 8.0) leads to the substantial growth in the molecular mass of the complexes included into its constitution. At pH = 5.0, the molecular mass of the complex compounds in the electrolyte is relatively small (much less than 1200 g/mol). At pH = 7.0, there are complexes with their molecular masses of about 1200 g/mol in the solution, and, at pH = 8.0, these complexes prevail (about 90%).

The anion $[Co_4Cit_4]^{8-}$ with a molecular mass of 992 g/mol and a hexahedron structure was established to be one of the electrolyte's components [6]. This was shown by the coincidence of the positions of the peaks in the gel-chromatograms of the solutions of the syn-

thesized $[Co_4Cit_4]^{8-}$ and the electrolyte produced by separation.

It is shown that only the $[Co_4Cit_4]^{8-}$ anion and a heteropolynuclear Co−W-citrate complex with the relation Co : W being 1 : 1 are high molecular complex compounds characterized by the above mentioned values of the molecular masses. It is established that a heteropolynuclear Co−W-citrate complex is formed in the electrolyte and the growth in the pH value favorably affects its formation.

Obviously, the electrodeposition of the Co−W alloy takes place from the heteropolynuclear Co−W-citrate complex. The fact that the electrodeposition of Co from the $[Co_4Cit_4]^{8-}$ anion takes place was shown.

It may be suggested that the elemental composition of the coatings formed in the case of the electrodeposition of Co−W is determined, on the one hand, by the composition of the heteropolynuclear complex and, on the other hand, by the near-electrode layer pH that depends on the rate of the parallel reaction of the hydrogen evolution (determined both by the electrodeposition potential and by the hydrodynamic conditions) [7]. The growth in the near-electrode layer pH moves the complexation equilibrium towards the formation of products with a high molecular mass.

The evidence of the deposition of Co−W coatings from the corresponding Co−W complexes formed in the solution was previously presented in [8] using the example of the electrodeposition of them from gluconate electrolytes.

REFERENCES

1. Brenner, F., Electrodeposition of Alloys, New York: Academic Press Inc., 1963.

2. Podlaha, E.J. and Landolt, D., Induced Codeposition. I. An Experimental Investigation of Ni−Mo Alloys, *J. Electrochem. Soc.*, 1996, vol. 143, no. 3, pp. 885−892.

3. Podlaha, E.J. and Landolt, D., Induced Codeposition. II. A Mathematical Model Describing the Electrodeposition of Ni−Mo Alloys, *J. Electrochem. Soc.*, 1996, vol. 143, no. 3, pp. 893−899.

4. Eliaz, N. and Gileadi E., Induced Codeposition of Alloys of Tungsten, Molybdenum and Rhenium with Transition Metals, *Mod. Aspects Electrochem.*, 2008, vol. 42, pp. 191−301.

5. Belevskii, S.S., Kosova, A.P., Yushchenko, S.P., Yahova, E.A., Shulman, A.I., and Dikusar, A.I., Changes in the Properties of Citrate Electrolyte Used to Manufacture Cobalt-Tungsten Coatings, *Surf. Eng. Appl. Electrochem.*, 2011, vol. 47, no. 1, pp. 4−8.

6. Hudson, T.A., Berry, K.J., Moubaraki, B., Murray, K.S., and Robson, R., Citrate, in Collaboration with a Guanidinium Ion, as a Generator of Cubane-like Complexes with a Range of Metal Cations: Synthesis, Structures, and Magnetic Properties of $[C(NH_2)_3]_8[(MII)_4(cit)_4] \cdot 8H_2O$ (M = Mg, Mn, Fe, Co, Ni, and Zn; cit = Citrate), *Inorg. Chem.*, 2006, vol. 45, no. 9, pp. 35−49.

7. Belevskii, S.S., Cesiulis, H., Tsyntsaru, N.I., and Dikusar, A.I., The Role of Mass Transfer in the Formation of the Composition and Structure of CoW Coatings Electrodeposited from Citrate Solutions, *Surf. Eng. Appl. Electrochem.*, 2010, vol. 46, no. 6, pp. 570−578.

8. Weston, D.P., Hurris, S.J., Shipway, P.H., Weston, N.J., and Yap, C.N., Establishing Relationship between Bath Chemistry Electrodeposition and Microstructure of Co−W Alloy Coatings Produced from a Gluconate Bath, *Electrochim. Acta*, 2010, vol. 55, pp. 5695−5708.